Università
degli Studi
di Padova

UNIVERSITÀ DEGLI STUDI DI PADOVA

Dipartimento di Fisica e Astronomia “Galileo Galilei”
Scuola di dottorato di ricerca in Astronomia
Ciclo XXVII

Open Clusters as Tracers of the Galactic Disk

Direttore della Scuola: Ch.mo Prof. Giampaolo Piotto
Supervisore: Dr. Antonella Vallenari

Dottorando: Tristan Cantat-Gaudin

Padova, 27 Gennaio 2015

Je demande pardon à mon grand-père d'avoir écrit ce tapuscrit en Anglais.
Je sais qu'il te plaira quand même.

Abstract

Open clusters (OCs) are routinely used as reliable tracers of the properties and evolution of the galactic disk, as they can be found at all galactocentric distances and span a wide range of ages. More than 3000 OCs are listed in catalogues, although few have been studied in details.

The goal of this work is to study the properties of open clusters. This work was conducted in the framework of the *Gaia*-ESO Survey(GES). GES is an observational campaign targeting more than 100,000 stars in all major components of the Milky Way, including stars in a hundred open clusters. It uses the FLAMES instrument at the VLT to produce high and medium-resolution spectra, which provide accurate radial velocities and individual elemental abundances. In this framework, the goals of the Thesis are:

- to study the properties of OCs and of their stars from photometry and spectroscopy to derive their age, the extinction and the chemical composition of the stars, to begin to build a homogeneous data base. Looking at literature data it is clear that different authors derive substantially different chemical compositions, and in general OC parameters.

- the study of OCs and their chemical homogeneity (or inhomogeneity) can cast light on what is still an open issue: the presence of multiple populations in clusters. While multiple generations of stars are now ubiquitously found in globular clusters in the Milky Way and in the Magellanic Clouds, they have not been yet detected in open clusters. What is the main driver of the self-pollution process?

- to study the cluster formation process. All, or at least a significant fraction of stars form in clusters. Young clusters (a few Myr) can retain some of the properties of the molecular cloud they originate from and give us insight about the cluster assembly process. The first GES data release contains data for the young OC Gamma Velorum, in which two (dynamically different) subpopulations have been identified. This cluster can serve as a test case for star formation mechanisms.

- the study of the OCs can shed light on the disk properties, in particular on the presence of a chemical gradient. Studying the distribution of chemical elements across the Galactic disk has been a central question in astronomy for the past decade. The exact shape of this metallicity gradient, revealed by various tracers such as Cepheids, Planetary Nebulae or HII regions is not quite clear. OCs suggest a flattening of the gradient in the outer disk. Here I will investigate the issue using the GES data set.

Methods: The data analysis of the GES is a complex task carried out by different groups. When dealing with a huge quantity of astronomical data, it is essential to have tools that economically process large amounts of information and produce repeatable results. As part of the GES I developed an automated tool to measure the EWs in spectra of FGK stars in a fully automatic way. This tool, called DAOSPEC Option Optimizer pipeline (DOOp), uses DAOSPEC and optimizes its key parameters in order to make the measurements as robust as possible. This tool was widely tested on synthetic and observational spectra. Stellar parameters and elemental abundances are derived with the code FAMA developed with the aim of dealing with large batches of stars. FAMA uses the widely used software MOOG and optimizes stellar parameters in order to satisfy the excitation and ionization balance, following the classical equivalent width procedure. The construction of a metallicity scale, based on high-quality spectra of benchmark stars is fundamental to interpret the spectroscopic results in the context of the Galaxy formation and evolution. We take advantage of the variety of analysis methods represented within the GES collaboration, including DOOp+ FAMA in order to produce a homogeneous metallicity scale. Those reference stars can be used to assess the precision and accuracy of a given method.

Results: Using archival photometric data, I presents an in-depth study of NGC 6705 and Trumpler 20 for which I derive ages of 250–320 Myr and 1.25–1.66 Gyr (respectively). I take advantage of the wide field covered by the VPHAS data to map extinction using field red clump stars as tracers and show that the core of NGC 6705 is situated in an area of low reddening, but the outskirts are seen projected on areas of various levels of extinction, making it difficult to estimate accurately the stellar density, and making estimates of the tidal radius of NGC 6705 unreliable. Differential extinction in the region of Trumpler 20

is estimated using main sequence stars. I find a mass of $6850 \pm 1900\,M_{\odot}$ for NGC 6705, from the luminosity function although strong mass segregation and and patchy extinction in the outskirts of the cluster make this number a lower limit, and derive a total mass of $6700 \pm 800\,M_{\odot}$ for Tr 20. These estimates are in agreement with the mass derived from the velocity dispersion. We find that the apparently broad turn-off region in the CMD of Tr 20 can be explained by differential reddening, but the origin of its notorious extended red clump remains unclear. I presents a membership determination and spectroscopic study for NGC 6705, Trumpler 20, and NGC 4815. We find mean iron abundances [Fe/H]=0.10, 0.17 and 0.16 dex for these three inner disk clusters. I show that within the uncertainties, they are chemically homogeneous clusters. This result adds weight to the hypothesis that only clusters above the mass of 4×10^4 solar masses may be massive enough to form multiple populations.

I study the star-forming region Gamma Velorum, which has recently been shown to be made up of two different populations (A and B) with different kinematical signatures. N-Body simulations suggest that one of the populations (population B) is unbound and rapidly expanding. In addition, the B population is less dense and less concentrated. It also appears marginally more fractal. The supervirial state of population B indicates that star formation efficiency was lower than in A, or that the parent molecular cloud was dispersed very quickly. The presence of multiple clustering of stars as in this region is not peculiar, and is often observed in large star forming regions in the Milky Way and in the Magellanic Clouds.

I present abundance determinations from archived Keck (HIRES) data for four outer disk clusters (Berkeley 22, Berkeley 29, Berkeley 66, and Saurer 1). From their α-element abundances I see no clear sign that these objects are associated with the galactic anticentre structure. Complementing our sample of clusters with preliminary data from the newer GES releases, I confirm that the metallicity gradient is steep in the inner disk and much shallower (or flat) in the outer disk. The presence of a bimodal gradient has important implications on the possible scenarios of galaxy formation and evolution and is predicted by a variety of theoretical models. It comes as a natural outcome of the models involving radial migration.

Riassunto

Gli ammassi aperti sono comunemente utilizzati come traccianti delle proprietà e dell'evoluzione del disco Galattico, dato che sono presenti a tutte le distanze Galattocentriche e hanno una ampia distribuzione di età. I cataloghi esistenti includono più di 3000 ammassi, sebbene solo una minima parte sia stata studiata in dettaglio. Lo scopo del lavoro è studiare le proprietà di un campione di ammassi aperti. Questo lavoro si svolge nel contesto della Gaia-ESO Survey (GES). La GES è una campagna di osservazioni spettoscopiche al telescopio VLT, con lo strumento FLAMES. Osserverà circa 100,000 stelle nella nostra Galassia e circa un centinaio di ammassi. In questo contesto, la Tesi si propone di:

- Studiare le proprietà di un campione di ammassi aperti , per derivare le età, le metallicità da dati di fotometria e spettroscopia. Questo è il primo nucleo di oggetti per la costruzione di un data base omogeneo in grado affrontare il problema della distribuzione di metallicità del disco. I dati di letteratura mostrano chiaramente che autori diversi derivano valori molto diversi e spesso non consistenti della metallicità e in generale dei parametri degli ammassi.

- studiare il problema della omogeneità chimica negli ammassi, che è legato alla presenza di popolazioni multiple. Al momento generazioni multiple sono state trovate solo negli ammassi globulari della nostra Galassia e delle nubi di Magellano, ma non sono ancora state individuate negli ammassi aperti. Questo ci lascia con la domanda ancora aperta su quale sia il fattore determinante nella formazione di popolazioni multiple

- Si ritiene che la maggior parte delle stelle si formi in ammassi. Ammassi giovani possono darci informazioni sul processo di formazione, dato che ancora mantengono alcune delle proprietà della nube dalla quale si sono formate. I primi dati GES contengono l'ammasso Gamma Velorum, dove sono state identificate due sottopopolazioni. Questo oggetto costituisce un test dei modelli di formazione

- Lo studio degli ammassi aperti è fondamentale per definire le proprietà del disco e in particolare per chiarire le caratteristiche del gradiente chimico radiale. La forma esatta del gradiente radiale, come tracciata da varie classi di oggetti (Cefeidi, Nebulose Planetarie, regioni HII) è ancora oggetto di discussione. Gli ammassi aperti suggeriscono un appiattimento del gradiente nel disco esterno. Questo problema è discusso usando gli ammassi.

Metodi: I dati GES vengono analizzati da diversi gruppi, con dei tools automatici che sono in grado di processare grandi quantità di dati e produrre risultati ripetibili. Come parte della GES ho sviluppato un tool automatico per misurare le larghezze equivalenti delle stelle FGK. Questo tool (DOOp) si basa su DAOSPEC per fare le misure e ottimizza i parametri fondamentali, rendendo i risultati solidi. DOOp è stato ampiamente testato su stelle sintetiche e osservate. I parametri stellari e le abbondanze chimiche sono state derivate con la procedura automatica FAMA, in grado di gestire grandi quantità di dati. FAMA si basa sul codice MOOG, ampiamente usato in litteratura, e ottimizza i parametri stellari fino a raggiungere l'equilibrio di eccitazione e ionizzazione , secondo il metodo delle larghezze equivalenti. La costruzione di una scala delle metallicità è stata fondamentale per omogenizzare i risultati ottenuti da metodi diversi. Abbiamo utilizzato un gruppo di stelle di riferimento di proprietà ben conosciute che sono state analizzate con vari metodi inclusi DOOp e FAMA. Questa analisi ha permesso di derivare la precisione e l'accuratezza dei vari metodi.

Risultati: L'analisi di dati fotometrici di archivio ha permesso uno studio approfondito di NGC 6705 and Trumpler 20, per i quali ho derivato età rispettivamente di 250–320 Myr e 1.25–1.66 Gyr. L'uso della fotometria VPHAS+ ha permesso di derivare l'estinzione nella direzione dell'ammasso NGC 6705, utilizzando le stelle di red clump come traccianti. Mentre il centro dell'ammasso si trova una regione di bassa estinzione, le regioni esterne sono proiettate contro aree di estinzione più alta e variabile su piccola scala spaziale. Questo rende molto difficile stimare in modo attendibile il raggio mareale dell'ammasso. E' stato stimato l'arrossamento differenziale di Trumpler 20 usando le stelle di sequenza principale. Ho derivato una massa di $6850 \pm 1900\,\mathrm{M}_\odot$ per NGC 6705, dalla funzione di luminosità, anche se la presenza di segregazione di massa e di arrossamento differenziale rendono questo valore un limite inferiore. Nel caso di Trumpler 20 si ricava una massa di $6700 \pm 800\,\mathrm{M}_\odot$. Queste determinazioni sono in accordo con i valori ricavati dalla dispersione di velocità. In questo ammasso, l'allargamento anomalo della sequenza principale può essere in parte dovuto all'arrossamento differenziale. Questa ipotesi però non sembra essere in grado di spiegare la struttura peculiare del red clump. Sono state discusse le abbondanze chimiche di NGC 6705, Trumpler 20, and NGC 4815, derivando rispettivamente [Fe/H]=0.10, 0.17 and 0.16 dex. Questi ammassi del disco interno sono chimicamente omogenei. Le loro proprietà sono consistenti con lo scenario nel quale solo ammassi più massicci di circa $10^4\mathrm{M}_\odot$ sono in grado di produrre generazioni multiple.

Sono state analizzate le proprietà della regione di formazione stellare Gamma Velorum, dove sono state trovate due popolazioni (A e B) con differenti caratteristiche cinematiche. Simulazioni N-body suggeriscono che la componente B non è gravitazionalmente legata e si

sta espandendo rapidamente. Inoltre B ha più bassa densità stellare, ha una distribuzione meno concentrata, ed ha una struttura marginalmente più frattale. Il suo stato superviriale indica che la efficienza della formaione stellare è stata più bassa che nella componente A, o che la nube molecolare originaria è stata dispersa più velocemente. La copresenza di due modi di formazione trovati in questa regione non è peculiare, ma si ritrova in altre regioni giovani nella nostra Galassia e nelle Nubi di Magellano.

Sono state ricavate le abbondanze chimiche di alcuni ammassi del disco esterno, Berkeley 22, Berkeley 29, Berkeley 66, and Saurer 1, utilizzando dati di archivio KECK (HIRES). Le abbondanze degli elementi α sono per tutti gli ammassi in accordo con l'ipotesi che si tratti di oggetti di disco e non che siano associati alla struttura trovata nell'anti-centro Galattico. Questi ammassi, insieme a quelli GES hanno permesso di studiare il gradiente radiale del disco, confermando l'appiattimento nelle regioni esterne. La presenza di un gradiente bimodale ha importanti implicazioni per comprendere la formazione del disco ed e' predetta da vari modelli teorici. In particolare è un risultato naturale del processo di migrazione radiale

INTRODUCTION

Open clusters (OCs) are systems made up of a few dozens to several thousands of gravitationally bound stars. Those stars share a common history, in that they form at the same time (they are **coeval**) from the same molecular cloud (they have the same original **chemical composition**). From photometric data, it is possible to estimate the age and distance of an open cluster with a relatively good accuracy with respect to other astronomical objects. Since they are distributed all across the disk of our Galaxy (known OCs have galactocentric radii from 4 kpc out to 22 kpc), they are natural tracers of the Galactic disk. Moreover, they span a wide range of ages (from a few Myr to 9 Gyr), enabling to probe properties of the disk at different epochs and tackle the question of the evolution of the Milky Way.

In this framework, the main aspects this Thesis focuses on are the following:

- Studying the properties of the OCs and of their stars from photometry and spectroscopy to derive the age, the extinction and the chemical composition of the stars to begin to build an homogeneous data base. Looking at literature data, it is clear that different authors derive substantially different chemical compositions, and in general, OC parameters. In this Thesis I will make use of photometric data, and of *Gaia*-ESO Survey (GES) spectroscopic data. The GES is an ongoing 5-year spectroscopic survey which aims at targetting 100,000 stars from all major components of the Milky Way, including 100 OCs. The spectroscopic data used in this work is based on the first GES data release, and on literature data.

- The study of OCs and their chemical homogeneity and inhomogeneity can cast light on a still open issue, related to the multiple populations in clusters. While multiple generations of stars are now ubiquitously found in globular clusters in the Milky Way and in the Magellanic Clouds, they have not been yet detected in open clusters. What is the main drive of the self-pollution process? It has been suggested that this fundamental difference is due to the inferior mass of OCs. If the initial cluster mass is the main parameter governing the multiple population formation, what is the mass limit? Further insight about this scenario will be derived through careful analyses of a few massive OCs.

- All, or at least a significant fraction of stars form in clusters. The process through which clusters are disrupted and their stars dispersed among the field population of the Galactic disk is not well understood yet. Young clusters (a few Myr) can retain some of the properties of the molecular cloud they originate from and give us insight about the cluster assembly process. The first GES data release contains data for the young OC Gamma Velorum, in which two (dynamically different) subpopulations have been identified. This cluster can serve as a test case for star formation mechanisms.

- The study of the OCs can cast light on the properties of the disk, in particular on the presence of a chemical gradient. Studying the distribution of chemical elements across the Galactic disk has been a central question in astronomy for the past decade. It has been established that the outer parts of the Galaxy are more metal-poor than the central regions, and that the chemical distribution can be represented as a unidimensional, negative **radial metallicity gradient**. The exact shape of this metallicity gradient, revealed by various tracers such as Cepheids, Planetary Nebulae or HII regions is not quite clear. The gradient traced by OCs appears to present a negative slope of about $-0.06\,\mathrm{dex\,kpc^{-1}}$ in the inner 10 or 12 kpc of the disk, and to flatten in the outer parts. Hints have been found that OCs of different ages may trace different slopes, or that the transition radius between the negative and the flat regime may have changed. The picture is still unclear. Less than 10% of the 2000 known OCs have associated metallicity estimates, and few come from high-resolution spectroscopy. The results available in the literature come from a variety of authors using a variety of methods, and do not constitute a homogeneous sample. Here I will investigate the issue using the GES data set, where special care is paid to deriving careful calibration of the metallicity scale.

The outline of this PhD Thesis is as follows. Chapter 1 presents a review of the current state of knowledge on open clusters and the Galactic disk. In Chapter 2 I introduce the *Gaia*-ESO Survey, and Chapter 3 presents the methods that I developed and/or helped developing to respond to the technical challenges posed by the analysis of the large amount of data acquired by GES. Chapter 4 presents an in-depth photometric study of NGC 6705 and Trumpler 20 in which ages, distances and masses (in particular) were derived. Chapter 5 presents a spectroscopic study of NGC 6705, Trumpler 20, and NGC 4815, focusing in particular on membership determinations and the chemical homogeneity of clusters. Chapter 6 is an analysis of the stellar distribution in the young cluster Gamma Velorum, aiming at studying the formation process which led to its peculiar dynamical structure. Chapter 7 presents abundance determinations for Berkeley 22, Berkeley 29, Berkeley 66, and Saurer 1, and comments on the metallicity gradient as traced by our sample in the inner and outer disk. Finally, Chapter 8 presents the main conclusions.

CONTENTS

LIST OF ACRONYMS AND ABBREVIATIONS

2MASS Two Micron All Sky Survey in near-infrared passbands
CMD Colour-Magnitude Diagram
DAML02 The catalogue of open clusters by Dias et al. (2002)
DOOp Daospec Option Optimiser pipeline (Cantat-Gaudin et al., 2014a)
DR Differential Reddening
EP Excitation Potential
ESO European Southern Observatory
EW Equivalent Width
EWR Reduced Equivalent Width
FAMA Fast Automatic Moog Analysis (Magrini et al., 2013)
FWHM Full Witdh at Half Maximum
GASS Galactic Anticentre Stellar Structure
GC Globular CLuster
GES *Gaia*-ESO Survey
HR Hertzsprung-Russel
IMF Initial mass function
MS Main Sequence
MST Minimum Spanning Tree
MSTO Main Sequence Turn Off
MW Milky Way

MWSC Milky Way Star Clusters catalogue (Kharchenko et al., 2013)
OC Open Cluster
R Resolution of a spectrum or resolving power of an instrument: $R = \lambda/\Delta\lambda$
RC Red Clump
RGB Red Giant Branch
S/N Signal-to-noise ratio
SDSS Sload Digital Sky Survey
UVES Ultraviolet and Visual Echelle Spectrograph, mounted on the 8.2m VLT-UT2.
VLT Very Large Telescope, operated by ESO at Cerro Paranal, Chile.
WFI Wide Field Imager, mounted on the 2.2m MPG/ESO telescope at La Silla.

CHAPTER 1

STATE OF THE ART: OPEN CLUSTERS AND THE GALACTIC DISK

Our Galaxy is a large stellar system, in which the majority of stars do not form isolated, but rather form in clusters (Baumgardt & Kroupa, 2007). Those groups of stars retain some of the properties of the environment in which they were born, and in particular they retain the chemical composition of the gas cloud they originate from. Since it is possible to estimate the age of stellar cluster with sufficient accuracy, open clusters (OCs) are good tracers of the properties of the Galaxy at different locations and different epochs. This chapter summarises our knowledge of the structure of our Galaxy and what different tracers, including open clusters, reveal about the galactic disk.

1.1 Open clusters

Groups of stars that are visible to the naked eye such as the Pleiades or the Hyades have been identified as "clusters" for a long time. Among the modern-day catalogues of clusters we can cite the web interface WEBDA (Mermilliod, 1995)[1], which references previous catalogues of Lauberts (1982) and Lynga (1987) catalogue. The number of known OCs

---

[1] `http://www.univie.ac.at/webda/`

increased in the late 1990's after the data of the HIPPARCOS mission was available, and Dias et al. (2002) (hereafter DAML02) compiled a catalogue of 1700 objects, including morphological parameters and, when available, metallicities.

More recently, (Kharchenko et al., 2013) studied 3784 object, confirming 2808 of them (74%) are OCs, and they derived astrophysical parameters in their catalogue called Milky Way Star Clusters (MWSC). They did not derive new metallicities for those objects.

In this section, we will flip through some of these catalogues and describe the main properties of open clusters.

1.1.1 Definition

Orignally, a group of stars that stands out as an overdensity and presents a dense, spherical distribution was classified as a **globular cluster** (GC), and less rich or more irregularly shaped groups were called **open clusters**. Remarking that they lie preferably along the path of the Milky Way, Trumpler (1925) called OCs **galactic clusters**. Today's definition is still not very stringent, and in particular it fails to clearly distinguish OCs from GCs, because of the variety of angular sizes, densities and ages they can exhibit. The working definition of Friel (1995) is that OCs are *"sparsely populated, loosely concentrated, barely gravitationally bound systems of a few tens or hundreds of stars"*. The condition that the stars must be physically related and gravitationally linked is important, as it sets a lower limit on the mass and number of cluster members. Lada & Lada (2003) use a physically motivated working definition of a star cluster, requiring that it needs to be *"stable against tidal disruption"*. In practice, the cluster needs to be dense enough to avoid being torn apart by the galactic tidal field (stellar density $\rho_* > 0.1\,\mathrm{M}_\odot$, Bok, 1934) and by passing molecular clouds ($\rho_* > 1\,\mathrm{M}_\odot$, Spitzer, 1958). They establish that in order to survive 10^8 yrs, such a cluster must have at least 35 member stars. Less rich systems can be classified as **stellar associations**, which will get disrupted on short timescales.

On the high-mass end, the morphological arguments for the distinction between OCs and GCs are less clear. Some of the least massive GCs, like for instance Terzan 7, do not present a perfectly regular spherical distribution, while massive OCs like NGC 6791 appear more spherical. To this day there is no obvious definition that can distinguish a GC from an OC. However, OCs are always associated with the disk of our Galaxy while GCs are mostly associated with its halo. Open clusters are also younger than GCs, which are typically older than 10 Gyr (although some OCs like Be 17 can reach ages of 9 Gyr, Bragaglia et al., 2006) and more metal-rich. A new approach to the distinction between OCs and GCs was brought by Carretta et al. (2010), who have studied the chemical homogeneity of 19 GCs and observe inhomogeneities in abundances of Na and O for all of them. Stars with higher Na abundances tend to have lower O. They suggest this Na-O anticorrelation could be a universal feature of GCs, and since OCs with inhomogeneous populations have not been discovered, a fundamental difference between GCs and OCs. The driving factor for the presence of an anticorrelation could be the mass of the cluster, but it could also reflect the different nature and origin of these two types of clusters. More details about chemical inhomogeneities in clusters are discussed in Sect. 1.1.3.

In this section, we review the main properties of open clusters.

1.1.2 Properties

Spatial distribution

Open clusters are mostly found along the Milky Way strip, and belong to the disk of the Galaxy. The top panel of Fig. 1.1 shows the sky distribution of all 2174 OCs in the current version of the DAML02 catalogue. The distribution clearly follows the galactic plane, with OCs constrained at low galactic latitudes for a dispersion of only 8° around the plane. The bottom panel of Fig. 1.1 shows the distribution projected on the galactic plane. Some OCs can be found 4 kpc from the galactic centre, while others can be seen as far as 20 kpc.

Open clusters span a large range of ages, from a few Myr to several Gyr. The oldest known OCs reach 10 Gyr (Be 39 and NGC 6791, Bragaglia et al., 2012; Geisler et al., 2012, respectively). The age distribution for the 1629 DAML02 OCs that have age estimates (75% of the catalogue) is shown in the upper panel of Fig. 1.2. Some differences can be observed between the spatial distribution of young and old OCs. In particular, old clusters exhibit a wider distribution above the galactic plane while younger OCs have a tighter distribution (Bonatto et al., 2006; Buckner & Froebrich, 2014), as illustrated in the bottom panel of Fig. 1.2, where the DAML02 sample has been split into two age groups around the age of 200 Myr (log(t)=8.3). The dispersion in altitude for the old sample is 305 pc, while for the young sample it is only 135 pc. We can also see that clusters in the inner disk tend to be younger than in the outer disk. In a dense environment such as the inner disk, a cluster is more likely to be disrupted early than in the outer disk where its survival rate may be higher.

The observed lack of old clusters in the inner regions of the disk may also be partially due to observational biases, simply because against a crowded background it is easier to detect the bright, blue stars of a young cluster than the fainter and redder stars of an older cluster. Interstellar extinction also contributes to this problem, and recently near-IR surveys like 2MASS and VVV have been proved more efficient than optical data to detect new clusters (Borissova et al., 2011; Froebrich et al., 2007; Schmeja et al., 2014).

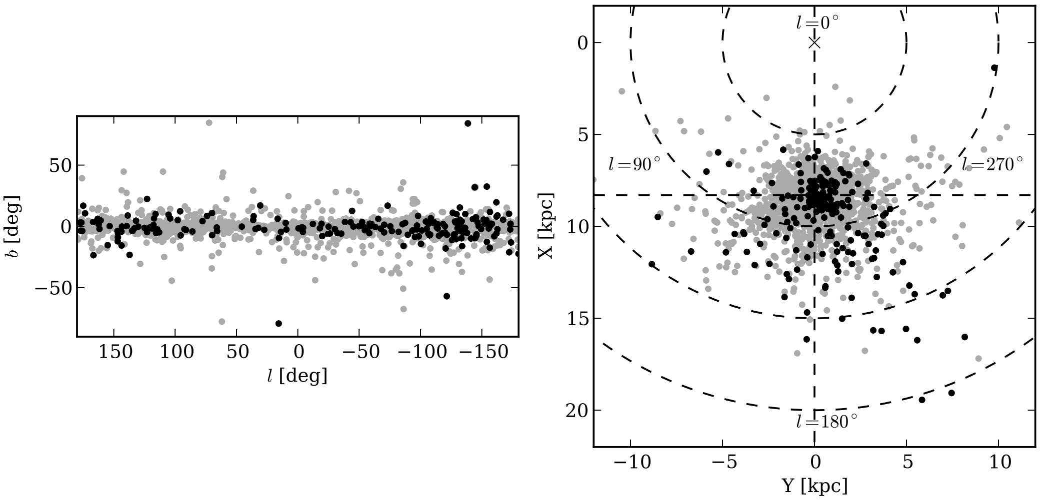

Figure 1.1: *Left:* sky position of all 2174 OCs of the DAML02 catalogue, in galactic (l, b) coordinates. *Right:* distribution of all 1657 DAML02 OCs that have corresponding distance estimates, projected on the galactic plane (assuming a solar galactocentric distance of 8.3 kpc). In both panels, the black points indicate clusters for which metallicity values are available.

Young OCs happen to trace closely the gas distribution in the disk, which is spread in a thin sheet of scale height 50–100 pc along the galactic plane. During the life of a cluster, irregularities in the gravitational potential of the Galaxy increase its random motion, leading it away from the plane. As a consequence, the scale height for old clusters is larger than for younger ones.

This thickening of the vertical distribution of clusters is not the only difference in distributions between young and old objects. Since star formation in our Galaxy occurs mainly in the spiral arms (Martínez-García & Puerari, 2014; Roberts, 1969), the younger stars (which have not been dispersed away from their birth sites) trace the spiral structure. Dias & Lépine (2005) show that young OCs (ages <10 Myr) trace the spiral arms, while older clusters have moved away from their birthplace and have lost their originally tighlty constrained spatial distribution (Fig. 1.3).

Cluster formation, evolution, disruption

Bastian (2011) offers a review on cluster formation and disruption. Clusters are formed

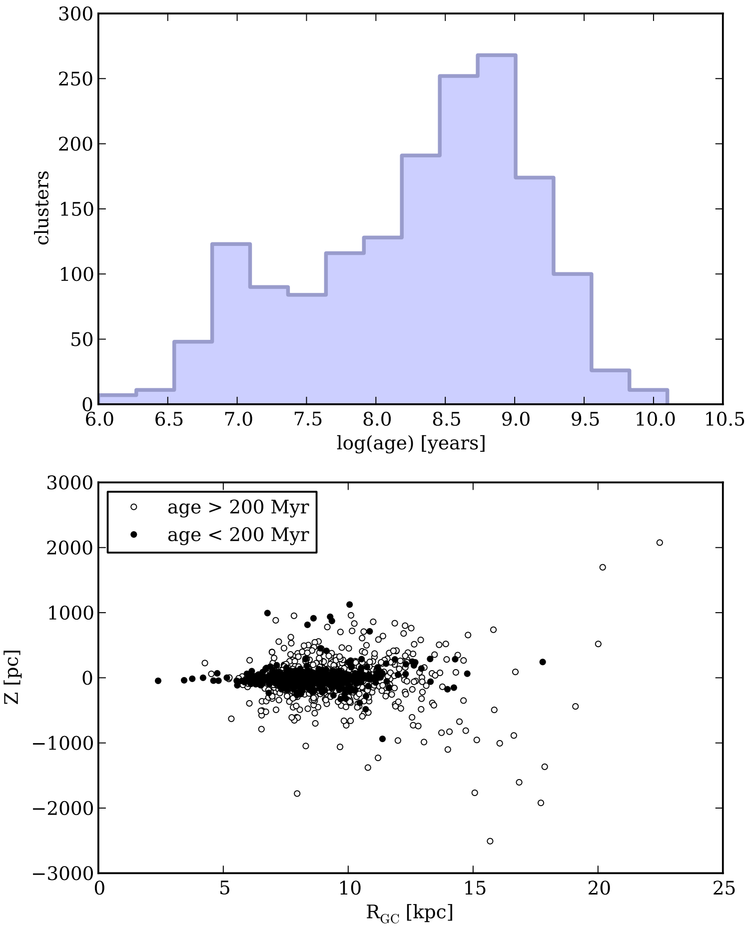

Figure 1.2: *Top:* age distribution of the 1629 OCs with age estimates in the DAML02 catalogue. *Bottom:* height above the galactic plane against galactocentric radius, for two different age groups.

in the dense cores of giant molecular clouds (GMCs). Clusters that are still surrounded by their primordial gas are called **embedded clusters**. Gutermuth et al. (2008) studied the star distribution in the embedded star-forming region NGC 1333. They show that younger stars trace very well the filamentary distribution of gas in the region, showing that clusters do not form as centrally concentrated systems, but rather as filamentary systems that follow the hierarchical structure of their parent GMC. The stars forming from this structure may merge and form a stellar system, or they may disperse.

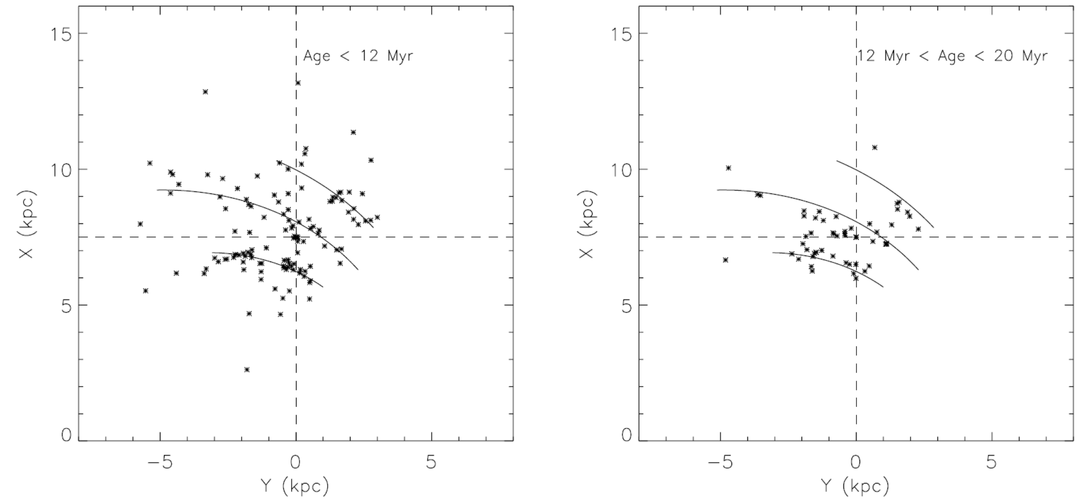

Figure 1.3: Dias & Lépine (2005) have shown that young clusters (left) trace the spiral arm pattern more closely than older clusters.

In its early phase, a cluster is made up of both stars and gas. Stellar feedback expulses the wind from the cluster. If the star+gas cluster was in virial equilibrium, the loss of gas leaves it in a supervirial state: the cluster will expand towards a new virial equilibrium. A significant amount of stellar mass can be lost in this process (**infant weight-loss**). When a GMC collapses into a star cluster, only a fraction of the gas (typically 30–60%, Lada & Lada, 2003) is turned into stars. Bastian & Goodwin (2006) indicate that if the star formation efficieny (the fraction of gas that is turned into stars) is under 30%, the cluster will be entirely disrupted after the gas content is lost **infant mortality**.

Embedded clusters, which are enshrouded in gas and dust, may be invisible at optical wavelengths. They are more easily detected in IR bands. For instance, Dutra & Bica (2001) have discovered 42 previously unknown OCs using data from the infrared catalaogue 2MASS. More recently, Borissova et al. (2011) found 96 new open clusters and stellar groups in the VVV survey data (most of which are less than 5 Myr old), suggesting many OCs are still to be detected in the years to come.

1.1.3 Chemical compositions

The metallicity of an open cluster can be estimated photometrically (from its CMD) or from spectroscopy of individual stars. Only 202 OCs (9%) of the DAML02 clusters have associated metallicities, and most of them are close to the Sun. The distant OCs for which metallicities were determined are often outer disk clusters (see Fig. 1.1). Their metallicity distribution is shown in Fig. 1.4. The higher number of known OCs with solar metallicities reflects the fact that most known clusters, and in particular those with metallicity estimates, are in the solar neighbourhood. About half the metallicities quoted in the DAML02 catalogue were obtained by photometric methods such as UBV colour excess (Loktin, 1998), DDO (Twarog & Anthony-Twarog, 1994) or Strömgren (Anthony-Twarog & Twarog, 2006) photometry, while the other half comes from spectroscopy.

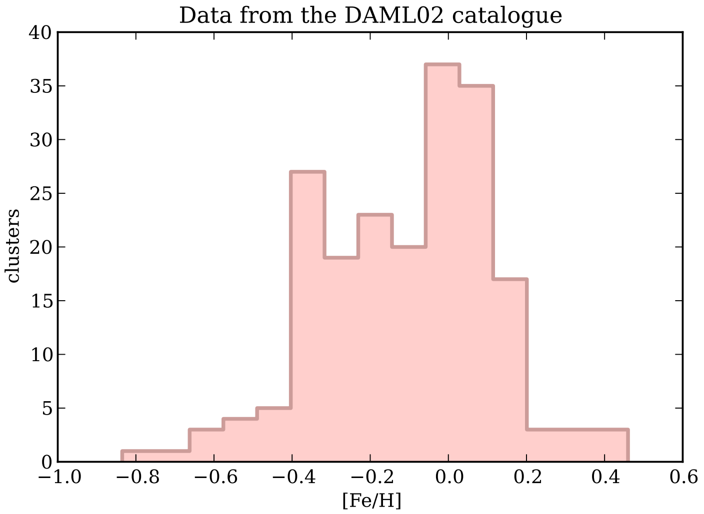

Figure 1.4: Metallicity distribution of OCs in the DAML02 catalogue.

An important observation that can be made combining information on age and metallicity is the absence of a clear **age-metallicity relation** (see Fig. 1.5). Although young clusters of low metallicity seem rarer, the correlation between the age of a cluster and its metallicity is very loose, as noted in many studies (Bragaglia & Tosi, 2006; Carraro et al., 2007; Friel & Janes, 1993; Friel et al., 2002; Jacobson et al., 2011; Magrini et al., 2009a; Pancino et al., 2010).

While photometric determinations of metallicity only provide a one-dimensional measurement of the heavy element content, spectroscopy allows for individual elemental abundances to be estimated. We have learnt in the last decade that in most globular clusters, star-to-star variations in Na, O, Mg, Al, or Si abundances can be observed (see e.g. the reviews by Gratton et al., 2004, 2012). This discovery of chemical inhomogeneities in globular clusters, which were believed to be homogeneous simple populations naturally asked the

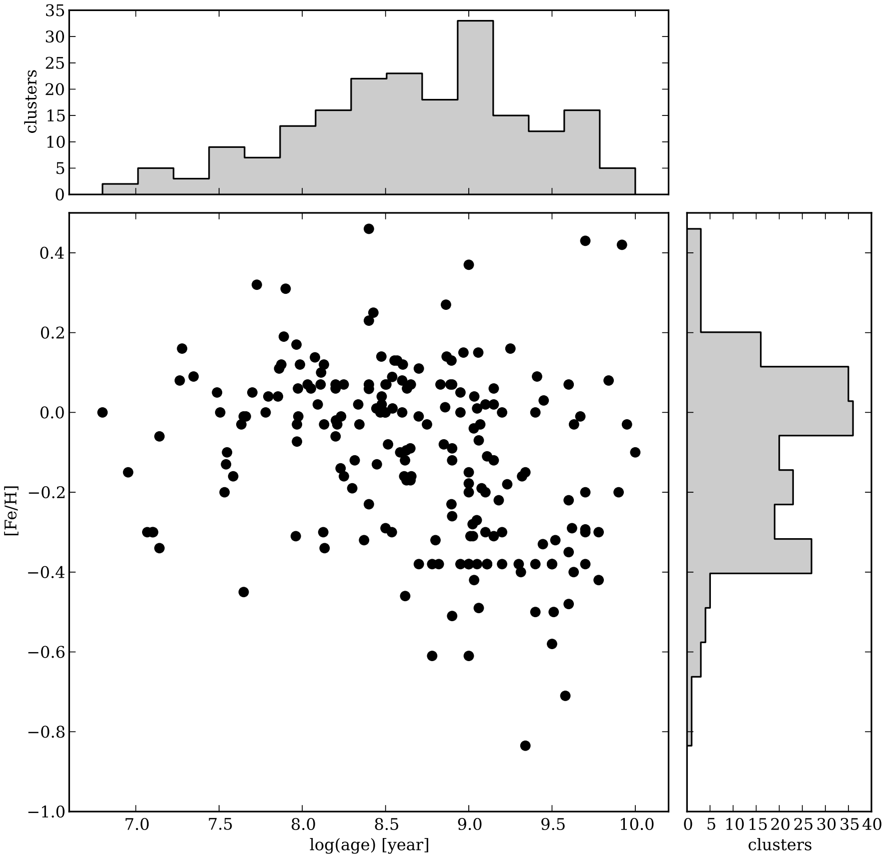

Figure 1.5: Age and metallicity distribution for DAML02 clusters.

question of the homogeneity of open clusters. So far, no conclusive evidence for chemically inhomogeneous OCs have been found, leading Carretta et al. (2010) to propose a definition to distinguish OCs from GCs, based on the presence of chemically inhomogeneous populations.

All these models predict that the mass of a cluster is a driving parameter in the appearance of multiple populations (retaining more processed material and making accretion more efficient), which could explain why GCs exhibit multiple populations and OCs do not. This has prompted studies of low-mass GCs and high-mass OCs. The low-mass GCs Terzan 7 and Palomar 12 were shown to be chemically homogeneous. A currently controversial object is the massive open cluster NGC 6791, in which (Geisler et al., 2012) observe chemical inhomogeneities while (Bragaglia et al., 2014) find none. More high-resolution spectroscopy of clusters sitting around the $\sim 10^4 \mathrm{M}_\odot$ mass threshold proposed by Carretta et al. (2010) and Bland-Hawthorn et al. (2010) are needed in order to better define the fundamental difference between OCs and GCs.

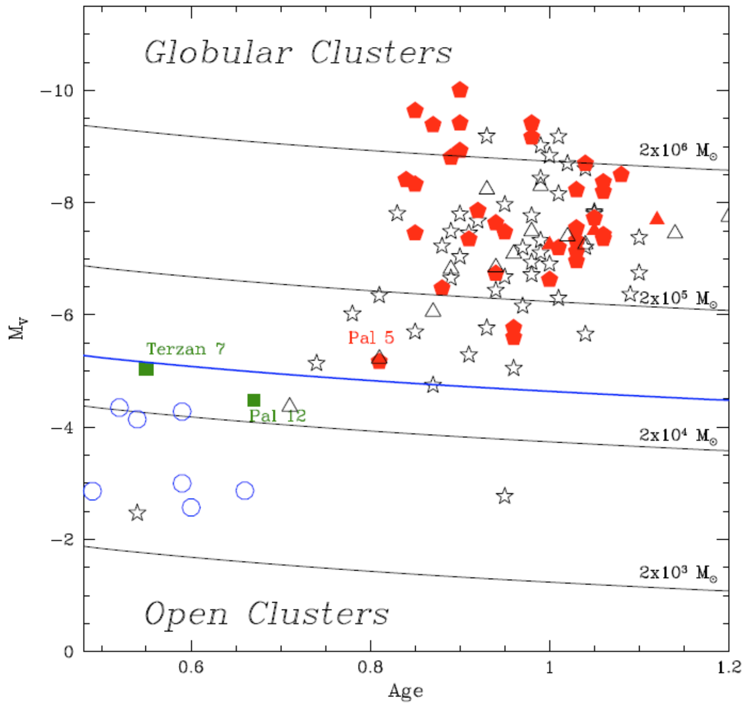

Figure 1.6: Age and mass for the set of clusters of Carretta et al. (2010). Red symbols indicate clusters for which multiple populations were detected.

1.2 Structure of the galactic disk

The general shape of our Galaxy is a large, flat structure. In the night sky, the plane of the Galaxy appears as a bright circular stripe, traditionally refered to as "the Milky Way". The brightness of this stripe may seem uniform in all direction and suggest that we sit in the middle of a disk-shaped Galaxy. It has been known since Shapley (1918) that the position of the Sun is in fact roughly half way between the centre and the edge of the disk, and current estimates place the galactocentric radius of the Sun around 8.3 kpc (Eisenhauer et al., 2005; Reid, 1993), for a total radius of the disk around 15 kpc. The Sun sits approximately 15–20 pc above the plane of the Galaxy (Magnani et al., 1996). Apart from this disk-like structure, our Galaxy exhibits a thicker feature which dominates in the inner 3 kpc (Launhardt et al., 2002) called the galactic bulge. The bulge has been shown to be elongated (Babusiaux & Gilmore, 2005) and form a barred, or more complex structure. The Galaxy is also surrounded with a spherical halo that extends out to 200 kpc (Zaritsky, 1999).

This decomposition in three main structures (disk, bulge/bar, halo) is the traditional view on our Galaxy. This study focuses on the structure and chemical distribution in the disk. The disk contains an estimated 5×10^{10} $M_\odot$ of stars, which constitutes most of the 1×10^{11} $M_\odot$ of baryonic mass of the Galaxy. It also hosts most of the Galaxy's stock of gas, which means that star formation almost exclusively takes place in the disk.

The stellar density profile perpendicular to the plane of the Galaxy cannot be modeled as a single exponential disk, but is rather better fitted with a two-exponential decomposition into a **thin disk** and a **thick disk**. This was first shown in the Milky Way by Gilmore & Reid (1983) (see Fig. 1.7), and is accepted to be a common feature of galactic disks (Burstein, 1979; Tsikoudi, 1979; Yoachim & Dalcanton, 2006). The current scale height estimates for the two exponential components are 300 pc for the thin disk and 900 pc for the thick disk (Jurić et al., 2008) with scale lengths of 2.5 kpc and 3.6 kpc, repectively (Robin et al., 2003).

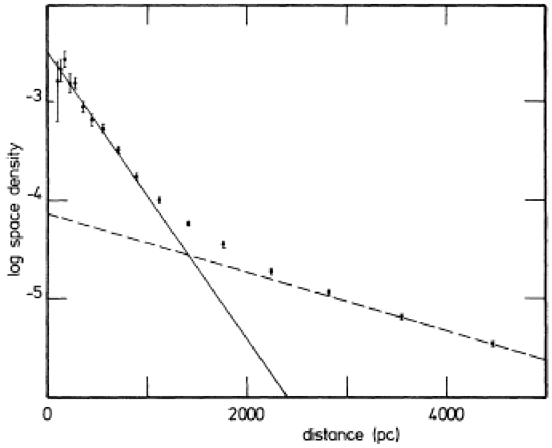

Figure 1.7: Vertical stellar density profile from Gilmore & Reid (1983). The density profile is best reproduced with two exponential components of scale height 300 and 1350 pc, corresponding to the thin and thick disk (respectively).

The dichotomy between the two components of the disk is not just a matter of stellar density distribution. It has been shown that the thin and thick disk are chemically distinct (e.g. Bensby et al., 2003; Gratton et al., 2000) and form a bi-modal distribution, with the thick disk stars being more metal-poor and showing higher relative abundances of α elements, indicating that they are older. The thick disk stars are also kinematically hotter (Bensby et al., 2005; Chiba & Beers, 2000), suggesting a different dynamical history. The existence of the thick disk could be a natural dynamical evolution of the disk, or due to mergers that have heated a (previously thin) disk. Recently, Bovy et al. (2012) argued that the apparent bi-modal distribution may be an artefact of sampling biases, and that it could be conceptually better to think of the thin/thick disk distinction as continuous rather than bi-modal.

About one fifth of the disk mass is in the form of gas. The gas exists in three forms: i) dark, cold (10–20 K) molecular clouds (mostly H_2 with traces of CO), ii) diffuse cold (~100 K, Spitzer & Savedoff, 1950) clouds of atomic hydrogen called HI regions, and iii) hot (several thousand K) HII regions where the gas is ionised by hot, young stars. The HI distribution can be followed with radiotelescopes using the 21-cm H emission line. Such studies reveal a thin sheet of HI with scale height 100-200pc (Dickey & Lockman, 1990).

A notable feature of the disk of our Galaxy is the presence of a spiral pattern. The presence of a spiral structure seems to be a ubiquitous feature of disk galaxies, and observations show that ours is no exception (Morgan et al., 1952). The disk holds most of the gas stock, and is therefore the locus of most star formation. Because of the presence of a spiral pattern, that induces shockwaves and triggers gravitational collapse of gas clouds, star formation is more efficient in the arms than in the inter-arms region and the distribution of gas and young stars reveals a spiral structure. The exact shape of the spiral is difficult to determine since we are sitting inside of it. Drimmel (2000) use infrared K-band photometry to trace two spiral arms, while Levine et al. (2006) see four arms in their 21-cm radio data. Statistical compilations (Vallée, 2002, 2005) show an increasing number of studies concluding to the existence of four distinct arms, and a pitch-angle of 10°–20°, which is typical of spiral disks (Kennicutt, 1981). Following Hubble's classification (Hubble, 1926), our Galaxy is a late-type, Sbc spiral.

The disk of our Galaxy is not perfectly flat. Beyond the solar radius it bends towards the north galactic pole for $0^\circ < l < 180^\circ$ (1st and 2nd galactic quadrants), and towards the south for $180^\circ < l < 360^\circ$ (3rd and 4th galactic quadrants), as was first observed through ionised hydrogen emission (Burke, 1957; Kerr, 1957; Westerhout, 1957). This feature, called **warp**, is common among external galaxies (Briggs, 1990; García-Ruiz et al., 2002b). Cox et al. (1996) show that the stellar content of disks warps in the same way as the HI profile, indicating a gravitational origin for the warp. In our Galaxy, the bending of the disk possibly originates from the presence of dwarf galaxies satellites such as the Large Magellanic Cloud (García-Ruiz et al., 2002a; Weinberg & Blitz, 2006).

1.3 Abundance gradients

1.3.1 Gradients revealed by different tracers

The distribution of heavy chemical elements is not homogeneous across the Galaxy. The inner regions of the disk are seen to be more metal-rich than the outer parts. It is usually assumed that chemical elements are well-mixed in annuli of a given galactocentric radius, and the elemental distribution in the disk is usually studied in terms of a one-dimensional **radial metallicity gradient**, with a direct correspondance between the galactocentric radius of an object and its metal content. Tracers of different ages testify for different epochs and represent different evolutionary stages of the Galaxy. This section summarises the current state of our observational knowledge of the galactic metallicity gradient revealed by different tracers.

Cepheids

Cepheids are variable stars that have been used as distance indicators even since it was shown that they feature a tight period/luminosity relation (Leavitt & Pickering, 1912), which can be refined by considering the metallicity dependence of the period (e.g. Groenewegen, 2013). Being able to relatively easily pinpoint their position in the Galaxy makes them natural tracers of the structure of the disk. They are also cool enough for their spectra to feature a absorption lines for many elements. Most Cepheids studies are remarkably consistent and report a steady, negative gradient of $-0.06\,\mathrm{dex\,kpc^{-1}}$ (see Caputo et al., 2001; Genovali et al., 2013; Harris, 1981; Lemasle et al., 2013, and references therein) (Fig. 1.8). However, the data of Lépine et al. (2011) suggest a step distribution, with a break 1 kpc beyond the solar radius, along with an azimuthal gradient in the solar neighbourhood. They also notice a relatively low number of Cepheids at the radius of the break, and attribute this distribution and the observed gradients to the influence of the spiral pattern on the disk.

Planetary Nebulae

Planetary Nebulae (PNe) represent the final phase in the evolution of stars with masses ranging from 0.8 to $8\,\mathrm{M}_\odot$ (Maciel et al., 2009). This mass range corresponds to progenitors

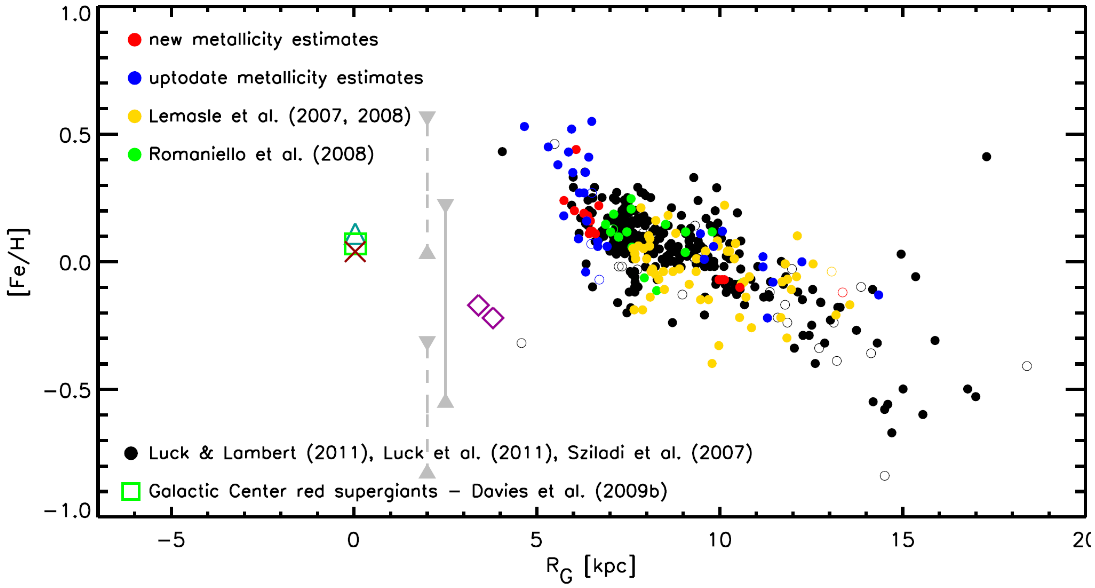

Figure 1.8: Metallicity gradient of Genovali et al. (2013) traced with cepheids.

that formed a few 10^7 years ago (for the most massive ones) to several 10^9 years ago (for the least massive).

Pasquali & Perinotto (1993) find a slope of $-0.05\,\mathrm{dex\,kpc^{-1}}$ and note the possibility that the interstellar medium was more inhomogeneous in the past than in the present time. The data gathered by Henry et al. (2010) shows a steeper slope of $-0.058\,\mathrm{dex\,kpc^{-1}}$ and suggests a possible steepening of the gradient in the outer disk. The oxygen gradient slope obtained by Stanghellini & Haywood (2010) is $-0.023\,\mathrm{dex\,kpc^{-1}}$, and they note that the gradient is steeper for those PNe with the most massive (and most short-lived, therefore more recent) progenitors, hence suggesting that the gradient might be steepening with time.

HII regions

Ionised hydrogen traces the regions of star formation, and therefore their chemical abundances reveal the current composition of the interstellar medium. Metallicity determinations are obtained from radio recombination lines, which are not obscured by galactic extinction and therefore allows for detections at large distances from the Sun. This method relies on the determination of electron temperatures, which are higher in low-metallicity regions and therefore allow to trace the abundance gradient across the disk (Shaver et al., 1983). However, the relation between electron temperature and metallicity also depends on the exact composition in heavy elements, making the abundance determinations more uncertain (Rood et al., 2007).

Distance determinations to HII regions are obtained from the so-called “kinematic distance” method which conists in comparing the observed radial velocity of a region with the rotation curve of the Galaxy, and are less accurate than for other tracers. Despite these difficulties, all recent results (Rood et al., 2007; Rudolph et al., 2006; Simpson et al., 1995) agree on the presence of a negative metallicity gradient of $-0.03\,\mathrm{dex\,kpc^{-1}}$ to $-0.08\,\mathrm{dex\,kpc^{-1}}$, with a possible dependence on galactic azimuth (Balser et al., 2011).

OB stars

O and B stars are massive, hot and luminous. Early B-type stars have a mass around $10\,\mathrm{M_\odot}$ and an age of only 10 Myr, and therefore trace the present-day gradient.

Studies report gradients from $-0.03\,\mathrm{dex\,kpc^{-1}}$ to $-0.07\,\mathrm{dex\,kpc^{-1}}$ (Daflon & Cunha, 2004; Gummersbach et al., 1998; Smartt & Rolleston, 1997). Rolleston et al. (2000) consider the possibility of a step function in the metallicity gradient.

Field stars

Dwarf stars present the advantage of being numerous and offer richer samples, but are observable out to shorter distances. Boeche et al. (2013) use a sample of spectroscopic targets from the Geneva-Copenhagen Survey to establish a slope of $-0.065\,\mathrm{dex\,kpc^{-1}}$ in the average metallicity gradient, and find a value of $-0.043\,\mathrm{dex\,kpc^{-1}}$ from a RAVE Survey sample. In both cases, they note that the gradient as traced by stars beyond the solar radius could be shallower than inside. Recio-Blanco et al. (2014), using *Gaia*-ESO Survey data, find a metallicity gradient of $-0.058\,\mathrm{dex\,kpc^{-1}}$ in the thin disk, and no signficant gradient in the thick disk. Bergemann et al. (2014) find $-0.068\,\mathrm{dex\,kpc^{-1}}$.

Using the giant stars available in the RAVE sample, Boeche et al. (2014) find a radial gradient of $-0.055\,\mathrm{dex\,kpc^{-1}}$, which flattens for stars further away from the galactic plane. They also observe a slight negative vertical metallicity gradient.

Open clusters

The first study of the radial metallicity gradient as traced by OCs was published by Janes (1979) (see Fig. 1.9). They estimate photometric metallicities for a set of 41 clusters with galactocentric radii ranging from 8 to 14 kpc, and reveal a negative trend of $-0.05 \pm 0.01\,\mathrm{dex\,kpc^{-1}}$ in metallicity. Similar results were obtained by Panagia & Tosi (1981), Janes et al. (1988), Friel & Janes (1993) or Thogersen et al. (1993). Twarog et al. (1997) proposed that the gradient could be better explained, rather than with a single steady slope, by a broken slope, or a step function, with a boundary at the galactocentric radius of 10 kpc (Fig. 1.10).

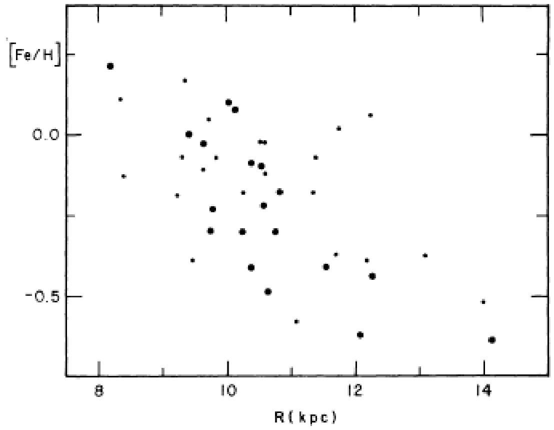

Figure 1.9: Metallicity gradient established by Janes (1979). Small dots represent clusters with metallicity determinations from either DDO or *UBV* photometry. Large dots represent clusters that have both.

Open clusters span a wide range of ages (from a few Myr to several Gyr) which are easier to reliably determine than for other tracers, making them excellent probes of disk evolution (Piskunov et al., 2006). Panagia & Tosi (1981), Cameron (1985), Friel (1995), Carraro et al. (1998) find no significant age-metallicity relation. An increasing number of clusters have associated metallicities obtained from spectroscopy, rather than photometry, allowing for more accurate abundance estimates. Friel et al. (2002) observed a radial metallicity gradient of $-0.06\,\mathrm{dex\,kpc^{-1}}$, and suggested that OCs older than 3 Gyr trace a steeper gradient than the younger ones. The exact opposite was found by Salaris et al. (2004), with old clusters tracing a shallower gradient.

New instruments have made it possible to collect high-resolution spectroscopy for large samples of OCs, and numerous studies have confirmed the idea of Twarog et al. (1997) that the metallicity gradient presents two separate regimes. The current picture is that the inner gradient is steeper, and the outer gradient is either shallow or flat, with a break ocurring somewhere between 10 and 12 kpc (Carraro et al., 2004, 2007; Pancino et al., 2010; Sestito et al., 2008; Villanova et al., 2005; Yong et al., 2005). By grouping clusters into different age bins, it is possible to trace different slopes for the inner gradient, and a

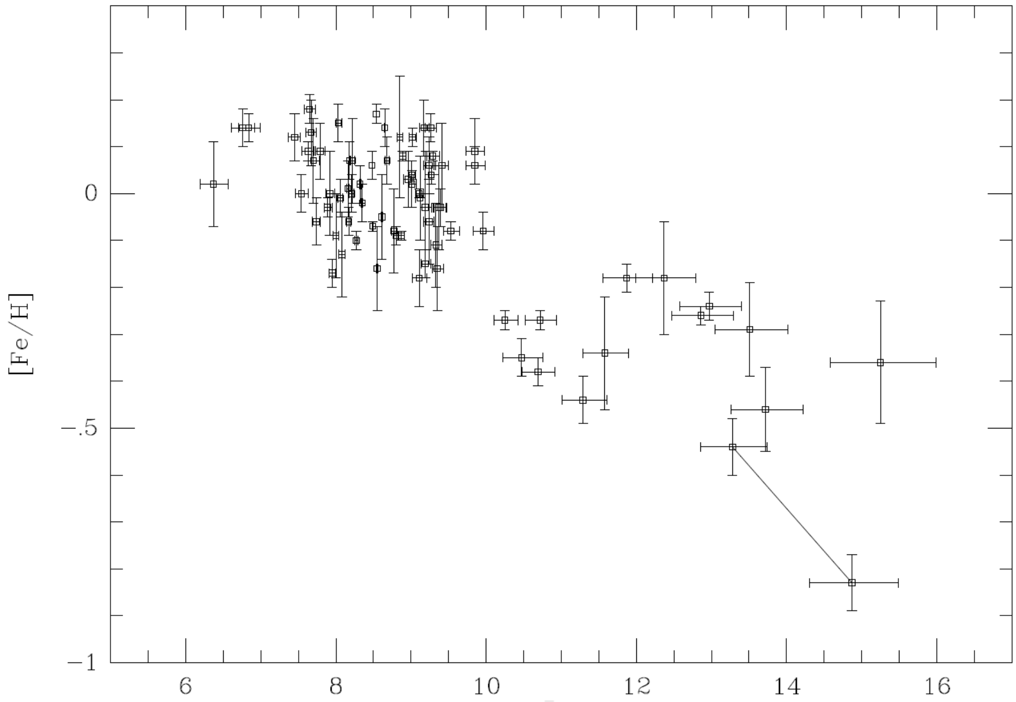

Figure 1.10: Twarog et al. (1997) suggested that the metallicity distribution across the Galactic disk may be better represented by a step function or a broken slope.

possible change in the transition radius. Magrini et al. (2009a), Andreuzzi et al. (2011), Jacobson et al. (2011) and Frinchaboy et al. (2013) see a steeper inner gradient for older OCs (see Fig. 1.11). However, Yong et al. (2012) do not notice a significant change in the inner gradient with time (Fig. 1.12). Our knowledge is rather uncertain due to the lack of homogeneity within the samples. Moreover, only a small number of OCs have been studied in the outer regions of the disk.

An interesting observational fact is that no OC study has so far concluded to the presence of a vertical metallicity gradient.

1.3.2 On the theoretical side: formation of a metallicity gradient

The first succesful attempt to link Galaxy structure and chemistry in order to establish a scenario for the evolution of the Galaxy was published by Eggen et al. (1962), usually considered the first "galactic archaeology" study. Their data suggested a rapid collapse of a smooth protocloud, on a timescale of around 10^8 yr. This view was challenged by the

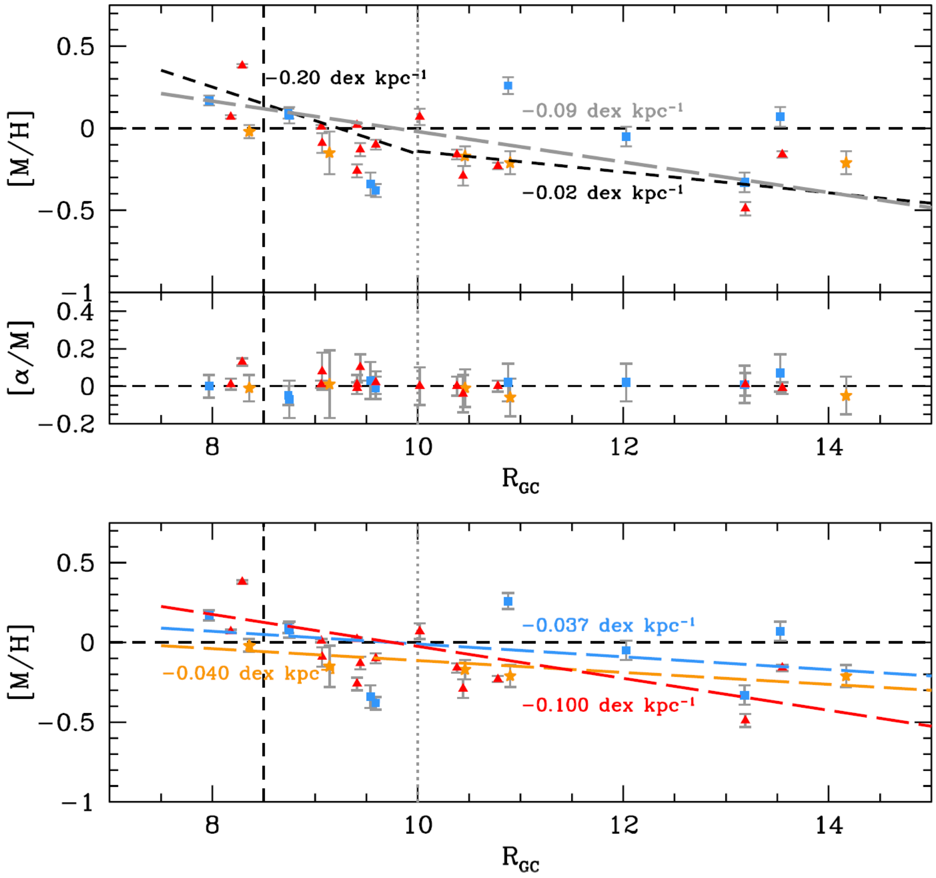

Figure 1.11: Metallicity gradient by Frinchaboy et al. (2013), showing the slope obtained fitting a single slope or a broken slope (upper panel). The lower panel shows the slope obtained with old, intermediate, and young clusters (red, orange and blue symbols respectively).

observations of Searle & Zinn (1978) who showed that the halo stars are not all the same age, and suggested our Galaxy has accreted independent fragments through the course of its life. This scenario, called "hierarchical model" is the most popular today, and is in agreement with cosmological models although still meets observational problems since we observe less fragments in the halo than models predict (see e.g. Belokurov, 2013).

The disk has retained less obvious fossil information than the halo, because a lot of its initial structure was erased in the dynamical processes that led to its current shape. However, a lot of information can be recovered from the study of its chemical gradient. A

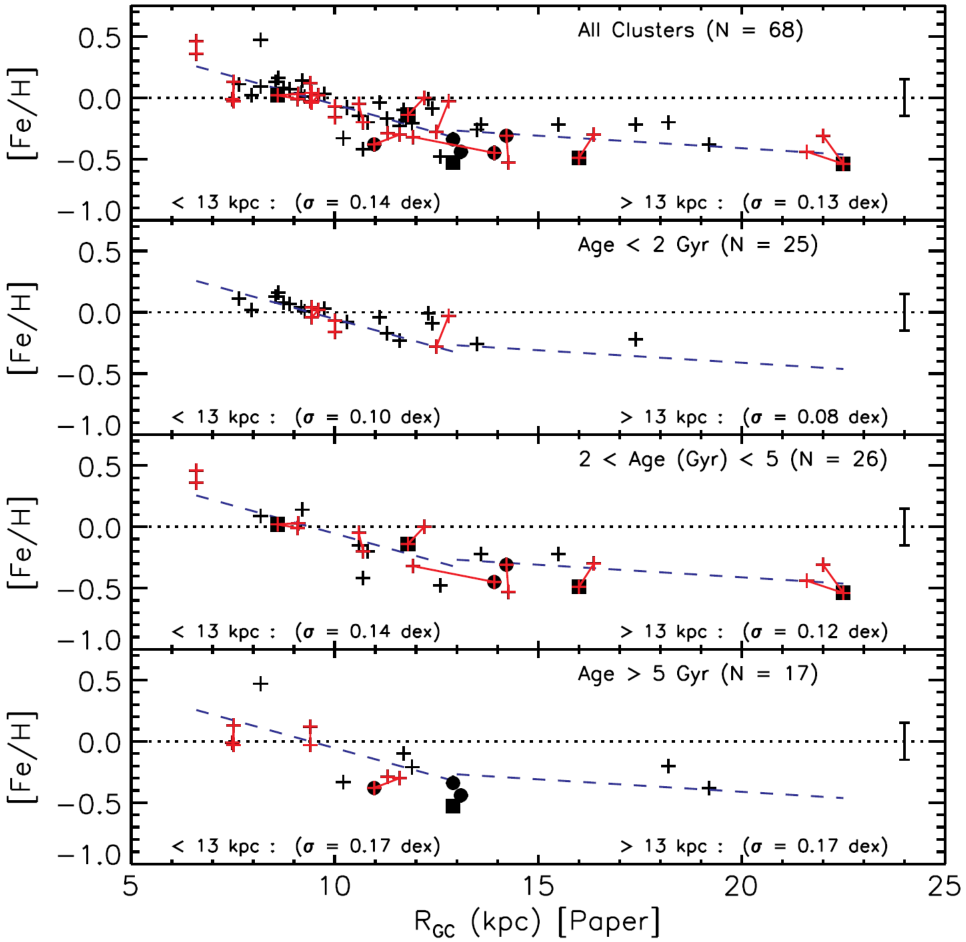

Figure 1.12: Yong et al. (2012) do not observe a significantly different slope for the metallicity gradient for old and young OCs.

valid Galaxy evolution model must reproduce several of the observed properties of the disk: i) the (negative) slope of the metallicity gradient and its evolution with time, ii) the shape (linear, broken slope or step) of the gradient, and iii) the lack of present-day age-metallicity relation.

Galaxy evolution models that are not based on dynamical simulations are called “analytical models”, while those including an underlying dynamical evolution models are called “chemodynamical models”. The first type allows for a direct understanding of how the efficiency of certain processes influences the evolution of the system, whereas the latter gives insights on the peculiar dynamical processes that take place during the lifetime of the disk.

Nucleosynthesis and Galaxy evolution

Before presenting Galaxy evolution models, we will recall some key concepts that all models rely on. The primordial nucleosynthesis that took place minutes after the Big Bang only produced H, He, and traces of Li (Gamow, 1946). All elements heavier than those three were created later in stellar interiors, as first suggested in the seminal stellar nucleosynthesis paper of Burbidge et al. (1957, also referred to as the "B^2HF" paper) (see also the extensive review of Wallerstein et al., 1997).

Stars form the material present the interstellar medium: this material is not just what stars are surrounded with, it is also what they are made of (Ferrière, 2001). Once locked inside stars, this material goes through series of nuclear reactions and is eventually released, enriching the ISM in heavy elements, until this material forms stars again. In this cycle of matter, the abundances of heavy elements can be used as a "cosmic clock", telling us the amount of processing a certain material has been through.

Some of the most efficient processes in producing and releasing enriched material are **supernovae** (SNe). Stars with masses ranging from $8\,\mathrm{M}_\odot$ to $40\,\mathrm{M}_\odot$ can reach the temperature and pressure conditions necessary to fuse elements heavier than C, producing (among others) elements such as Mg, Ti, Ca, Si (the so-called **α-elements**) or O, up to the synthesis of elements as heavy as Fe. After a life of a few 10^7 yr, those stars explode in what is called a **type-II supernova**, releasing the processed material into the ISM.

Another canal that releases processed material in the ISM is **Type-Ia supernovae**. These events involve a binary system of stars less massive than $8\,\mathrm{M}_\odot$. One of the stars completes its life cycle and stops sustaining nuclear fusion, hence becoming a white dwarf. If this white dwarf accretes material from its companion, a violent episode of new nuclear fusion can occur in which heavy elements, and Fe in particular, are synthetised and released in the ISM, but no α-elements. Because SNe Ia involve lower-mass progenitors than SNe II, the mechanism takes place over longer time scales, from 10^8 yr to 10^9 yr.

As a consequence, a closed box containing a simple stellar population will see its ISM enriched in both α-elements and Fe in the early phase of its evolution, then enriched in Fe only. In a more complex system involving many stellar generations, establishing [Fe/H] and [α/Fe] abundance ratios tells us what blend of material the stars formed from, and therefore, during which stage of Galaxy evolution they were born. Different star formation rates in different regions of the Galaxy will lead to different distributions of various elements, and establish an abundance gradient, that may vary as our Galaxy evolves.

From a theoretical point of view: analytical models

The main mechanisms that can play a role in shaping the metallicity gradient are: i) a radial variation of stellar yields because of a different IMF (Guesten & Mezger, 1982) or stellar metal production (Peimbert & Serrano, 1982), ii) a radial variation of the star formation efficiency (Fu et al., 2009), iii) a radial variation of the infall rate of gas from outside the disk [2].

Molla et al. (1996) point out that several or all of these three mechanisms could be at work together. Adjusting the efficiency of those mechanisms can either amplify or wash out an intial metallicity gradient (Goetz & Koeppen, 1992). For instance, the models of Tosi (1988), Chiappini et al. (1997), or Chiappini et al. (2001) predict a steepening of the gradient with time. In those scenarios, the inner disk accretes more gas, which leads to a higher star-formation rate and a faster chemical enrichment than in the outer parts. The models of Chiappini et al. (2001) or Romano et al. (2010) are actually based on a two-infall scenario, with a rapid (monolithic) collapse forming the thick disk and inner halo over 1 Gyr, followed by a continuous gas accretion (reflecting the hierarchical model) and an inside-out formation of the thin disk (following the idea of Matteucci & Francois, 1989) over 7 Gyr.

Other models predict that the metallicity gradient should flatten with time. They indicate that at first the SFR is higher in the inner regions of the disk, which establishes a strong negative gradient, then the chemical enrichment reaches a plateau while the metallicity of the outer disk keeps on increasing, catching up with the metallicity of the inner disk. Such models are presented in Mollá et al. (1997), Portinari & Chiosi (1999) or Hou et al. (2000).

The model of Magrini et al. (2009a) produces a global increase of the metallicity, which does not change the slope of the gradient in the range 7 – 22 kpc (Fig. 1.13).

---

[2] We know that our Galaxy accretes gas, or else the gas supply ($\sim 10^9\,\mathrm{M}_\odot$) would disappear and the Galaxy would be unable to sustain star formation at current rates (SFR may have been even higher in the past, Just, 2002). Gas accretion is also invoked to solve the so-called "G-dwarf problem" in which a closed-box model cannot explain the low number of observed metal-poor dwarfs in the Galaxy (Caimmi, 2008; Sánchez Almeida et al., 2014). Colavitti et al. (2009) stress the importance of deriving the infall law from simulations considering a cosmological context. Another clue that extragalactic material is being accreted comes from deuterium abundances (Prodanović & Fields, 2008). All of the D in the universe originates from the primordial nucleosynthesis, while stars can only destroy it, not produce it. The high D abundances osberved in the Galaxy imply that the stocks are being replenished.

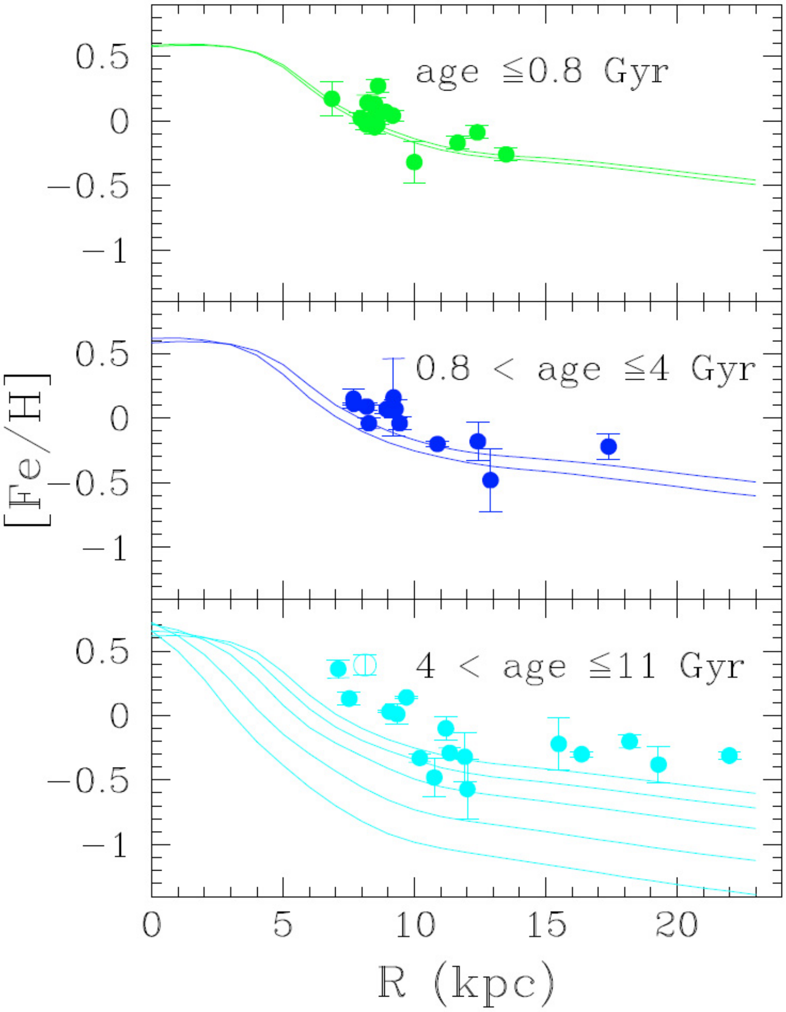

Figure 1.13: Predicted metallicity gradient at different epochs from the model of Magrini et al. (2009a). The dots are open clusters of corresponding age.

Metallicity gradients observed in other spiral galaxies

The early work of Vila-Costas & Edmunds (1992) and Zaritsky et al. (1994) have shown that negative radial metallicity gradients are a general feature of disk galaxies. Both suggest that barred spiral may have shallower gradients, indicating that the presence of a bar plays a role in the chemical evolution of galaxies. Working with a sample of 18 galaxies, Rupke et al. (2010) remark that isolated galaxies tend to have steeper gradients than interacting galaxies, and suggest this observation may be due to metal-poor gas infalls onto interacting galaxies. This result indicates that the cosmological context and the process of galactic assembly can impact the chemical evolution of a galaxy.

Just like in the Milky Way, broken slopes with a flattening in the outer disk are observed in the radial metallicity gradient of other galaxies (see e.g. Bresolin et al., 2009; Stanghellini et al., 2014; Vlajić et al., 2011; Worthey et al., 2005). The difficulty to resolve individual objects in outer galaxies means that fewer tracers are available with respect to studies of the Milky Way. Most studies rely on HII regions, and probe the current-day gradient. Studies based on PNe are able to trace the gradient at previous times and compare two epochs (e.g. Magrini et al., 2009b), but the impossibility to obtain CMDs for clusters in other galaxies prevents the study of the time evolution of their gradients for now.

Chemodynamical models of the disk

Recent models of Galaxy evolution attempt to consider both chemistry and dynamics. The presence of a spiral pattern in the disk of the Galaxy has consequences on stellar and gas dynamics. In particular, a ring-like minimum in the gas density was first observed by Kerr (1969) about 1 kpc outwards of the Sun. The spiral wave theory and hydrodynamical simulations predict the existence of this region of low gas density at the corotation radius (where the the rotation speed of the gas is equal to the spiral pattern speed). This “barrier” between the inner and outer disk implies there can be different star formation rates inside and outside corotation, and a discontinuity in the metallicity gradient can arise (Amôres et al., 2009; Lépine et al., 2014), as observed by (Simpson et al., 1995) following HII regions, (Twarog et al., 1997) with OCs, (Smartt & Rolleston, 1997) with B stars, or (Caputo et al., 2001) with Cepheids.

Stars on ellipitcal orbits can cross the corotation radius, but Sellwood & Binney (2002) have shown that even those stars with circular orbits can travel over a large distance because of resonant interactions with transient spiral density waves. The efficiency of this stellar migration mechanism (often refered to as “Sellwood-Binney mechanism”) explains the lack of age-metallicity relation for old stars in the solar neighbourhood (Edvardsson et al., 1993), and tends to flatten metallicity gradients. The simulations of Roškar et al. (2008) indicate that up to 50% of old stars in the solar neighbourhood could have formed at a different galactocentric radius.

The analytical model of Schönrich & Binney (2009) takes into account migration and shows that a thick disk can build up by secular evolution of the disk, requiring no merger event heating a previously built disk. However, Lépine et al. (2011) point out that their model does not consider the non-axisymmetric features of the Galaxy such as the bar and spiral pattern, making it impossible to faithfully reproduce the abundance gradients around the corotation radius. The model of Minchev et al. (2013), on the other hand, relies on a dynamical simulation that includes early-on gas-rich mergers in order to reproduce the observed properties of the Galaxy at present time. One of their results is that radial migration tends to wash out metallicity gradients over time. They also find that the metallicity and current position of the Sun are compatible with a most probable birth radius between 4.4 kpc and 7.7 kpc. The influence of migration on the evolution of the disk is still under discussion and needs to be ascertained from the theoretical and observational point of view.

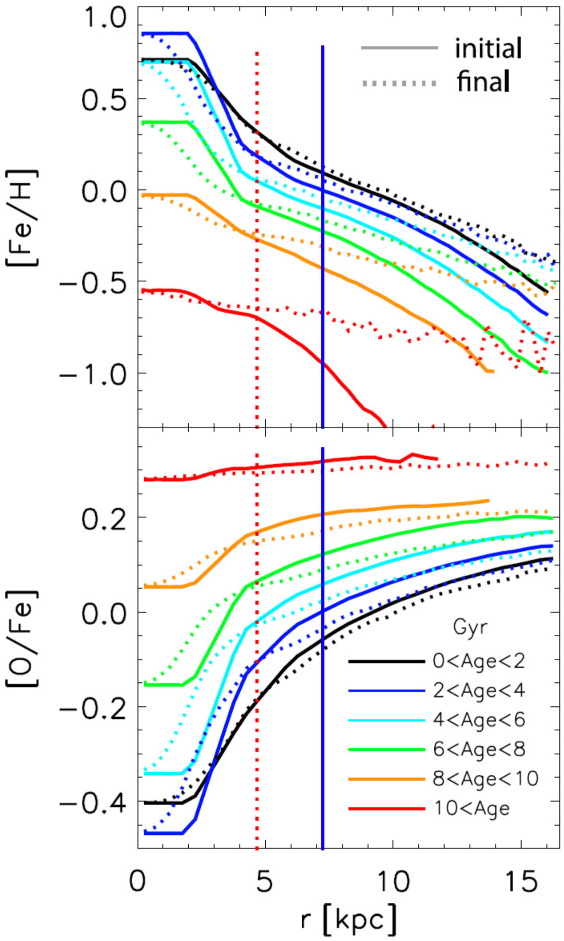

Figure 1.14: Metallicity gradients at different epochs, from Minchev et al. (2013). In their model, dynamical evolution including migration washes out established gradients.

CHAPTER 2

THE *GAIA*-ESO SURVEY

The *Gaia*-ESO Survey (GES) is a large-scale, high resolution spectroscopic survey currently carried out with the FLAMES instrument on the VLT (Gilmore et al., 2012; Randich et al., 2013). Its targets include 10^5 stars in all major stellar components of the Galaxy, as well as a large number of open clusters, from young to old, distributed across the galactic disk. The survey was designed as a complement to the limited spectroscopic capabilities of the *Gaia* space mission (Lindegren et al., 2008; Perryman et al., 2001) and makes use of the GIRAFFE (R∼20 000) and UVES (R∼47 000) spectrographs of the Fibre Large Array Multi Element Spectrograph (FLAMES Pasquini et al., 2002) at the VLT UT-2.

Stellar parameters and elemental abundances for the stars observed during the first six months of the campaign were delivered to the members of the collaboration as an internal data release (internal data release 1, or GESviDR1Final) for the purpose of science verification and validation. The work presented in this Thesis is focused on OCs, and the presentation of the GES data and data analysis will be restricted to OCs.

2.1 Organisation

The GES consortium is structured in several working groups (WGs).

The selection of cluster targets is performed by WG4, and described in Bragaglia et al. (in prep.).

The reduction of the GIRAFFE and UVES spectra by WG7 is described in Lewis et al. (in prep.) and Sacco et al. (2014), respectively.

The data analysis is performed independently by teams using different methods, but making use of the same model atmospheres (MARCS, Gustafsson et al., 2008) and the same line list (Heiter et al., in prep.). The analysis of the GIRAFFE data by WG10 is described in Recio-Blanco et al. (in prep.), and the analysis of UVES spectra by WG11 is described in Smiljanic et al. (2014). The results are then gathered and controlled to produce a homogenised set (for a comparison of the results obtained with different spectroscopic methods, see for instance Jofré et al., 2014).

2.2 Observing strategy

2.2.1 Selecting clusters

The aims of GES cluster science is to provide further insight on how clusters form, evolve and eventually dissolve, to use clusters as templates for stellar evolution at different masses, ages and metallicities, and to use clusters for a detailed study of the properties and evolution of the Miky Way thin disk. Those goals require gathering a sample of clusters spanning a wide range of ages (from a few Myr to several Gyr)

The list of OCs observed by GES is built to span a wide range of ages, metallicities, masses and distances. Figure 2.1 shows the main parameters of a list of potential intermediate-age and old OC targets.

2.2.2 Targeted stars

GIRAFFE targets

The GIRAFFE instrument, used in MEDUSA mode, allows to observe up to 132 targets at a time and provide medium resolution spectra covering spectral ranges of about 200 Å all across the visible spectrum (see Fig. 2.2). The selection of GIRAFFE targets is aimed at observing an unbiased sample of cluster stars, rather than trying to maximise the the number of high-probability cluster members, and is therefore based on photometric criteria only. In rich clusters, only a significant fraction of stars may be targeted in order to avoid excessive use of telescope time.

The faint magnitude limit for GIRAFFE targets is $V \sim 19$, at which it is possible to reach S/N$\sim$20 in about 2 hours. The exact exposure times and expected S/N for the various GIRAFFE setups are described in the WG4 target selection paper (Bragaglia et al., in prep.).

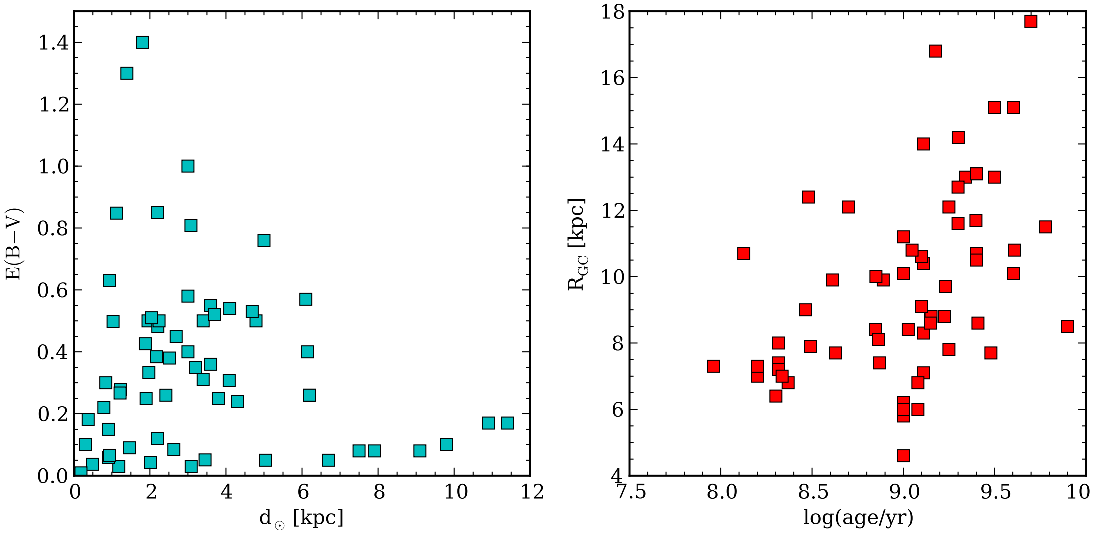

Figure 2.1: Main parameters of intermediate and old OCs selected as potential GES targets.

UVES targets

UVES can observe a maximum of 8 targets simultaneously and offers a higher resolution ($R \sim 47\,000$) than GIRAFFE. In OCs, UVES targets are chosen to be red clump stars (when they are present) to ensure the best homogeneity among different clusters. Unlike GIRAFFE targets (for which we aim at providing an unbiased sample), UVES targets are not only selected according to their photometry but also chosen on the basis of auxiliary information such as previously known radial velocities, proper motions etc, in order to observe the most secure cluster members.

The faint magnitude limit for UVES targets is $V \sim 16.5$, which is the limit to obtain $S/N \sim 50$ in about 6 hours.

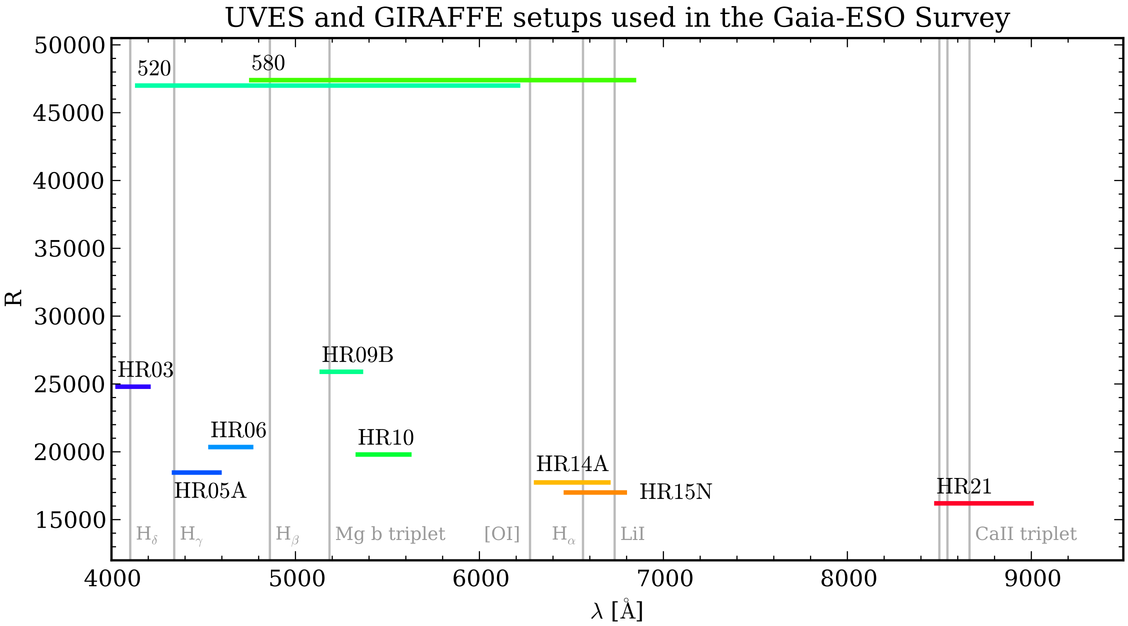

Figure 2.2: Wavelength coverage and resolving power $R = \lambda/\Delta\lambda$ for the UVES ($R > 45\,000$) and GIRAFFE ($R < 26\,000$) setups used by GES. Strong spectral lines are indicated for reference.

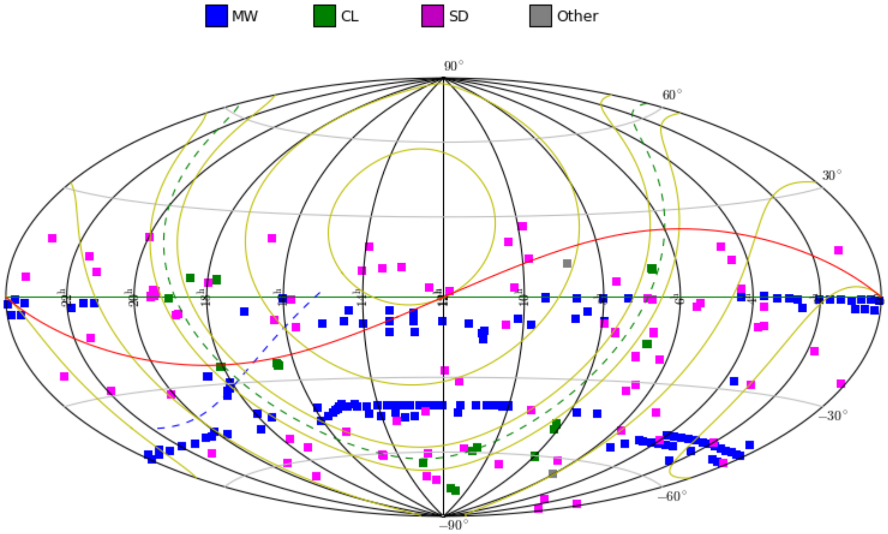

Figure 2.3: Map of observed GES targets in equatorial coordinates as of January 2015, provided by the Cambridge Astronomy Survey Unit (CASU), showing Milky Way fields (MW), cluster targets (CL) and calibration fields (SD).

CHAPTER 3

THE METHODS WE DEVELOPED FOR THE GAIA-ESO SURVEY

We are presently living in an era of large astronomical surveys that are delivering huge amounts of data, such as for instance APOGEE (Apache Point Observatory Galactic Evolution Experiment, Allende Prieto et al., 2008) and RAVE (Radial Velocity Experiment, Zwitter et al., 2008) and those to come in the near future such as GALAH (Galactic Archaeology with HERMES, Barden et al., 2010), 4MOST (4-metre Multi-Object Spectroscopic Telescope, de Jong, 2011) or MOONS (Multi-Object Optical and Near-infrared Spectrograph, Cirasuolo et al., 2011). The *Gaia*-ESO Survey will be targeting more than 10^5 stars over the course of five years. When dealing with a huge quantity of astronomical data, it is essential to have tools that economically process large amounts of information and produce repeatable results.

Some automatic spectrum analysis procedures rely on the minimisation of the χ^2 difference between the observed spectrum and a set of synthetic ones (for instance SME, Valenti & Piskunov, 1996), or the projection of the spectrum on a vector basis constructed from theoretical spectra (Recio-Blanco et al., 2006, MATISSE), both used within GES. Other procedures are based on the classical method consisting in measuring equivalent widths (EWs) that can be analysed with codes like Moog (Sneden et al., 2012) or WIDTH9 (Kurucz, 2005). Equivalent widths analysis is widely used, and codes like FAMA (Magrini et al., 2013) or GALA (Mucciarelli et al., 2013) were developed recently.

This chapter presents two tools that were developed to fit the needs of a data analysis in the context of the Gaia-ESO Survey. The first one is a tool developed to measure the EWs of a large number of spectra in a fully automatic way. This code, called DAOSPEC Option Optimiser pipeline (DOOp), uses DAOSPEC (Stetson & Pancino, 2008) to measure the EWs and optimises its key parameters in order to make the measurements as robust and repeatable as possible, and is presented in Sect. 3.1. The second code is FAMA (Fast Automatic Moog Analysis), presented in Sect. 3.2. It is based on Moog, and performs stellar parameter determinations from equivalent widths, following the excitation/ionisation balance method[1]. Finally, Sect. 3.3 present the result of a study comparing different methods used within GES on a set of reference (benchmark) stars.

---

[1] The general background this method relies on is presented in Appendix B.

3.1 DOOp: measuring EWs

DOOp (Cantat-Gaudin et al., 2014a) is a wrapper for DAOSPEC (Stetson & Pancino, 2008, hereafter SP08) that allows to measure EWs in batches of hundreds or thousands of spectra with a minimum of human intervention. It is available to the community, along with a user guide, via its webpage: `http://web.oapd.inaf.it/GaiaESO/DOOp`

3.1.1 DAOSPEC in a nutshell

The DAOSPEC code is fully described in SP08, and we will simply note its main characteristics and underline a few points that are important for the best use of DOOp: DAOSPEC is an automated Fortran program to measure EWs of absorption lines in high-resolution (typically, higher than 20 000) and high signal to noise (S/N higher than 30) spectra of stellar atmospheres. The measured lines are matched with a user-provided line list.

The code employs a fixed full width at half maximum (or scaled with wavelength for echelle spectra) to facilitate deblending, and estimates the continuum with Legendre polynomials after all the fitted lines are removed from the spectrum. These two characteristics are not present in codes like SPECTRE (Fitzpatrick & Sneden, 1987), ARES (Sousa et al., 2007), or EWDET (Ramírez et al., 2001), that all leave the full width at half maximum as a free parameter for each line, as is commonly done when measuring EWs with the IRAF task *splot*. This makes DAOSPEC especially useful on crowded spectra.

One important feature of DAOSPEC (see Fig. 4 in SP08) is that the continuum on which the EW fits are based is not the *true continuum* of the spectrum (i.e., the continuous star emission after all the lines are excluded), but an *effective continuum*, which is the true continuum depressed by a statistical estimate of the contaminating lines (the unresolved or undetected ones, producing a sort of line blanketing). This greatly improves the estimate of the unblended EW of each line in crowded spectra, as demonstrated in Sect. 3.2.1 of SP08, but it is often perceived as being too low by those who are used to employing traditional interactive methods for the continuum fitting procedure. The discrepancy between the true continuum and the effective continuum increases with line crowding (i.e., spectrum metallicity, especially for giants) and with decreasing S/N or resolution of the spectra.

Full width at half maximum (FWHM) and continuum placement are strictly correlated: if the continuum level of a spectrum is altered, so is the FWHM of each line. This is why the three most important parameters for a successful use of DAOSPEC are: (1) the FWHM estimate; (2) the continuum placement; and (3) the residual core flux parameter, which is the flux at the core of saturated lines, expressed in percent of the local continuum level; therefore, DOOp is designed to provide the best fine-tuning of these three parameters.

Another characteristic of DAOSPEC, which is uncommon for EW measurement programs (both interactive and automated), is that it provides a number of quality estimates of each EW measurement. These are the formal fitting errors in the single line, the quality parameter Q of each single line (a comparison of the local residuals around each line with the average residuals of the whole spectrum), and the average residuals, expressed as a percentage, over the whole spectrum. The codes mentioned before do not, to our knowledge, provide an uncertainty on the fit of individual lines (except for EWDET), and none of them performs a global estimate of the quality of fit. These features of DAOSPEC are used by DOOp to estimate the effects of a systematically incorrect continuum placement, for example.

The DAOSPEC code relies on statistical evaluation to consistently estimate the FWHM of the lines and place the effective continuum across the whole spectral range, which means that it performs better on wider ranges than on smaller ones. When dealing with spectra from an echelle spectrograph that delivers individual orders, it is safer to use a merged spectrum rather than measuring each order separately. This applies of course also to DOOp.

3.1.2 DOO pipeline

The DOOp code is an algorithm which optimises the parameters of DAOSPEC in order to get the best measurements of EWs. The fine tuning of the parameters is obtained through a fully automatic and iterative procedure and is tailored to the intrinsic characteristic of the spectrum that is going to be analysed. This procedure is performed by different scripts written in BASH[2] and IRAF[3] built around DAOSPEC.

The DAOSPEC parameters on which DOOp focuses are the following:

- short wavelength limit (SH)
- long wavelength limit (LO)
- minimum radial velocity (MI)
- maximum radial velocity (MA)
- residual core flux (RE)

---

[2] BASH is a Unix shell, a free software in common with all the operating systems based on UNIX and Linux.

[3] IRAF is distributed by the National Optical Astronomical Observatory which is operated by the Association of Universities for Researches in Astronomy, under cooperative agreement with the National Science Foundation.

- FWHM (FW)

An exhaustive description of these parameters can be found in SP08 or in the DAOSPEC manual publicly available[4]. Here we describe briefly their meaning. The SH and LO parameters specify the spectral range over which DAOSPEC will measure equivalent widths. The MI and MA parameters set the velocity range in which DAOSPEC is allowed to estimate the radial velocity (RV) of the star. Imposing a restricted range of possible RV through MI and MA reduces the risk of mismatching the lines (for instance in spectra with very few or very broad lines) and helps to find the right value. It also reduces the computation time. The RE parameter tells the program the residual flux at the core of the deepest line in the spectrum. The FW sets the estimate of the resolution of the spectrum in units of pixel. All the other DAOSPEC parameters are set to default values but some of them must be specified in the input file of DOOp (see Sect. 3.1.2).

Among these, the most important is the order of the polynomial (OR) used to fit the continuum. This parameter is *not* optimised by DOOp, and is kept fixed to the value provided by the user. The OR parameter should be chosen with care and in Sect. 3.1.2 we discuss its importance and its impact on the EW measurement.

The choice of continuum order

The choice of continuum fitting when analysing a stellar spectrum is always of great importance. A good model of the continuum must follow the main large-scale features in a spectrum, and a general rule of thumb is to use a polynomial of an order similar to the number of waves seen in the spectrum. For a large wavelength range, one must use a polynomial of higher order. Different choices of continuum can result in differences in EWs of up to 2 mÅ for some lines, as will be illustrated in Sect. 3.1.4 when comparing measurements with literature values obtained with DAOSPEC.

Basic functioning

The work flow of the pipeline is summarised in Fig. 3.1. The pipeline reads two input files. One is needed to set the basic options of the algorithm of the whole pipeline, such as the names of the output files and the convergence parameters for Module 2 (described later in this section). The other input file contains the list of spectra to analyse and a set of six parameters for each of them. The first five parameters are the DAOSPEC parameters OR (order of the polynomial for continuum fitting), FW (first guess of the FWHM), FI (=1

---

[4] `www3.cadc-ccda.hia-iha.nrc-cnrc.gc.ca/community/STETSON/daospec` or `www.bo.astro.it/~pancino/projects/daospec.html`

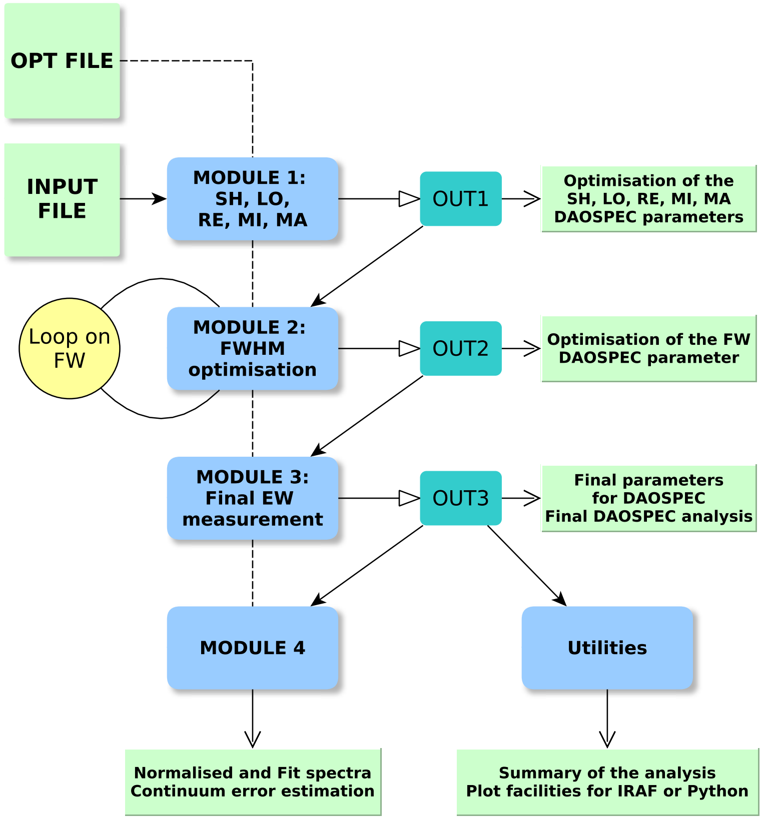

Figure 3.1: The tasks performed by DOOp are organised in several modules. The figure shows the dependencies of the modules and their main results.

if this FWHM must be kept fixed, =0 if it must be optimised), RE (residual core flux) and RV (radial velocity). If RE and RV are known their value can be given by the user to save computation time, otherwise setting a value of 0 means they will be derived by the pipeline. The last parameter sets which algorithm the pipeline must use to optimise the FWHM. At the moment two possibilities are allowed (see next paragraphs). All the parameters must be explicitly specified. To ensure that DOOp performs well on a list of spectra it is always better to analyse together spectra of the same resolution, that were collected with the same instrument.

After these two files are set, DOOp is ready to work. The measurements will be carried by four modules performing different tasks:

- Module 1: this module provides the SH, LO, RE, MI, and MA parameters, as well as the first EW estimates. The SH, LO, and RE values are determined calling IRAF twice with two different IRAF scripts. The first looks for the starting and ending wavelength of the spectrum avoiding glitches and bad values that may be found at the spectrum borders, setting the two parameters as the first/last wavelength for which the spectrum has a non-negative value. The second looks for the strongest lines in the spectrum (Hα, Hβ, Mg b triplet, CaII triplet) to set properly the RE parameter. If negative values are found, or if none of these strong lines are detected, a default value is imposed. The MI and MA parameters are set accordingly to the input RV: if 0, then a wide range is imposed, otherwise a smaller range is used. These ranges can be defined by the user (± 500 km/s and ± 10 km/s are typically reasonable values). At the end of Module 1 a first EW measurement is performed on the spectra for which DAOSPEC did not encounter computational problems. This measurement is not the best one, as not all the parameters are optimised.

- Module 2: this module provides the best FWHM parameter for DAOSPEC. For each analysed spectrum, an initial value of FWHM is needed. If the user wishes to optimise the FWHM (by setting the parameter FI=0), DAOSPEC runs once and Module 2 compares the output FWHM to the input (user-given) value. If a convergence criterion (by default, the output value has to be within 3% of the input) is not reached, then DAOSPEC runs again, using the output value as a new initial guess. The user can choose how many of the spectra in the list have to reach convergence (in percent). In some cases, the spectra under analysis are known a priori to present the same FWHM but its estimate is made difficult in some spectra (for instance because of different signal-to-noise ratios). In such a case it can be sufficient to reach convergence for only 50 or 70% of them and use the median value of the FWHM to measure the others (which is done by Module 3). In the most general case of a batch containing spectra of potentially different FWHMs (because the spectra were obtained with different instruments, under different sky conditions or because of rotating stars) it is recommended to require 100% of the spectra to reach convergence of the FWHM, so that this parameter is estimated in an independant way for each spectrum. If after 30 iterations the FWHM has not converged for some spectra, Module 3 will take care of them.

- Module 3: this module determines the FWHM that will be used for the final EW measurements. It computes the median FWHM of all the spectra for which it converged. Depending on the choice of the user, it will use this median value for the spectra that did not converge, or for all the spectra in the batch *including those that converged*. This second option may be more suitable if all the spectra are known a priori to have the same FWHM. Of course, the spectra for which the user had required to use a fixed FWHM (by setting FI=1) are measured using the FWHM given by the user. The output of DAOSPEC at the end of Module 3 are *the final EW measurements of DOOp*.

- Module 4 is designed to perform two different tasks. One is to provide the fit and normalised spectra in FITS format, because DAOSPEC only provides the continuum and residual FITS files. The other task is to provide EW measurements obtained by over- and underestimating the continuum level. The amount by which the continuum will be shifted is proportional to the dispersion of the residuals in the final DAOSPEC fit. The results coming out of these experiments can be used to quantify the error in the EW measurement due to the placement of the continuum. For UVES spectra (R=47 000), the dispersion of the residuals of the fit ranges typically from 3% for a S/N of 30, to 1% or less for a S/N above 100. Altering the continuum placement by these amounts can lead to differences of 10 and 3 mÅ respectively, although this is certainly a conservative estimate and can depend on other factors such as the metallicity of the star. A description of how the EWs are changed when altering the continuum placement is done by SP08 in their Sect. 3.4.3 and Fig. 2. Module 4 uses IRAF script to obtain the FITS files, while DAOSPEC is called to perform the EW measurements on the spectra with artificially imposed continuum levels. This module works with the output produced by Module 3.

- Utilities: together with the main algorithm of the pipeline, small scripts are provided to perform standard operations on the output files obtained by Module 3. They are presently used to produce the input files for the abundance analysis programs GALA and FAMA and to print out a summary of the analysis, including a log of the possible errors. With a provided script, the user can easily visualise and compare the spectra and their corresponding fit (see Fig. 3.2).

One advantage of the pipeline is that it can be easily customised. For example, if only the RV measurement is needed, one can set the pipeline to use only Module 1. If, instead, one wants to test the effect of changing the continuum order while keeping all the other parameters fixed, it is also possible. Furthermore, if the user prefers to pre-normalise their spectra using a personal routine, indicating a continuum order of -1 tells DAOSPEC not to perform any normalisation.

Examples of the resulting fits obtained with DOOp on a spectrum of Arcturus can be seen in Figs. 3.2 and 3.3.

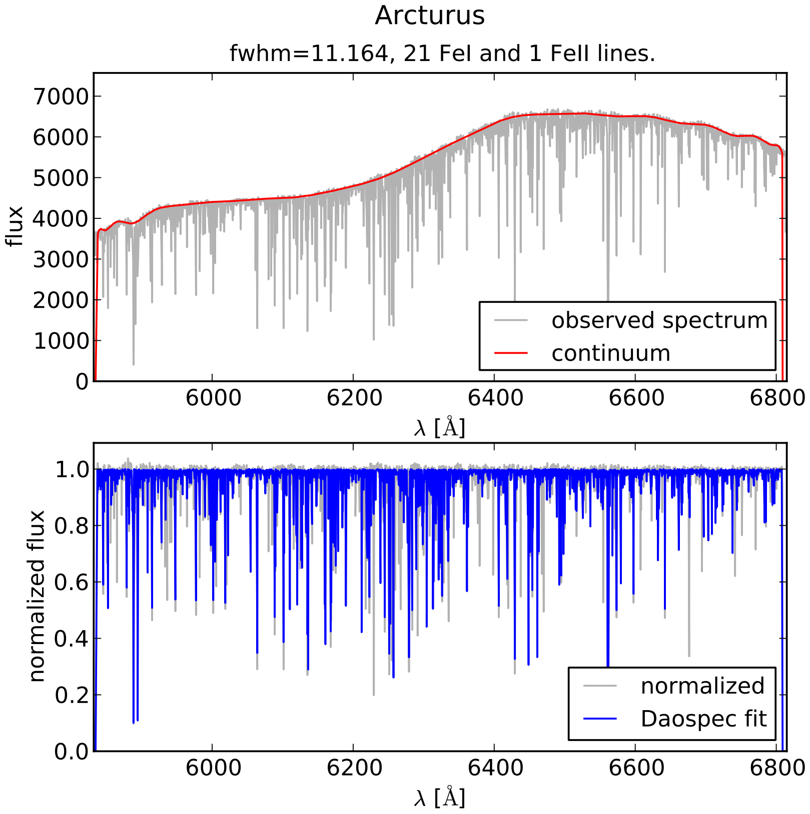

Figure 3.2: UVES-POP spectrum of Arcturus seen through the graphical interface of DOOp. *Top:* original spectrum and fitted continuum. The flux is given in arbitrary units, as the instrument response was not corrected for. Information is displayed on the FWHM of the lines and the number of lines that were identified from the line list. *Bottom:* normalised spectrum and fit.

Technical aspects

DOOp exploits the versatility of the BASH shell, which usually comes together with a set of smaller stable and powerful programs to perform operations on files and data. It uses the BASH language and a small set of these programs to handle all the logical operations needed to accomplish the optimisation of the DAOSPEC parameters. The external programs used

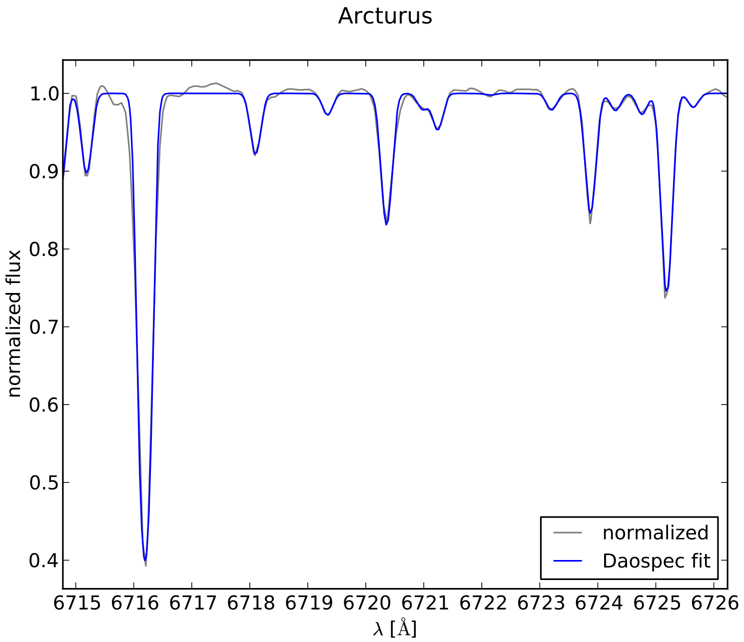

Figure 3.3: Detail of the normalised spectrum of Arcturus from Fig. 3.2 and corresponding fit.

by the pipeline are DAOSPEC, IRAF, and Python. The latter is called to display the interactively zoomable plots that allow the quality of the fits to be controlled.

On one hand, a script code is more fragile than monolithic codes because it does not pass any compilation checks and moreover the use of different programs interacting together can be less portable. On the other hand, script languages (Perl, Python, and JavaScript, to name a few well-known examples) are now widely used to make small programs for which the computational speed is not a key requirement. They are particularly intuitive, easy, and fast to use and their popularity often ensures the portability of the code.

From the beginning, DOOp was meant to be used by different groups in different locations and the need for portability was a top priority. It has been tested on different operating systems with different versions of BASH and IRAF, hence we can guarantee a full compatibility with at least the software we could test. It has been used on 32-bit and 64-bit Linux kernels (Ubuntu and Cent OS distributions) and with Mac OS. The BASH versions of the machines used range from the old 3.2.48 (2007) to the newer 4.1.2 (2009). We used two different IRAF versions: 2.14 and 2.16.

The advantage of DOOp over using DAOSPEC manually

The DOOp pipeline provides a robust method of measuring EWs in stellar spectra by limiting as much as possible human intervention in the process and facilitating the control of the results. This makes it especially convenient when dealing with batches of hundreds or thousands of spectra produced during observational campaigns such as the *Gaia*-ESO Survey (GES), and when different groups work with the same data.

For example, the estimate of the RE parameter usually requires manual measurements for each spectrum, while DOOp performs automatic measurements. It also automatically sets the SH and LO parameters for each spectrum, with great gain of time, and reduces the velocity range in which DAOSPEC looks for the radial velocity when the RV parameter is at least approximately known.

Ensuring that DAOSPEC converges to the best value for the FWHM in the spectrum can be a very lengthy procedure if done manually, even for a single spectrum. We show in Sect. 3.1.3 how the choice of initial FWHM can affect the convergence and the final EW measurements. The DOOp code takes care of this convergence process automatically.

The DAOSPEC code works by fitting gaussians to the absorption lines but does not return any file containing the global fitted spectrum. Instead, it returns a FITS file containing the continuum that was fitted, and a second file containing the residuals of the fit. The DOOp code automatically combines these files with the original spectrum to create a file containing the fitted spectrum. It also contains tools for direct plotting of the results (using the popular Python library Matplotlib). Each module prints out a log file containing a summary of its action on each spectrum, thus allowing an efficient control over the whole procedure.

When DAOSPEC is run, the format of the output files matches the line list provided by the user. In its current version, DOOp can automatically convert the output files produced by DAOSPEC to the format needed by FAMA and GALA if the user provides a line list in the right format. Given the structure of DOOp, organised in independent modules, adapting the code to work with a custom format of line list or produce a specific format of output can be easily done. In any case, the output files of DAOSPEC are kept by DOOp, and one can use them exactly as they would when running DAOSPEC manually.

3.1.3 Tests on synthetic spectra

We applied DOOp to the synthetic spectra used by SP08 to explore the boundaries in S/N, resolution, and pixel sampling under which DAOSPEC performs optimally. We did not run the tests on the spectra of resolution 5 000 and 10 000, as SP08 show that these resolutions are too low for DAOSPEC to perform well (and too low for a reliable EW analysis).

Convergence of the FWHM

We have run tests on the synthetic spectra used in SP08 to compare the EWs recovered after single run of DAOSPEC (which means that no condition on the convergence of the FWHM is imposed) and a run of DOOp (which automatically imposes the convergence of the FWHM), on spectra of various resolutions and signal-to-noise ratios. The true FWHM of these synthetic spectra is 5 px. The top-right and bottom-right panels of Fig. 3.4 show the average difference between the true EWs and the EWs measured with DAOSPEC after one run only, starting from different initial values of the FWHM. The measurements are clearly dependent on the initial FWHM. The top-left and bottom-left panels of the same figure show the difference between the true and measured EWs, after DOOp has imposed the convergence of the FWHM. It is clear that the convergence process carried out by DOOp makes the measurements independent of the input FWHM. This experiment was conducted on spectra at various resolutions and signal-to-noise ratios, showing that DOOp is more stable in all cases.

Ensuring the convergence of the FWHM can also have consequences on the line detection. Starting from a too large value will cause DAOSPEC to ignore some features that it should actually be fitting. Running DAOSPEC again using the newly found FWHM as a new initial value for the convergence helps to find all the lines. Figure 3.5 shows two fits obtained with an input FWHM of 10 px, on a spectrum of resolution R=20 000 and S/N=100. When DAOSPEC is run only once with a wrong input FWHM it may fail to detect all the lines, but imposing the convergence process improves the line detection.

Equivalent widths

We have compared the measurements of DOOp, with those of SP08, who optimised manually all the parameters (implying multiple runs of DAOSPEC). The spectra used for these tests are the same as in Sect. 3.1.3, with an additional four spectra of different pixel sampling (true FWHM of 1, 2, 3 and 10 px). The results of DOOp show excellent agreement with those obtained by SP08. The average differences and the dispersion between both sets of measurements are reported in Table 3.1. The fit uncertainty is the average uncertainty on the fit of the single lines, that DAOSPEC computes from the least-square fitting procedure (see SP08 for details). The difference and uncertainty decrease with pixel sampling, resolution and signal-to-noise, as is expected. Four of these cases are illustrated in Fig. 3.6.

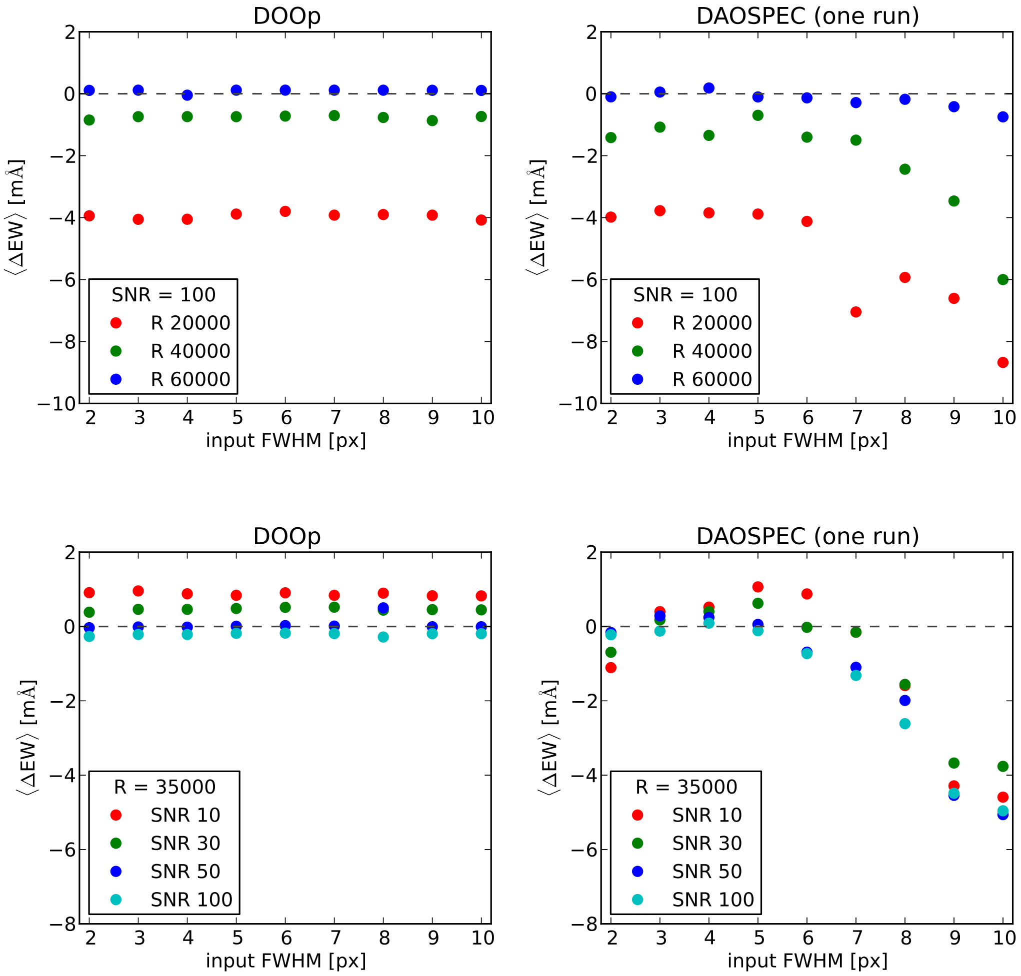

Figure 3.4: Difference between our measurements and the true EW for synthetic spectra with a true FWHM of 5 px, at various resolutions and S/N. *Top-left:* average difference between the EWs measured with DOOp and the true EWs, for various input values of the FWHM, in synthetic spectra at three different resolutions. *Top-right:* same as top-left panel, but for measurements obtained without imposing the convergence of the FWHM. *Bottom-left:* same as top-left panel, for spectra of four different S/N. *Bottom-right:* same as bottom-left, but without imposing the convergence of the FWHM.

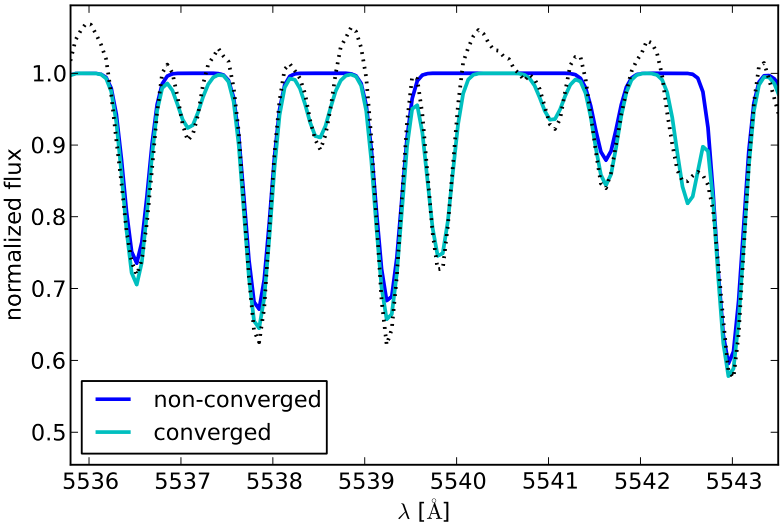

Figure 3.5: The dotted line is a synthetic spectrum of resolution R=20 000. The true value of the FWHM for this spectrum is 5 px, but for this test we have used 10 px as a starting point. The blue line is the fit obtained with DAOSPEC run only once. The cyan line is the fit obtained after convergence of the FWHM. Refining the value of the FWHM not only allows for a better fit of the line profiles, but also avoids DAOSPEC missing some lines.

Table 3.1: Comparison between the EWs measured by DOOp and by DAOSPEC on synthetic spectra.

R	S/N	FWHM [px]	⟨ΔEW⟩ [mÅ]	r.m.s. [mÅ]	fit uncertainty [mÅ]
35 000	100	1	-0.7	0.2	5.1
35 000	100	2	-0.3	0.1	6.3
35 000	100	3	-0.4	0.1	4.6
35 000	100	10	0.3	0.2	2.6
20 000	100	5	-0.3	0.4	5.6
40 000	100	5	-0.3	0.1	3.4
60 000	100	5	0.0	0.3	1.8
35 000	10	5	-0.6	0.1	4.8
35 000	30	5	-0.6	0.3	3.7
35 000	50	5	-0.6	0.1	3.6
35 000	100	5	-0.4	0.3	3.4

Notes. The difference is given in the sense DOOp-SP08.

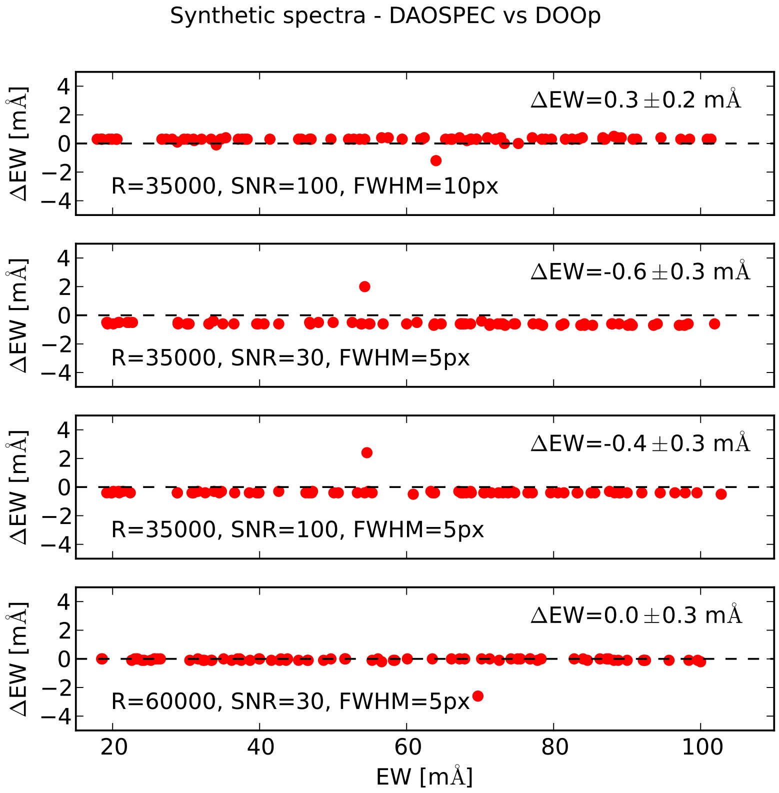

Figure 3.6: Difference in EW (in the sense DOOp-SP08) for lines in four different synthetic spectra. The results for all the synthetic spectra used in these tests are given in Table 3.1.

3.1.4 Comparing the measurements of DOOp with literature

We have checked the measurements obtained with DOOp against already published measurements obtained with other methods, to ensure that our method is able to reproduce the same results, in particular those of DAOSPEC used manually, on real stellar spectra. The stars used in these comparisons are giant, metal-rich stars (-0.5<[Fe/H]<0.1).

DOOp vs SPLOT

We have measured EWs in a spectrum of Arcturus downloaded from the UVES-POP archive[5] (Bagnulo et al., 2003) and degraded from a resolution of 80 000 to 47 000, which is

---

[5] `http://www.eso.org/sci/observing/tools/uvespop.html`

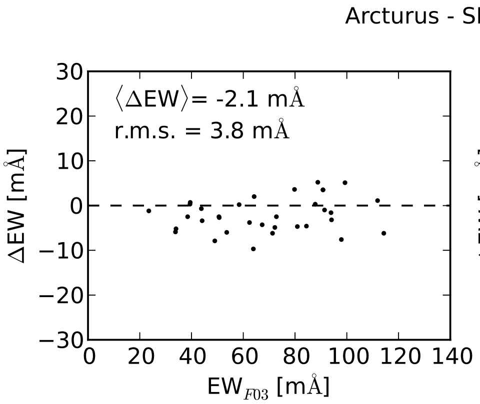

Figure 3.7: Difference in EW (in the sense DOOp-F03) plotted against EW (left panel) and wavelength (right panel) for Arcturus. The average difference is -2.1 mÅ, with an r.m.s. dispersion of 3.8 mÅ.

the resolution of the UVES-FLAMES spectra. These EWs were compared with measurements by Friel et al. (2003), hereafter F03, on the high resolution spectrum of Arcturus published by Hinkle et al. (2000). They have normalised the spectrum using the IRAF CONTINUUM task and measured the EWs using the IRAF task SPLOT. The comparison (Fig. 3.7) shows good agreement. The DOOp measurements have a general offset of -2.1 mÅ, with an r.m.s. dispersion of 3.8 mÅ. An offset of this magnitude is consistent with the way DAOSPEC sets the continuum level (as discussed in Sect. 3.1.1 above).

DOOp vs SPECTRE

We have measured EWs in two stars of NGC 2477 and six stars of Be 29, in UVES spectra previously measured and published by Sestito et al. (2008) and Bragaglia et al. (2008) (hereafter B08), respectively. These stars are red giants of nearly solar metallicity. The authors have normalised the spectra using the IRAF task CONTINUUM, and fitted Gaussian profiles using the code SPECTRE. We measure in general smaller EWs by 1 to 5 mÅ. Again, this can be explained by the behaviour of DAOSPEC in terms of continuum placement. The results for two stars of NGC 2477 are illustrated in Fig. 3.8. The identifiers of the stars are taken from the ESO Imaging Survey catalogue, as reported in B08. The offset between the measurements of B08 and those of DOOp is inside the range of differences expected when comparing different methods (see for instance the comparisons of SP08 between DAOSPEC and other tools). The slightly different offset observed between the

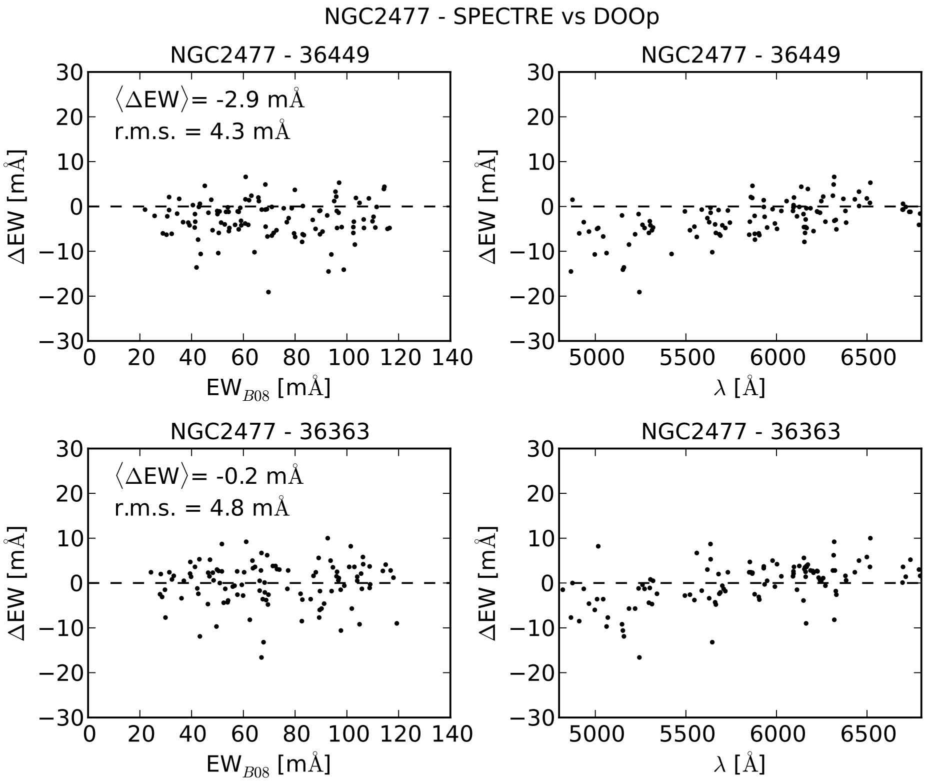

Figure 3.8: Difference in EW (in the sense DOOp-B08) plotted against EW (left) and wavelength (right) for two stars of NGC 2477.

blue and red part of the spectral range comes from the fact that UVES spectra are split between a blue and a red arm, and both ranges were measured independently (by B08 and by us), resulting in a slightly different continuum adjustment.

DOOp vs DAOSPEC

As a final test we have compared our EWs with measurements by Pancino et al. (2010), hereafter P10, using DAOSPEC on three stars of Cr 110 and two stars of NGC 2420. These stars are red giants of solar metallicity. The spectra have a resolution of 30 000 and a S/N of 70. Figure 3.9 shows the perfect agreement between the two sets of measurements for two stars of Cr 110 (identifiers from Dawson & Ianna, 1998). Such a good agreement is expected if the FWHM and residual core flux were carefully set when using DAOSPEC

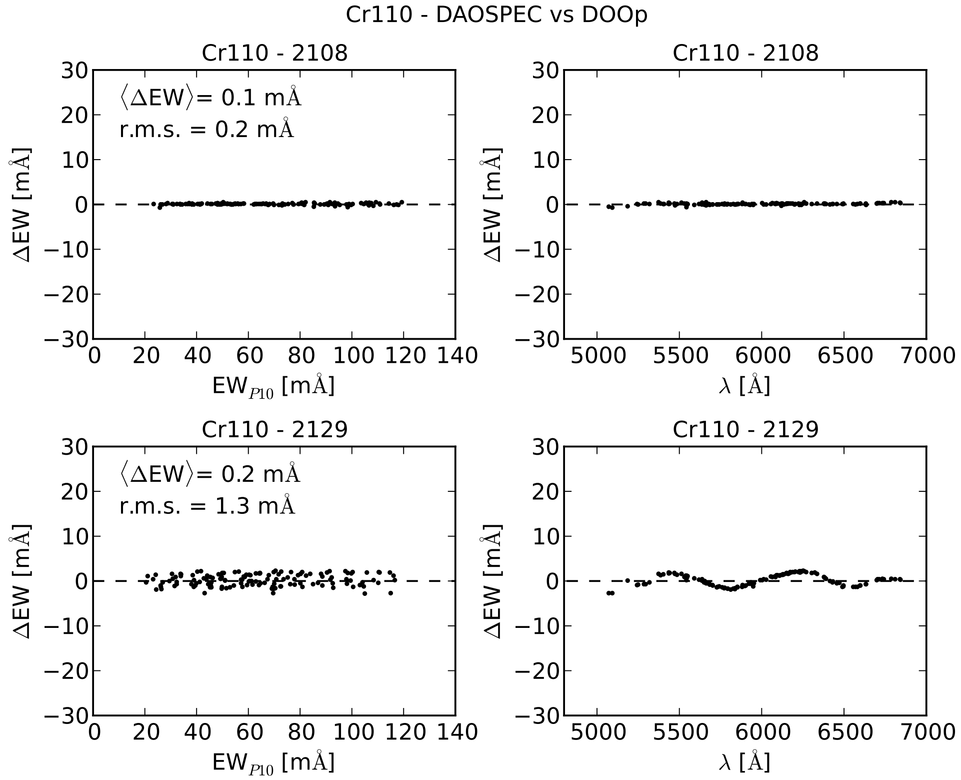

Figure 3.9: Difference in EW (in the sense DOOp-P10) plotted against EW (left) and wavelength (right) for two stars of Cr 110.

manually, which can be time consuming. The DOOp code does not produce better results than those expected from the most careful use of DAOSPEC, but making the procedure automatic reduces the sources of errors and makes it humanly possible to deal with large numbers of spectra.

However, the critical issue of setting the continuum remains. The refinements of choosing a continuum order remain arbitrary, and two users fitting a continuum of slightly different order on the same spectrum may find slight differences in the measurements of EWs (rms of about 2 mÅ). The star 2129 of Fig. 3.9 is an example of such a case, where small differences varying across the spectral range can be observed.

3.1.5 Analysis of benchmark stars

To assess the effect of the different EW measurements on the determination of the stellar parameters, the stars used in Sect. 3.1.4 are not ideal test cases because the authors use different line lists, and using only the lines in common between their lists and ours does not provide sufficient statistics (for instance, we need enough FeII lines in common to derive a reliable gravity).

As a final validation for the whole procedure, we measured the EWs for four well-studied stars, Arcturus, Procyon, HD 23249, and the Sun. The first three are bright stars (V=-0.04, 0.37, and 3.51, respectively) for which a rich literature is available in the PASTEL database[6] (Soubiran et al., 2010). Their spectra were taken from the UVES-POP archive. These spectra were obtained at the VLT with the UVES instrument at a resolution R$\sim$ 80 000 that we degraded to 47 000 (which is the nominal resolution of the GES UVES spectra). The list of spectral lines we have used is the GES line list (Heiter et al. in prep.). The available UVES-POP data cover the optical range, from 3040 to 10 400 Å, of which we have used the ranges $4760 - 5770$ and $5840 - 6840$ Å. These are the ranges covered by most of the GES UVES spectra (corresponding to the setting 580), where the line list is well-defined.

The solar spectrum we analysed was taken from the HARPS archive[7], degraded from a resolution R$\sim$120 000 to 47 000. After running DOOp, we passed the output files to FAMA to obtain the atmospheric parameters of these stars.

The effective temperatures, surface gravities and metallicities we obtain for these four stars are in good agreement with the values available in literature, as shown in Fig. 3.10 and 3.11, and summarised in Table 3.2.

---

[6] `http://vizier.u-strasbg.fr/viz-bin/VizieR?-source=B/pastel`

[7] `http://archive.eso.org/wdb/wdb/eso/repro/form`

Table 3.2: Atmospheric parameters of the four benchmark stars.

star	T_{eff} [K]	ΔT_{eff} [K]	$\log g$	$\Delta\log g$	[Fe/H]	Δ[Fe/H]
Literature						
Arcturus	4302	120	1.68	0.31	-0.53	0.12
HD 23249	5025	255	3.84	0.17	0.07	0.15
Procyon	6583	162	4.06	0.15	-0.01	0.16
Sun	5777	...	4.44	...	0	...
This study						
Arcturus	4352	31	1.78	0.12	-0.45	0.13
HD 23249	5108	73	3.82	0.15	0.07	0.15
Procyon	6647	35	3.83	0.08	0.02	0.06
Sun	5755	40	4.30	0.20	0.02	0.09

Notes. For the literature values the numbers are the average values found in PASTEL, and their associated errors are their standard deviations. For this study, the parameters and their errors are given by FAMA.

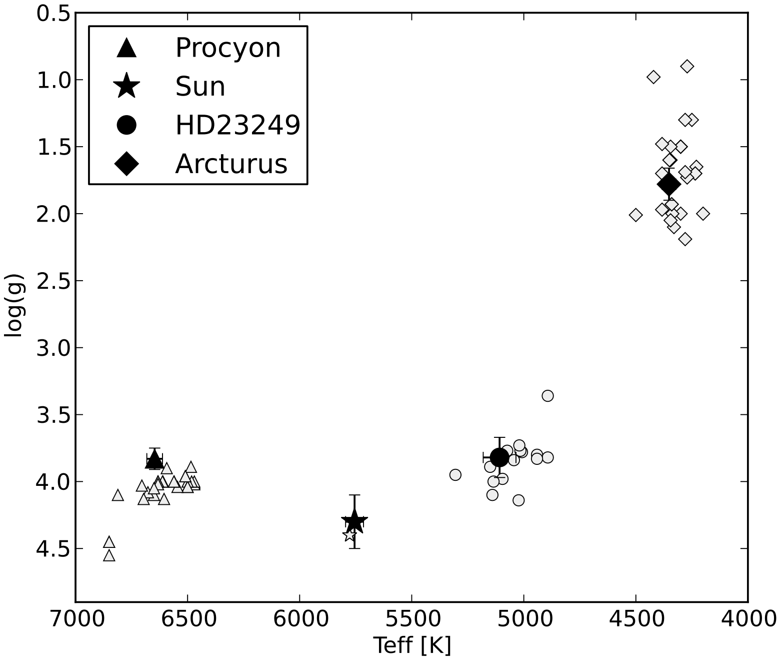

Figure 3.10: T_{eff} and $\log g$ for our four benchmarks. The filled symbols are our results, while the empty symbols are the various values found in the literature.

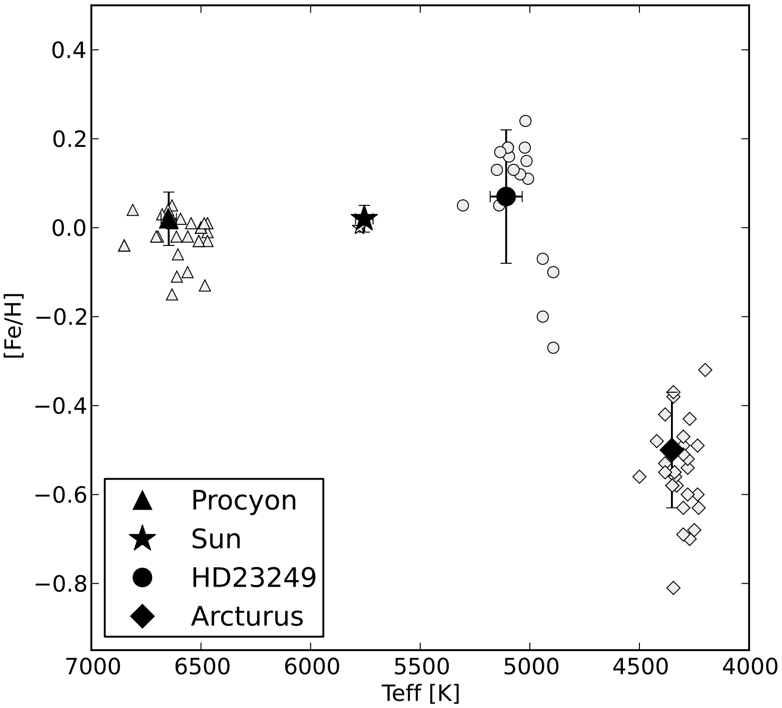

Figure 3.11: As in previous figure, but for T_{eff} and [Fe/H].

3.2 FAMA: obtaining stellar parameters

The code FAMA (Fast Automatic Moog Analysis, described in details in Magrini et al., 2013) is based on the `abfind` driver of the Fortran code Moog (Sneden, 1973; Sneden et al., 2012). It performs an automatic derivation of stellar parameters (effective temperature $T_{\rm eff}$, surface gravity log g, microturbulence v_{mic}) and individual elemental abundances from a list of equivalent widths, following the so-called **excitation/ionisation balance** method (described in more details in Appendix B).

3.2.1 The standard excitation/ionisation balance

Tools such as Moog employ a given model atmosphere (representing the photosphere of a star with a given $T_{\rm eff}$, log g, v_{mic}) and apply radiative transfer equations to determine an elemental abundance from the measured equivalent width of a line. In the case where the stellar parameters are known, the problem boils down to the simple task of obtaining an abundance for each line measured in the spectrum.

When the stellar parameters are not known, if a sufficient number of lines are measured, it is possible to derive the effective temperature, surface gravity and microturbulent velocity of a stellar photosphere. The procedure starts with assuming a model atmosphere (as close as possible to the true parameters, but in theory any random first-guess can work). Given this model, elemental abundances for all measured lines are derived (for instance, using Moog). Lines that provide discrepant abundances by more than a certain threshold are discarded (we refer to this step as *σ-clipping*). Then a diagnostic is run in order to determine if the first-guess model is correct, and if not, what could be a better choice of $T_{\rm eff}$, log g and v_{mic} for the model atmosphere. The diagnostic is done in three steps (one for each stellar parameter):

- The effective temperature ($T_{\rm eff}$) is satisfactory if no trends are seen in a **abundance vs excitation potential** plot. When such a trend is seen, $T_{\rm eff}$ must be adjusted. If a positive correlation is seen between abundance and excitation potential (lines with higher excitation potential (EP) showing larger abundances), then the choice of $T_{\rm eff}$ is too low and must be increased (if lines of higher E.P. show lower abundances, $T_{\rm eff}$ must be decreased).

- The surface gravity (log g) is correct if neutral and ionised species of the same element yield the same abundances. If the gravity is too high, the abundance of ionised species will be too high (and too low if the chosen gravity is too low).

- Microturbulence (v_{mic}) is adjusted by hunting trends between abundance and **reduced equivalent width** ($\log_{10} EW/\lambda$). If a positive trend is seen (lines with larger reduced EW producing larger abundances) then the choice of v_{mic} is too low and must be increased.

Physical justifications for this approach are given in Appendix B.

3.2.2 Obtaining a reliable convergence

FAMA performs an iterative process, adjusting $\mathrm{T}_{\mathrm{eff}}$, log g and v_{mic} by large amounts (i.e. 300 K or 0.8 dex) when the equilibrium is far from being satisfied, and making finer adjustments when the equilibrium is about to be reached. Because of degeneracies between the parameters and because of local minima, the process may converge to a different result depending on the chosen starting point.

We performed a test involving 50 synthetic spectra generated from Kurucz model atmospheres spanning a wide range in effective temperature and surface gravity, with a signal-to-noise ratio of 100. When then measured equivalent widths, and atmospherical parameters were determined, using the **same starting point** for all stars. We found that starting with a model at 5500 K, the effective temperature of cool stars was systematically overestimated, while the effective temperature of hot stars tended to be underestimated. With an initial temperature of 6800 K, the effective temperature of cool stars is even more overestimated (see Fig. 3.12).

The convergence process can be made more reliable if the initial model is reasonably close to the true parameters of the star. Effective temperatures can be estimated from photometric calibrations (e.g. Casagrande et al., 2010) if photometry is available. Surface gravity can be estimated from stellar isochrones. At the very least, the analysis of a dwarf star should be made with atmospherical parameters that represent a dwarf star, and the analysis of a giant with suitable parameters. When the first-guess model atmosphere is used to compute the first set of abundances, FAMA performs a σ-clipping which eliminates lines with discrepant abundances from the analysis. If the chosen model is too far from the true atmospherical parameters of the star, the σ-clipping will bias the result by discarding valid lines.

The bias illustrated in Fig. 3.12 led us to imagine a more robust convergence scheme. My first approach to the problem was to start from a first-guess model, converge to a result, then use this result as the centre of the region to explore in the parameter space. 27 new convergence procedures are carried out, corresponding to various combinations of

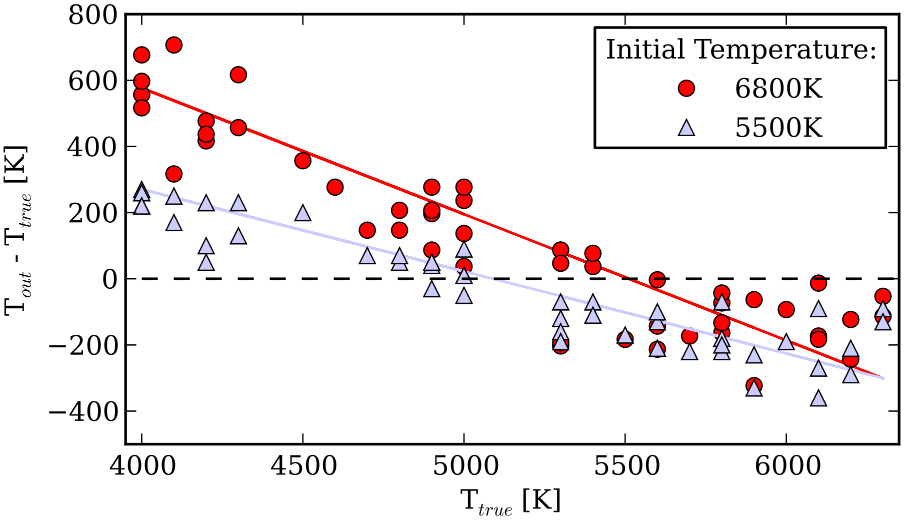

Figure 3.12: Temperature determinations on a set of 50 synthetic spectra of known parameters, for two different choices of temperature of the initial model.

$T_{\rm eff}$, log g and v_{mic}. For each of them, the σ-clipping step is performed on the original list of measured lines.

To obtain the final stellar parameters, one can choose to average the results of all 27 runs. This approach also allows to estimate the uncertainty on each parameter by simply evaluating the dispersion in the results. Figure 3.13 illustrates this process, showing the initial starting point, then the grid of secondary starting points and their corresponding convergence points (projected on the $T_{\rm eff}$ – log g plane).

Repeating the convergence process 26 times proved time-consuming. The current implementation of FAMA is based on 6 runs, each one using as a starting point the result of the previous one, and applying a new σ-clipping to the original list of lines. At each of these 6 runs the convergence condition on minimising the slopes is made more stringent. This approach is very robust against the chosen initial model, as illustrated on Fig. 3.14. Devising an efficient optimisation scheme that is independent of the the chosen starting point is especially important when dealing with survey data involving many hundreds of spectra.

The final uncertainty on the atmospherical parameters is evaluated from the uncertainty on the fitted slope, as explained in details in Sect. 3 of Magrini et al. (2013). The uncertainty on the final individual abundances is given in two ways. The first value is simply the

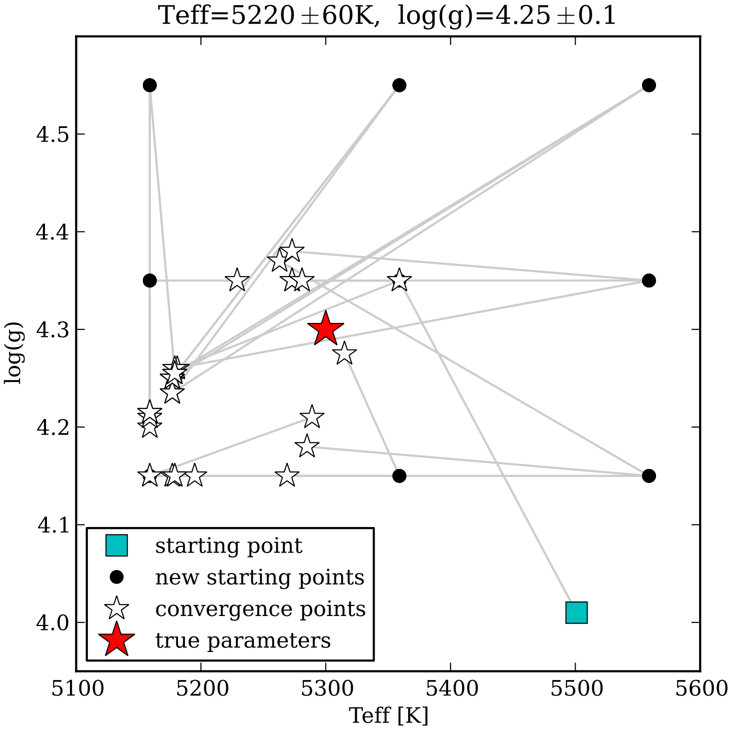

Figure 3.13: Illustration of the convergence process and the various initial and final points in the parameter space, projected on the $T_{\rm eff} - \log\ g$ plane.

standard deviation aroung the mean abundance obtained for the lines of a given element. The second source of error comes from the uncertainty on the stellar parameters. The errors are calculated by comparing the abundances obtained with the best set of parameters, and those obtained with the parameters which provide the least good ionisation and excitation equilibrium.

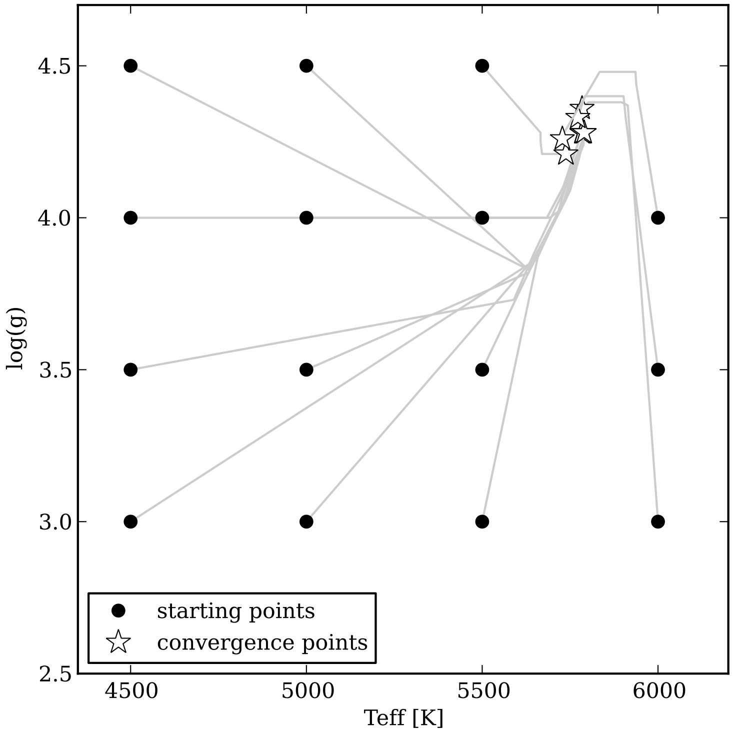

Figure 3.14: Illustration of the convergence process of FAMA on an observed solar spectrum, for different arbitrarily chosen starting points. The final convergence point is independent from the initial model atmosphere chosen by the user.

3.3 Benchmark stars: building a homogeneous metallicity scale

The diversity of aproaches to determining stellar parameters and elemental abundances leads to large scatters in the results that can be found literature, even for bright and well-studied targets (see e.g. Table 3.2 and associated Fig. 3.10 and 3.11). Numerous studies of the galactic disk and halo are based on large samples of stars for which chemical information is available. Quantifying the differences between various models and observational studies is sometimes problematic because of the various methods and reference scales adopted. Many factors can contribute to inhomogeneities between studies:

- the instrument: different spectrometers offer different wavelength coverage, resolution and signal-to-noise ratios.
- the atomic data: many spectroscopic studies use lists of lines extracted from the NIST (Wiese et al., 1996) and VALD (Kupka et al., 1999)databases. Most authors make their own subset of reliable lines, based on the blended lines they identify in known spectra or the possibility to reproduce known elemental abundances (see e.g. Sousa et al., 2008).
- the atmospherical models: MARCS (Gustafsson et al., 2008) and ATLAS (Kurucz, 2005) are widely used. Allende Prieto et al. (2004) find that they can lead to abundance differences of 0.1 dex even with identical input parameters.
- the method: analyses of a stellar spectrum can rely on different methods, such as measuring EWs or fitting synthetic spectra. Different approaches to measuring EWs are found in the literature. The normalisation of the spectrum continuum also has consequences on the final results.
- NLTE corrections: departure from local thermodynamical equilibrium can have consequences on the derived abundances of some elements, especially in the metal-poor regime (Lind et al., 2011).
- solar scaling: for convenience, the elemental abundance of an element X is traditionally expressed relative to its solar value: $[\mathrm{X/H}]=\log\left(\frac{n(X)}{n(H)}\right)-\log\left(\frac{n(X)}{n(H)}\right)_{\odot}$. Different studies use different references for solar abundances (e.g. Anders & Grevesse, 1989; Asplund et al., 2005; Grevesse et al., 2007), which makes direct comparisons uneasy especially when the authors do not explicitly quote the adopted reference.

3.3.1 Library of benchmark stars

The *Gaia* mission will observe the whole sky and provide a homogeneous dataset of a billion stars, for which the *Gaia* astrophysical parameter inference system (Apsis, Bailer-Jones et al., 2013) will estimate stellar parameters. The calibration of Apsis relies on a set of benchmark stars, for which the radius and distance is known with high accuracy (thanks to HIPPARCOS parallaxes), allowing for direct determination of their effective temperature and surface gravity. A sample of 34 stars was built by Heiter et al. (in prep.). Their parameters are presented in Fig. 3.15 and listed in Table 3.3.

Blanco-Cuaresma et al. (2014b) have compiled a library of high-resolution (typically $R > 80\,000$) and high signal-to-noise ratio (typically in the range $150 - 450$) spectra for those stars, using data observed with the NARVAL, HARPS and UVES spectrometers. For some stars, spectra from more than one instrument are available. HARPS is mounted on the ESO 3.6 m telescope in La Silla (Mayor et al., 2003) and the spectra were reduced with the HARPS data reduction software (version 3.1). NARVAL is mounted on the 2 m Bernard Lyot telescope at the Pic du Midi. The data were reduced with the Libre-ESpRIT pipeline (Donati et al., 1997). UVES is located on the 8.2 m ESO VLT-UT2 telescope at Paranal (Dekker et al., 2000). The library includes spectra from the Advanced Data Products collection, which were reduced with the standard UVES pipeline (version 3.2, Ballester et al., 2000), and spectra from the UVES Paranal Observatory Project (UVES-POP), which were reduced through a different procedure (Bagnulo et al., 2003). The available spectra for each star are listed in Table 3.3.

In order to establish a common metallicity scale for these benchmark stars, several nodes working on the data analysis of the *Gaia*-ESO Survey have applied their own pipeline to this spectral library. All analyses were conducted using the same fundamental T_{eff} and $\log\ g$, as well as the same model atmospheres (1D hydrostatic, Gustafsson et al., 2008) and atomic data. The adopted line list is the one prepared for the *Gaia*-ESO Survey. Some of these nodes have used spectral fitting methods (LUMBA and ULB), some rely on EWs (Bologna, EPINARBO, Porto and UCM) and one method is based on parametrisation and projection (Nice). Those methods are presented in greater details in Jofré et al. (2014).

3.3.2 Applying the EPINARBO tools

The library of Blanco-Cuaresma et al. (2014b) contains very high-resolution spectra ($R = 80\,000$ to $R = 115\,000$). Where the resolution is too high and the line profiles are too far from gaussian, DAOSPEC may fail to measure reliable EWs. For this reason we convolved the spectra to a resolution of 47 000 before measuring EWs. We then applied FAMA to

Table 3.3: Reference parameters for the 34 benchmark stars.

Star	$T_{\rm eff}$	log g	[Fe/H]	v_{mic}	spectra
18 Sco	5810	4.44	0.01	1.08	N,H
61 Cyg A	4374	4.63	-0.33	0.86	N
61 Cyg B	4044	4.67	-0.38	0.85	N
α Cen A	5792	4.3	0.24	1.11	H,U
α Cen B	5231	4.53	0.22	0.93	H
α Cet	3796	0.68	-0.45	1.36	N,H,U
α Tau	3927	1.11	-0.37	1.36	N,H
Arcturus	4286	1.64	-0.53	1.25	N,H,U,UP
β Ara	4173	1.04	-0.05	1.24	H
β Gem	4858	2.9	0.12	1.22	H
β Hyi	5873	3.98	-0.07	1.16	H,U,UP
β Vir	6083	4.1	0.21	1.24	N,H
δ Eri	4954	3.75	0.06	1.0	N,H,U,UP
ϵ Eri	5076	4.6	-0.1	0.88	H,U,UP
ϵ For	5123	3.52	-0.62	1.02	H
ϵ Vir	4983	2.77	0.13	1.23	N,H
η Boo	6099	3.8	0.3	1.3	N,H
γ Sge	3807	1.05	-0.16	1.43	N
Gmb 1830	4827	4.6	-1.46	0.82	N
HD 49933	6635	4.2	-0.46	1.48	H
HD 84937	6356	4.15	-2.09	1.29	N,H,U,UP
HD 107328	4496	2.09	-0.34	1.23	N,H
HD 122563	4587	1.61	-2.74	1.13	N,H,U,UP
HD 140283	5514	3.57	-2.43	1.05	N,H,U,UP
HD 220009	4275	1.47	-0.75	1.23	N,H
HD 22879	5868	4.27	-0.88	1.09	N,H
ξ Hya	5044	2.87	0.14	1.23	H
μ Ara	5902	4.3	0.33	1.15	H,U
μ Cas	5308	4.41	-0.82	0.91	N
μ Leo	4474	2.51	0.26	1.28	N
ψ Phe	3472	0.51	-1.23	1.54	H
Procyon	6554	3.99	-0.04	1.48	N,H,U,UP
τ Cet	5414	4.49	-0.5	0.94	N,H
Sun	5777	4.44	0.02	1.07	N,H,U

Notes. Stellar parameters from Heiter et al. (in prep.). The iron abundances are the final LTE [Fe/H] values (see Table 3 in Jofré et al., 2014). The last column indicates the origin of the spectra: HARPS (H), NARVAL (N), UVES (U) and the UVES-POP library (UP).

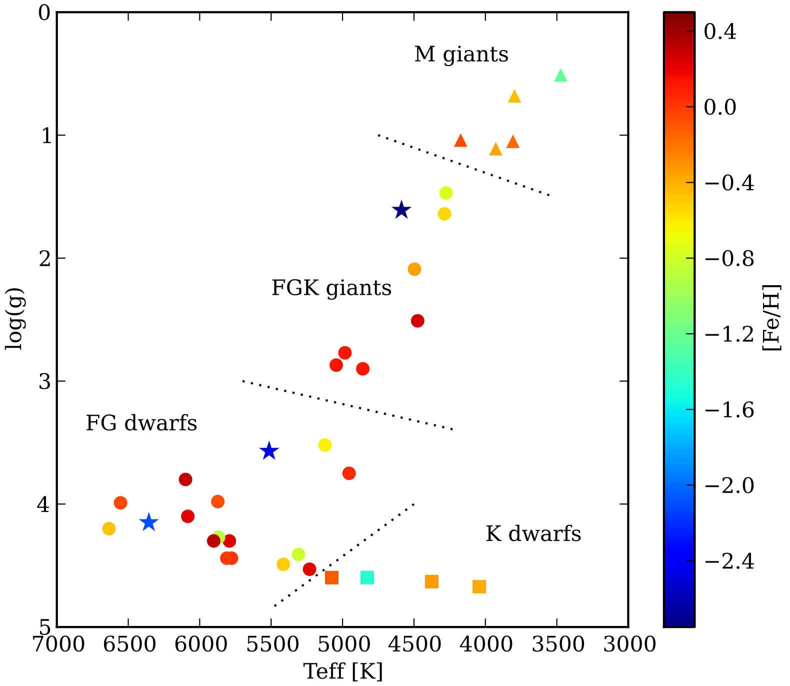

Figure 3.15: Reference parameters for the 34 benchmark stars (data from Heiter et al., in prep.). The groups are those defined by Jofré et al. (2014), who also consider a fifth group of metal-poor stars (indicated here with starred symbols).

the measured EWs, allowing for optimisation of the v_{mic} parameter but keeping $\mathrm{T_{eff}}$ and log g fixed. We rejected lines with abundances discrepant by more than one sigma, and provided abundances for all valid lines. Non-LTE corrections were not applied.

The final Fe abundances we obtain differ from the reference value by on average 0.05 dex (see Fig. 3.16). For stars with several available from different instruments, the dispersion between the results obtained with the different spectra is typically under 0.05 dex. Since we fixed the value of log g instead of adjusting it, the ionisation equilibrium is not necessarily satisfied and we find on average a difference of 0.16 dex between FeI and FeII abundances. In a few cases, which all correspond to cool stars, we determine iron abundances that are lower than the reference value by more than 0.2 dex. Those stars are: the cool K dwarfs Gmb 1830 and 61 Cyg A, the M giants α Cet and α Tau, and the K giant δ Eri. It is not surprising that the most discrepant stars are late-type stars, as estimating the continuum level and measuring unblended lines is more difficult in the atmospheres of cool stars. A fragment of the spectrum of two of these stars is shown in Fig. 3.17.

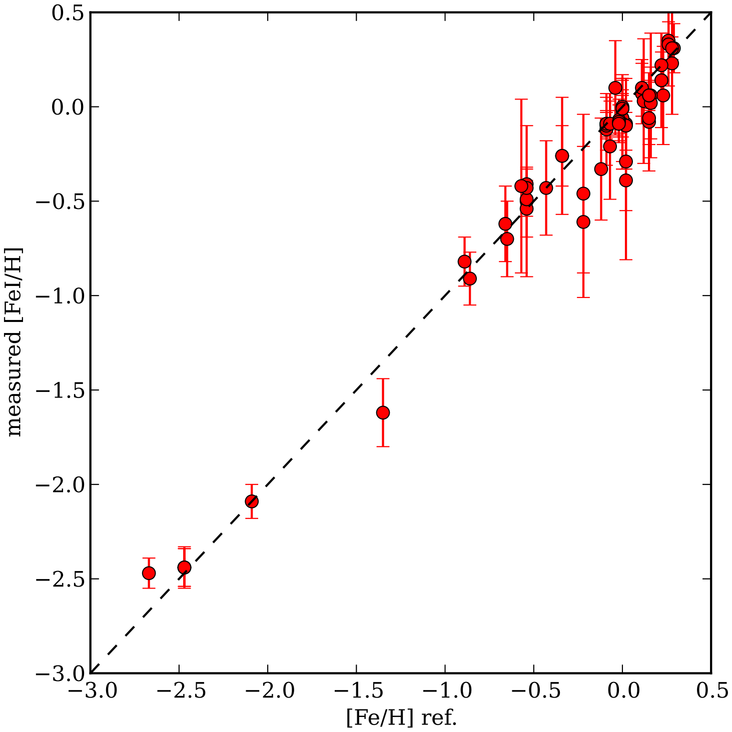

Figure 3.16: Comparison between the FeI abundance computed with our method and the final metallicity obtained combining the results of all groups (listed in Table 3.3). The error bars indicate the dispersion in abundance among the FeI lines.

3.3.3 Comparisons between nodes

Common line list: selected lines

Even though all nodes worked with a common line list (a common selection of FeI and FeII lines and homogeneous atomic data), some lines may be undectable, or discarded from the analysis based on various criteria. Different nodes end up using significantly different subsets to perform their abundance determinations.

For those comparisons only lines with log(EW/λ)<4.8 were considered, in order to keep only those lines that are on the linear part of the curve of growth, as the transition from the linear to the saturated regime occurs near log(EW/λ)$\sim$5, quite independently of the stellar type (Villada & Rossi, 1987). From this point a subset of 224 FeI lines and 18 FeII lines, used by at least three different groups and providing a bundances discrepant by less than 2σ from the mean abundance was identified.

Those of those selected lines that were used by all the groups are tagged as "golden lines" (see details in Sect. 6.3 of Jofré et al., 2014). The sample of golden lines is different for the different spectral types.

Metal-poor stars

This group includes the stars HD 122563, HD 140283, and HD 84937. The average line-to-line scatter in abundances is 0.12 dex. For the final metallicity of these stars, the mean dispersion between the results provided by the different nodes is only 0.06 dex. The spectra of metal-poor stars present few absorption lines, making it easier to place the continuum level (see Fig. 3.17), which explains the good agreement between all nodes. However, the low number of identifiable lines means that less statistics is available. This would especially be a problem in the case of a full analysis, leaving $T_{\rm eff}$ and log g as free parameters.

Metal-poor stars are more sensitive to NLTE effects (Lind et al., 2011). Applying NLTE corrections increased the abundances by 0.1 dex.

FG dwarfs

This group includes δ Eri, ϵ For, α Cen A and B, μ Cas, τ Cet, 18 Sco, Sun, HD 22879, μ Ara, β Hyi, β Vir, η Boo, Procyon, and HD 49933. The average line-to-line scatter in abundances is 0.13 dex, but is reduced to 0.01 by using the selection of "golden lines" (see Sect. 3.3.3). The node-to-node scatter is 0.07 dex.

For those stars, applying NLTE corrections changes the abundances by less than 0.03.

FGK giants

This group includes Arcturus, μ Leo, β Gem, ϵ Vir, ξ Hya, HD 220009, and HD 107328. For those stars, the node-to-node scatter here is 0.08 dex. The global node-to-node scatter for all lines is 0.2 dex, but can be reduced to 0.08 dex by using the selection of golden lines.

M giants

This group includes ψ Phe, α Cet, β Ara, γ Sge, and α Tau. The analysis of those cool stars is made difficult by the presence of molecular absorption bands, which in particular make the continuum placement uneasy (see a fragment of the spectrum of α Cet on Fig. 3.17). On average for each star, nodes obtain a line-to-line scatter of 0.5 dex.

K dwarfs

This group includes Gmb 1830, 61 Cyg A, 61 Cyg B, and ϵ Eri. The abundances obtained for identifiable lines in these stars usually do not satisfy ionisation and excitation equilibria. In particular, unphysically high abundances are obtained for FeII lines, showing the difficulty to measure unblended ionised iron lines in those spectra. For illustration, a fragment of the NARVAL spectrum of 61 Cyg A is shown on Fig. 3.17.

FeI abundances are more reliable. For the two components of the binary system 61 Cyg (for which we expect the iron abundance to be identical), the mean abundances are -0.33 and -0.38 (for A and B, respectively).

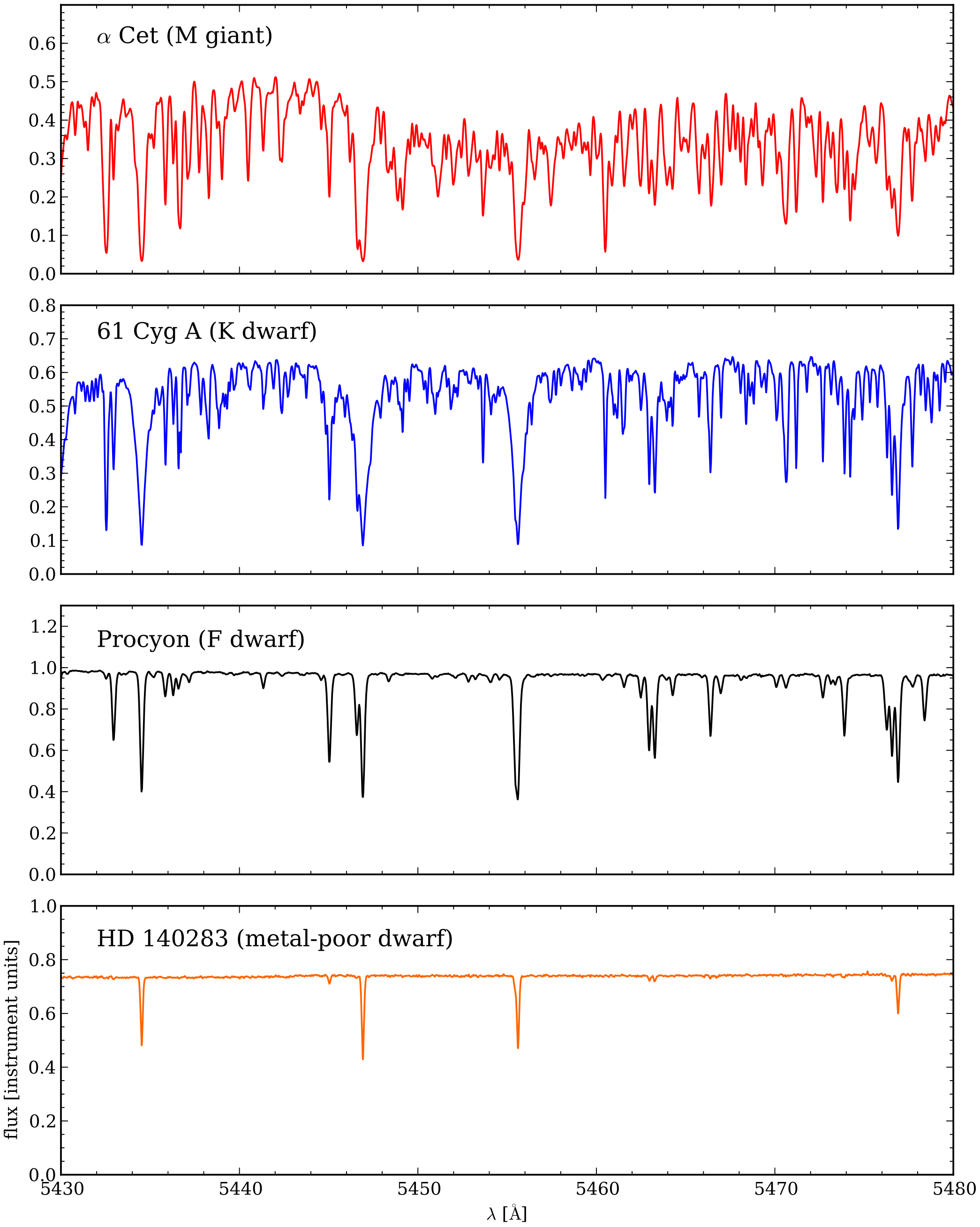

Figure 3.17: Fragments of NARVAL spectra for four of our benchmark stars. Identifying the continuum level and measuring clean, unblended lines is more difficult in cool, late-type stars (upper panels).

CHAPTER 4

PHOTOMETRIC STUDIES OF OPEN CLUSTERS

In this chapter we rely of photometric data to study two massive inner-disk OCs, and estimate in particular their age. Beyond their importance in tracing the galactic radial metallicity gradient, those clusters are interesting objects in their own right. In Sect. 4.1 we present a study of NGC 6705, which shows strong signs of mass segregation and may be losing stars to the galactic population (those results are already published in Cantat-Gaudin et al., 2014b). Section 4.2 presents a study of Trumpler 20, whose CMD features a broad main-sequence turn-off and what seems to be an extended red clump and deserves further investigation. This study of Trumpler 20 is published in Donati et al. (2014).

4.1 NGC 6705

The open cluster NGC 6705 (M 11, Mel 213, Cr 391, OCl 76) is a massive and concentrated OC located in the first galactic quadrant (Messina et al., 2010; Santos et al., 2005) at the galactic coordinates ($l = 27.3$, $b = -2.8$). This cluster, one of the three intermediate-age clusters observed in the first GES internal data release, contains a total of several thousand solar masses (McNamara & Sanders, 1977; Santos et al., 2005), which places it near the limit between the most massive OCs and the least massive GCs (Bragaglia et al., 2012). Since it is located towards the central parts of the Galaxy it is projected against a dense background, but its rich main sequence and populated red clump clearly stand out in a colour-magnitude diagram.

NGC 6705 is situated in a clear area and suffers from relatively little extinction for an object at such a low galactic latitude. Moreover, its position inside the solar circle makes it an important tracer of the inner disk gradient.

Figure 4.1: M11 photographed by the ESO Wide Field Imager (WFI) on the MPG/ESO 2.2-metre telescope at La Silla Observatory.

4.1.1 The data

WFI BVI photometry

The photometry used in this paper has been extracted from archival images in B, V and I taken on the 13 May 1999 with the Wide Field Imager at the MPG/ESO 2.2m Telescope for the ESO Imaging Survey (ESO programme 163.O-0741(C), PI Renzini). The sample of images comprises for each band two long exposure time images (240 sec each for a total of

480 sec), in order to reach a photometric precision of 20% at V$\simeq$ 21 mag, and single short (20 sec) exposure carefully chosen not to saturate the brighter targets.

Data reduction has been performed using the ESO/Alambic software (Vandame, 2002) especially designed for mosaic CCD cameras and providing fully astrometrically and photometrically calibrated images with special care to the so-called "illumination correction". The photometry was performed using the Daophot/Allstar software (Stetson, 1987) wrapped in an automatic procedure that performed the PSF calculation and all the steps for extracting the final magnitudes. The PSF photometry from the short and long exposures for each single band have been combined in a single photometric dataset using the Daomaster program. The internal astrometric accuracy (both within the short/long exposures and in the different bands) turned out to be better than 0.05 arcsec, while the external comparison with the 2MASS catalogue gave an rms of $\simeq 0.20$ arcsec.

The observations consist in a single $33' \times 34'$ field centred on the cluster, completely covering the photometry of Sung et al. (1999). The geometry of the WFI imaging is shown in Fig 4.7. We tied our instrumental WFI photometry to their photometric calibration, comparing the magnitudes of the common objects and calculating solutions for the zero point and colour term for each pass band. In the magnitude range V<14 the dispersion is of the order of 0.05 magnitudes, increasing to 0.1 for stars as faint as V$\sim$ 17 (see the upper panels of Fig. 4.2). Unfortunately, the *B*-band filter of WFI is quite far from the Johnson *B* filter with a large colour term of $\simeq$-0.33 mag. After applying the calibration, the *B* magnitudes present a residual second-order trend in colour that appears as a residual offset of -0.05 mag for the extreme blue and red stars. We decided not to apply any correction for this effect and instead used the photometry of Sung et al. (1999) for all objects with $V < 12$ and $(B - V) > 1$. For fainter stars, the photometries show good agreement, with a residual offset of $\simeq$0.02 mag at V=14, increasing to 0.1 mag at $V \simeq$17. The comparison between our photometry and that of Sung et al. (1999) is shown in the upper three panels of Fig. 4.2.

Our data were also compared with the *BV* photometric data of Koo et al. (2007), acquired in a search for variable stars. The comparison (lower panels of Fig. 4.2) also shows good agreement with no systematics, with a dispersion of 0.08 for $V < 14$, increasing for fainter magnitudes.

Since the cluster is very dense, our photometry suffers from crowding effects, especially in the central parts. The completeness of the photometry was estimated as usual by randomly adding stars of magnitude V ranging from 16 to 22 and running the source detection step again, then counting how many of the added stars were recovered. This method allows to estimate the completeness for each magnitude bin in a given region of

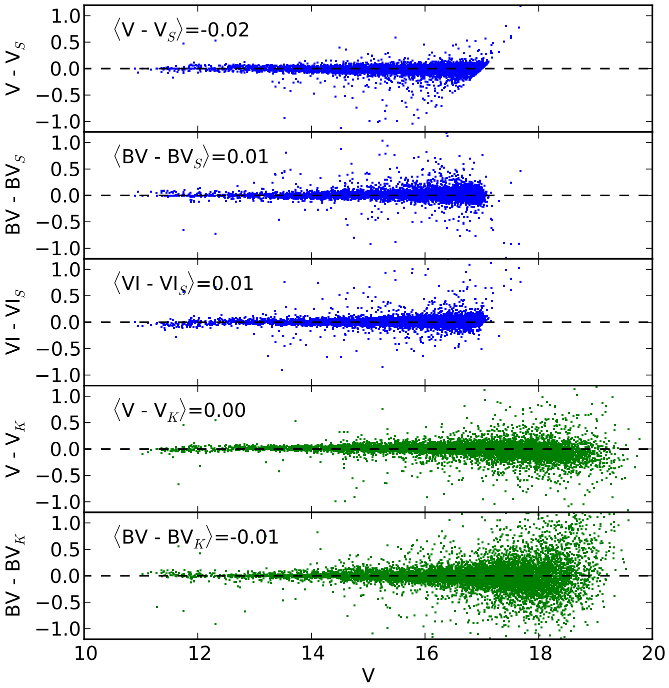

Figure 4.2: *Upper three panels:* comparison of our photometry with that of Sung et al. (1999). *Lower two panels:* comparison with Koo et al. (2007). The labels indicate the residual zero point differences.

the cluster. The completeness is better than 50% up to magnitude $V \simeq 18$ in the central regions and $V \simeq 19.7$ in the less crowded outskirts (see Fig. 4.3).

The data contain a total of 123 037 stars. The BV CMD shows a very clear main sequence standing out of the background as can be seen in Fig. 4.4. Evolved stars are also visible with a red clump located around $(B-V, V) = (1.5, 12)$. The lower panels of Fig. 4.4 show that the main sequence can be easily followed down to V=16 in the inner regions of the cluster, while the top right-hand panel shows that the signature of the cluster is not visible outside of $18'$.

VPHAS+ *ri* photometry

The VPHAS+ observations used here are r- and i-band data from three fields (numbered 212, 213, and 237) that overlap near the sky position of NGC 6705. A general description of this public survey that continues to execute using the OmegaCAM instrument on the

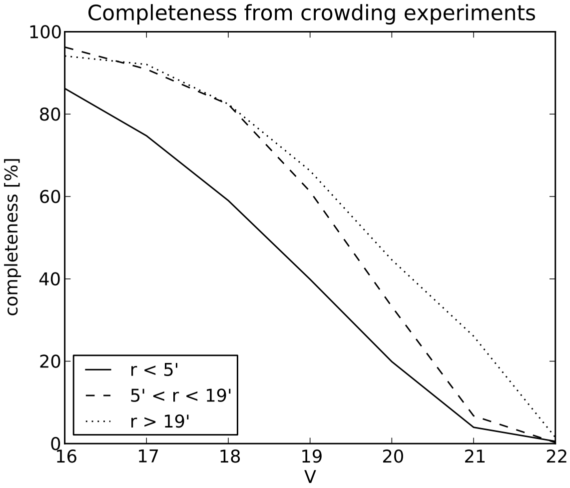

Figure 4.3: Completeness of our photometry obtained from crowding experiments for different regions of the cluster.

VLT Survey Telescope is provided by Drew et al. (2014). The images and catalogue were provided were kindly provided by J. Drew before publication. Each pointing captures a square degree at a time, with the centre of NGC 6705 falling within a couple of arcminutes of the southern edge of field 212, and towards the boundary with 237. The data were all obtained at a time of very good seeing (0.5 to 0.6 arcseconds) during the night of 7 July 2012 when the moon was relatively bright (FLI = 0.77). In r, the formal 10-σ magnitude limit falls between 20.5 and 20.8 with a likely completeness limit of ∼19.5, while these limits are approximately 0.5–0.7 magnitudes brighter in the i band. All magnitudes are specified in the Vega system.

The CMD of the inner $12'$ is shown in Fig. 4.5. The data are used in Sect. 4.1.2 to derive the extinction map of the region surrounding the cluster. Owing to the very good seeing, stars brighter than $r \sim 12$ are partially saturated in both r and i bands, making the position of the main sequence turn-off point and red clump stars quite uncertain in the CMD.

4.1.2 Extinction maps

When looking towards the inner parts of the Galaxy, the line of sight often meets regions of high extinction. Before discussing the age and the structure of NGC 6705, we need to assess whether the studied region is affected by differential extinction. The available VPHAS+ ri

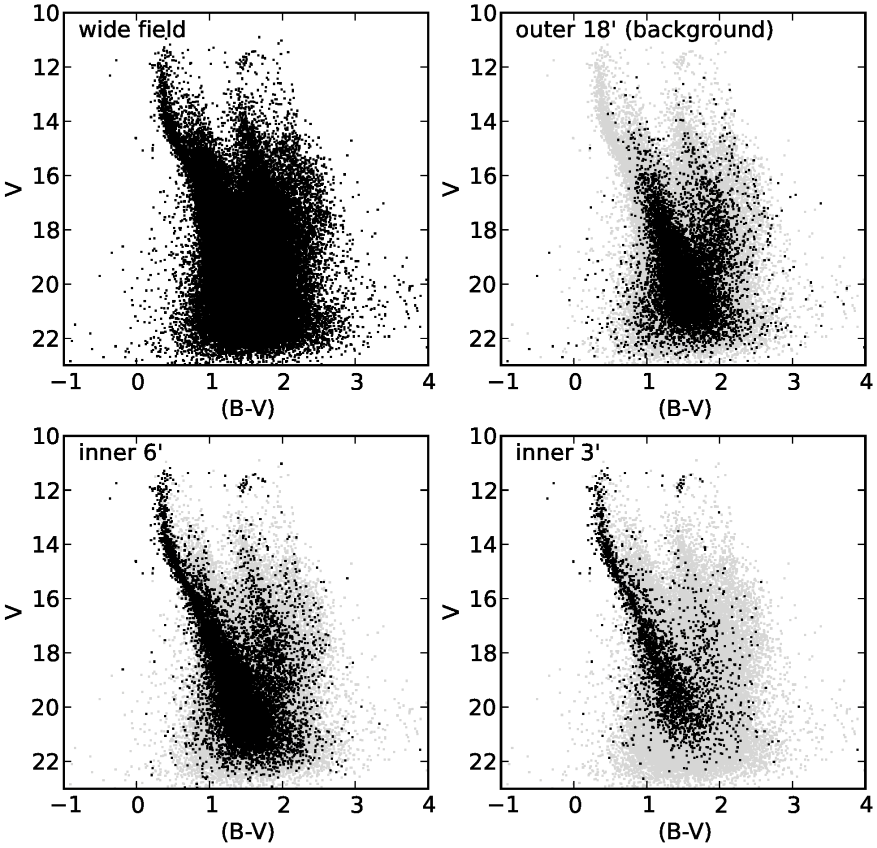

Figure 4.4: *Top left:* BV CMD of all 123 037 in our sample. *Top right:* CMD of the outer $18'$, which we consider as our background field. *Bottom left* and *bottom right:* CMD of the inner $6'$ and $3'$. In the last three panels, the grey points correspond to the wide-field CMD.

photometry covers a very wide field, much larger than our BVI photometry, which allows us to study the extinction of the background around the cluster. The ri CMD of the inner $12'$ of the cluster is shown in Fig. 4.5. The PARSEC isochrone (Bressan et al., 2012) shown in that figure corresponds to the parameters of the best fit of the BV photometry (see Sect. 4.1.4). First we make use of the GIRAFFE members to derive the extinction law in the direction of the cluster. Figure 4.6 presents the colour-colour diagrams in the passbands $BVIri$. To fit the data, we need to adopt the relations $E(V-I) = 1.24(\pm 0.05) \times E(B-V)$ and $E(r-i) = 0.68(\pm 0.04) \times E(B-V)$. While the ratio $E(V-I)/E(B-V)$ is consistent with the total-to-selective extinction ratio $\mathrm{R}_V = A_V/E(B-V)$=3.1 using the Fitzpatrick

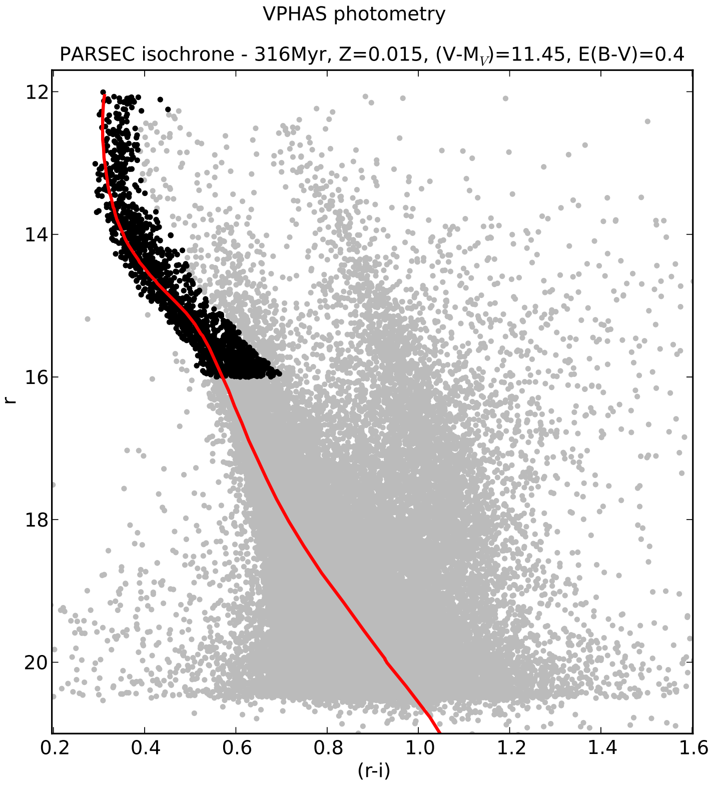

Figure 4.5: VPHAS+ ri CMD of the central 12′ of the cluster. The spatial distribution of the selected stars (black points) is shown in Fig. 4.7. The solid line corresponds to the PARSEC isochrone of best parameters, shifted for distance modulus and extinction (see Sect. 4.1.4 for detail). Stars brighter than $r = 12$ suffer from saturation and are not shown here.

(1999) law, the relation $E(r-i)/E(B-V)$ is slightly larger than the value of $E(r-i) = 0.6 \times E(B-V)$ given by Yuan et al. (2013).

Red clump stars in intermediate and old populations are often used in the literature as distance and extinction indicators. The PARSEC isochrones indicate that the $r-i$ colour of the red clump varies by 0.07 for ages from 2 to 10 Gyr, and by 0.14 for Z from 0.001 to 0.03. The small dependence of their magnitude and colour on age and metallicity makes them good tracers of the extinction across the field.

We simulated a field corresponding to the coordinate of the cluster using the Padova Galaxy Model (Vallenari et al., 2006). The red clump stars in the model have an absolute r

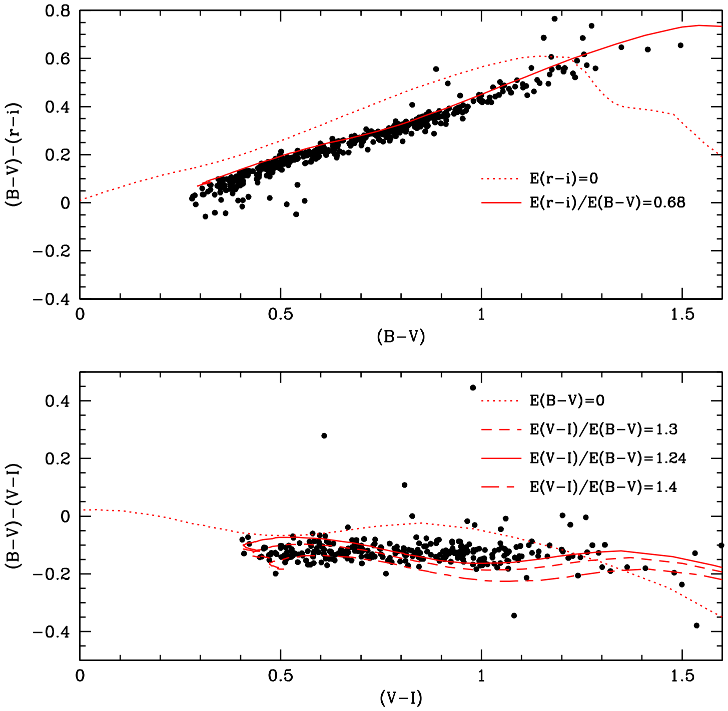

Figure 4.6: colour-colour diagrams for NGC 6705 GIRAFFE members main-sequence stars, compared with the relation expected from PARSEC isochrones for various extinction laws.

magnitude of 0.55 and an intrinsic colour $(r-i) = 0.525$. We followed the colour excess of the red clump stars at different distances. The field was divided into cells of $0.25° \times 0.25°$. In each of these cells, we computed the reddening as follows: the red giant stars falling in the magnitude range that corresponds to the distance range we want to probe (for instance, $11.5 < r < 13$ for $2-4\,\mathrm{kpc}$) were divided into bins of 0.05 in the $(r-i)$ colour, and we looked for the most populated colour bin. This colour was then compared to the reference value of $(r-i) = 0.525$, to find the colour excess. We applied the procedure a second time, looking at a fainter magnitude slice, to take into account that one must look at fainter magnitudes to probe stars that are more reddened. We found that going for more iterations did not significantly change the results. After this second step, the final colour excess $E(r-i)$ was converted to $E(B-V)$ using the relation $E(r-i) = 0.68 \times E(B-V)$. Our bins of 0.05 in $r-i$ colour correspond to a resolution of 0.07 in $E(B-V)$. The extinction map we obtain for the distance range $2-4\,\mathrm{kpc}$ is visible in Fig. 4.7.

The inner region of the cluster studied with the WFI BVI photometry sits in a zone of relatively low and uniform extinction, with $E(B-V) = 0.40$ out to $11'$ from the centre. A higher extinction is found at $DEC >$ -6°and $RA < 283.25°$, with $E(B-V)$ up to 0.7. A comparison with the map by Schlegel et al. (1998) shows consistency, with the north-west quadrant being the most reddened. However, the maps of Schlegel et al. (1998) give the integrated extinction along the line of sight, while we restrict our determination to the distance range 2–4 kpc. For this reason, our values of extinction are lower, and the distribution is not directly comparable.

Although the cluster itself lies in a window of constant extinction, the bottom left-hand panel of Fig. 4.7 shows clearly that the star density distribution of the photometrically selected VPHAS+ cluster stars (Fig. 4.5) is correlated with the extinction, making the background density inhomogeneous.

In the bottom right-hand panel of Fig. 4.7 we show the distribution of photometrically selected stars from the 2MASS catalogue with $J < 15$ (Fig. 4.8). The infrared bands of the 2MASS data are less affected by extinction than the r and i bands of VPHAS+, and the relations by Yuan et al. (2013) tell us that a reddening of $E(B-V) = 0.7$ translates to an extinction of 0.54 mag in the J band. The distribution obtained for the 2MASS stars is similar to the one obtained for the VPHAS+ stars, with a hole in the distribution in the north-east quadrant and a steep drop in the stellar density in the north-west. Further details on this density distribution are given when we establish the luminosity profile of the cluster (Sect. 4.1.3).

4.1.3 Cluster structure

To derive the cluster structure, we make use of the WFI photometry in the inner region and of the VPHAS+ data in the external parts.

Center determination

To determine the position of the centre of the cluster, we first made a photometric selection that includes the brightest stars (red clump and upper main sequence). We used the method described by Donati et al. (2012) that consists in finding the barycentre of the sample, then retaining the 70% of the stars that lie closest to this barycentre and repeat the procedure until convergence to the actual centre of the cluster. The uncertainty on the final position arguably depends on the uncertainty in the selection of cluster members. Selecting only the brightest stars gives a better-defined membership but also poorer statistics. Using different magnitude cuts from V=13 to 16, the position of the centre is at $\alpha_{2000} = 18^h51^m4^s$, $\delta_{2000} = -6°16'22''$ ($RA = 282.767°$,$DEC = -6.273°$) with an uncertainty of 2”.

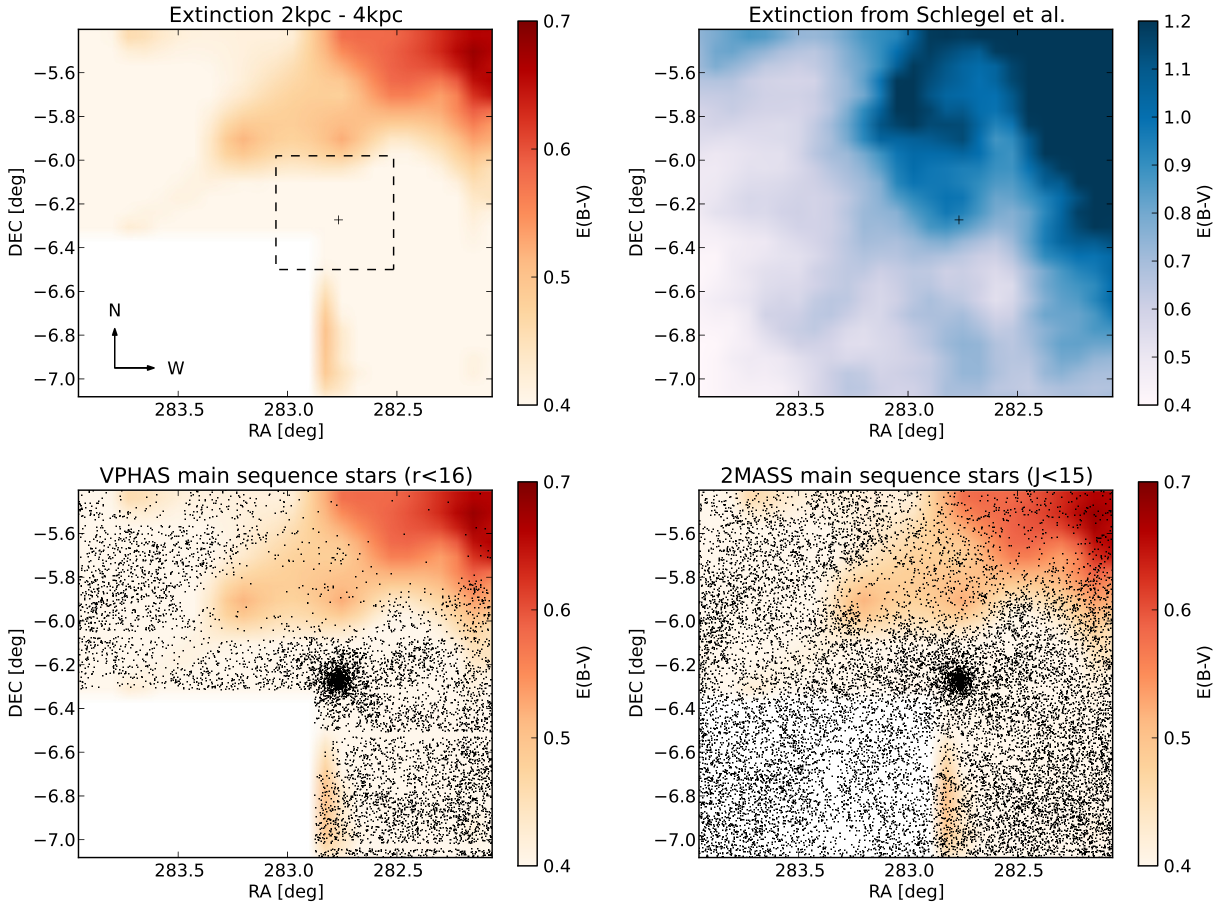

Figure 4.7: *Top left:* extinction map obtained from VPHAS+ photometry in the distance range 2-4 kpc. The cross indicates the center of the cluster. The dashed line shows the footprint of our BVI photometry. *Bottom left:* same extinction map. The black points are cluster stars selected from the $(r-i, r)$ VPHAS+ CMD, with $r < 16$. The CCD gaps are visible as horizontal lines. *Top right:* extinction map from Schlegel et al. (1998) for this field. *Bottom right:* same as bottom left, but with 2MASS main-sequence stars ($J < 15$).

Radial density profile

We derived the luminosity profile using the V-band magnitudes. Through a χ^2 minimisation, we fitted a single mass two-parameter King profile (King, 1962):

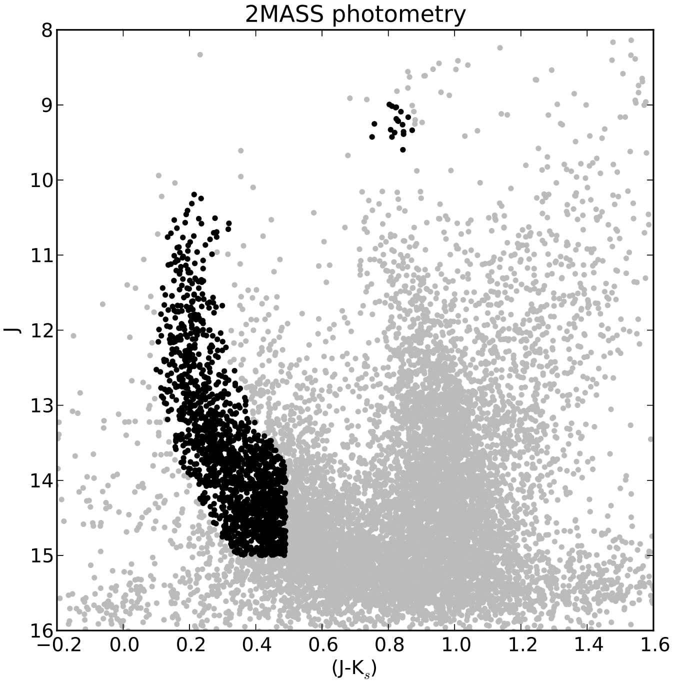

Figure 4.8: 2MASS CMD of the inner 12′ of NGC 6705. The spatial distribution corresponding to the photometric selection (black points) is shown in Fig. 4.7 on a larger field.

$$f(r) = \sigma_{bg} + \frac{\sigma_0}{1 + (r/r_{core})^2} \tag{4.1}$$

where σ_{bg} the background luminosity, σ_0 the central luminosity and r_{core} the core radius are left as free parameters.

The data was corrected for completeness in each radius and magnitude bin. Using all the stars with $V < 18$, we obtain a core radius of $1.23 \pm 0.28'$ (Fig. 4.9). This value is in agreement with the value of $1.81 \pm 0.71'$ found by Santos et al. (2005) (hereafter S05) using main-sequence stars brighter than J=15. Taking our distance estimate (Sect. 4.1.4) into account, we obtained a core radius of 0.69 ± 0.24 pc in physical units.

The much wider field offered by the VPHAS+ data enables us to trace the luminosity profile in the most distant parts of the cluster. We established the luminosity profiles in three different quadrants (Fig. 4.10). We can see that the three profiles are similar inside 10′, with the small differences explained by statistics and a patchy extinction, but

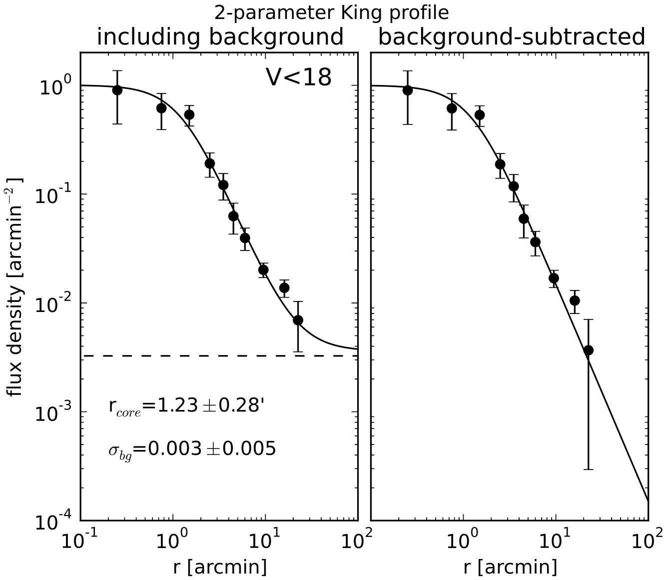

Figure 4.9: Observed luminosity profile of NGC 6705 (black dots) for stars with $V < 18$, fitted with a two-parameter King profile (continuous line), including background (left) and after subtracting the background (right). The flux density was normalised to the central luminosity so that $\sigma_0 = 1$.

show different behaviours at larger radii. As one could expect from the extinction map of Fig. 4.7, the luminosity in the north-west quadrant drops to lower values than in the other two. In the north-east quadrant, a dip is visible between $25'$ and $40'$, corresponding to a region of stronger extinction of the background (see Fig. 4.7). In the south-west quadrant, beyond $20'$, the background density increases with radius as the extinction decreases. Since outside of the core the luminosity profile is mainly shaped by extinction, it is not possible to estimate the tidal radius of NGC 6705 by fitting a three-parameter King profile. The value of $r_{tidal} = 52 \pm 27'$ reported by S05 falls exactly in the distance range affected by strong extinction. S05 also observed a deviation of the luminosity profile from their model between $11'$ and $16'$, and suggest this excess could be due to low-mass stars moving to larger radii due to mass segregation. Without a proper model for the background density, it seems very difficult to draw conclusions on the structure of the cluster beyond $10'$.

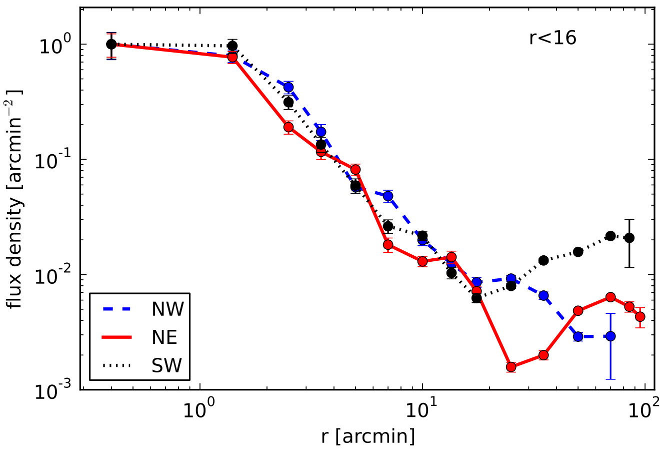

Figure 4.10: Stellar density profiles for the north-west, north-east and south-west quadrants (NW, NE, and SW) of the VPHAS+ photometry of NGC 6705, using stars with $r < 16$. The profiles in the three quadrants were normalised to the flux in the innermost bin. The background level was not subtracted.

Mass segregation from the luminosity profile

Mass segregation is an internal dynamical phenomenon that takes place in star clusters and leads the most massive stars to be more tightly clumped than the least massive ones (Spitzer, 1969). A certain number of methods can be used to see whether mass segregation is occurring in a cluster, for instance showing the initial mass function (IMF) is flatter in the inner regions (Gouliermis et al., 2004), applying a minimum spanning tree analysis (Allison et al., 2009, , see Sect. 4.1.3), comparing the cumulative radial distribution in different mass bins (Sharma et al., 2008), or directly comparing the distance to the centre for stars of different brightness. Here we compare the density profiles of stars in different mass ranges (cf. Sect. 4.1.3) and compare the slope of the mass function in different regions of the cluster (our Sect. 4.1.4, and S05).

Figure 4.11 shows the luminosity profiles established in four different magnitude ranges: 10 – 13, 13 – 15, 15 – 16, and 16 – 18. For our best-fitting PARSEC isochrone, these correspond to the mass ranges: $M > 2.14\,M_{\odot}$, 2.14 – 1.37, 1.37 – 1.14, and 1.14 – 0.81. For stars with $V > 16$, we applied a completeness correction based on the distance and magnitude.

In the faintest range ($16 < V < 18$) we discarded the data point corresponding to the most central bin ($r < 0.5'$), owing to the very low completeness for faint stars at the centre of the cluster. It is clear that the core radius increases as fainter stars are considered from $1.02 \pm 0.25'$ in the range $10 < V < 13$ to $3.62 \pm 1.12'$ in the range $16 < V < 18$. This result is consistent with results by Sung et al. (1999), although they do not quantify the increase in radius for the distribution of progressively fainter stars.

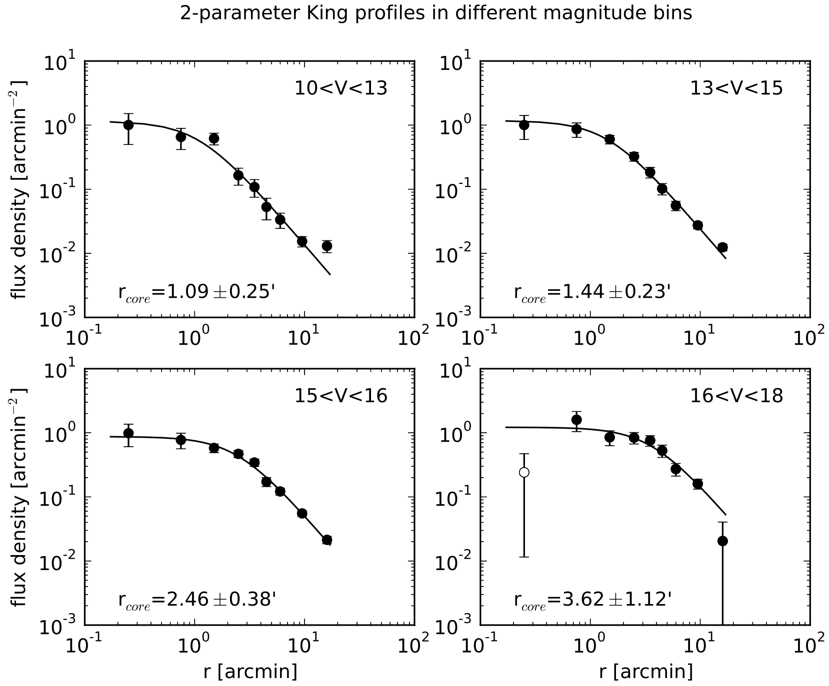

Figure 4.11: Observed and fitted luminosity profiles obtained with stars in different magnitude ranges. The background was fitted and subtracted. In the bottom right panel, the open symbol is the datapoint that was discarded when fitting the luminosity profile.

Mass segregation from the Λ parameter

Mass segregation can be quantified by means of the Λ parameter (Allison et al., 2009). The method consists in comparing the length $l_{N,massive}$ of the minimum spanning tree (MST) connecting the N most massive cluster stars with that of the MST connecting a set of N randomly selected cluster stars ($l_{N,random}$). Mass segregation is quantified through the parameter $\Lambda = \frac{\langle l_{N,random} \rangle}{l_{N,massive}}$, where $\langle l_{N,random} \rangle$ is the mean MST length obtained for a large number (at least a hundred) of randomly selected sets of N stars. If the MST connecting the massive stars is shorter than the MST of randomly selected stars ($\Lambda > 1$), then there is evidence for mass segregation. The uncertainty on Λ can simply be estimated by considering the standard dispersion on $l_{N,random}$.

We have applied the approach of Parker et al. (2011) who, instead of progressively increasing the value of N when computing Λ for the N brightest stars, use a moving window containing a fixed number of 40 stars to calculate Λ in different mass ranges. We also followed the recommendation of Maschberger & Clarke (2011) and used the median MST length of $l_{N,random}$ instead of the mean. This approach has proven more robust with respect to stars located in outlying positions that can have a significant influence on the determination of Λ.

Figure 4.12 shows the value of Λ obtained in various V-magnitude ranges. We can see that stars brigther than $V = 13.4$ (corresponding to a mass of $2.6\,\mathrm{M}_\odot$ for PARSEC isochrones) are clearly segregated. Λ for fainter stars converges to a value slightly lower than 1. A value of Λ under 1 is an indication of stars being inversely segregated (less tightly distributed than the cluster as a whole). Here we attribute this effect to the poor completeness for faint stars in the inner regions.

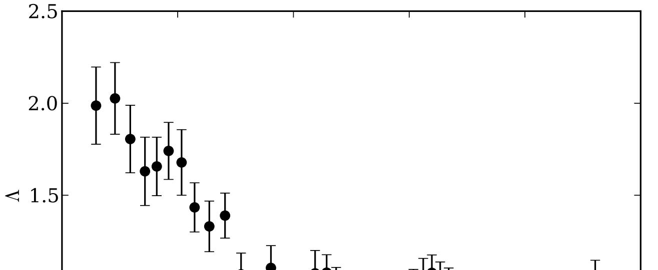

Figure 4.12: Λ parameter in different V-magnitude bins. Λ is clearly above 1 for stars brighter than $V = 13.4$ ($2.6\,\mathrm{M}_\odot$), indicating mass segregation.

4.1.4 Age determination

In this section we give an estimate of the age, distance, and metallicity of NGC 6705 from the CMD analysis of the WFI photometry, which corresponds to the part of the cluster that is not affected by variable extinction. We first compared the CMD with PARSEC (Bressan et al., 2012) and Dartmouth (Dotter et al., 2008) isochrones, then proceeded to fit a synthetic luminosity function in the inner region of the cluster.

Comparison with theoretical isochrones

We have compared the BVI CMD of the inner $6'$ of NGC 6705 with PARSEC and Dartmouth isochrones. The age, distance modulus, reddening and metallicity of the cluster can be estimated by matching the key features of the CMD (such as the main sequence slope and the positions of the main sequence turn-off and the red clump) traced by the cluster members established in Sect. 5.2.2 to the shape of the theoretical isochrones.

The PARSEC isochrone that reproduces best the morphology of the CMD is a model of 316 Myr ($\log t$=8.5), solar metallicity (Z=0.0152), $E(B-V) = 0.40$ and $(V-M_V) = 11.45$ ($d_\odot = 1995 \pm 180$ pc). The left-hand side panels of Fig. 4.13 show this isochrone, along with different choices of distance modulus, extinction, ages, and metallicities. Using a PARSEC isochrone of slightly super-solar metallicity produces a marginally compatible fit. On the other hand, a sub-solar metallicity fails to reproduce the position of both the red clump and the main sequence turn off at the same time. We estimate the uncertainty on the extinction to be of the order of 0.03, the uncertainty on the age 50 Myr. For an age of 316 Myr, the mass of the main sequence turn off stars is $3.2\,M_\odot$.

The best set of parameters for fitting a Dartmouth isochrone is an age of 250 Myr, extinction $E(B-V) = 0.37$, and distance modulus $(V-M_V) = 11.6$ ($d_\odot$=2090 pc), as shown in Fig. 4.13. Again, using isochrones of super-solar metallicities produces a less satisfying fit than a solar metallicity. The age of 250 Myr is in agreement with the result of S05, who used Dartmouth isochrones on 2MASS photometry. This age corresponds to a turn off mass of $3.47\,M_\odot$. The best fits for these two sets of isochrones are both shown on Fig. 4.14 for a direct comparison.

As already discussed, PARSEC and Dartmouth isochrones give different determination of the age. This difference is due to the fact that the red clump stars tend to be brighter in the PARSEC tracks than in the Dartmouth tracks, because of a different choice of mixing-length parameter and solar metallicity reference (see Sect. 5.6 of Bressan et al., 2012). As a consequence, a PARSEC isochrone of higher age is needed to reproduce the position of the red clump.

To fit the $(V-I)$ colour in Fig. 4.14 we adopt the relation $E(V-I)/E(B-V) = 1.24$ derived in Section 4.1.2. Fig. 4.15 shows the position of the 21 UVES cluster members in the $(\mathrm{T_{eff}} - \log g)$ plane. PARSEC isochrones of age 316 Myr and solar or slightly super-solar metallicity are compatible with the location of the red clump stars.

Luminosity function

To confirm the results obtained from the comparison with theoretical isochrones, we studied the luminosity function (LF) of the inner 0.1° (6′) of the cluster. This region is large enough to provide good statistics, without being too contaminated by background stars. A photometric selection was made, following the main sequence down to magnitude V=18. We considered the stars farther than 0.3° (18′) from the centre of the cluster as our background field (see Fig. 4.4). The LF of the background field was subtracted from the LF of the cluster, taking the respective completeness and area of the two regions into account. The error on the luminosity function takes the statistical error on both the cluster and the background into account.

Synthetic populations were computed using PARSEC tracks (Bressan et al., 2012), varying the age and metallicity, as well as the slope α of the IMF and the distance modulus. The reddening was kept fixed to a value of $E(B-V) = 0.40$. The LF of the synthetic populations were compared with the observed LF using a χ^2 method and imposing a constrain on the colour of the main sequence and red clump.

Using isochrones of solar metallicity provide the lowest χ^2, and isochrones with [Fe/H]= +0.10 provide very similar results, while using [Fe/H]= −0.10 provides worse fits. The χ^2 maps (Fig. 4.16) show the confidence interval of the parameters that reproduce the observed LF. From these maps we estimate the parameters of the cluster as $\log t$=8.55±0.1, $(V - M_V) = 11.55 \pm 0.3$, and the IMF slope $\alpha = 2.95 \pm 0.2$.

In this procedure, we did not take into account that some of the stars may be unresolved binary (or multiple) systems. Weidner et al. (2009) indicate that even in the extreme case where 100% of the stars are in multiple systems, the α parameter may be underestimated by 0.1 at most.

Mass function and total mass

In this section we derive the mass of the cluster using its LF. We produce the LF of the cluster in three annuli (corresponding to distance the ranges $0' - 3'$, $3' - 6'$, and $6' - 9'$) and convert the V magnitudes to masses using a PARSEC isochrone with the parameters determined in Sect. 4.1.4. The observed magnitude range (V <18) corresponds to a mass

Table 4.1: Slope of the mass function in different regions on the cluster.

Radius (')	α
This study	
0 - 1.8	0.50 ± 0.15
0 - 3	1.18 ± 0.11
3 - 6	3.01 ± 0.11
6 - 9	3.79 ± 0.10
0 - 9	2.70 ± 0.19
1.8 - 9	3.29 ± 0.07
Santos et al. (2005)	
0 - 1.8	0.27 ± 0.15
1.8 - 10	2.41 ± 0.10
10 - 21	3.88 ± 0.20
0 - 21	2.49 ± 0.09

Notes. α is the parameter in the mass function: $N(M)\,dM \propto M^{-\alpha}$.

range of 1 to 3.2 $M_\odot$. We chose to limit ourselves to the inner $9'$. At larger radii, the cluster is hardly visible against the field stars, and our procedure that consists in subtracting the LF of the background from the observed one becomes very uncertain.

In each region, we derived the parameter α, defined as $N(M)\,dM \propto M^{-\alpha}$. The results of the fit are shown in Fig. 4.17. The value of α increases with the radius, indicating that the mass function gets steeper because of a deficit of high-mass stars. In the most central region, $\alpha = 1.18$ indicates an excess of high-mass stars with respect to what would be expected from the Salpeter IMF ($\alpha = 2.35$). Over the whole range $0 - 9'$, the slope of the mass function is $\alpha = 2.70 \pm 0.2$.

The previous studies of the evolution of the slope of the IMF with the radius have also found that the mass function was flatter in the inner region. S05 found a slope of $\alpha = 0.27$ in the inner $1.8'$, $\alpha = 2.41$ in the region $1.8 - 10'$, and $\alpha = 3.88$ in the region $10 - 21'$. Sung et al. (1999) find slopes of $\alpha = 0.5$ to 1.7 inside $3'$. The slope values found by those two studies are listed in Table 4.1 along with our estimates. The distance ranges given by S05 were converted back from parsecs to arcminutes using their value of the distance.

In theory, if the mass function of a cluster is known for its brightest stars, it is possible to extrapolate the mass functions down to lower masses and estimate the total stellar mass contained in the cluster. When dealing with mass-segregated OCs that were possibly affected by evaporation and tidal mass loss, inferring the mass function from the observed range to the lower masses is affected by large uncertainties. To obtain the slope of the

Table 4.2: Mass contained in different regions of the cluster.

Region [′]	α	Observed [$M_\odot$]	Extrapolated (power law) [$M_\odot$]	Extrapolated (Kroupa) [$M_\odot$]
0 – 3	1.18 ± 0.11	242 ± 64	375 ± 56	664 ± 115
3 – 6	3.01 ± 0.11	241 ± 46	4303 ± 1127	1430 ± 151
6 – 9	3.79 ± 0.10	181 ± 43	18 888 ± 4702	1437 ± 242
Total		664 ± 153	26 566 ± 5885	3531 ± 508
0 – 9	2.70 ± 0.19	700 ± 310	6851 ± 1865	3683 ± 1063

Notes. α is the parameter in the mass function: $N(M)\,dM \propto M^{-\alpha}$. The stars were observed down to $1\,M_\odot$. The extrapolation was done down to $0.08\,M_\odot$.

mass function in the unobserved range (under $1\,M_\odot$) we used two methods. The simplest one is to assume that the slope of the power law derived from the stars with $M<1\,M_\odot$ is the same over the full mass range. The second one is to use the IMF by Kroupa (2001): $\alpha = 1.3$ for $0.08 < M_\odot < 0.5$ and $\alpha = 2.3$ for $0.5 < M_\odot < 1$. For masses over $1\,M_\odot$ we used the values obtained from our fit. In the inner region ($r< 3'$), we observe a nearly flat mass function, which means that using this slope over the whole mass range produces fewer low-mass stars than using the Kroupa IMF. In the other two regions, the mass function is steeper, and in the low-mass range it is well over the prediction of the Kroupa IMF. The result of integrating these mass functions are shown in Table 4.2 for the different choices of mass function in the different regions.

When integrating the mass function over the whole $0 - 9'$ region, we obtained values between $3683 \pm 1063\,M_\odot$ (using the Kroupa IMF under $1\,M_\odot$) and $6851 \pm 1865\,M_\odot$ (using the extrapolated power-law). This latter number is compatible with the number quoted by S05, who estimate a total mass of $6500 \pm 2100\,M_\odot$ inside $10'$, and $11\,000 \pm 3800\ M_\odot$ inside $21'$ using the IMF slopes listed in Table 4.2, and the Kroupa IMF under $1\,M_\odot$). Our determination does not take the presence of binary stars whose percentage is unknown into account. The effect of the presence of unresolved binaries on the observed α parameter is weak, but according to Weidner et al. (2009), not accounting for the presence of multiple systems can hide 15 to 60% of the stellar mass of a cluster. In addition, less massive stars could be either lost from the cluster due to the effect of the disk tidal field, or located in a surrounding halo. For these reasons, our determination is a lower limit to the cluster mass. Owing to the large uncertainties on the determinations, the derived values of the mass of NGC 6705 are in reasonable agreement with the virial masses derived in Sect. 5.2.3.

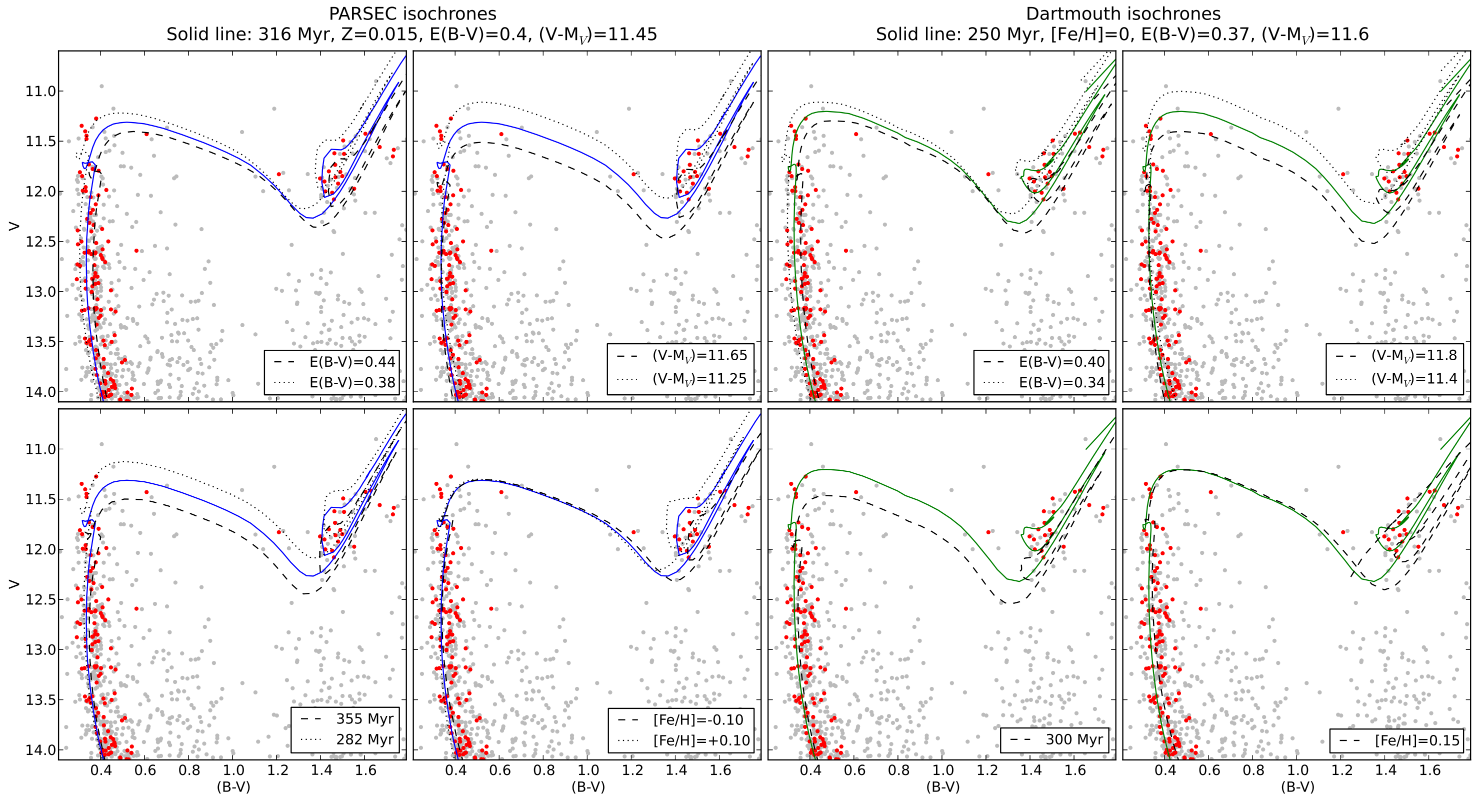

Figure 4.13: Comparisons of the BV CMD with PARSEC and Dartmouth isochrones of various parameters. The grey points are all the stars in our photometry, and the radial velocity members are marked in red. *Left-hand side panels:* The best-fitting PARSEC isochrone (solid blue line) corresponds to an age of 316 Myr, a solar metallicity, a reddening $E(B-V) = 0.40$ and a distance modulus $(V - M_V) = 11.45$. The four panels show the change in the isochrone when modifying the extinction, distance modulus, age and metallicity with respect to the best-fitting isochrone. *Right-hand side panels:* same procedure with Dartmouth isochrones. The best-fitting isochrone is the solid green line. In all cases, the data are uncorrected for extinction. The isochrones are shifted along the extinction vector.

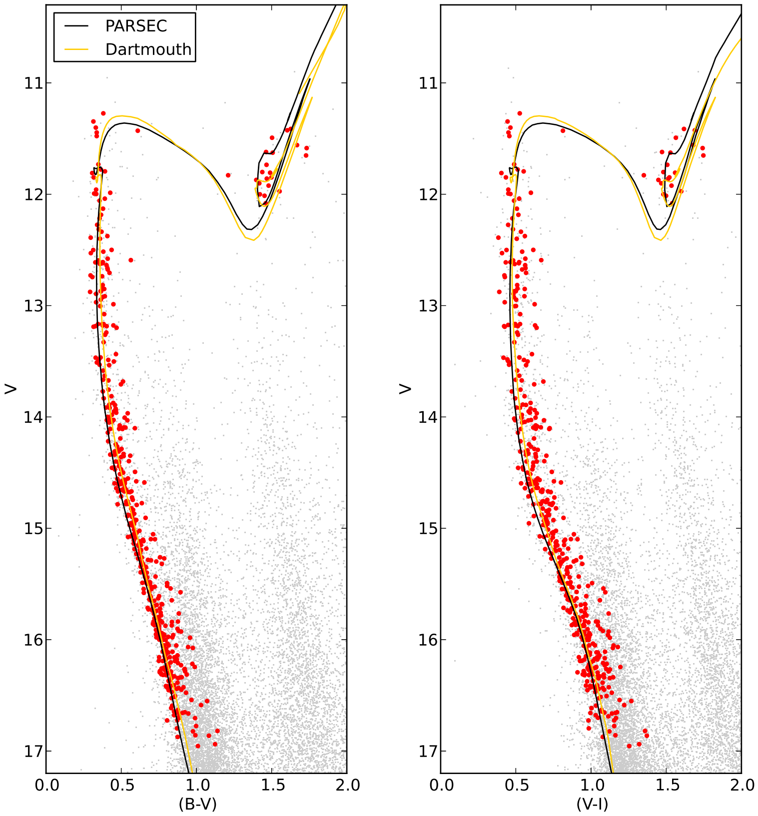

Figure 4.14: Comparison between theoretical isochrones and our photometry (PARSEC isochrone of solar metallicity, 316 Myr, shifted by $E(B-V) = 0.40$ and $(V-M_V) = 11.45$) and Dartmouth isochrone of solar metallicity, 250 Myr, $E(B-V) = 0.37$, $(V-M_V) = 11.6$). The grey points are all the stars in our photometry, while the red points are the radial velocity members.

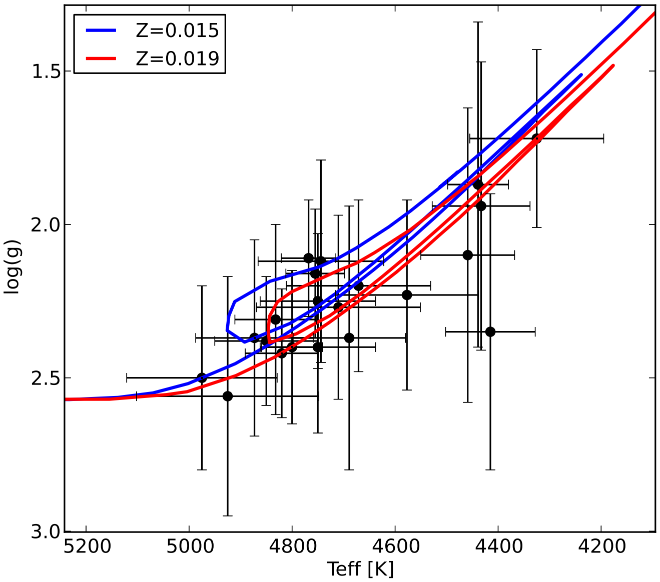

Figure 4.15: Position of the 21 UVES members of NGC 6705 in the theoretical plane. The position of the red clump is reproduced well with a PARSEC isochrone of age log *t*=8.5 and Z=0.015 ([Fe/H]=0) or Z=0.019 ([Fe/H]=0.1).

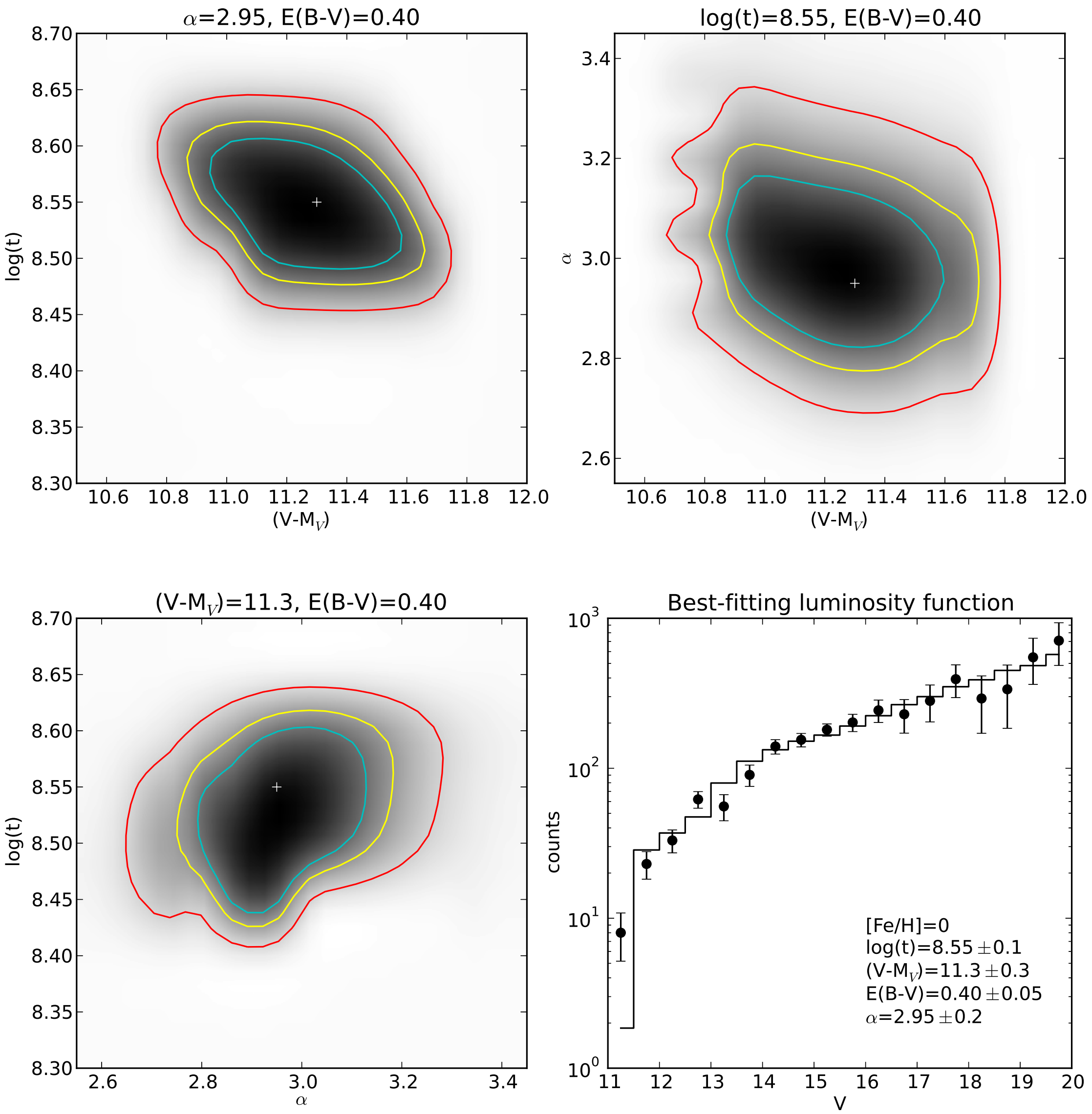

Figure 4.16: Probability contours for the fit of the luminosity function. The cyan, yellow, and red lines show the 50%, 68%, and 90% confidence regions, respectively. The white cross indicates the best-fitting solution. The bottom right panel shows the observed LF (cleaned from the background) and the best-fitting theoretical one. The bins with $V > 18$ are shown but were not used in the fitting procedure.

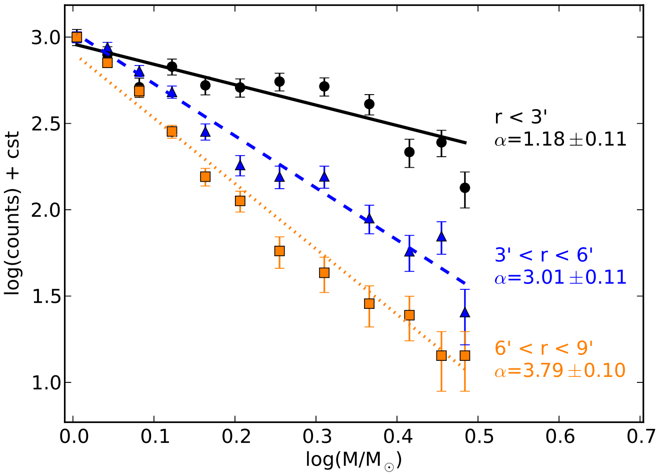

Figure 4.17: Mass functions obtained in three different regions of the cluster, showing the flattening of the IMF in the centre. The y-axis was shifted so that the observed number of stars in the lowest mass bin is the same for all three.

4.2 Trumpler 20

The open cluster Trumpler 20 (Tr 20) is a relatively old (∼1 Gyr) inner disk OC, located about 3 kpc from the Sun in the fourth Galactic quadrant at $(l, b) = (301.475°, b = 2.221°)$, or (RA,DEC)=($12°39'32''$,-$60^h37^m36^s$) (Seleznev et al., 2010). Few OCs older than 1 Gyr are known (less than 20% of the clusters in DAML02), although they consitute ideal probes of the Galactic disk evolution (see for instance Bragaglia & Tosi, 2006; Friel, 1995; Lépine et al., 2011; Magrini et al., 2009a; Pancino et al., 2010; Yong et al., 2012). Fewer OCs have been studied inside the solar circle than outside, and inner disk clusters deserve more attention in order to derive not only elemental abundances from spectroscopy, but also accurate age and distance determinations from photometry.

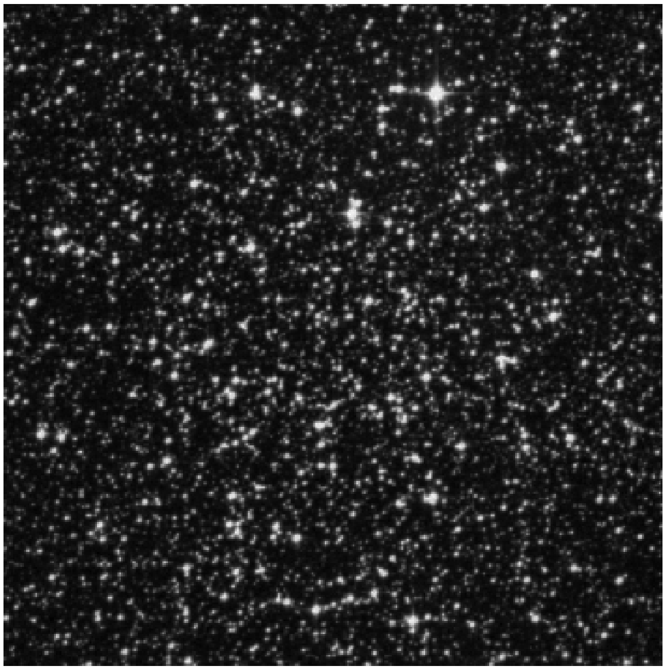

Figure 4.18: DSS image of Trumpler 20. The field is $10' \times 10'$.

The first study of Tr 20 to estimate its evolutionary status from photometry is that of McSwain & Gies (2005). A misidentification of the cluster CMD led them to fit an isochrone corresponding to an age of 160 Myr (see their Fig. 59). Platais et al. (2008) used *BVI* photometry down to magnitude $V = 18.5$ on a $20' \times 20'$ field of view. Based on a spectrum acquired with the FEROS spectrometer ($R = 48\,000$), they find a mean metallicity [Fe/H]=-

0.11 for one red clump star. Using Padova isochrones (Girardi et al., 2000a) of sub-solar metallicity, they estimate an age of 1.3 Gyr and a distance modulus of 12.6 mag, for an extinction E($B-V$)=0.46. They note that the upper main sequence is not tightly defined, and cleaning the CMD from field stars should provide better determinations.

Seleznev et al. (2010) made use of VI photometry on a $13.5'\times13.5'$ field of view, reaching down to magnitude $V\sim22$. They adopt Padova isochrones of solar metallicity and estimate an age of 1.5 Gyr, a distance modulus of 12.4 mag and an extinction $E(B-V)=0.48$. Relying on both their optical photometry and 2MASS infrared photometry, they estimate a cluster radius of $5.4'$. They also mention the peculiar morphology of the red clump, which seems bi-modal in the CMD.

A study by Carraro et al. (2010), based on $UBVI$ photometry makes use of two-colour diagrams and Padova isochrones of solar metallicity to derive an age of 1.4 Gyr. They estimate a distance modulus of 12.6 mag, but find a lower value of $E(B-V)$=0.35 for the extinction. They explain the broad aspect of the upper main sequence and red clump by the presence of unresolved binaries and field contamination.

Platais et al. (2012) show that a significant amount of differential reddening is present and plays a role in shaping the cluster CMD morphology, and rule out the possibility that the extended red clump and main-sequence turn-off (MSTO) is due to the presence of multiple populations in Tr 20.

The figures presented in this section are published in Donati et al. (2014).

4.2.1 CMD and differential reddening

The position of Tr 20 in the Galactic disk means that the presence of patchy dust structures along the lines of sight may produce a non-uniform reddening across the field of view. This differential extinction affects the morphology of the CMD in a similar way to photometric errors, except that it has a stronger effect on bright stars for which photometric errors are negligeable.

Differential reddening is not the only possible explanation to a broad main-sequence turn-off. For instance, a significant age spread during the star formation process can broad the MSTO in the late phases of cluster evolution. Unresolved binaries also contribute to the broadening because they appear brighter/redder than single stars. A metallicity spread could also produce a similar effect, with the more metal-rich stars appearing redder, but no evidence exists for metallicity spreads in OCs. Stellar rotation is another possible explanation. Fast-rotating stars such as MSTO stars can appear brighter and redder (Bastian & de Mink, 2009; Li et al., 2012), although Girardi et al. (2011) have shown that this effect is rather small.

The study of Platais et al. (2012) shows the presence of a significant differential reddening (DR) reaching $\Delta E(B-V) = 0.1$, which affects the CMD morphology. The individual DR values they derive are unfortunately not publicly available. We have produced our own DR map adopting a different approach, based on the method described in Milone et al. (2012). The details of the method are given in Sect. 4.2 of Donati et al. (2014). This procedure was based on the photometry of Carraro et al. (2010), because it reaches fainter magnitudes than the data of Platais et al. (2008) and allows to follow the MS on a wider magnitude range. The DR map is shown in Fig. 4.19. The final, de-reddened CMD is shown in Fig. 4.20.

Correction for DR clearly reduces the spread of the MSTO, and the RC stars appear more clumped as well on the CMD. The correction however does not change the luminosity and colour of those age-sensitive indicators. An important point is that despite the tighter distribution obtained for the RC stars after extinction correction, the red clump still seems extended or bi-modal. This peculiar morphology is discussed in Sect. 5.3.1.

The (de-reddened) CMD of Tr 20 was compared with four sets of theoretical isochrones: PARSEC (Bressan et al., 2012), BASTI (Pietrinferni et al., 2004), Victoria-Regina (VandenBerg et al., 2006) and Darmouth (Dotter et al., 2008). The chosen metallicity corresponds to the spectroscopic value [Fe/H]=+0.17 (see Sect.5.3.2). Depending on the adopted set of isochrones, age determinations vary from 1.25 Gyr to 1.66 Gyr, with a distance modulus between 12.64 and 12.72 mag.

4.2.2 Radius and mass

We made a broad photometric selection to remove very obvious field polluters from the sample, keeping the MS, MSTO, and RC stars. We determined the position of the cluster centre by an iterative process using the same method as described in Donati et al. (2012). We computed the barycentre of the positions of the stars, then took the 70% of stars closest to this position and recomputed their barycentre, and iterated until convergence on a central position. To avoid selecting too many field stars we set magnitude cuts at $V = 16$, 17, and 18. This led to similar results because the position we obtain is identical within $0.5'$ around the coordinates: $RA = 12^h37^m32^s.8; DEC = -60°37'37''.4$.

Tr 20 is densely populated and stands out against the field stars, which enabled us to follow its density profile. Carraro et al. (2010) indicate that the completeness of their photometry is better than 90% for magnitudes $V < 19$. To be conservative, we only used stars brighter than $V = 18$. We performed a least-squares fit of a two-parameter King profile (King, 1962):

$$f(r) = \sigma_{bg} + \frac{\sigma_0}{1 + (r/r_c)^2} \tag{4.2}$$

where σ_{bg} the background density, σ_0 the central density, and r_c the core radius are left as free parameters. The observed profile and the best-fit are shown in Fig. 4.21. Using a three-parameter King model that also takes into account a tidal radius does not improve the goodness of fit. This means that the tidal radius of Tr 20 is larger than our field of view, and the region where the density profile starts to decrease faster is too far out for our data.

Since the model fitting provides a value for the background stellar density, we were able to remove its contribution to the star counts. The density profile was integrated to obtain the total number of stars contained in the cluster. Assuming a Salpeter mass function and the best-fitting PARSEC isochrone, we produced a synthetic population that contains the same number of stars as Tr 20 in the magnitude range $V < 18$. We added all the masses of stars down to $0.08\,\mathrm{M}_\odot$ and found a total mass of about $6800\,\mathrm{M}_\odot$.

Varying the age of the isochrone within the uncertainties gives an estimate of the error on the total mass. This whole operation was also performed by selecting stars brighter than $V = 17$ and $V = 16$, which yielded very similar results. Finally, we estimated the total mass of Tr 20 to be $6700 \pm 800\,\mathrm{M}_\odot$. We can draw a more conservative estimate by adding the contribution of the random errors to the star counts. Considering the Poissonian uncertainty, we find masses between the extreme values of 5500 and $8000\,\mathrm{M}_\odot$.

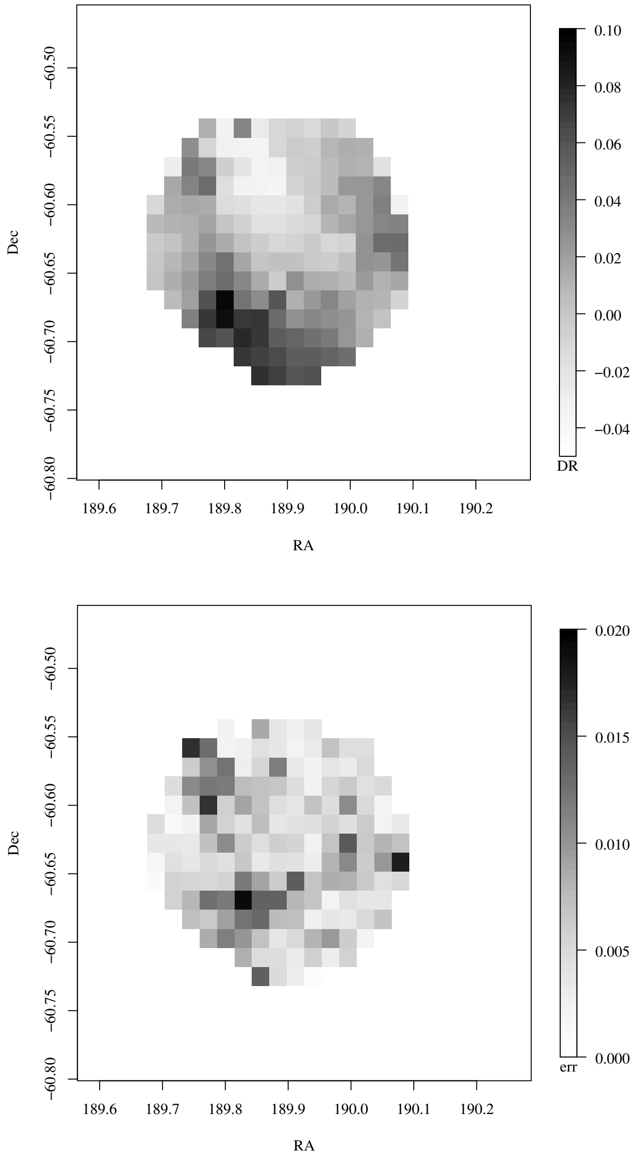

Figure 4.19: *Upper panel:* colour deviation from the fiducial line, in bins of $50'' \times 50''$ for the inner $6'$ of the cluster. *Lower panel:* corresponding error map.

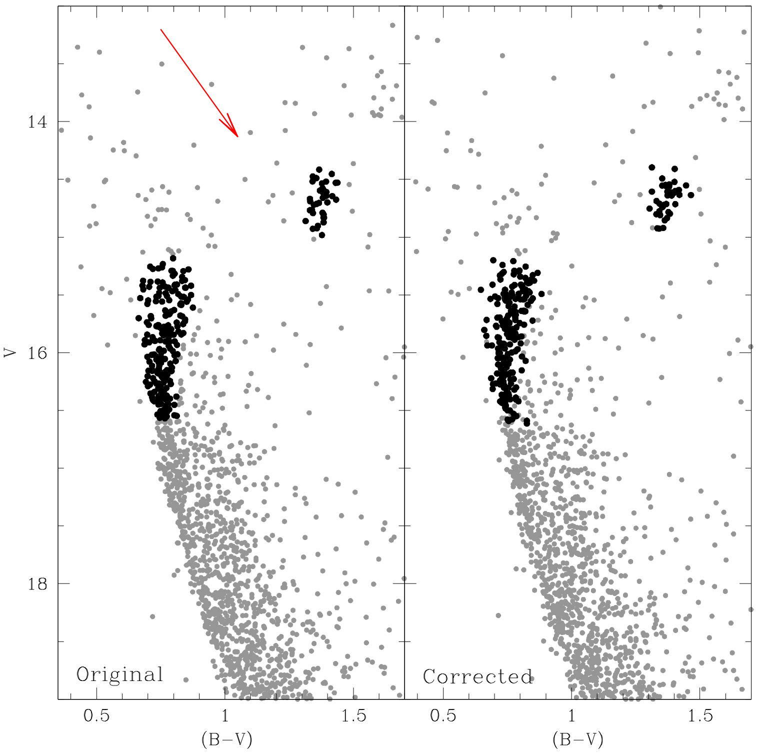

Figure 4.20: CMD for the inner 4′ of Tr 20, using the photometry of Carraro et al. (2010), before and after correction for differential reddening. The arrow is the direction of the reddening vector. Black points correspond to the MSTO and RC stars.

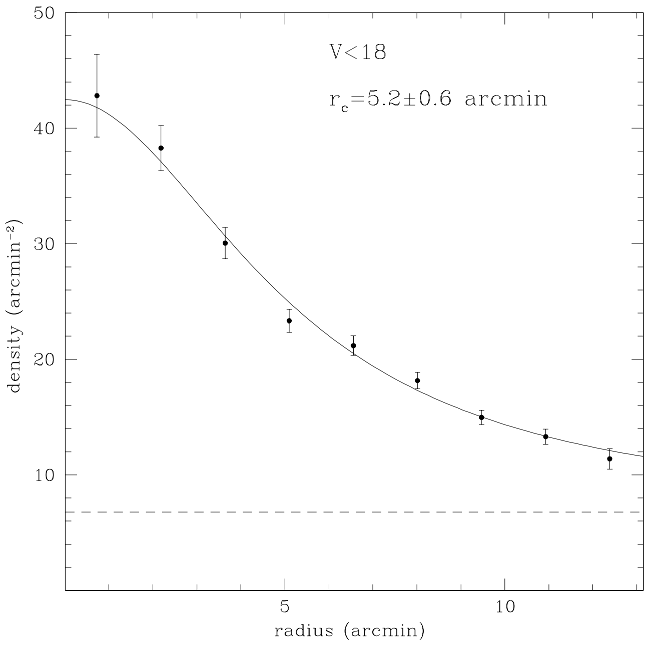

Figure 4.21: Density profile of Tr 20 using stars with $V < 18$. The error bars are the random errors. The best fit is a two-parametric King model of core radius 5.2 ± 0.6 arcmin.

4.3 Summary

NGC 6705

We derive an age of 250 to 316 Myr for this cluster (depending on the set of isochrones employed) and a distance modulus of 11.45±0.2, corresponding to a distance of 1950±200 pc from the Sun. The cluster sits in a region of uniform extinction $E(B-V) = 0.4$, but out of $10'$ from the cluster centre variable extinction shapes the background stellar density. We confirm via several diagnostics that NGC 6705 shows strong signs of mass segregation and that its outer regions contain a high proportion of low-mass stars. Because those faint stars are poorly contrasted against the field population and because of the variable extinction in those outer regions, it is difficult to accurately estimate the total stellar content. We estimate that a total mass of $6851 \pm 1865\,\mathrm{M}_{\odot}$ is contained within $9'$ of the centre, which constitutes a lower limit for the total cluster mass.

Trumpler 20

Our age estimate for Tr 20 range from 1.25 to 1.66 Gyr, depending on the set of isochrone used. Differential extinction affects the morphology of the CMD, and correcting for extinction reduces the observed spread in colour for turn-off stars. However, it does not reduce the colour spread among red clump stars. This extended clump is discussed in Sect. 5.3.1. Trumpler 20 does not exhibit signs of mass segregation. We estimate a total stellar content of 5500 to $8000\,\mathrm{M}_{\odot}$.

CHAPTER 5

SPECTROSCOPY AND ELEMENTAL ABUNDANCES FOR 3 *GAIA*-ESO SURVEY CLUSTERS

5.1 Chemical inhomogeneities and multiple populations

Once thought to be the best example of simple stellar populations (coeval, mono-metallic systems), the globular clusters (GCs) have been shown to be instead complex objects. In particular, evidence that they host distinct populations (possibly, distinct generations) of stars has been mounting. Gratton et al. (2004, 2012) present reviews based on spectroscopy, while Piotto (2009) and Milone et al. (2012) can be consulted for results based on photometry.

While variations in iron content seem limited to very few cases, the most notable being ω Cen (e.g. Johnson & Pilachowski, 2010; Lee et al., 1999) and M 22 (e.g. Marino et al., 2011), GC stars show large star-to-star variations in some light elements, like C, N, O, Na, Mg, and Al. It has been known for a long time that there are variations in the CN and CH bands strengths, with spreads and bimodal distributions (e.g. Kraft, 1979, 1994, for reviews), and not all the variations can be attributed to internal processes like mixing. Na and O have been extensively studied as summarised in the review by Gratton et al. (2004) and Carretta et al. (2009a,b), which show an anti-correlation: in the same GC there are stars with "normal" O and Na (normal with respect to the cluster metallicity) and stars showing a (strong) depletion in O and an enhancement in Na. Most of the stars have a modified composition. A similar anti-correlation can be found between Mg and Al, but not in all clusters, and with lower depletions than in O (e.g. Carretta et al., 2009a; Marino et al., 2008). Most importantly, these star-to-star variations occur also in unevolved, main-sequence stars, as demonstrated first by Gratton et al. (2001) and Ramírez & Cohen (2002) and later confirmed on much larger samples (e.g. D'Orazi et al., 2010; Lind et al., 2009). These low mass stars cannot have produced these variations, since their cores do not reach the high temperatures necessary for the relevant proton-capture reactions[1] and, in any case, the stars lack the mixing mechanism needed to bring processed material to the surface[2]. This implies that the chemical inhomogeneities were already present in the gas out of which these stars formed. This has led to the belief that GCs are made of at least two generations of stars, with the second generation formed from gas polluted by the material processed by the first. Exactly which kind of first-generation stars were the polluters is debated; the most promising candidates are intermediate mass asymptotic giant branch stars (Ventura et al., 2001) and fast rotating massive stars (Decressin et al., 2007), but refinements and comparisons to robust observational constraints are required.

The multiple populations scenario for GCs requires that the cluster is massive enough to retain some of its primordial gas at the start of any subsequent star formation; indeed, existing models postulate that GCs were many times more massive at the time of their formation than they appear today (e.g. D'Ercole et al., 2008). Such models suffer from several drawkbacks. For instance, they do not explain the observed properties of the young massive clusters (Bastian et al., 2013), or the abundance patterns of the halo stars (see e.g. Martell et al., 2011). Recently, a mechanism based on accretion on circumstellar discs, not requiring multiple generation of stars has been presented by Bastian & Silva-Villa (2013). This model does not require that clusters were initially extremely massive. In any case, the efficiency of the accretion process depends on the density and velocity dispersion of the cluster, that both scale with the cluster mass, suggesting that more massive clusters should exhibit broader chemical inhomogeneities.

---

[1] During their life, stars process the initial material they are made of, via different reaction mechanisms. All stars convert their H intro heavier elements, but several reaction chains can occur in massive stars (for which the core reaches sufficient temperatures). For instance, the net effect of the CNO cycle is to burn O into N. The NeNa chain burns Ne into Na, and the MgAl chain burns Mg into Al (e.g. Arnould et al., 1999; Cavallo et al., 1996; Wallerstein et al., 1997). The composition of the star's interior is enhanced in some elements and depleted in others. This enriched (or "polluted") material is released to the interstellar medium when the star dies.

[2] Thermonuclear reactions take place in stellar interiors, but the light we receive is emitted by the photosphere. We cannot detect material enriched by the star itself if there are no convective envelopes to bring the processed material to the surface.

Carretta et al. (2010), combining the data on 18 GCs of the FLAMES survey (Carretta et al., 2009b) and literature studies, showed that all Galactic GCs for which Na and O abundances were available presented a Na-O anti-correlation, i.e., multiple populations. The only possible exceptions were Terzan 7 and Palomar 12, two young and low-mass GCs belonging to the Sagittarius dwarf galaxy. This apparent universality of the Na-O anti correlation was suggested to be a defining property of GCs, separating them from the other clusters where only a single population is present. Cluster mass seems to play a determinant role in this separation and, studies of low-mass GCs and massive and old open clusters (OCs) are needed to determine the mass threshold under which no multiple populations can be formed. This scenario needs however to be verified observationally, which motivated further studies in this “grey zone” between the two kind of clusters. Recent additions include the GCs Rup 106 (Villanova et al., 2013), which shows no Na-O anti-correlation, and Terzan 8 (Carretta et al., 2014), in which the second generation, if present, represents a minority, and two of the most massive and oldest OCs, Berkeley 39 and NGC 6791. High-resolution spectroscopy in 30 stars of Berkeley 39 by Bragaglia et al. (2012) showed a single, homogeneous population. Geisler et al. (2012) have found signs of a bi-modal Na distribution in NGC 6791, which would make it the first known OC with multiple populations. This suggestion was not been confirmed by the study of Bragaglia et al. (2014), who find no variations exceeding the errors within this cluster. Further studies are called for to settle the issue.

This chapter makes use of the elemental abundances obtained by GES with UVES to probe the chemical properties of the massive open clusters NGC 6709, Trumpler 20 and NGC 4815. (those results are published in Cantat-Gaudin et al., 2014b; Donati et al., 2014; Friel et al., 2014, respectively).

5.2 NGC 6705

5.2.1 The data

GES spectroscopic data

The target selection for NGC 6705 and the exposure times for the various setups are described in the target selection paper of Bragaglia et al. (in prep.). For the GIRAFFE targets, potential members were selected on the basis of their optical and infrared photometry following the cluster main sequence, and the proper motions from the UCAC4 catalog (see Zacharias et al., 2012) were used in order to discard objects whose proper motions are more than five sigma from the cluster centroid. In total, 1028 main-sequence stars were

Table 5.1: Summary of GES GIRAFFE observations

Setup	Central λ [nm]	Spectral range [nm]	R	nb Stars	Median S/N
HR3	412.4	403.3–420.1	24 800	166	24
HR5A	447.1	434.0–458.7	18 470	166	25
HR6	465.6	453.8–475.9	20 350	166	21
HR9B	525.8	514.3–535.6	25 900	526	37
HR10	447.1	533.9–561.9	18 470	284	50
HR14A	651.5	630.8–670.1	17 740	166	44
HR15N	665.0	647.0–679.0	17 000	1028	52
HR21	875.7	848.4–900.1	18 470	284	55

Table 5.2: Positions, *BV* photometry, radial velocities, and membership probabilities of the GIRAFFE targets.

Star	*RA*	*DEC*	*B*	*V*	RV	Membership probability
18505884-0614409	282.7452	-6.2447	15.161	14.642	34.3 ± 1.3	0.91
18505976-0616255	282.7490	-6.2738	14.808	14.314	31.8 ± 2.2	0.81
18505998-0617359	282.7499	-6.2933	14.695	14.247	37.4 ± 0.9	0.92
				...		
18514946-0620231	282.9561	-6.3398	19.767	18.475	120.7 ± 1.5	0.0

Notes. The full table (containing 1028 rows) is available online at: `http://cdsarc.u-strasbg.fr/viz-bin/Cat?J/A+A/569/A17`

observed with eight GIRAFFE setups. All the red giants located in the clump region in the inner 12′ were observed with the UVES setup 580 (25 targets). The number of targets observed with each GIRAFFE setup are summarised in Table 5.1. The coordinates, B, V, J, H, and K magnitudes, radial velocities and membership probabilities (see Sect. 5.2.2) are shown in Table 5.2.

The spatial distribution of the targets is shown in the top left-hand panel of Fig. 5.1, and the *BV* photometry of the targets is the WFI photometry presented in this study. The bottom left-hand panel of Fig. 5.1 shows the radial velocity (RV) distribution of all the GIRAFFE targets. From the GESviDR1Final data release, we have RVs for 1028 GIRAFFE targets and 25 UVES targets.

The 25 UVES stars have well-defined values of effective temperature, surface gravity, and microturbulence derived directly from these spectra (summarised in Table 5.3). While elemental abundances are available for various elements in the GESviDR1Final data release, this work focused on the abundances of Fe, Al, Mg, Na, and Si (Table 5.4). The reference solar abundances used by GES are those of Grevesse et al. (2007).

Because the main-sequence targets are hot, fast-rotating stars, preliminary metallicity determinations from GIRAFFE are for the moment available for 255 GIRAFFE stars only in GESviDR1Final, with large quoted uncertainties. These data will be re-analysed in subsequent GES data releases. We have decided not to consider these results and to focus only on the metallicity determination obtained from the UVES spectra.

HARPS Archive data

We compared our results with those obtained using an HARPS archive data set taken by the program Search for Planets around Evolved Intermediate-Mass Stars (Lovis & Mayor, 2007). Twenty-nine stars in the cluster have been monitored for a total of more than 70 hours of on-target integrations and 271 spectra taken. The observing programme covered several periods from P79 (2007) to P83 (2009). In the ESO archive, the observed dataset is already reduced, providing a measure of the RVs. Owing to its high resolving power (R∼115 000) and simultaneous wavelength calibration, HARPS delivers a typical radial velocity error of about 0.06 $\mathrm{km\,s^{-1}}$ for these stars. Nineteen of them stars were also observed by GES with the UVES instrument, allowing for a sanity check of our UVES measurements, but none were observed with GIRAFFE. Figure 5.2 shows a comparison between the RVs derived from UVES and HARPS spectra. The nominal uncertainty on the UVES RVs is $0.6\,\mathrm{km\,s^{-1}}$. The measurements from UVES are systematically lower by $0.8\,\mathrm{km\,s^{-1}}$ on average, with a standard deviation of $0.4\,\mathrm{km\,s^{-1}}$. We corrected for the differences in zero point between the GIRAFFE, UVES, and HARPS radial velocities when using them together later in this study.

5.2.2 Membership

The spectroscopic targets were photometrically selected to be likely cluster members, but this selection obviously includes a significant number of field stars, which can be separated from the cluster stars on the basis of their RVs. Figure 5.1 shows the RV distribution of the field stars expected from the Besançon model (Robin et al., 2003). We selected from the simulation the stars belonging to the bright main sequence region, with $B - V < 1.2$ and $V < 17$ (the region of the CMD covered by the majority of the GIRAFFE targets) and scaled the distribution so that its tails (RV $< 20\,\mathrm{km\,s^{-1}}$ and RV $> 50\,\mathrm{km\,s^{-1}}$) contain the same number of objects as those of the observed distribution. The Besançon model

Table 5.3: Photometry and stellar parameters of the UVES stars.

Star	*RA* [°]	*DEC* [°]	*B*	*V*	*J*	*H*	K_s	RV [km s^{-1}]	T$_{\rm eff}$ [K]	log *g*	[Fe/H]	v$_{mic}$ [km s^{-1}]
						Members						
18503724-0614364	282.6552	-6.2434	13.423	12.001	9.427	8.808	8.616	35.2	4820 ± 71	2.42 ± 0.21	0.03 ± 0.14	1.82 ± 0.13
18504737-0617184	282.6974	-6.2884	13.381	11.652	8.527	7.808	7.523	31.8	4325 ± 130	1.72 ± 0.29	0.03 ± 0.15	1.56 ± 0.16
18505494-0616182	282.7289	-6.2717	13.328	11.860	9.199	8.498	8.318	34.8	4689 ± 109	2.37 ± 0.43	0.13 ± 0.09	1.46 ± 0.12
18505581-0618148	282.7325	-6.3041	13.050	11.414	8.557	7.895	7.698	35.1	4577 ± 139	2.23 ± 0.31	0.17 ± 0.18	1.60 ± 0.24
18505755-0613461	282.7398	-6.2295	13.041	11.830	9.426	8.852	8.675	30.4	4873 ± 114	2.37 ± 0.32	0.03 ± 0.14	1.33 ± 0.19
18505944-0612435	282.7477	-6.2121	13.270	11.872	9.330	8.722	8.523	34.6	4925 ± 177	2.56 ± 0.39	0.19 ± 0.18	1.50 ± 0.50
18510023-0616594	282.7510	-6.2832	13.319	11.586	8.524	7.776	7.589	35.2	4433 ± 95	1.94 ± 0.47	0.17 ± 0.12	1.50 ± 0.14
18510032-0617183	282.7513	-6.2884	13.542	12.081	9.368	8.751	8.549	35.2	4850 ± 100	2.38 ± 0.21	0.07 ± 0.15	1.60 ± 0.33
18510200-0617265	282.7583	-6.2907	13.030	11.426	8.446	7.766	7.493	32.0	4415 ± 87	2.35 ± 0.45	0.18 ± 0.14	1.48 ± 0.07
18510289-0615301	282.7620	-6.2584	13.467	12.014	9.389	8.758	8.543	32.8	4750 ± 112	2.40 ± 0.28	0.05 ± 0.07	1.45 ± 0.13
18510341-0616202	282.7642	-6.2723	13.239	11.801	9.216	8.579	8.386	36.3	4975 ± 146	2.50 ± 0.30	0.07 ± 0.15	1.94 ± 0.27
18510358-0616112	282.7649	-6.2698	13.320	11.902	9.357	8.691	8.511	34.7	4832 ± 79	2.31 ± 0.31	0.15 ± 0.08	1.62 ± 0.19
18510786-0617119	282.7828	-6.2866	13.084	11.621	9.030	8.399	8.206	33.6	4768 ± 53	2.11 ± 0.19	0.03 ± 0.14	1.80 ± 0.28
18510833-0616532	282.7847	-6.2814	13.202	11.736	8.911	8.311	8.227	33.3	4750 ± 112	2.25 ± 0.22	0.18 ± 0.10	1.60 ± 0.25
18511013-0615486	282.7922	-6.2635	12.996	11.493	8.613	7.933	7.705	36.9	4439 ± 59	1.87 ± 0.53	0.10 ± 0.12	1.50 ± 0.10
18511048-0615470	282.7937	-6.2631	13.134	11.627	8.817	8.224	7.991	33.3	4744 ± 122	2.12 ± 0.33	0.05 ± 0.14	1.70 ± 0.30
18511452-0616551	282.8105	-6.2820	13.403	11.923	9.263	8.620	8.420	35.1	4800 ± 59	2.40 ± 0.25	0.11 ± 0.08	1.69 ± 0.20
18511534-0618359	282.8139	-6.3100	13.527	11.974	9.163	8.507	8.303	33.7	4755 ± 57	2.16 ± 0.21	0.05 ± 0.22	1.79 ± 0.17
18511571-0618146	282.8155	-6.3041	13.297	11.807	9.088	8.445	8.211	35.0	4710 ± 159	2.27 ± 0.30	0.15 ± 0.12	1.60 ± 0.18
18512662-0614537	282.8609	-6.2482	13.228	11.559	8.611	7.921	7.700	33.8	4459 ± 91	2.10 ± 0.48	0.12 ± 0.17	1.48 ± 0.19
18514130-0620125	282.9221	-6.3368	13.348	11.849	9.185	8.570	8.361	33.2	4671 ± 140	2.20 ± 0.28	0.07 ± 0.19	1.62 ± 0.20
						Non-members						
18510093-0614564	282.7539	-6.2490	12.677	11.462	9.016	8.395	8.205	41.4	4755 ± 35	2.30 ± 0.24	-0.10 ± 0.10	1.50 ± 0.15
18510837-0617495	282.7849	-6.2971	13.438	11.674	8.469	7.649	7.429	-72.5	4217 ± 83	1.62 ± 0.33	-0.10 ± 0.12	1.47 ± 0.16
18512283-0621589	282.8451	-6.3664	13.604	11.879	8.831	8.084	7.872	3.4	4305 ± 95	2.08 ± 0.34	0.18 ± 0.18	1.61 ± 0.21
18513636-0617499	282.9015	-6.2972	13.075	11.128	7.295	6.451	6.127	-1.4	4041 ± 225	1.57 ± 0.42	-0.20 ± 0.20	1.45 ± 0.03

Notes. The photometry was not corrected for extinction. The nominal uncertainty on UVES radial velocities is 0.6 km s^{-1}.

Table 5.4: Elemental abundances for the UVES stars.

Star	[Fe/H]	[Al/Fe]	[Mg/Fe]	[Na/Fe]	[Si/Fe]
			Members		
18503724-0614364	0.03 ± 0.14	0.12 ± 0.15	0.23 ± 0.17	0.51 ± 0.17	0.09 ± 0.15
18504737-0617184	0.03 ± 0.15	0.17 ± 0.17	0.23 ± 0.15	0.74 ± 0.21	0.03 ± 0.17
18505494-0616182	0.13 ± 0.09	0.26 ± 0.09	0.14 ± 0.09	0.5 ± 0.11	0.07 ± 0.09
18505581-0618148	0.17 ± 0.18	0.10± 0.18	0.12 ± 0.20	0.32 ± 0.21	0.05 ± 0.19
18505755-0613461	0.03 ± 0.14	-0.04 ± 0.38	0.10± 0.15	0.52 ± 0.14	0.07 ± 0.15
18505944-0612435	0.19 ± 0.18	0.14 ± 0.18	0.14 ± 0.22	0.49 ± 0.19	-0.04 ± 0.19
18510023-0616594	0.17 ± 0.12	0.21 ± 0.12	0.20 ± 0.16	0.39 ± 0.13	0.02 ± 0.18
18510032-0617183	0.07 ± 0.15	0.20 ± 0.15	0.21 ± 0.18	0.53 ± 0.16	0.02 ± 0.16
18510200-0617265	0.18 ± 0.14	0.13 ± 0.15	0.16 ± 0.16	0.17 ± 0.14	0.02 ± 0.15
18510289-0615301	0.05 ± 0.07	0.22 ± 0.07	0.13 ± 0.13	0.53 ± 0.11	0.05 ± 0.09
18510341-0616202	0.07 ± 0.15	0.19 ± 0.15	0.30 ± 0.16	0.54 ± 0.17	-0.07 ± 0.17
18510358-0616112	0.15 ± 0.08	0.18 ± 0.08	0.12 ± 0.10	0.49 ± 0.10	0.07 ± 0.11
18510786-0617119	0.03 ± 0.14	0.25 ± 0.14	0.42 ± 0.14	0.58 ± 0.18	0.08 ± 0.18
18510833-0616532	0.18 ± 0.10	0.18 ± 0.10	0.19 ± 0.14	0.51 ± 0.13	-0.06 ± 0.12
18511013-0615486	0.10 ± 0.12	0.23 ± 0.12	0.23 ± 0.16	0.52 ± 0.15	0.07 ± 0.14
18511048-0615470	0.05 ± 0.14	0.23 ± 0.15	0.39 ± 0.14	0.54 ± 0.21	-0.03 ± 0.23
18511452-0616551	0.11 ± 0.08	0.15 ± 0.11	0.15 ± 0.29	0.55 ± 0.16	0.06 ± 0.11
18511534-0618359	0.05 ± 0.22	0.25 ± 0.22	0.33 ± 0.24	0.49 ± 0.23	0.08 ± 0.24
18511571-0618146	0.15 ± 0.12	0.20 ± 0.13	0.09 ± 0.17	0.45 ± 0.14	0.0 ± 0.13
18512662-0614537	0.12 ± 0.17	0.29 ± 0.17	0.24 ± 0.22	0.59 ± 0.21	0.13 ± 0.22
18514130-0620125	0.07 ± 0.19	0.21 ± 0.19	0.11 ± 0.21	0.45 ± 0.20	0.01 ± 0.20
μ	0.10 ± 0.04	0.20 ± 0.04	0.19 ± 0.05	0.48 ± 0.05	0.04 ± 0.04
σ	$0^{+0.04}$	$0^{+0.05}$	$0^{+0.07}$	$0^{+0.06}$	$0^{+0.05}$
			Non-members		
18510093-0614564	-0.10± 0.10	0.23 ± 0.11	0.11 ± 0.16	0.45 ± 0.13	0.07 ± 0.12
18510837-0617495	-0.10± 0.12	0.20 ± 0.12	0.28 ± 0.14	0.32 ± 0.12	0.02 ± 0.13
18512283-0621589	0.18 ± 0.18	0.27 ± 0.20	0.24 ± 0.20	0.38 ± 0.23	0.06 ± 0.20
18513636-0617499	-0.20 ± 0.20	0.53 ± 0.21	0.43 ± 0.20	0.41 ± 0.23	0.06 ± 0.21
Sun[a]	7.45	6.37	7.53	6.17	7.51

Notes. [a] The solar reference abundances are those of Grevesse et al. (2007). μ and σ are the intrinsic mean and dispersion, respectively (cf. Sect. 5.2.4).

reproduces the observed RV distribution of the background very well, while the signature of the cluster is clearly visible as a peak around 36 km s^{-1}.

We performed a membership determination for GIRAFFE and UVES stars independently.

Membership of the GIRAFFE stars

We determined the membership of the GIRAFFE stars from the HR15N radial velocities only, because of the good signal-to-noise ratio (S/N) of these spectra and because all 1028 GIRAFFE stars were observed with this setup. The analysis of the data obtained with the other gratings will be available in further data releases.

We applied a classical parametric procedure where the radial velocity distribution is fitted with two Gaussian components: one for the cluster members and one for the field stars. We followed the procedure described in Cabrera-Cano & Alfaro (1985), but only based on the RVs. The method computes the membership probabilities through an iterative method. The probability density function (hereafter PDF) model is defined as

$$\phi_i(v_i) = n_c \phi_{i,c}(v_i) + n_f \phi_{i,f}(v_i) \tag{5.1}$$

where n_c and n_f are the priors of the cluster member and field stars distributions, respectively, $\phi_i(v_i)$ is the PDF for the whole sample, and $\phi_{i,c}(v_i)$ and $\phi_{i,f}(v_i)$ are the PDFs for the cluster members and the field stars related to the i-th star.

The membership probabilities are obtained making use of these PDFs and by using Bayes' theorem as follows:

$$P_c(v_i) = \frac{n_c \phi_{i,c}(v_i)}{\phi_i(v_i)} \tag{5.2}$$

where $P_c(v_i)$ is the probability of the i-th star to be a cluster member. According to Bayes' minimum error rate decision rule, a threshold value of 0.5 minimises the misclassification. At the end of the analysis, 536 stars (out of 1028) have a membership probability higher than 0.5. The mean RV of these stars is 35.9 km s^{-1}, with a standard deviation of 2.8 km s^{-1}.

Undetected member binaries may have discrepant RVs and be classified as non-members by this procedure. Rigourously speaking, the RV distribution of the members may deviate from a Gaussian. The measured RVs of unresolved binaries are the combination of the motion of the centre of mass and of the orbital motion, and they tend to have larger uncertainties than isolated stars. The result of convolving a binary model with a normal distribution is a modification of the tails of the Gaussian, by extending and increasing them. Here some unresolved pairs may therefore be classified as non-members.

Membership of the UVES stars

We have stellar parameters and accurate metallicities for the 25 UVES targets of NGC 6705, including three stars that show a very discrepant RV and are not members of the clusters (see Fig. 5.3). A fourth star (18510093-0614564) has an outlying radial velocity of $41.4\,\mathrm{km\,s^{-1}}$, even though its photometry is compatible with the other cluster members. As a possible explanation, this star could be a single-lined binary made of a red clump star and a main-sequence star. Being much hotter, the main-sequence companion contributes to the spectrum with only a continuum emission, making the lines shallower. This hypothesis would explain why this star has a discrepant radial velocity, and is also an outlier in metallicity, with $[\mathrm{Fe/H}] = -0.10 \pm 0.10$ (see following section). In the absence of further elements, we did not consider it as a member in the rest of this study.

Finally, 21 stars can be considered as bona-fide members of the cluster. The mean RV for the UVES members is $34.1\,\mathrm{km\,s^{-1}}$ (with a standard deviation of $1.5\,\mathrm{km\,s^{-1}}$), which is lower than the mean value of $35.9\pm2.8\,\mathrm{km\,s^{-1}}$ found for GIRAFFE stars. The lack of targets in common between both instruments do not allow for a solid comparison of the systematics between UVES and GIRAFFE, and both results are compatible within their standard deviations. In the first GES data release, Sacco et al. (2014) note an average offset of $0.87\,\mathrm{km\,s^{-1}}$ between the UVES and GIRAFFE HR15N radial velocities, which is consistent with the offset we observe here.

5.2.3 Kinematics

Rotation

Since NGC 6705 is a massive system and radial velocities are available for a large number of targets, we looked for hints of the rotational signature of the cluster, as is routinely done for GCs (see e.g. Bellazzini et al., 2012; Bianchini et al., 2013; Cote et al., 1995). We first corrected the GIRAFFE radial velocities for the offset observed in Sect.5.2.1, then applied the procedure to the whole sample. The method consists in dividing the cluster in two and selecting one half according to a position angle ϕ measured here from north to east ($\phi = 0°$ corresponds to the north half, while $\phi = +90°$ and $\phi = -90°$ correspond to the east and west halves, respectively). The mean radial velocity is computed in the selected region. Varying the angle ϕ by steps of $5°$, we trace the mean radial velocity in different regions. For a rotating object, we expect the radial velocities to follow a sinusoidal dependence on the position angle ϕ, being equal to the mean radial velocity of the cluster when ϕ corresponds to the orientation of the rotation axis (projected on the sky), following the equation

$$\Delta V_r = A_{rot} sin(\phi_0 + \phi) \tag{5.3}$$

where A_{rot} corresponds to the amplitude of the rotation and ϕ_0 is the position angle of the rotation axis. We estimated the uncertainty on the mean radial velocity by bootstrapping: in each position angle bin, containing N datapoints, we created 100 sets of N datapoints by randomly sampling the radial velocity dataset, calculated the mean velocity for each one, and computed the standard deviation of these results. The best-fitting sine function corresponds to an orientation angle $\phi_0 = 4 \pm 45^\circ$ and an amplitude $A_{rot} = 0.3 \pm 0.1\,\mathrm{km\,s^{-1}}$ around the mean radial velocity (Fig. 5.4). Since the RV is averaged over the full range of radii covered by the sample, the derived A_{rot} is a lower limit to the maximum rotation amplitude, depending on the rotational gradient of the cluster. The observed pattern is, however, very weak, with an amplitude much smaller than the velocity dispersion of the cluster, and we can conclude that rotation does not play a significant role in the observed velocity dispersion in NGC 6705.

Intrinsic velocity dispersion

Owing to uncertainties on the radial velocities of each invididual star, the velocity dispersions we observe in our samples ($2.8\,\mathrm{km\,s^{-1}}$ for the GIRAFFE sample, $1.5\,\mathrm{km\,s^{-1}}$ for the combined HARPS and UVES sample) are larger than the true, intrinsic dispersion of those stars. Assuming this intrinsic distribution is Gaussian, and that the quoted uncertainties $\{\epsilon_1, ..., \epsilon_N\}$ on the observed radial velocities $\{v_1, ..., v_N\}$ are Gaussian errors, it is possible to estimate the dispersion σ and the mean radial velocity μ of the true underlying distribution (see e.g. Walker et al., 2006).

The probability of measuring the radial velocity v_i by sampling a random point from a normal distribution that has mean μ and dispersion σ is

$$P(v_i, \mu, \sigma) = \frac{1}{\sqrt{2\pi\,(\sigma^2 + {\epsilon_i}^2)}} \exp\left(-\frac{1}{2}\frac{(v_i - \mu)^2}{\sigma^2 + {\epsilon_i}^2}\right) \tag{5.4}$$

For a sample of N stars, the joint probability is simply the product of the N individual probabilities:

$$\mathcal{L} = P(\{v_1, ..., v_N\}, \mu, \sigma) = \prod_{i=1}^{N} \frac{1}{\sqrt{2\pi\,(\sigma^2 + {\epsilon_i}^2)}} \exp\left(-\frac{1}{2}\frac{(v_i - \mu)^2}{\sigma^2 + {\epsilon_i}^2}\right) \tag{5.5}$$

and the best estimates of μ and σ are those that maximise $\mathcal{L}$. Applying this method to our sample of GIRAFFE RVs, we found the values $\mu_G = 36.0 \pm 0.2\,\mathrm{km\,s^{-1}}$ and $\sigma_G =$

$2.5 \pm 0.1\,\mathrm{km\,s^{-1}}$. For the HARPS+UVES sample, the results are $\mu_{H+U} = 34.8 \pm 0.4\,\mathrm{km\,s^{-1}}$ and $\sigma_{H+U} = 1.3^{+0.3}_{-0.2}\,\mathrm{km\,s^{-1}}$. We do not expect such large difference between the radial velocity dispersion of both samples. The most likely source of this difference is that the quoted uncertainties on the GIRAFFE radial velocities are underestimated. The GIRAFFE targets are hot, fast-rotating stars for which RVs can be difficult to measure, and the main source of dispersion in the GIRAFFE sample is likely to be the measurement errors. This hypothesis may be tested when the final analysis is available for all gratings in a later GES data release.

Virial mass

A complete kinematical study of the cluster would require proper motions and radial velocities for a significant share of the stars. We do not have such a dataset, but we have accurate radial velocities for 31 red clump stars of NGC 6705 (combining the HARPS and UVES datasets) that we can use to estimate a lower limit to the total mass of the cluster.

NGC 6705 exhibits mass segregation, which is a sign of a dynamically relaxed cluster, at least in its core. The mass of a dynamically relaxed cluster is related to its average radius and velocity dispersion through the virial theorem:

$$M_{tot} = \frac{2\langle v^2\rangle\langle R\rangle}{G} \tag{5.6}$$

where G is the gravitational constant, $\langle R\rangle$ the average radius, and $\langle v^2\rangle = v_\mu^2 + v_\sigma^2 + v_r^2$ the three-dimensional velocity dispersion. In this study we only have access to the radial velocity dispersion v_r. However, assuming that the velocity distribution is isotropic, the three components of the velocity dispersion are equal and we can write

$$\langle v^2\rangle = v_\mu^2 + v_\sigma^2 + v_r^2 = 3v_r^2 \tag{5.7}$$

With $\sqrt{\langle v_r^2\rangle} = 1.34^{+0.32}_{-0.22}\,\mathrm{km\,s^{-1}}$ and an average radius $\langle R\rangle = 3.42'$ (2.0±0.2 pc) (with the most distant star located at an agular distance of 10.1′) this equation yields $\mathrm{M}_{tot} = 5083 \pm 1600\,\mathrm{M}_\odot$. The number is in good agreement with the virial mass obtained by McNamara & Sanders (1977) with the same method, but using proper motions ($5621\,\mathrm{M}_\odot$). It is possible to plug in the values obtained from the GIRAFFE targets, which spread out to 12.6′ and show a larger average radial distance and a considerably higher velocity dispersion (4.52′ and $2.8\,\mathrm{km\,s^{-1}}$, respectively). The result is a mass of $21\,900 \pm 2700\,\mathrm{M}_\odot$. Since the velocity dispersion of the GIRAFFE stars is affected by the larger uncertainty on the radial velocities, this value can be considered an upper limit.

This simple method only provides a first-order estimation. A more sophisticated approach would include detailed kinematical modelling, for instance adopting a multi-mass model approach as is generally done for GCs (see for instance Miocchi, 2006). This is, however, beyond the scope of this study. The calculation presented here only considers the positions and radial velocities of the massive stars in the central region and may suffer from biases due to the low number of selected targets. With a mass of the order of $5 \times 10^3\,\mathrm{M}_\odot$ contained in the inner part (within 2 pc), we confirm that NGC 6705 is a relatively massive OC.

5.2.4 Chemical analysis of the red clump stars

The average iron abundance of the bona-fide members from UVES spectroscopy is [Fe/H]=0.10 with a dispersion of 0.06. This value agrees with Gonzalez & Wallerstein (2000), who found iron abundances between 0.07 and 0.20 from high-resolution spectroscopy of ten K giants of NGC 6705 and with the values we derived from isochrone fitting. In this section we study the relations between the abundances of Al and of other proton-capture elements Na, Mg, and Si. Al and Na abundances are plotted against $\mathrm{T}_{\mathrm{eff}}$ and log g in Fig. 5.5. These abundances do not display any significant trend. We observe star-to-star variations in the Al and Na content of the order of 0.2 dex, inside the expected uncertainties. Similar diagnostics for Mg and Si are shown in Magrini et al. (2014).

Abundances of Al, Mg, Si, and Na are plotted in Fig. 5.6. In case of multiple populations, correlations between the abundances of Al and Si, and between Al and Na, and anti-correlations between Si and Mg and between Al and Mg (Gratton et al., 2012) can be found. Models predict that Al should show correlations with elements that are enhanced by the action of the Ne–Na (such as Na) and Mg–Al cycles, and is anti-correlated with elements that are depleted in H burning at high temperature (such as O and Mg). We do not see any sign of such (anti-)correlations within our uncertainties.

One star shows a low Al abundance with a large uncertainty, with [Al/Fe]= -0.04 ± 0.38, probably due to the low number of detected lines for this element. Two outliers in Na abundance could suggest an internal spread, but they are still compatible with a homogeneous cluster within the uncertainties. The star with the highest Na abundance ([Na/Fe]=+0.74 dex) has the lowest Fe abundance in the sample ([Fe/H]=+0.03 dex), while the star with the lowest Na content ([Na/Fe]=+0.17 dex) has a Fe content [Fe/H]=+0.18 dex. This suggests that the apparent discrepant [Na/Fe] for that star can be explained by considering the uncertainties on both Na and Fe abundances.

The mean [Na/Fe] for the cluster members is 0.48 dex. This value is significantly higher than the Na abundance derived in field stars. Soubiran & Girard (2005) show that at high metallicities thin disk stars exhibit an average of [Na/Fe]=0.11 dex, even though they notice a rise at super-solar metallicities. For all elements presented here, the abundances were calculated in the LTE approximation. Na is subject to deviations from LTE (e.g. Lind et al., 2011). The effect of non-LTE correction in stars of super-solar metallicity is expected to be small, but could lower the Na abundance of our sample by 0.15–0.20 dex at most. On a side note, since the corrections depend on the evolutionary stage of the star, we expect them to affect all of the red clump stars in the same way and not to create an additional spread in Na.

The approach presented in Sect. 5.2.3 to estimating the intrinsic radial velocity dispersion of the sample can also be applied to the elemental abundances. Assuming an intrinsic Gaussian distribution of the abundance for each element, the most probable mean abundance (μ) and intrinsic dispersion (σ) we computed are listed in Table 5.4. For all five elements, the observed distribution is compatible with the cluster being homogeneous, and the observed spread can be entirely attributed to the individual uncertainties.

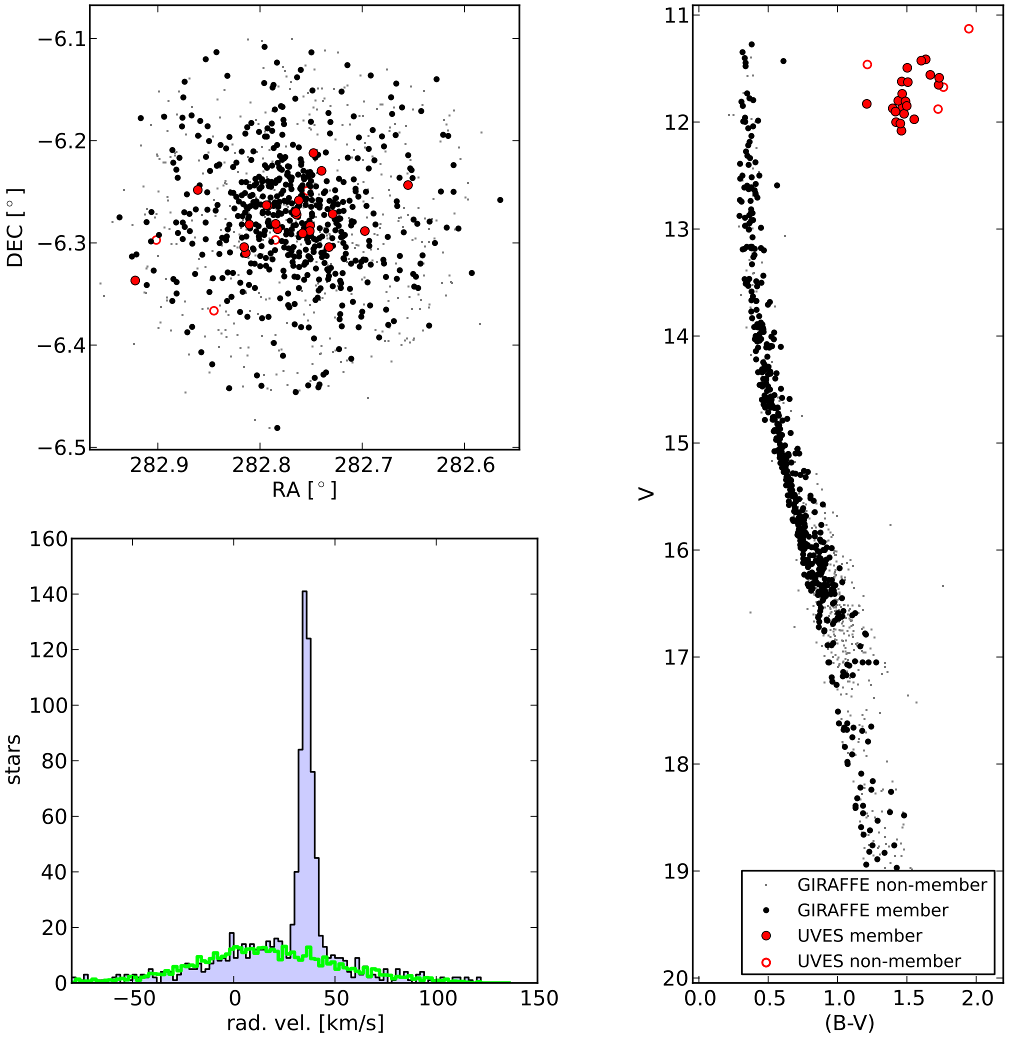

Figure 5.1: *Top left*: positions of the GIRAFFE (black dots for members, grey points for non-members) and UVES targets (red dots for members, empy red symbols for non-members). *Bottom left:* radial velocity distribution of the GIRAFFE targets. The green line shows the expected radial velocity distribution of the field stars from the Besançon model (Robin et al., 2003). *Right:* CMD of all the GES stars.

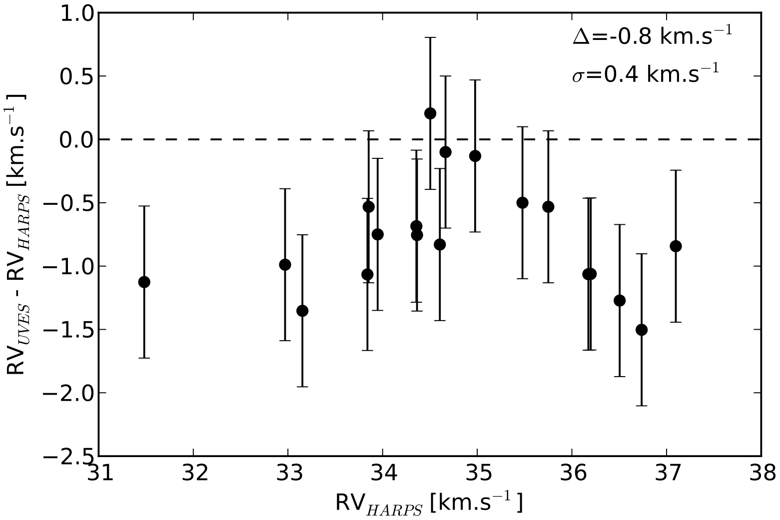

Figure 5.2: Comparison between the radial velocity measurements from HARPS spectra and UVES spectra for 19 red giants.

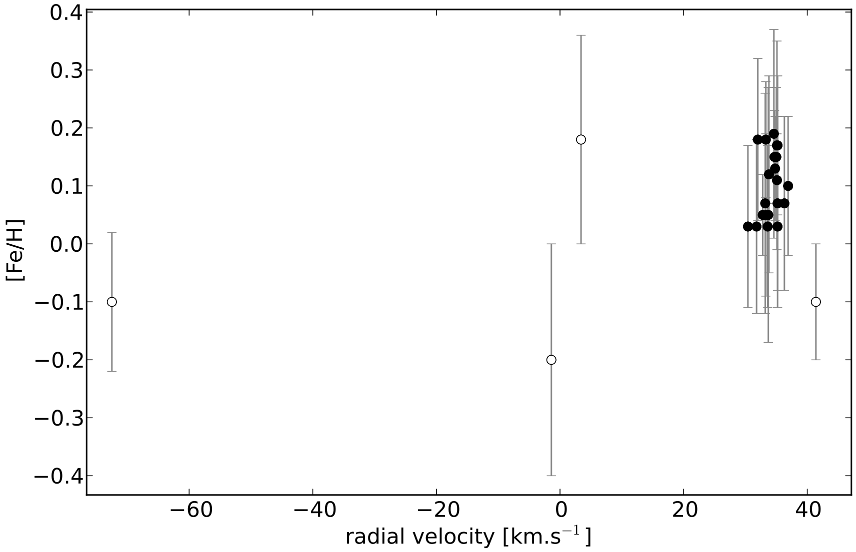

Figure 5.3: Identification of the red clump cluster members from radial velocities and iron abundance. The error bars for the radial velocities are smaller than the symbols. The 21 filled circles correspond to the members, while the 4 open circles are the stars we consider non-members.

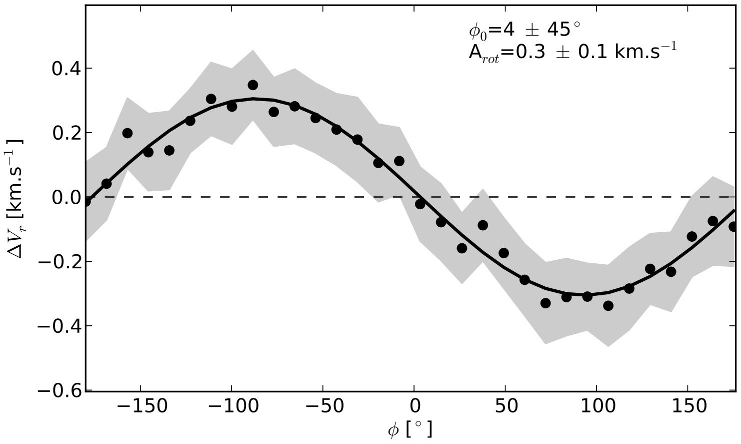

Figure 5.4: Rotation curve obtained from the cluster members. The shaded region shows the uncertainty estimated via bootstrapping. The best-fitting sine corresponds to a position angle of the rotation axis $\phi_0 = 4^\circ$ and an amplitude $A_{rot} = 0.3\,\mathrm{km\,s^{-1}}$.

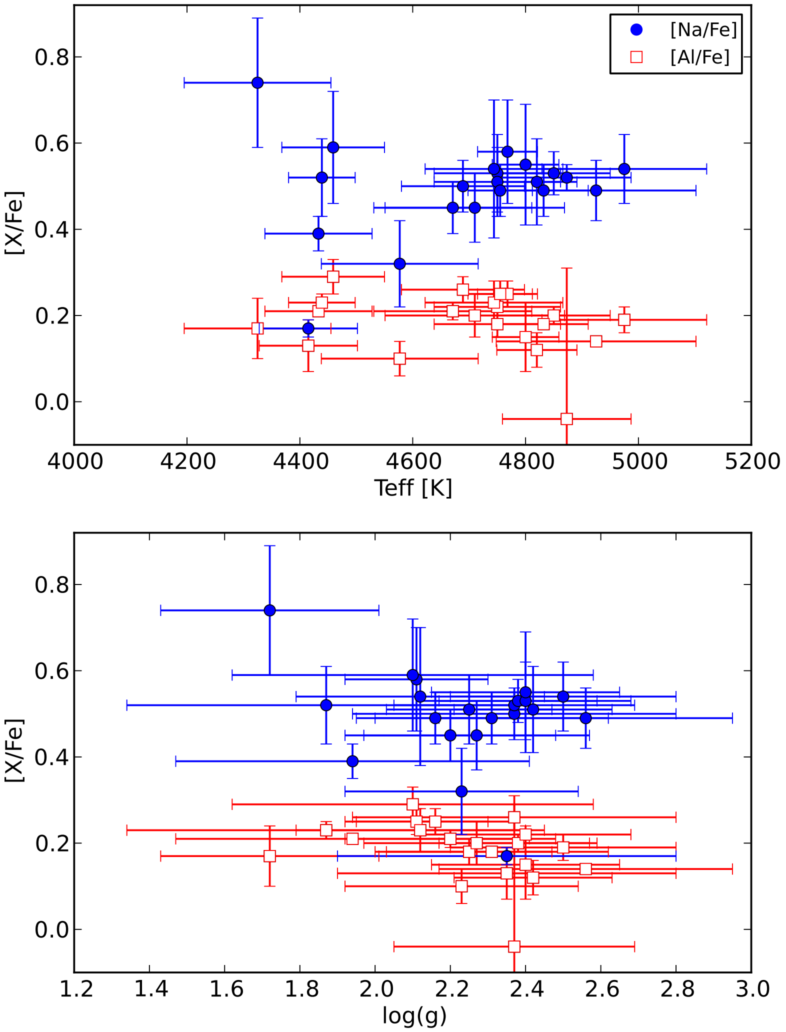

Figure 5.5: Solar-scaled abundances of [Na/Fe] (blue filled dots) and [Al/Fe] (red open squares) for the 21 UVES member stars, as a function of $T_{\rm eff}$ and $\log g$.

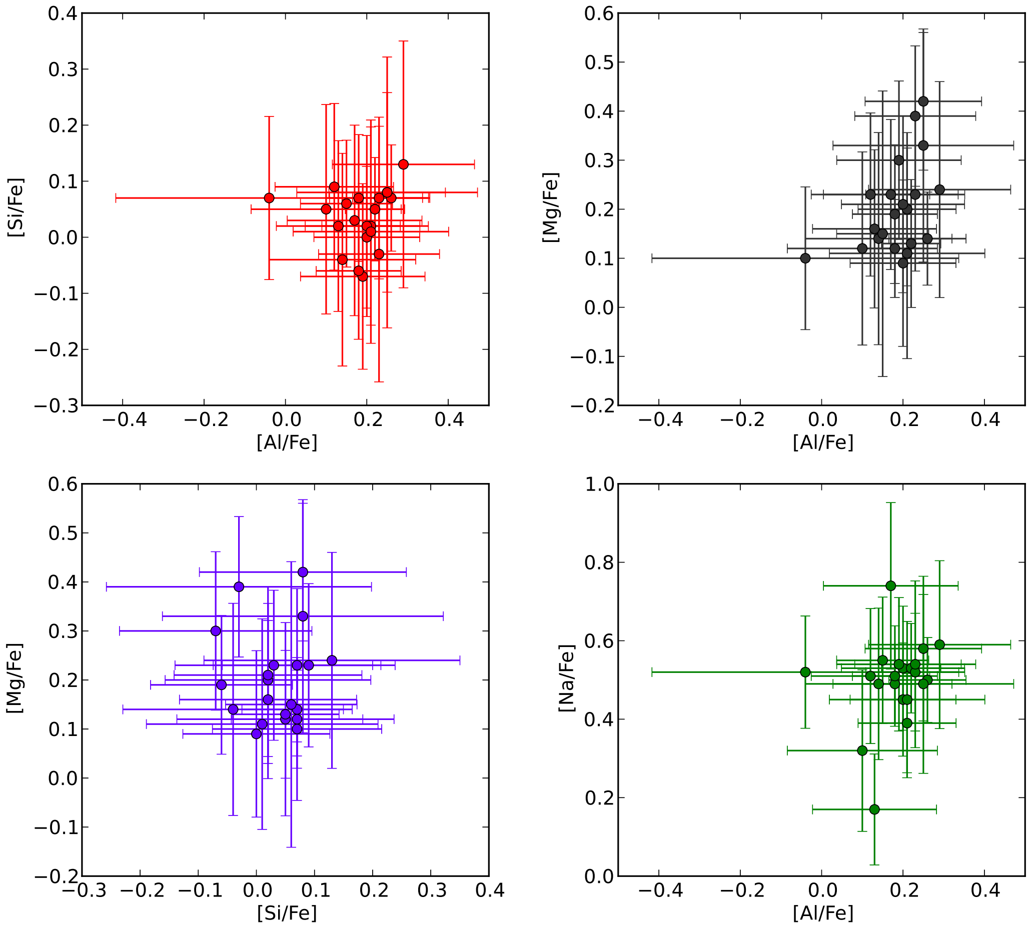

Figure 5.6: Abundances of Al, Si, Mg and Na for the 21 red clump stars. None of the "classical" correlations or anti-correlations between elemental abundances are observed in this cluster, which seems chemically homogeneous within our uncertainties.

5.3 Trumpler 20

5.3.1 Data and membership selection

GES data provides radial velocities for 1370 stars in Tr 20. The radial velocity distribution, in which the signature of the cluster is clearly visible around -40 km s^{-1}, is shown in Fig. 5.7.

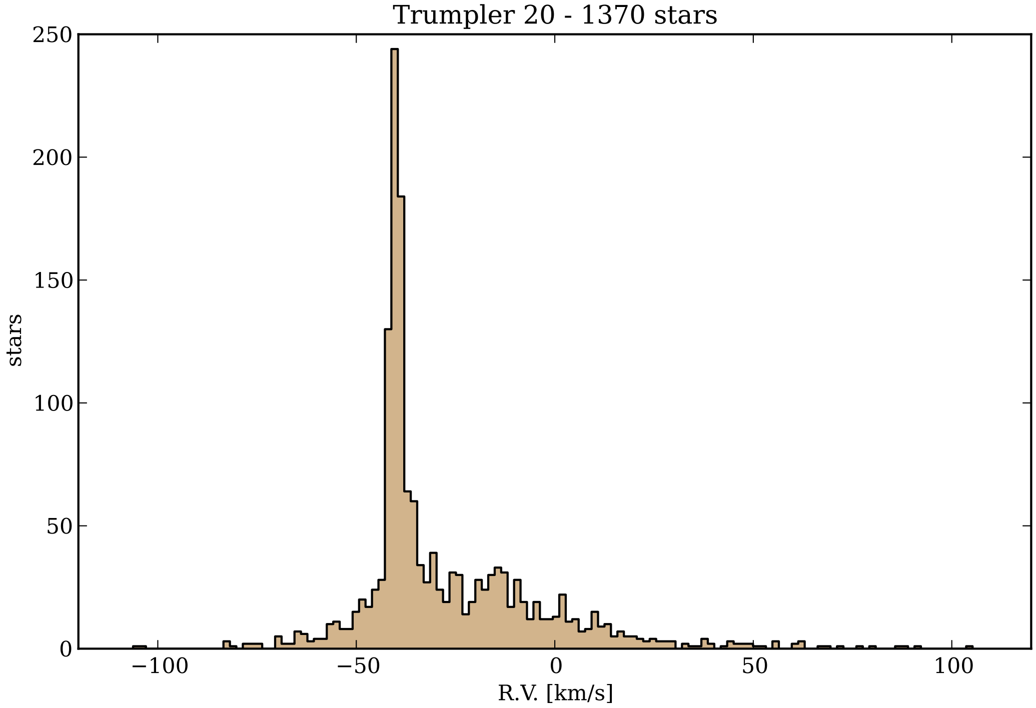

Figure 5.7: Radial velocity distribution for all 1370 targets of Tr 20. The signature of the cluster is clearly visible around -40 km s^{-1}.

The data contains 13 UVES targets, which are all members according to their radial velocities. Their mean iron abundance is [Fe/H]=+0.17, with a dispersion of 0.03. This result is significantly higher than the value of -0.11 quoted by Platais et al. (2008).

5.3.2 The red clump

The photometric study presented in Sect. 4.2.1 has evidentiated a peculiar morphology of the red clump. We can study the distribution of the UVES red clump stars in the $T_{\rm eff}$ – $\log\ g$ space. We verify that this extended distribution is visible. Red clump stars with surface gravities as high as log $g = 3$ cannot be reproduced with a PARSEC isochrone of age 1.6 Gyr (Fig. 5.8) or with any other choice of age.

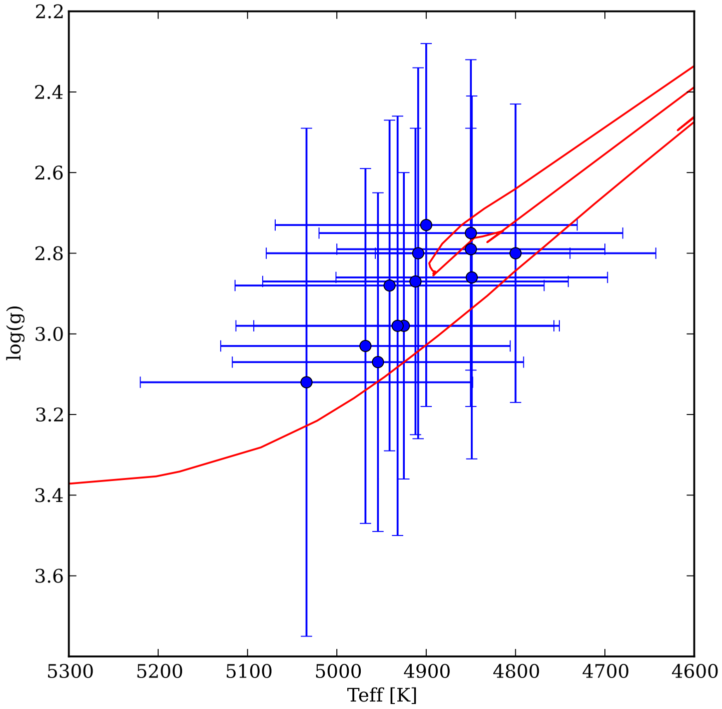

Figure 5.8: Distribution of the 13 UVES red clump stars of Trumpler 20 in the $T_{\rm eff}$ – log g space. The red line is a PARSEC isochrone for an age of 1.6 Gyr.

Structured RCs have been observed in other OCs. The works of (Mermilliod & Mayor, 1989, 1990) and (Mermilliod et al., 1997) present about ten intermediate-age MW OCs that show this peculiarity. The first interpretation of these findings, confirmed by the subsequent works of (Girardi, 1999) and (Girardi et al., 2000b), is the possibility that some stars in the RC phase have undergone evolution through helium-core flash, while others have not, because of small differences in the exact core mass. Such differences require a considerable mass spread for clump stars of about 0.2 $M_\odot$, however, which could in principle result from different mechanisms:

- the natural mass range of core-helium burning stars found in single isochrones, although the current models do not have the level of detail necessary to completely explore this possibility;

- an age spread broader than 100 Myr (observed in Magellanic Clouds clusters but never observed in Galactic OCs);
- star-to-star variations in the mass-loss rates during the RGB phase. Recent asteroseismologic studies on the two OCs NGC 6791 and NGC 6819, the latter of which has an age and metallicity similar to Tr 20 (see Corsaro et al., 2012; Miglio et al., 2012), seem to indicate that no extreme mass-loss during RGB phases should be expected;
- different stellar rotation history;
- dispersion in the overshooting efficiency in the convective core, proposed e.g. by Bastian & de Mink (2009) or Li et al. (2012) but refuted by Girardi et al. (2011);
- binarity, if interaction and mass transfer or even mergers are considered.

The hypothesis involving a transition between non-degenerate and degenerate He-core ignition can explain the RC morphology in old OCs (1.4 to 1.6 Gyr), which corresponds to the case of Tr 20.

Alternatively, Carraro et al. (2011) studied NGC 5822 (0.9 Gyr old) and proposed that part of the stars of its apparently double RC might instead be RGB stars. With the abundance analysis of the UVES targets, the stars in the fainter part of the RC have a log g value too large to be fit by the RC phase of the evolutionary models considered in this work. They might possibly be giant stars in the RGB phase, even if they are too warm for the best-fit model derived in Sect. 4.2.1.

Finally, we note that double RCs are also evident in clusters of the Magellanic Clouds as shown in Glatt et al. (2008) and Milone et al. (2009) and demonstrated in Girardi et al. (2009). In these high-mass clusters the presence of stars of different age (due to a gap in star formation or a prolonged star formation) looks more probable, similarly to the massive old globular clusters of the MW.

Elemental abundances

The direct mean iron abundance for the 13 UVES stars is [Fe/H]=+0.17, with a dispersion of 0.03. Since Tr 20 is a massive cluster (5500 to 8000 $\mathrm{M}_\odot$, see Sect. 4.2.2) it is relevant to assess its chemical homogeneity. Applying the same statistical procedure as in Sect. 5.2.4, we determine that within the uncertainties the cluster can be considered chemically homogeneous, with the dispersion in abundances being explained by the errors. The computed abundances of Fe, Al, Si, Mg and Al are shown in Fig. 5.9 and listed in Table 5.5.

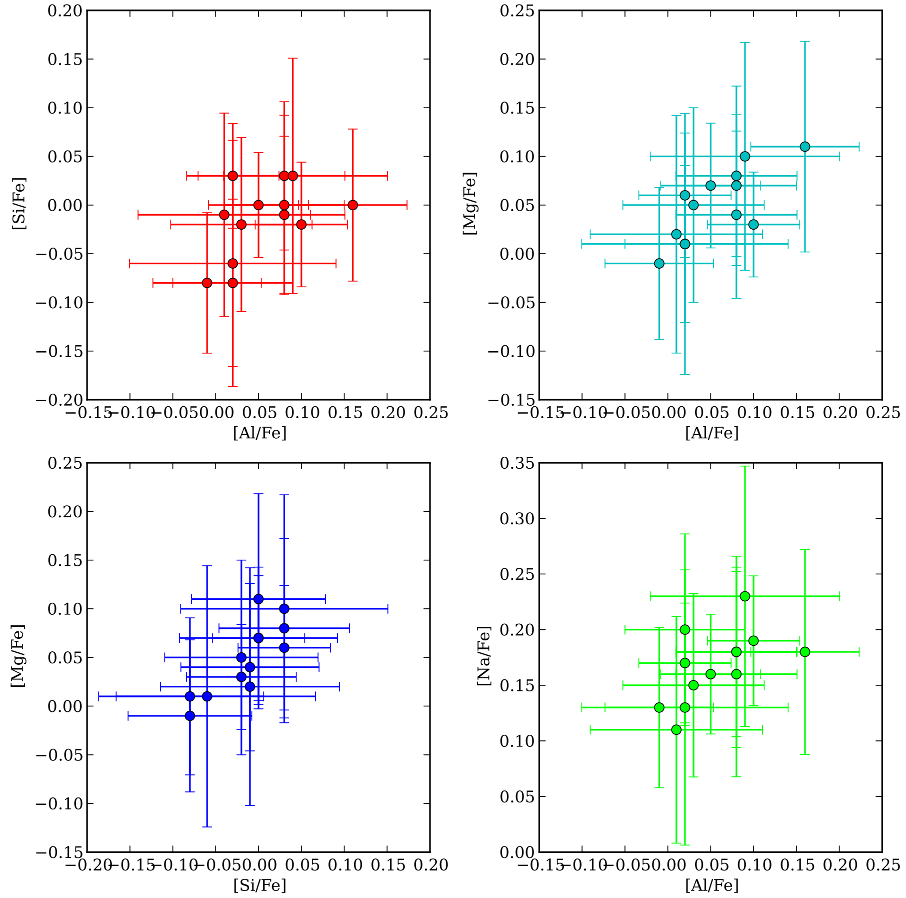

Figure 5.9: Abundances of Al, Si, Mg and Na for the 13 red clump stars. None of the "classical" correlations or anti-correlations between elemental abundances are observed in this cluster, which seems chemically homogeneous within our uncertainties.

Table 5.5: Mean abundance and intrinsic dispersion (obtained through the maximum likelihood method described in Sect. 5.2.4) for five elements in 13 red clump stars of Tr 20.

element	mean	disp.
Fe	0.16 ± 0.05	$0^{+0.07}$
Al	0.06 ± 0.03	$0^{+0.04}$
Mg	0.05 ± 0.03	$0^{+0.04}$
Si	-0.01 ± 0.03	$0^{+0.04}$
Na	0.17 ± 0.03	$0^{+0.04}$

5.4 NGC 4815

NGC 4815 is a populous OC of intermediate age (500 to 630 Myr) situated in the inner disk at coordinates RA= $12^h57^m59^s$, DEC= $64°57'36''$. Its estimated mass content for stars above $0.8\,\mathrm{M}_\odot$ is $880 \pm 230\,\mathrm{M}_\odot$ (Prisinzano et al., 2001). In an extensive study, Friel et al. (2014) determine a photometric distance modulus of 12 mag for this cluster, yielding a galactocentric radius of about 7 kpc. They derive a systemic radial velocity of $29\,\mathrm{km\,s^{-1}}$ for the cluster, with a dispersion of $4\,\mathrm{km\,s^{-1}}$. Of the 13 UVES targets for which we have accurate elemental abundances, five have radial velocities consistent with that of the cluster within $4\,\mathrm{km\,s^{-1}}$.

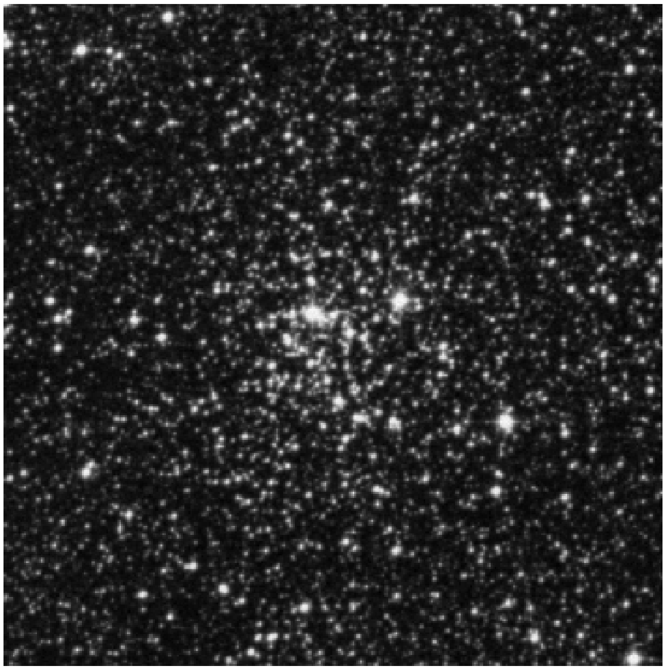

Figure 5.10: DSS image of NGC 4815. The field is $10' \times 10'$.

Elemental abundances

We have applied the same maximum likelihood as presented in Sect. 5.2.4 to the abundances of the five red clump members of NGC 4815. Despite the lower number of targets providing poorer statistics, we establish that the intrinsic dispersion between those five stars is very small and can be explained by the uncertainty on the abundances alone. This result is expected, given the low mass of NGC 4815.

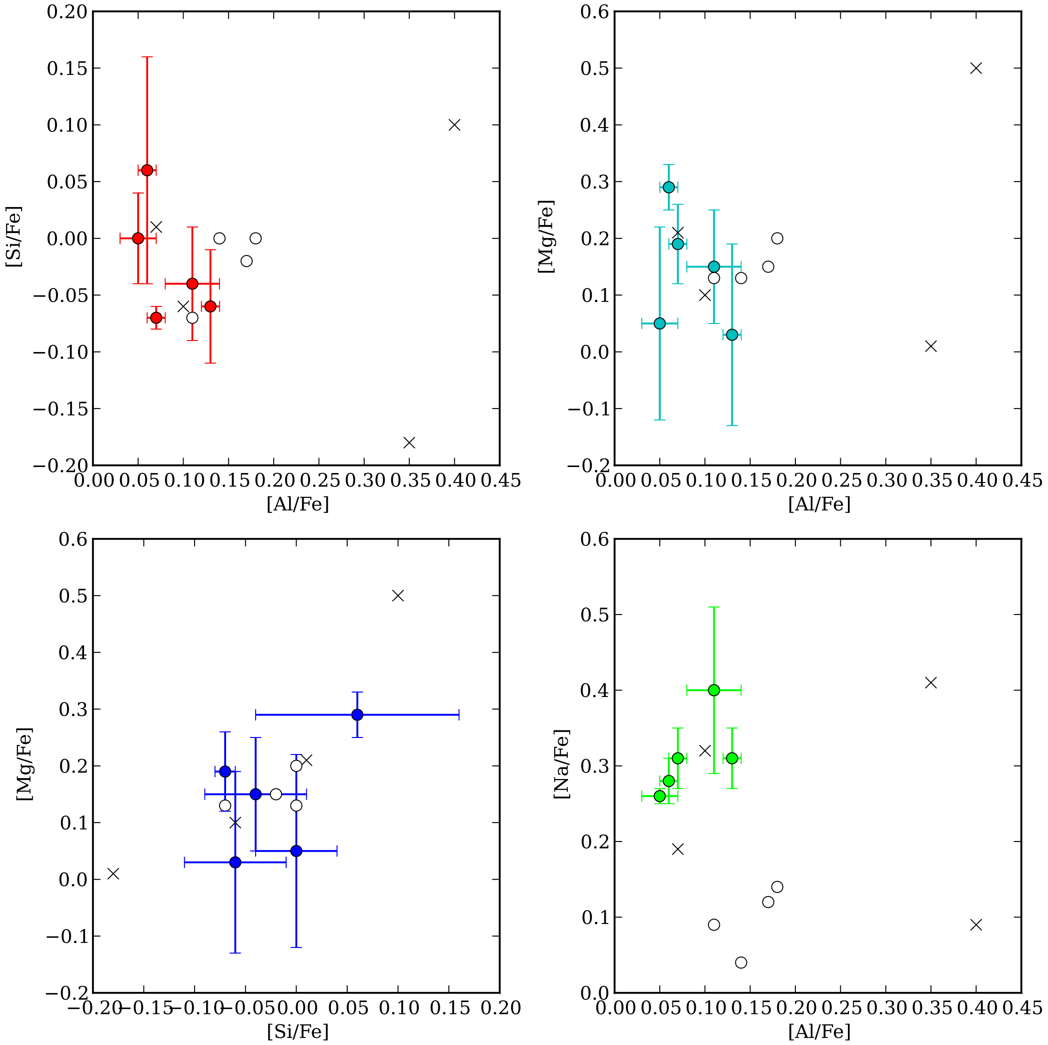

Figure 5.11: Abundances of Al, Si, Mg and Na for the 5 red clump members of NGC 4815 (filled dots). The crossed and empty symbols show the elemental abundances of field stars with RVs discrepant by more than 4 km s^{-1} and 10 km s^{-1}, respectively.

Table 5.6: Mean abundance and intrinsic dispersion (obtained through the maximum likelihood method described in Sect. 5.2.4) for four elements in 5 red clump stars of NGC 4815.

element	mean	disp.
Fe	0.05 ± 0.05	$0^{+0.07}$
Al	0.08 ± 0.03	$0.03^{+0.03}_{-0.01}$
Mg	$0.22\ ^{+0.11}_{-0.07}$	0.04 ± 0.04
Si	$-0.06\ ^{+0.05}_{-0.01}$	$0^{+0.06}$
Na	$0.27\ ^{+0.04}_{-0.01}$	$0^{+0.05}$

5.5 Summary

As far as we can see, NGC 6705, Trumpler 20, and NGC 4815 are homogeneous objects where the star-to-star scatter is explained by the uncertainties on the determination of the chemical abundances. Observationally, Carretta et al. (2010) suggests that clusters above a certain mass limit would develop multiple populations, and they derive the minimum (present-day) threshold mass of about $4 \times 10^4\,\mathrm{M}_\odot$. On the theoretical ground, by comparing the timescale of the mixing of heavy elements in protoclusters with the cluster formation timescale, Bland-Hawthorn et al. (2010) suggest that clusters up to $\sim 10^4\,\mathrm{M}_\odot$ masses, and possibly a significant fraction of those as massive as $\sim 10^5\ \mathrm{M}_\odot$, should be chemically homogeneous.

The mass of all three OCs studied in this chapter is lower than $10^4\,\mathrm{M}_\odot$ and well under the expected $4 \times 10^4\,\mathrm{M}_\odot$ mass threshold. Figure 3 of Carretta et al. (2010) (updated in Bragaglia et al., 2012) shows that the least massive GC known to present multiple populations is Pal 5, with a mass of $6.3 \times 10^4\,\mathrm{M}_\odot$. Terzan 7 and Pal 12, with masses of $3.9 \times 10^4\,\mathrm{M}_\odot$ and $2.8 \times 10^4\,\mathrm{M}_\odot$ (respectively) do not show multiple populations.

Owing to their masses, the chemical homogeneity of NGC 6705, Trumpler 20, and NGC 4815, and the lack of the abundance correlations is consistent with the mass being the driving factor of cluster chemical evolution. However, the properties of those clusters differ in several respects from most GCs: they are younger, have a supra-solar metallicity (Pal 5, the least massive GCs known to contain multiple populations, has a metallicity of -1.4 dex, see Carretta et al., 2010), and likely formed in a very different environment. While the lack of chemical inhomogeneities in those OCs confirms the above scenario, it cannot completely rule out alternative possibilities. To further our knowlegde of cluster chemical evolution, this result needs to be verified on a larger sample.

CHAPTER 6

TRACING THE STAR FORMATION PROCESS WITH GES DATA

The question of how stars form is central to astrophysics. Individually, stars appear as the result of the gravitational collapse of gas clouds. A single giant molecular cloud (GMC) can give birth to tens to thousands of stars (see e.g. Lada & Lada, 2003, and references therein). Most stars in the Milky Way are observed in isolation, and constitute what is generally called the *field population*. Only a small fraction of stars are observed bound in clusters or associations, but whether the field population is the result of cluster disruption or originates from a different star-forming mechanism is still not well understood.

Competitive accretion models consider that many small subclusters may form within a turbulent molecular cloud and subsequently merge on short timescales (Bonnell et al., 2003; Clark et al., 2007). In this scenario, the deeper potential well of denser clusters allows them to accrete more gas, and form more massive stars in their central regions, naturally producing primordial mass segregation (Bonnell, 2008; Bonnell & Bate, 2006). Those clusters do not remain bound forever, as a significant amount of mass can be lost and lead to the dissociation of the cluster (Hills, 1980). Mass loss may be driven by the heating and expulsion of gas by supernovae, stellar winds or ionising radiation (Bastian, 2011; Bastian & Goodwin, 2006; Baumgardt & Kroupa, 2007; Goodwin & Bastian, 2006; Tutukov, 1978).

An alternative mechanism considers that a whole hierarchy of environments can form stars, and that present-day clusters are stars that were born in dense regions (which are more efficient at forming stars), while loosely bound associations formed in less dense regions (Elmegreen, 2011). In this scenario, field stars are born in low-density environments and are never part of bound stellar systems (Bonnell et al., 2011; Bressert et al., 2010; Kruijssen, 2012).

Numerical simulations make predictions for the outcome of the star formation process in various scenarios (Girichidis et al., 2011; Krumholz et al., 2012; Offner & Krumholz, 2009). On the observational ground, our best tools are young OCs. Clusters of ages around 10 Myr are old enough to have no ongoing star formation, and are visible in optical wavelengths since they are no longer embedded, while they are still young enough to have retained some of the fundamental properties of the star-forming process, such as primordial mass segregation or the degree of fractal substructure of their parent GMC (see e.g. Delgado et al., 2013). The variety of observed morphologies for young clusters, from centrally concentrated (e.g. ρ Ophiucus or IC 348, Schmeja et al., 2008a,b) to regions featuring substructure (Taurus, Gomez et al., 1993), requires statistical tools in order to characterise and quantify the differences between the observed distributions. The question of whether different formation mechanisms exist or the morphology of clusters is altered by their internal evolution and interactions with their environment is still open, as we need to understand how stellar systems are assembled in the early stages of their formation.

The Gamma Velorum OB association (Vela OB2) (Brandt et al., 1971) is a region located around the massive binary system γ^2 Velorum (HD 68273). This double-lined spectroscopic binary is made up of $30\,\mathrm{M}_\odot$ O star (07.5III) and a $9\,\mathrm{M}_\odot$ Wolf-Rayet star (WC8) (De Marco & Schmutz, 1999). The distance to Vela OB2 has been estimated to be around 350 pc (Millour et al., 2007; North et al., 2007). Pozzo et al. (2000) identified X-ray sources corresponding to pre-main-sequence stars at distance 350-450pc and suggested these stars are physically associated with γ^2 Vel, which was subsequently confirmed by Jeffries et al. (2009) who established that these stars constitute a subcluster (Gamma Velorum) within the Vela OB2 association.

Recently, Jeffries et al. (2014) have used GES data to study the detailed kinematics of Gamma Velorum. They have selected cluster members based on the strength of their Li 6708 absorption line, and retained 208 stars. They show the radial velocity distribution of this sample is bi-modal, with two components (A and B) offset by $2.15 \pm 0.48\,\mathrm{km\,s^{-1}}$. B is less populated than A, while its radial velocity dispersion is higher ($\sigma_A = 0.34 \pm 0.16$ and $\sigma_B = 1.60 \pm 0.37$), indicating that its virial ratio is higher and suggesting it may be a group of unbound stars. In a colour-magnitude diagram the stars of population A appear slightly brighter, which would indicate that A is either closer to us (by 4 ± 5 pc) or younger (by 0.4 ± 0.6 Myr). The age of the system is estimated between 5 and 10 Myr, while the age of the massive binary γ^2 Vel is 5.5 ± 1 Myr (Eldridge, 2009). The measured EW of the Li 6708 line however shows that the stars of A are more lithium-depleted, which would make it 1–2 Myr older than B. To be both older and brighter than B, population A needs to be about 10 pc closer to us than B.

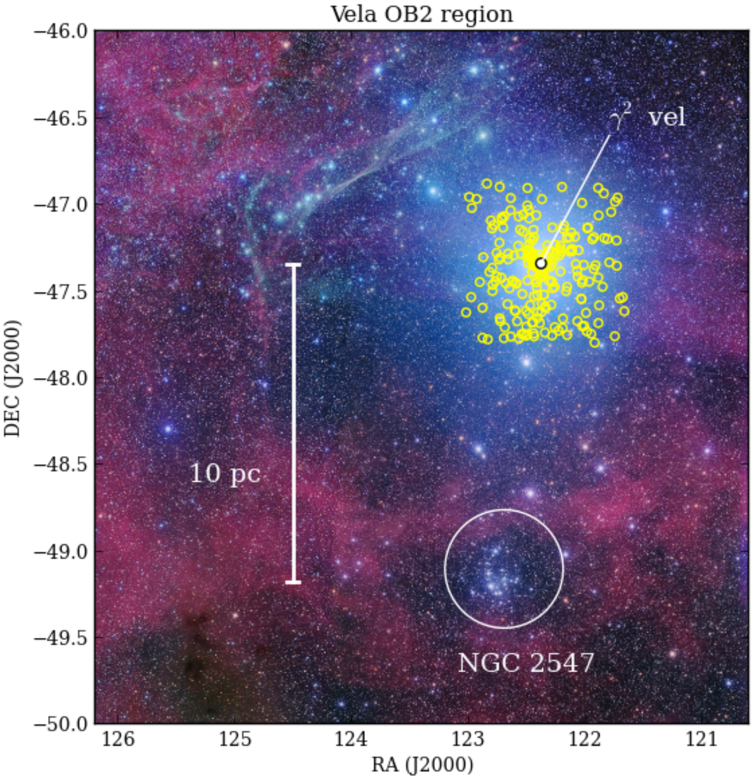

Figure 6.1: RGB mosaic image of the region of the Vela OB2 association. The yellow circles indicate the stars identified as members of the Gamma Velorum cluster by Jeffries et al. (2014). The physical scale of 10 pc is for an assumed distance of 350 pc. Image courtesy Robert Gendler.

In the following, we study the spatial distribution of the members of Gamma Velorum and compare it with the results of dynamical simulations, in order to better understand the star formation process in this region.

6.1 Dynamical simulations

In order to provide further insight on the physics of Gamma Velorum, Mapelli et al. (in prep.) have run N-body simulations. The hypothesis is that pop. A and B are two coeval subclusters formed from the same GMC, and are subsequently colliding.

The collision is investigated by means of direct-summation N-body simulations. The simulations were performed with the STARLAB public software environment (Portegies-Zwart et al., 2001), in the version modified by Mapelli et al. (2013) (see also Mapelli & Bressan, 2013). STARLAB integrates the dynamical evolution of a star cluster by means of a predictor-corrector Hermite scheme, and follows the stellar and binary evolution of the star cluster members. The subclusters are described as two Plummer spheres (Plummer, 1911), and the star particles were generated following a Kroupa IMF with masses ranging from $0.1\,\mathrm{M}_\odot$ to $150\,\mathrm{M}_\odot$. Stellar and binarity evolution is enabled, as described in Mapelli & Bressan (2013).

Several simulations were run with different sets of initial conditions. The main observational constrain to be reproduced is the structured, bimodal radial velocity distribution of Gamma Velorum. One of the main parameters to drive the evolution of a stellar system is the **initial energy balance** at the start of cluster formation, which can be characterised as the virial ratio T/Ω (where T and Ω are the total kinetic and potential energy of the stars). If this ratio is above 0.5 the cluster is **supervirial**. Its intrinsic radial velocity dispersion is too high with respect to its total mass, it will expand and unbound stars will escape the cluster. On the other hand, a cluster with a **subvirial** energetic balance (< 0.5) will remain bound.

The initial conditions that enable to best reproduce the observed properties of Gamma Velorum are those of run 1 and run 13 (see Table 6.1, Fig. 6.2, and details in Mapelli et al., in prep.), which both correspond to a very supervirial state for population B, and a slightly supervirial population A. In those runs, the two subclusters are placed at a distance of 5 pc from each other and are given an initial velocity kick in order to make them collide. An additional run, labelled run 21, was performed to explore the possibility that the two subclusters are not interacting, but are simply observed superposed along the same line of sight. The initial conditions of run 21 are identical to run 1, except that the two clusters are kicked in opposite directions and never collide.

The resulting projected sky distribution of run 1 and run 21 are indistinguishable (see Figs. 6.3 and 6.4). The radial velocity distribution in both cases is also very similar. Since the relative velocity of A and B is large with respect to the internal radial velocity of each subcluster, the final radial velocity distribution remains mainly unaffected by the collision.

Table 6.1: Initial conditions for three simulated runs.

Run	N_A	M_A	r_A	Q_A	N_B	M_B	r_B	Q_B	f_{bin}	Δ_v	D (pc)	m_1, m_2
1	780	506	2	1.0	585	271	1	4.5	0.46	2.4	5	32,14
13	156	97	2	4.0	117	48	1	8.0	0.46	2.2	5	3,3
21	780	506	2	1.0	585	271	1	4.5	0.46	-2.4	5	32,14

Notes. Run: identifying name of the run; N_A: number of particles in the first cluster (identified with pop. A); M_A: initial mass of the first cluster (in $M_\odot$); r_A: scale radius of the first cluster (in pc); Q_A: virial ratio of pop. A; N_B: number of particles in the second cluster (identified with pop. B); M_B: initial mass of the second cluster (in $M_\odot$); r_B: scale radius of the second cluster (in pc); Q_B: virial ratio of pop. B; Δ_v: initial velocity shift between the centres of mass of the two clusters (in $\mathrm{km\,s^{-1}}$); D: initial distance between the centres of mass of the two clusters (in pc); m_1, m_2: initial mass of the members of the most massive binary system in each run (in $M_\odot$).

Gaia parallaxes will provide valuable information on the line-of-sight distribution of these two populations.

In all cases, the simulated clusters quickly expand from their initial Plummer sphere distribution of scale radius $r_A = 2$ pc and $r_B = 1$ pc to half-mass radii of about ~ 10 pc, and stars belonging to subcluster B can be found as far as 15 pc from the centre of mass of the system at simulation time t=4.8 Myr. This distribution extends much further than the field covered by GES observations, as shown in Fig. 6.5. The fact that GES data only cover a small fraction of Gamma Velorum makes it impossible to characterise the large-scale structure of the cluster, but statistical tools can be applied in order to characterise the stellar distribution in the inner regions.

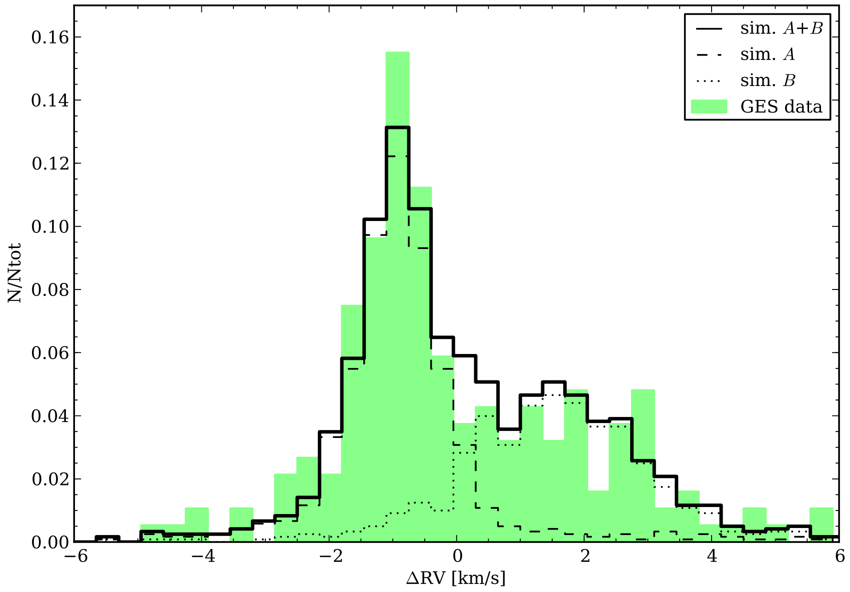

Figure 6.2: Radial velocity distribution (centred on the mean value) for the observed data of Jeffries et al. (2014) (green) and the simulated Run 1 (black lines).

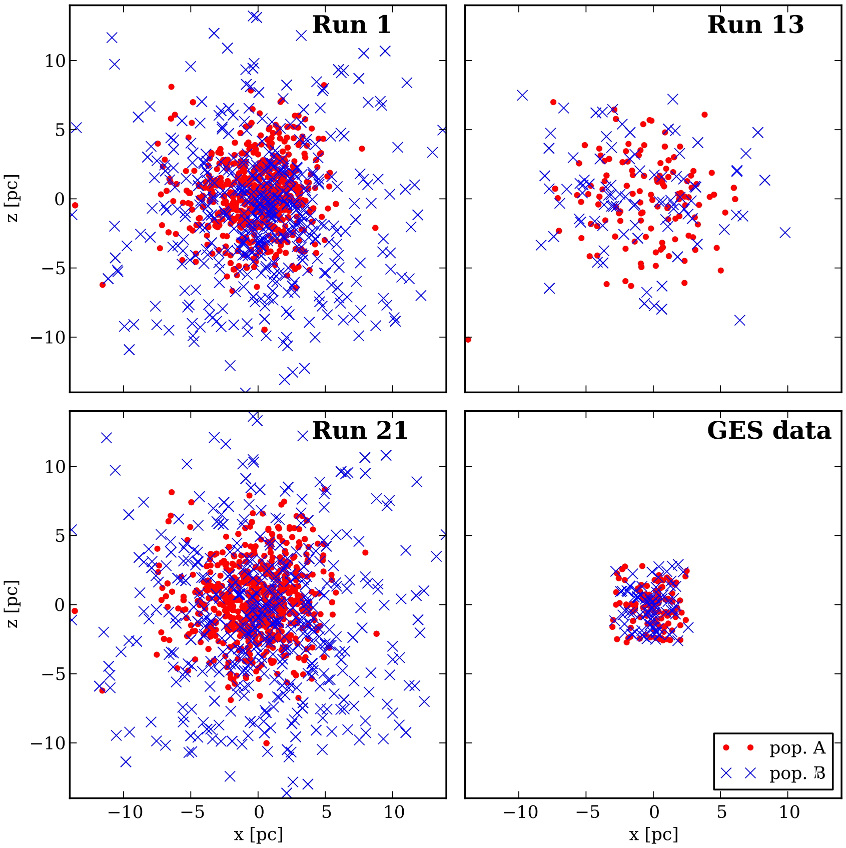

Figure 6.3: Projected (sky) distribution of the stars in simulation 1, 13, and 21, and sky distribution of the stars of Jeffries et al. (2014). The conversion from angular to physical distances assumes a distance of 350 pc. The origin of the coordinate system corresponds to the centre of mass for the simulation, and to the position of the γ^2 Vel star for the observed data.

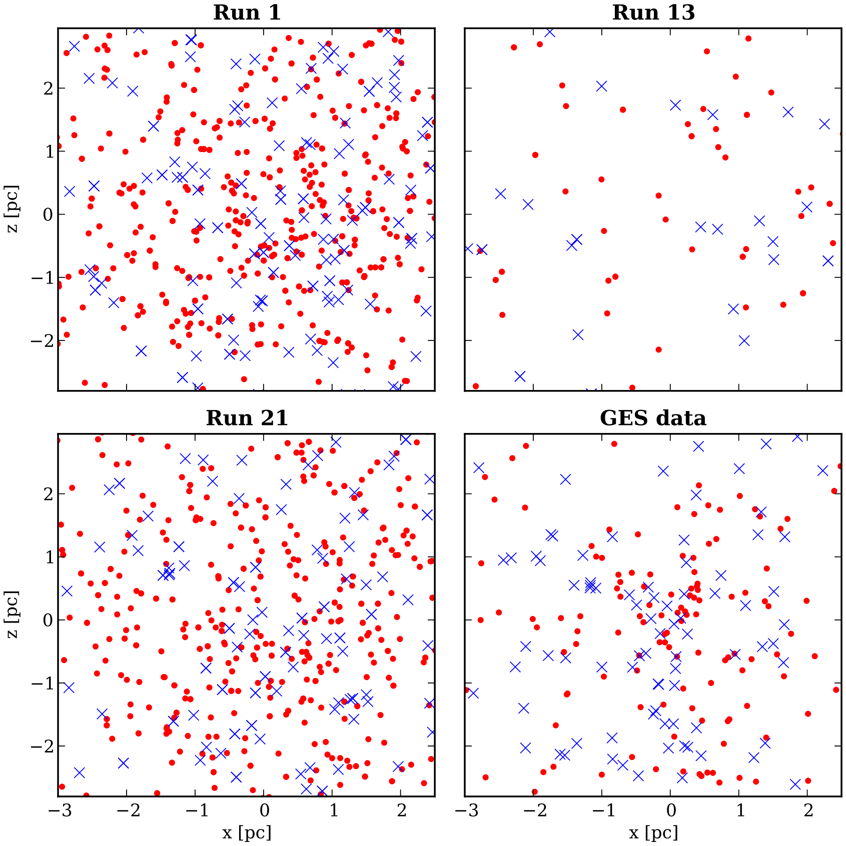

Figure 6.4: Same as Fig. 6.3, but with a field of view corresponding to the GES observations. Red dots indicate stars of population A, blue crosses those of population B.

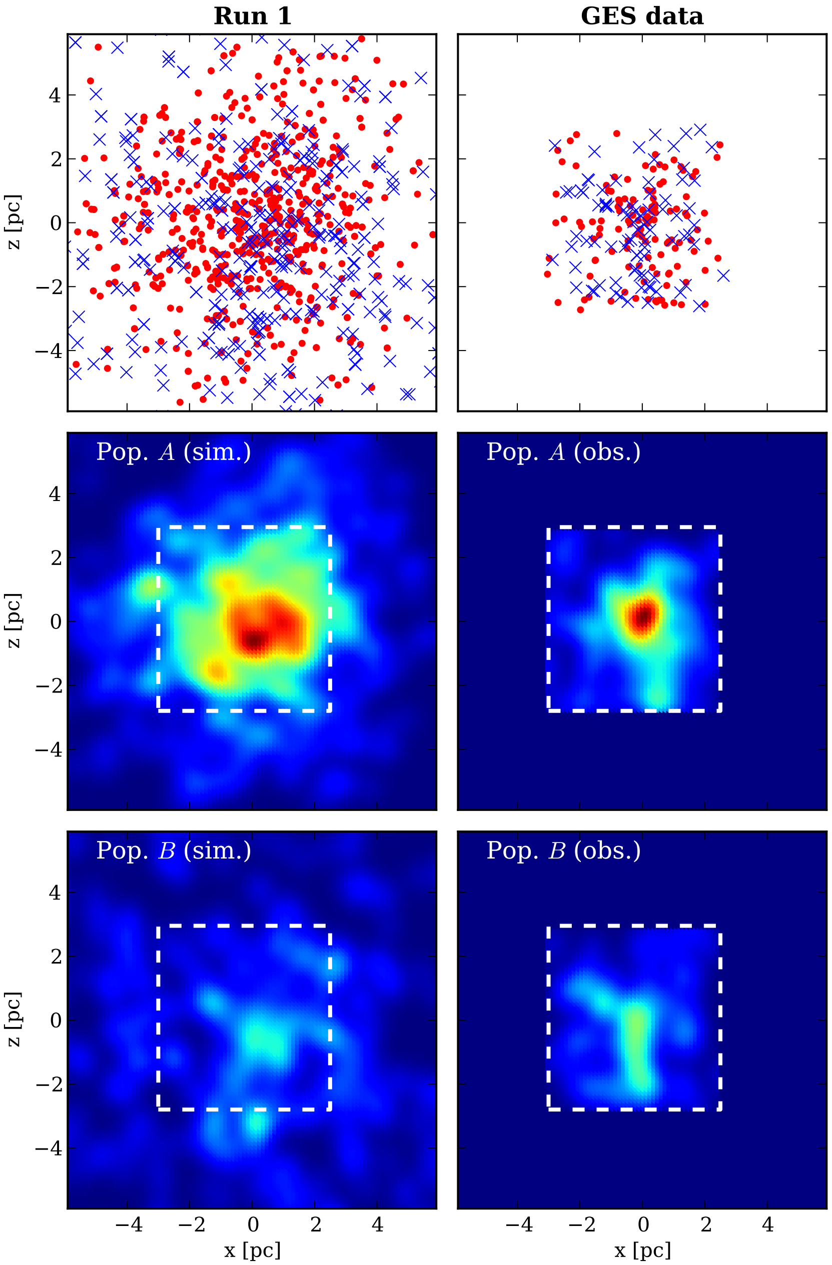

Figure 6.5: Sky distribution and kernel density maps (using a gaussian kernel of 0.4 pc) for populations A and B in the simulated run 1 (left column) and in the observations (right column). For the observed distribution, the stars were split between those with membership probability $p_A > 0.5$ and $p_A < 0.5$. The white box indicate the field covered by GES observations.

6.2 Statistical diagnostics

In this section I have applied statistical diagnostics (Kernel Density Estimate, two-point separation function, and quantified mass segregation and fractality through the Λ and Q parameters) in order to characterise and quantify the morphologial differences between the two populations identified in Gamma Velorum. In this study, the membership probability used for the 208 stars are those established by Jeffries et al. (2014), which are based on radial velocities only.

6.2.1 Density distribution

The Kernel Density Estimate (KDE) maps of Fig. 6.5, obtained by dividing stars between those with $p_A > 0.5$ and $p_A < 0.5$ show that the observed population A is denser than population B, but also presents a relatively centrally concentrated structure while pop. B seems elongated. Those KDE maps are shown again in Fig. 6.6 (left panels), along with two other maps based on a more stringent probability cut ($p_A > 0.75$ for pop. A and $p_A < 0.25$ for pop. B, right panels). The general appearance of pop. A is similar regardless of the probability cut applied (0.50 or 0.75 membership probability), and in particular the densest area of the distribution is centered on the position of the γ^2 Vel massive binary in both cases. For pop. B, the position of the maximum of density is different according to the probability selection we perform. The more stringent selection, corresponding to $p_A < 0.25$ (bottom right panel of Fig. 6.6), presents a density peak which is offset by about $20'$ (2 pc) from the position of γ^2 Vel. This may indicate that the massive binary is physically associated with pop. A, and not with B, although the extended and low-density nature of B makes it difficult to be certain that we are effectively looking at the core of the distribution. Accurate distance measurements, such as those which will be derived from *Gaia* parallaxes, should provide us with a clearer picture regarding the line-of-sight distribution in population A and B, and how γ^2 Vel relates to them.

The issue of determining the position of the centre of pop. B makes it difficult to draw a clear density profile. Figure 6.7 shows density profiles obtained for the whole sample, and for population A and B individually. The profile derived for pop. B depends on adopted centre (centred on the position of γ^2 Vel, or offset to the position of the maximum density derived from KDE maps). Since a “classical” radial density profile is not well-suited for the stellar distribution we are dealing with, Sect. 6.2.2 presents a characterisation of pop. A and B through their two-point separation functions.

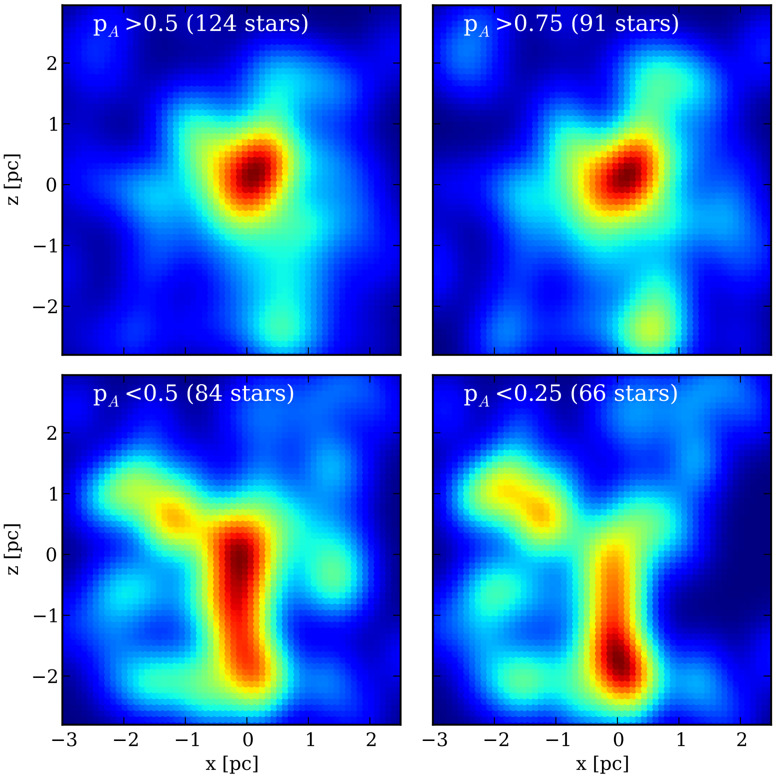

Figure 6.6: KDE maps (gaussian kernel of witdh 0.4 pc) for subgroups defined with different probability selections. The colour scale is different in all cases, so the darkest shade of red corresponds to the maximum density in a given subgroup. The conversion from angular coordinates to physical units assumes a distance of 350 pc, and the origin of the coordinates is centred on the position of the star γ^2 Vel.

6.2.2 Two-point separation function

When dealing with structures that are not centrally concentrated the **two-point separation function** can be more informative than a radial density profile, because it does not rely on prior assumptions on the geometry of the sky distribution. This statistical diagnostic has been applied in literature, for instance by Gomez et al. (1993) in order to study the distribution of pre-main sequence stars in the Taurus-Auriga molecular cloud, or by Gouliermis et al. (2014b) to study the star-forming region NGC 346 in the Small Magellanic Cloud. Other applications include Zhang et al. (2001) for the interstellar medium

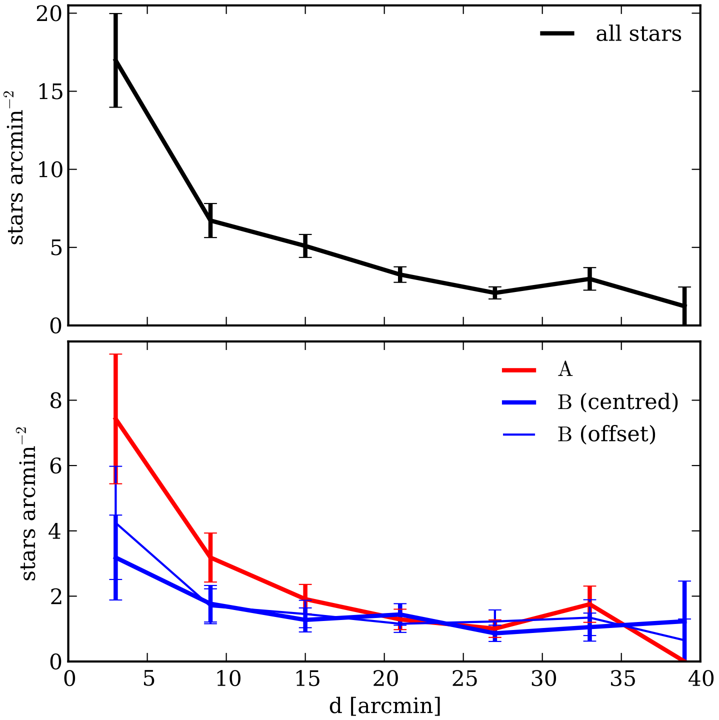

Figure 6.7: *Top:* radial stellar density profile obtained for the 208 members of Gamma Velorum, using the position of γ^2 Vel as centre. *Bottom:* Radial stellar density profiles for pop. A centred on γ^2 Vel (thick red line), for pop. B centred on γ^2 Vel (thick blue line) and for pop. B centred on its density peak (thin blue line). Populations A and B were split using $p_A > 0.75$ for pop. A and $p_A < 0.25$ for pop. B.

of the Antennae galaxy, Scheepmaker et al. (2009) in M 51 or Gouliermis et al. (2014a) in M 31.

The method consists in computing the distance between all possible pairs of stars in the sample, and establishing the density distribution of all possible distances. In a first step, the diagnostic was applied to the total (sky projected) stellar distribution in the simulated run 1 and run 13 (considering only the stars falling in the GES field of view), and to the whole of the observed GES data. The resulting separation functions are shown in the left panel of Fig. 6.8. For an easier interpretation, those distributions can be compared to a reference one. Here the choice of reference is a random, uniform distribution, shown as a dashed line in Fig. 6.8. The right panel of that Figure shows the ratio between the computed two-point separation function and the reference (uniform) one. The function obtained for run 13 is statistically very close to a uniform distribution, reflecting the sparse and extended sky distribution obtained in that particular simulation. On the other hand, the two-point separation function of run 1 is qualitatively closer to the observational data. The simulation does not, however, produce a high enough proportion of stars with separations under 1 pc. This result confirms the idea conveyed by the KDE maps of Fig. 6.5 that the star distribution simulated in run 1 is more smeared out and less clumpy than the observed one.

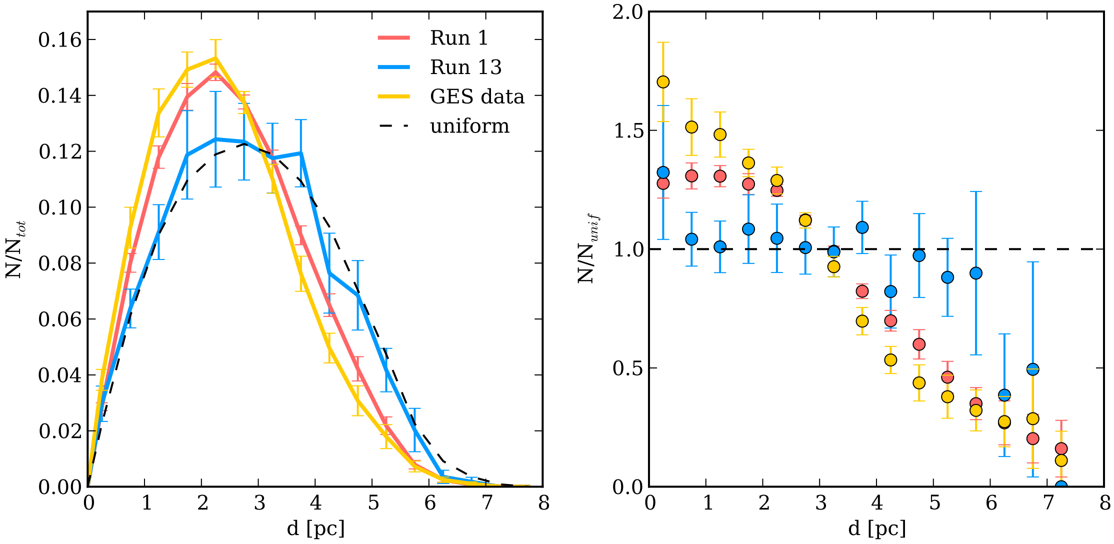

Figure 6.8: *Left:* two-point separation distribution for the simulated run 1 (pink) and run 13 (cyan), and for the observed GES data (yellow). The dashed line corresponds to a uniform distribution. *Right:* ratio between those distributions and the uniform distribution. The uncertainties are estimated by computing the standard deviation between 100 bootstrap samples of the original data. The conversion from angular coordinates to physical units assumes a distance of 350 pc.

In a second step, the same diagnostic was applied to characterise the difference between the observed population A and B. The stars were separated in two groups ($p_A > 0.75$ for population A and $p_A < 0.25$ for population B) and the two-point separation function was computed. The results are shown in Fig. 6.9. The right panel shows the ratio between those distributions and the reference (uniform) distribution. We can clearly see that both population A and population B present an excess of close pairs with respect to the uniform distribution, with A featuring a steeper slope (i.e. a stronger imbalance towards tightly distributed pairs). The exact slope of these relative distribution functions can be computed in order to quantify the difference between the observational data and the reference distribution (see e.g. Bastian et al., 2009a,b; Gieles et al., 2008, for applications in the Magellanic Clouds). A weighted least-square fit taking into account the uncertainty on each point yields a slope of -1.45 ± 0.15 for population A, against a significantly different -1.13 ± 0.16 for B. This result means that B is not only less dense, but also more loosely distributed than A. The low statistics and the small dimension of the observed field however prevents us from drawing conclusions on the exact shape of the separation function and does not reveal any particular substructure.

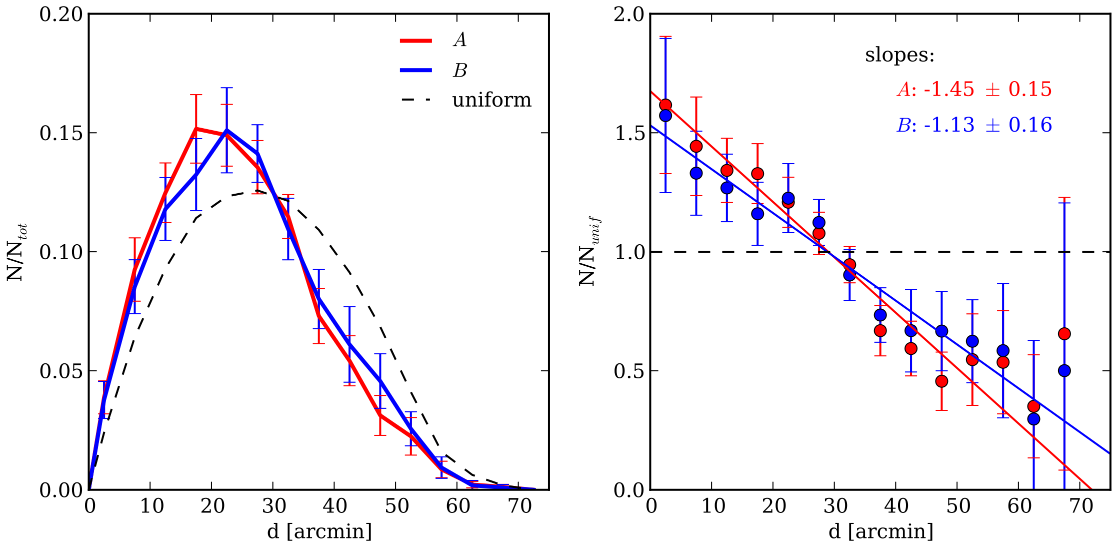

Figure 6.9: Same as Fig. 6.8, for the observed population A (red) and B (blue).

6.2.3 Fractality and mass segregation

During the first few Myr of their evolution, clusters retain some properties of the giant molecular cloud they originate from. The degree of mass segregation and fractal substructure present in a young cluster is linked with the original conditions at the time of formation (Delgado et al., 2013; Parker & Meyer, 2012).

During their evolution, clusters are expected to evolve from a fractal distribution (at birth) to a radial one (Klessen, 2011; Maschberger & Clarke, 2011; Sánchez & Alfaro, 2009). Quantifying the degree of substructure, or fractality, of a stellar distribution can be done by evaluating the ***Q*-parameter** as defined by Cartwright & Whitworth (2004): $Q \equiv \overline{m}/\overline{s}$, where $\overline{m}$ is the (normalised) mean edge length of the Minimum Spanning Tree, and $\overline{s}$ the mean separation between all possible pairs of stars in the system (divided by the overall radius of the cluster). For a random 3D distribution of stars projected in two dimensions, the expected value is $Q = 0.8$. Systems where the stars are more centrally concentrated have values of $Q > 0.8$, while substructured distributions will have $Q < 0.8$. (Parker & Meyer, 2012) have performed simulations and shown that clusters always evolve towards larger values of Q (i.e. erasing fractal substructure), but subvirial clusters erase substructure quicker than supervirial clusters, which expand and retain a certain level of substructure on longer timescales. (Parker & Meyer, 2012) call those two evolution paths “warm collapse” (for supervirial systems that expand and retain fractality) and “cold collapse” (for subvirial clusters in which fractality quickly disappears).

Another diagnostic that can be used along with the Q-parameter to understand the initial conditions at cluster formation is mass segregation, conveniently quantified through the Λ-parameter defined by (Allison et al., 2009), and introduced in this Thesis in 4.1.3. Mass segregation can be primordial (with the most massive stars forming in the central regions) or arise from a dynamical process. Either way, subvirial clusters are expected to exhibit a higher level of mass segregation than supervirial clusters, while a warm collapse opposes mass segregation.

Exploiting both Λ and Q diagnostics at the same time, Delgado et al. (2013) have studied the young clusters Be 94 and Be 96 (which seem to be both associated with the same HII region Sh2-132 Saurin et al., 2010). They show that Be 96 exhibits more mass segregation and less substructure than Be 94, while it appears younger (10 Myr against 30 Myr for Be 94), which could mean we are witnessing Be 96 undergoing a cold collapse and Be 94 undergoing a warm collapse. If the population B of Gamma Velorum is in a supervirial state, we expect to see in a similar way that it is undergoing a warm collapse, with a lower value of Q and Λ.

The value of Q for pop. A is 0.84, against 0.78 for pop. B, which means their levels of fractality are virtually undistinguishable, although this could be interepreted as pop. B being very slightly more substructured (top panels of Fig. 6.10).

To quantify mass segregation, the low number of stars in each population does not allow us to reliably apply the procedure described in 4.1.3. Instead, the stars were split each population into high-mass ($>0.8\,\mathrm{M}_\odot$) and low-mass ($<0.8\,\mathrm{M}_\odot$) groups, and Λ was computed for the high-mass group. In the case of pop. A, the most massive stars seem to be more concentrated in the central parts (bottom-left panel of Fig. 6.10) and yield a $\Lambda_A = 1.07 \pm 0.12$, which can be interpreted as a marginal sign of mass segregation. The massive stars of pop. B exhibit $\Lambda_B = 0.86 \pm 0.12$, which is significantly lower than a value of 1, and indicates inverse-segregation (bottom-right panel of Fig. 6.10). This peculiar distribution for B is either real, or a side-effect of the limited field of view which prevents us from appreciating the true, large-scale distribution of the stars. Both explanations are compatible with the hypothesis that B is more extended and more supervirial than A.

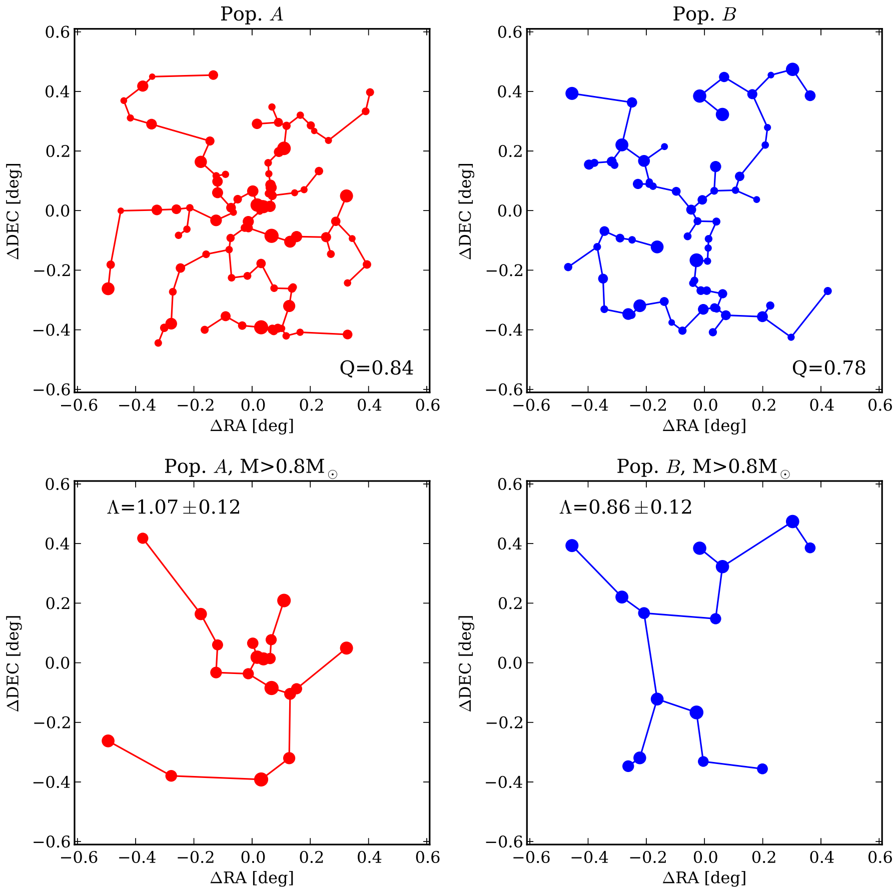

Figure 6.10: *Top:* MST for the stars of pop. A (left) and pop. B (right). *Bottom:* MST of pop. A and B., considering stars more massive than 0.8 $M_\odot$ only. The coordinates are given with respect to the position of γ^2 Vel.

6.3 Discussion

Despite the low number of objects in each of the subclusters, we see hints that both populations present a different dynamical state and morphology. These observations are compatible with a model of hierarchical formation, where population A would correspond to stars formed in a denser environment than population B. In this scenario, the unbound population B would be expanding simply because it was born in a less dense environment. Similar bi-modal modes of star formation have been observed by Sabbi et al. (2007) and Gouliermis et al. (2014b) in the young SMC cluster NGC 346. Unfortunately, the limited field of view of GES observations does not allow us to characterise the distribution of stars in Gamma Velorum on a larger scale.

However, we cannot rule out the competitive accretion scenario on the basis of this data alone. Competitive accretion considers that once formed, subclusters within a GMC may merge or be disrupted by dynamical interactions with their neighbours or through internal processes. The exact nature of the physical link between population A and B is not clear, as we do not know the distance between them or if they are in gravitational interaction. Population A presents hints of mass segregation, and also appears to host the massive binary γ^2 Vel at its centre. The competitive accretion model described by Bonnell (2008) predicts that more gas falls at the bottom of the potential wells of clusters, forming more massive stars, which can in turn accrete more material. Assuming a universal IMF, the presence of the massive binary system γ^2 Vel (with an initial mass of $35\,\mathrm{M}_\odot + 31.5\,\mathrm{M}_\odot$, Eldridge, 2009) in Gamma Velorum ($\sim 100\,\mathrm{M}_\odot$ in total) is not easily explained. The issue of the young age of γ^2 Vel, discussed by Jeffries et al. (2014), also indicates that it may have formed after the surrounding population in the merging of smaller objects.

Jeffries et al. (2014) propose a “captured cluster” scenario in which the whole region formed as one supervirial association, and population A would correspond to stars trapped in the potential well of γ^2 Vel. This scenario can only hold if it can be shown that pop. A and B are coeval (because they would, in fact, be one single population).

Recently, Sacco et al. (2015) have found stars bearing the radial velocity signature of pop. B in GES data of the nearby cluster NGC 2547 (see Fig.6.1). The presence of stars of pop. B as far as 10 pc from γ^2 Vel is allowed by our simulations, but is also compatible with the hierarchical scenario in which pop. B would form from low-density material on large scales. Unfortunately, the limited field of view covered by GES observation does not provide data for the intermediate region between Gamma Velorum and NGC 2547.

The upcoming *Gaia* mission is expected to deliver valuable data that may help understand the history of Gamma Velorum. Accurate parallaxes will solve the question of the line-of-sight distance between population A, B, and γ^2 Vel. By providing proper motions and radial velocities, *Gaia* will enable us to draw a much more precise picture of the dynamical state of the system. It will also allow us to study the region on a large scale and link together all the pieces of the puzzle.

CHAPTER 7

THE OUTER DISK AND THE METALLICITY GRADIENT

Open clusters have been used as tracers of the metallicity distribution in the Galactic disk since the work of Janes (1979). Multiple studies (Frinchaboy et al., 2013; Pancino et al., 2010; Sestito et al., 2008; Twarog et al., 1997; Yong et al., 2012) have shown that the radial metallicity gradient observed in the solar vicinity is not representative of the whole disk, as the gradient seems to be shallower or flat in the outer regions of the Galaxy.

A peculiar structure called *Monoceros stream* or *Monoceros ring* and often referred to as the *Galactic anticentre structure* (GASS) to underline is currently uknown nature, was first identified by Newberg et al. (2002) as a stellar overdensity at a distance of 11 – 16 kpc from the Sun. Whether these stars are the remains of a disrupted dwarf galaxy, overdensities due to a past minor merger, or the result of a warped and flared Galactic disk is currently unknown.

This Chapter presents a new analysis of high-resolution spectra of red clump stars in the four old outer disk OCs Be 66, Be 22, Be 29 and Sau 1, addresses the issue of the metallicity distribution in the Galactic disk and discusses the links between the disk and the GASS.

7.1 Four outer disk clusters: Be 66, Be 22, Be 29 and Sau 1

In order to complement the *Gaia*-ESO Survey sample of OCs, we have applied the tools presented in Sect. 3 to publicly available archival spectra of red clump stars belonging to Be 29 and Sau 1 (published by Carraro et al., 2004, hereafter C04) and Be 66 and Be 22 (published by Villanova et al., 2005, hereafter V05). The main parameters of these clusters are summarised in Table 7.5.

7.1.1 Keck archival data

The spectra analysed in this Section were acquired with the HIRES instrument (Vogt et al., 1994) mounted on the 10-meter telescope of the W. M. Keck Observatory (Hawaii), providing a resolution $R \sim 34,000$.

We obtained pre-reduced spectra through the Keck archive[1] for nine stars in total. Information on those nine targets is presented in Table 7.1. The stars of Sau 1 and Be 29 are those presented in C04. The stars of Be 22 and Be 66 are those of V05. The Keck archive contains an additional star for Be 22 (K414) that we have also included in our analysis.

The data is stored in the archive in the form of individual orders, for each available exposure. Multiple exposures covering the same spectral range for a given star were co-added (see example in Fig. 7.2) in order to reach a higher signal-to-noise ratio. Where the individual orders cover overlapping spectral ranges (see Fig. 7.1), they were merged together (see bottom panel of Fig. 7.2). Equivalent widths were then measured using DOOp, and the GES line list (Heiter et al. in prep.)

7.1.2 Stellar parameters and abundances

The stellar parameters and elemental abundances were obtained running FAMA with MARCS model atmospheres. We obtained results for all nine stars under analysis, including Be 66-K934 for which V05 did not derive stellar parameters. The results are presented in Table 7.2. The iron abundance provided by FAMA is computed with all Fe lines (discarding those discrepant by 2σ). In addition to this value, Table 7.2 shows $[\mathrm{Fe/H}]_{\mathrm{gold}}$ computed using the selection of “golden lines” presented in the study of Jofré et al. (2014). Using this particular selection has a negligeable influence on the iron abundance, typically changing the value by 0.02 dex and never more than 0.04 dex.

---

[1] `https://koa.ipac.caltech.edu/cgi-bin/KOA/nph-KOAlogin`

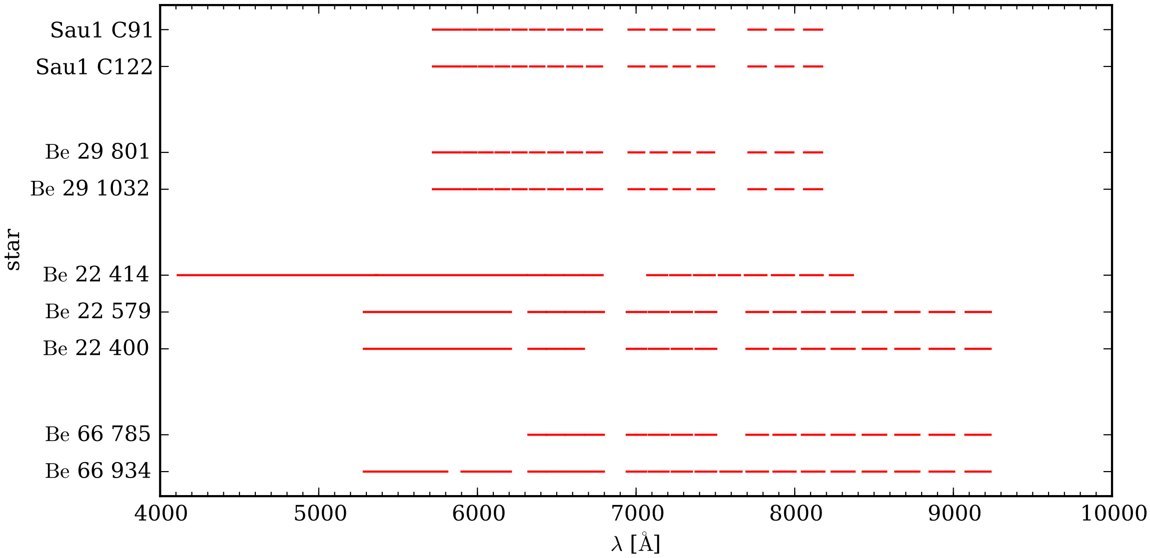

Figure 7.1: Spectral range covered by the available HIRES data. Where they overlap (appearing as continuous lines on this figure) the orders were merged before measuring EWs.

The solar-scaled abundance ratios with respect to iron are presented in Table 7.3 and continued in Table 7.4, and shown in Fig. 7.3. The global α abundance was computed using elements Mg, Si, Ca and Ti. In contradiction with C04, we do not observe a significant α-enhancement for Sau 1 and Be 29, which would go against their claim that these two objects resemble the halo population.

Sau 1

We find iron abundances [Fe/H]=-0.38±0.08 dex and [Fe/H]=-0.32±0.09 dex for the stars C91 and C122 respectively, in agreement with C04 who find iron abundances of -0.38 for both. Both stars appear slightly enhanced in Si, and enhanced in Al and Na with respect to the solar values, but our results do not reproduce the strong (+0.48 dex) Si and Na enhancement seen by C04.

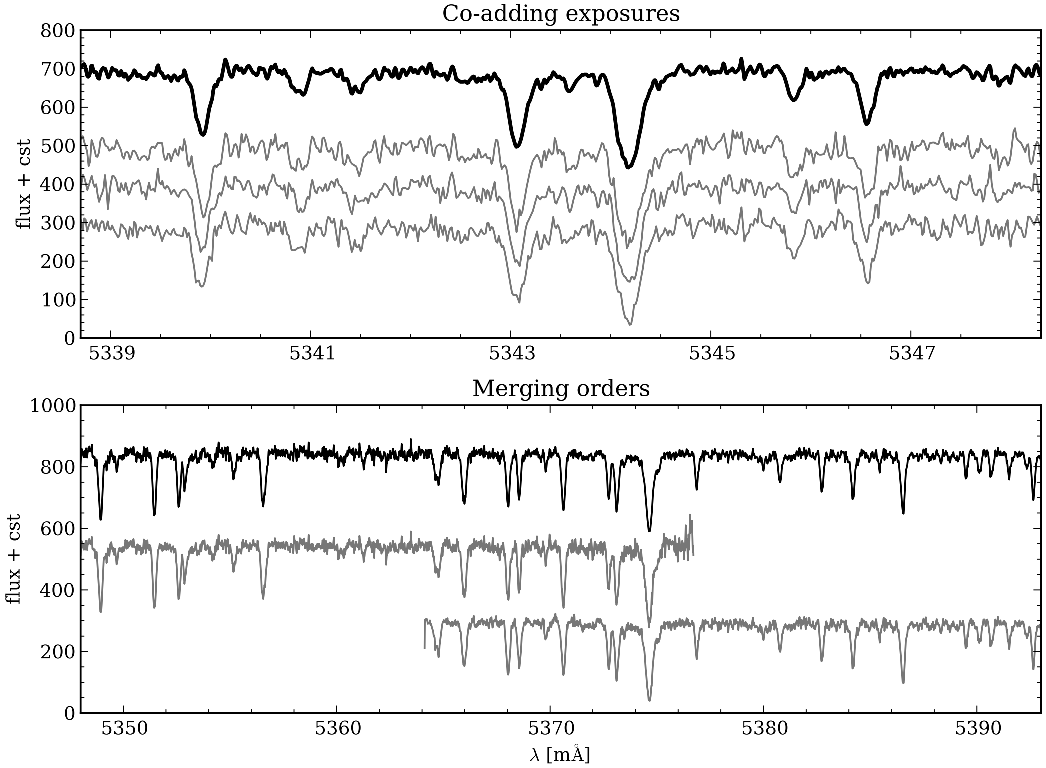

Figure 7.2: Fragment spectra of star Be22-K400. All fluxes are shown shifted by an arbitrary constant for clarity. *Top:* three different exposures (grey lines) co-added into a combined exposure (black line). *Bottom:* two different orders (grey lines), overlapping in the spectral range ∼5365–5375 Å can be stitched together into a merged spectrum (black line).

Be 29

We obtained iron abundances [Fe/H]=-0.38±0.09 dex and [Fe/H]=-0.49±0.10 dex for K801 and and K1032 respectively, in agreement with C04 who derived [Fe/H]=-0.45 and -0.45 dex. All elements present solar-like abundance ratios except Al and Na that appear slightly enhanced. This is in qualitative agreement with C04, who derived super-solar abundance ratios for all elements and note a stronger enhancement for Al and Na, but we find that the stars of Be 29 present abundance ratios that are closer to solar. This slight Na enhancement in outer disk clusters was already noted by Sestito et al. (2008), but suggest

Table 7.1: Target stars of Be 66, Be 22, Be 29 and Sau 1

OC	star*	RA	DEC	V	$V-I$	date	exposure time [s]
Sau 1	C91	07 20 54.75	+01 47 53.09	16.43	1.11	2004-01-14	2×2700
Sau 1	C122	07 20 57.08	+01 48 44.97	16.92	1.17	2004-01-14	2×3000
Be 29	K801	06 53 08.07	+16 55 40.53	16.579	1.061	2004-01-14	3×2400
Be 29	K1032	06 53 03.50	+16 55 08.50	16.561	1.049	2004-01-14	3×2400
Be 22	K400	05 58 30.97	+07 46 15.3	16.695	1.784	2004-12-01	3×1800
Be 22	K579	05 58 25.78	+07 45 31.2	16.876	1.804	2004-12-01	3×1500
Be 22	K414	05 58 25.92	+07 46 01.2	15.762	2.024	2006-12-28	$2 \times 2400 + 981$
Be 66	PJ785	03 04 02.90	+58 43 57.0	18.23	2.64	2004-12-01	3×2700
Be 66	PJ934	03 04 06.41	+58 43 31.0	18.23	2.64	2004-12-01	$3 \times 2700 + 1335$

Notes. * C: ID from Carraro & Baume (2003); K: ID from Kaluzny (1994); PJ: ID from Phelps & Janes (1996).

Table 7.2: Stellar parameters derived with FAMA.

OC	star	T_{eff}	log g	[Fe/H]	$[\mathrm{Fe/H}]_{\mathrm{gold}}$	σ[Fe/H]	v_{mic}
Sau 1	C91	5138 ± 106	2.57 ± 0.16	-0.37	-0.38	0.08	1.68 ± 0.02
Sau 1	C122	4900 ± 65	2.58 ± 0.07	-0.34	-0.32	0.09	1.43 ± 0.01
Be 29	K801	4966 ± 89	2.46 ± 0.12	-0.42	-0.38	0.09	1.37 ± 0.04
Be 29	K1032	5020 ± 98	2.4 ± 0.21	-0.49	-0.49	0.10	1.54 ± 0.01
Be 22	K400	4912 ± 92	3.09 ± 0.1	-0.14	-0.14	0.10	1.12 ± 0.04
Be 22	K579	4820 ± 95	2.71 ± 0.14	-0.19	-0.19	0.12	1.12 ± 0.02
Be 22	K414	4492 ± 84	2.41 ± 0.12	-0.20	-0.17	0.12	1.39 ± 0.0
Be 66	PJ785	4958 ± 99	2.48 ± 0.17	-0.14	-0.13	0.12	1.52 ± 0.02
Be 66	PJ934	4894 ± 109	2.49 ± 0.1	-0.16	-0.14	0.13	1.5 ± 0.01

that this apparent enhancement may be due to non-LTE effects.

Be 22

We derive [Fe/H]=-0.14±0.10 dex, -0.19±0.12 dex and -0.17±0.12 dex for the stars K400, K579 and K414 respectively. These values are 0.15 dex higher than those derived by V05 for K400 and K579. They note that the stars of Be 22 feature solar-scaled abundance ratios, although they find a solar-scaled value [Al/Fe]∼+0.3 dex. We also find solar-like abundance ratios, with a marginally higher [Al/Fe]=+0.26 dex and [Mg/Fe]=+0.22 dex for the star K414.

Table 7.3: Solar-scaled abundance ratios (relative to Fe) for Mg, Si, and Ca.

OC	star	[Mg/Fe]	nMg	[Si/Fe]	nSi	[Ca/Fe]	nCa
Sau 1	C91	...	0	0.11 ± 0.09	5	0.02 ± 0.14	12
Sau 1	C122	...	0	0.14 ± 0.11	2	0.02 ± 0.11	7
Be 29	K801	...	0	0.08 ± 0.10	4	0.03 ± 0.18	12
Be 29	K1032	...	0	0.09 ± 0.13	3	0.09 ± 0.14	9
Be 22	K400	-0.07 ± 0.10	2	-0.03 ± 0.12	10	0.00 ± 0.11	11
Be 22	K579	0.00 ± 0.12	3	0.01 ± 0.15	12	0.05 ± 0.14	13
Be 22	K414	0.22 ± 0.12	2	0.02 ± 0.13	9	-0.05 ± 0.13	5
Be 66	PJ785	-0.01 ± 0.12	3	-0.01 ± 0.15	3	-0.01 ± 0.14	2
Be 66	PJ934	-0.03 ± 0.14	2	-0.05 ± 0.17	12	-0.04± 0.19	13
[X/H]$_\odot$		7.53		7.51		6.31	

Notes. [X/Fe] indicates the solar-scaled abundances (solar reference values from Grevesse et al., 2007). nX indicates the number of lines used to compute the abundance of a given element. The uncertainties on the ratios were computed considering the dispersion for that element and for Fe.

Table 7.4: Solar-scaled abundance ratios (relative to Fe) for Ti, Al, and Na.

OC	star	[Ti/Fe]	nTi	[Al/Fe]	nAl	[Na/Fe]	nNa
Sau 1	C91	0.09 ± 0.09	9	0.33 ± 0.10	2	0.24 ± 0.09	2
Sau 1	C122	0.08 ± 0.10	13	0.18 ± 0.09	2	0.09 ± 0.12	2
Be 29	K801	0.03 ± 0.10	12	0.20 ± 0.10	2	0.13 ± 0.1	2
Be 29	K1032	0.06 ± 0.13	15	0.23 ± 0.10	2	0.11 ± 0.12	2
Be 22	K400	0.12 ± 0.13	36	-0.02 ± 0.10	2	-0.01 ± 0.1	2
Be 22	K579	0.03 ± 0.14	32	0.16 ± 0.13	4	0.02 ± 0.12	2
Be 22	K414	0.06 ± 0.15	39	0.26 ± 0.13	2	0.06 ± 0.12	3
Be 66	PJ785	0.15 ± 0.15	6	0.22 ± 0.12	3	...	0
Be 66	PJ934	0.02 ± 0.16	32	0.09 ± 0.14	3	0.11 ± 0.19	2
[X/H]$_\odot$		4.90		6.37		6.17	

Notes. [X/Fe] indicates the solar-scaled abundances (solar reference values from Grevesse et al., 2007). nX indicates the number of lines used to compute the abundance of a given element. The uncertainties on the ratios were computed considering the dispersion for that element and for Fe.

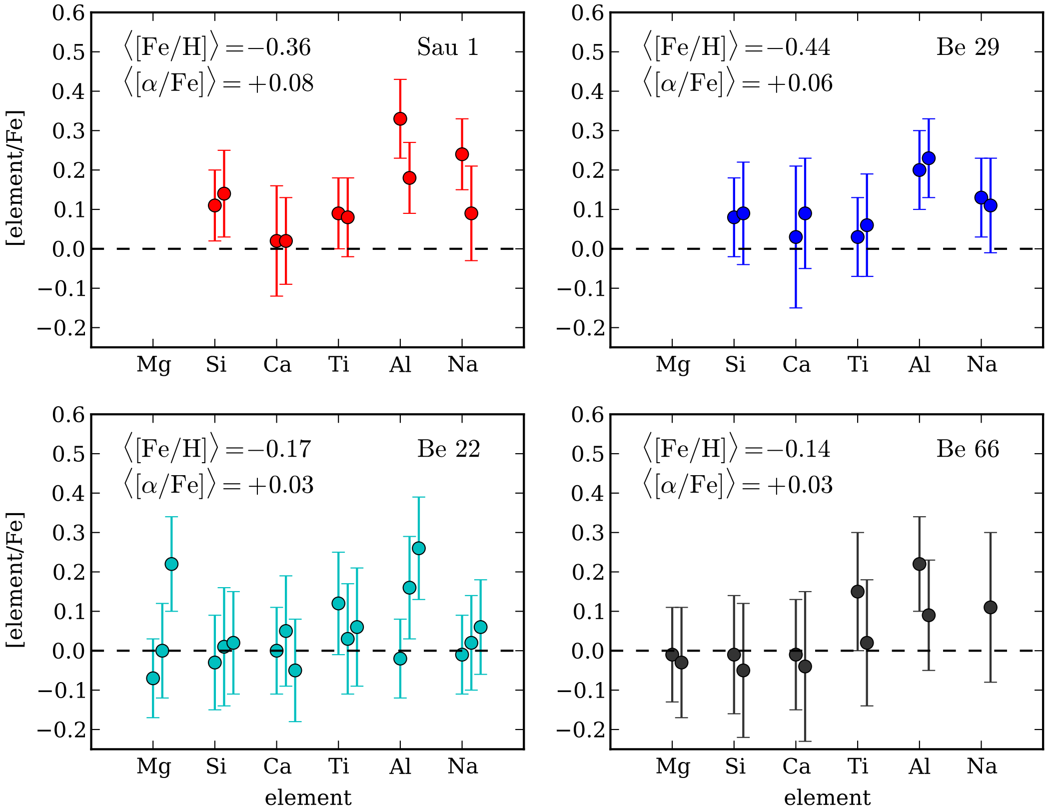

Figure 7.3: Abundance ratios of various elements (with respect to iron) derived for the target stars in Sau 1, Be 29, Be 22 and Be 66.

Be 66

In this cluster we derived abundances for two stars (PJ785 and PJ934), obtaining [Fe/H]=-0.13±0.12 dex and [Fe/H]=-0.14±0.13 dex, respectively. These metallicities are not compatible with the result presented by V05, who derived abundances for PJ785 only and found [Fe/H]=-0.48 dex. They quote solar abundance ratios for all elements except [Ti/Fe]=+0.48, but our results indicate solar ratios for this element as well. The lower number of lines measured for PJ785 reflects the shorter spectral range covered by the available data (see Fig.7.1).

7.2 The metallicity gradient

7.2.1 The metallicity gradient traced by open clusters

The seven OCs studied in this Thesis span a wide range of galactocentric radii, from 6 to 20 kpc. Their positions in the Galactic disk are shown in Fig. 7.4, where they are colour-coded by iron abundance. Those objects were analysed in a homogeneous manner and qualitatively confirm that inner-disk OCs are more metal-rich than their outer-disk counterparts. They do not, however, constitute a large enough sample to draw strong quantitative conclusions on the evolution of metallicity with galactocentric radius.

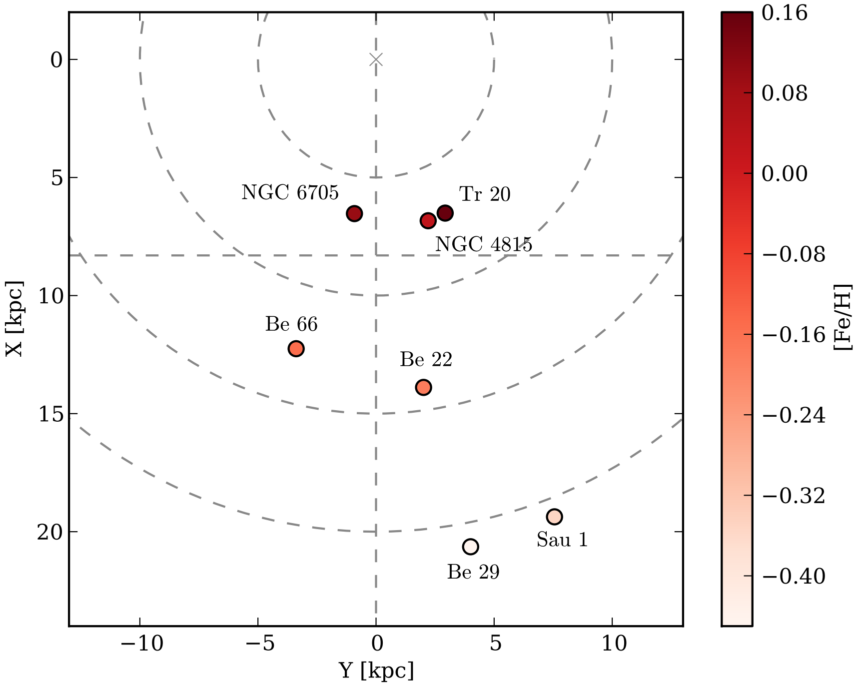

Figure 7.4: Position of the three inner disk and four outer disk OCs studied in this Thesis, colour-coded by iron abundance. The Sun is located at coordinates (X,Y)=(0,8.3). The dashed circles correspond to galactocentric distances of 5, 10, 15 and 20 kpc.

Using a small, homogeneous sample

The data presented in Fig. 7.5 has been compiled from various sources. Black (filled) symbols show the seven objects analysed in this Thesis. White dots show results obtained from a preliminary analysis of the latest data releases of the *Gaia*-ESO Survey (GES DR2-DR3). The final stellar parameters contained in the GES catalogue are a weighted median of the results delivered by different groups, performing the analysis with various methods. The procedure, detailed in Smiljanic et al. (2014), shows that our method faithfully reproduces the stellar parameters of metal-rich giant calibration stars. Figure 10 in Smiljanic et al. (2014) indicates that for red clump stars more metal-rich than [Fe/H]=-1 dex, our group (Epinarbo) obtains values close to the mean of all groups. Our results are therefore given a significant weight in the computation of the final stellar parameters for this stellar type. This makes us confident that the abundances derived in this Thesis can be reliably compared with those of the GES data releases.

Based on this larger sample of 17 objects (7 from this study, 10 from the newer GES data releases), we can attempt a quantitative analysis of the metallicity gradient. A simple model consisting in a bi-modal broken slope was fitted to the data by means of a weighted least squares procedure, taking into account the metallicity uncertainty. This broken-slope model enables us to estimate the gradient in the inner disk and the gradient in the outer disk (although it provides a very simplistic treatment of the transition between the two regimes).

The transition radius between the inner and outer gradient was left as a free parameter, but an additional condition was imposed that the metallicity must be continuous at the transition radius. The result of this fitting procedure is shown in Fig. 7.6. The slope of the inner gradient traced by this sample is $-0.078 \pm 0.025\,\mathrm{dex\,kpc^{-1}}$, which is slightly steeper than the values usually quoted in literature (see Sect. 1.3.1), but still consistent considering the uncertainty which arises from the relatively low number of clusters considered. The procedure also yields a transition radius of 10.6 kpc and a shallower negative gradient in the outer regions ($-0.01 \pm 0.04\,\mathrm{dex\,kpc^{-1}}$), but these values are affected by large uncertainties, as the sample only contains five objects in the outer disk and there is a strong degeneracy between the transition radius adopted and the computed slope in the outer region (see Fig. 7.6). The dispersion in metallicity for the four clusters in the galactocentric distance range 9–12 kpc is difficult to reproduce with a simple broken-slope model.

If we limit our study to the 12 OCs in the inner 12 kpc and fit a single line (Fig. 7.7), we obtain a steeper value of -0.14±0.01 $\mathrm{dex\,kpc^{-1}}$ for the gradient. Discarding the two metal-poor clusters in the 10–12 kpc range yields a similar gradient of -0.12±0.02 $\mathrm{dex\,kpc^{-1}}$. Our sample confirms that the metallicity gradient is steep in the inner disk, but we do not have

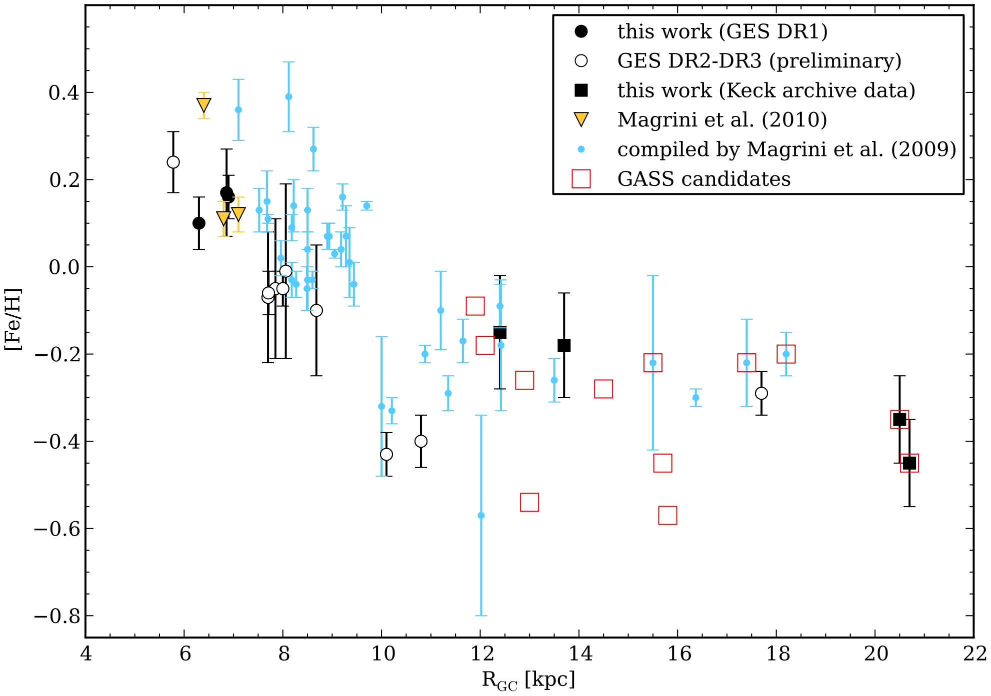

Figure 7.5: Metallicity against galactocentric radius for OCs studied by means of high-resolution spectroscopy. The filled symbols are the results derived in this work. The white dots are preliminary results based on the latest GES data releases. The red squares indicate the outer disk clusters listed in Table 7.5. Yellow triangles indicate the results of Magrini et al. (2010), blue dots the sample of Magrini et al. (2009a).

sufficient data to characterise its evolution at larger galactocentric distances.

Using a larger sample

Building a large, consistent sample of OCs is one of the aim of the *Gaia*-ESO Survey, and we are working to complement the sample with more data obtained with homogeneous methods. However, such a sample is still under construction, and to improve statistics we must resign (for now) to compile data from various sources. The blue dots of Fig. 7.5 are a sample of high-resolution spectroscopy metallicities collected by Magrini et al. (2009a) for 40 OCs. The yellow triangles are results obtained by Magrini et al. (2010) for three OCs. Using this wider sample, we find a slope of $-0.062 \pm 0.02\,\mathrm{dex\,kpc^{-1}}$ in the inner disk. Here

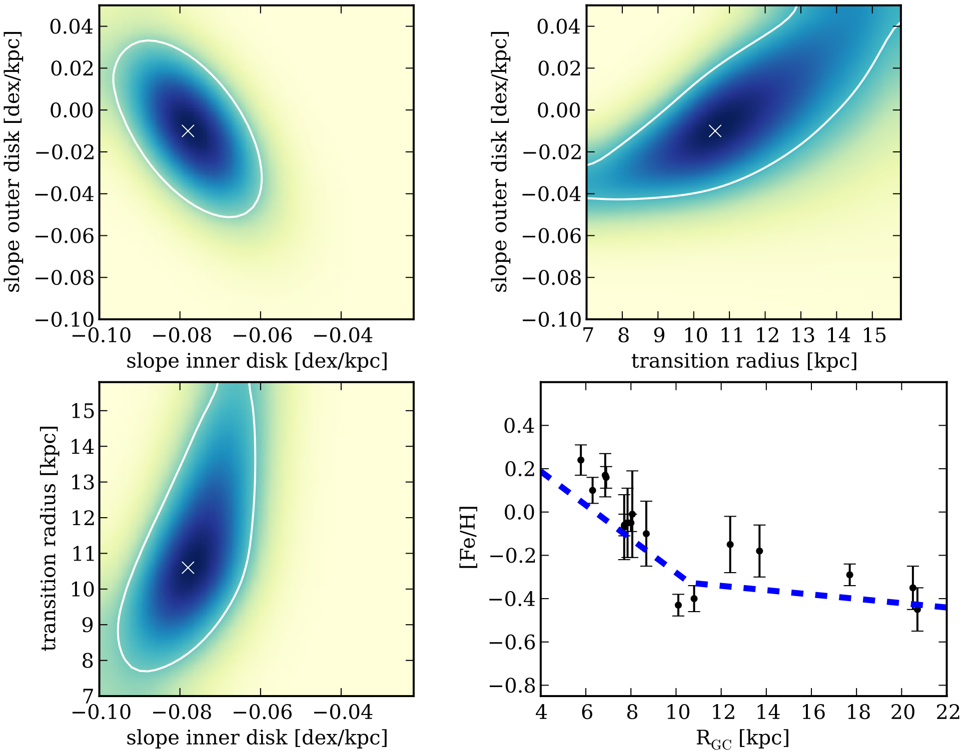

Figure 7.6: Probability maps for the fitting of a broken slope model. The white cross indicates the best-fitting parameters. The white contour indicates the region containing 68% of the probability (1-σ). The datapoints used are shown in the bottom right panel and are the results derived in this work and the preliminary GES DR2-DR3 results (also shown as black symbols and white symbols in Fig. 7.5).

again, the slope in the outer disk largely depends on the adopted transition radius, but the best-fit parameters correspond to an outer slope of $-0.015\,\mathrm{dex\,kpc^{-1}}$ and a transition radius of 11 kpc (see Fig. 7.8).

The inner gradient of $-0.062 \pm 0.02\,\mathrm{dex\,kpc^{-1}}$ we derive in the inner disk is shallower than the steep slope found by Sestito et al. (2008), who find gradients of -0.09 and -0.17 $\mathrm{dex\,kpc^{-1}}$ with metallicities obtained from low- and high-resolution spectroscopy (respectively). The decision to include in the inner disk the metal-poor clusters observed around transition radius certainly has the effect of steepening the computed gradient.

The model of Magrini et al. (2009a) yields a metallicity distribution transitioning from

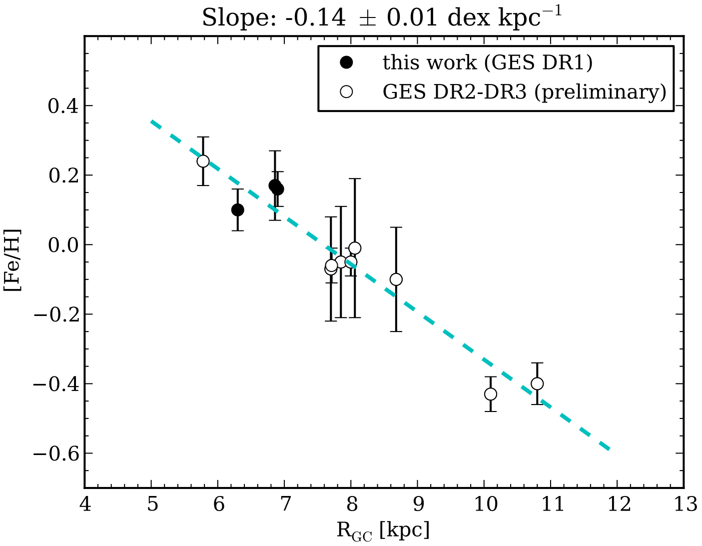

Figure 7.7: Gradient obtained by fitting a single straight line for OCs in the inner 12 kpc of the disk.

an inner gradient of -0.13 dex kpc^{-1} to an outer gradient of -0.02 dex kpc^{-1}, with a slope of -0.07 dex kpc^{-1} in the intermediate 7–12 kpc zone. These values are in good agreement with the observed inner gradient, but somehow too steep to account for the observation around transition radius.

These observations are incompatible with the model of Chiappini et al. (2001), which predicts a much shallower overall gradient shallower than -0.02 dex kpc^{-1} across the whole disk.

An apparent systematic offset can be seen between the metallicities determined in this study and the sample of Magrini et al. (2009a). The origin of this difference is not clear, as there are only four objects in common between both samples. For these clusters, the GES metallicities are on average 0.03 dex lower, and the mean difference between the GES and literature value is 0.06 dex. Not all literature sources quote the solar reference values they adopted to compute the final metallicity. The fitting procedure is helped by better statistics, but the results remain uncertain because of the inhomogeneous nature of the sample.

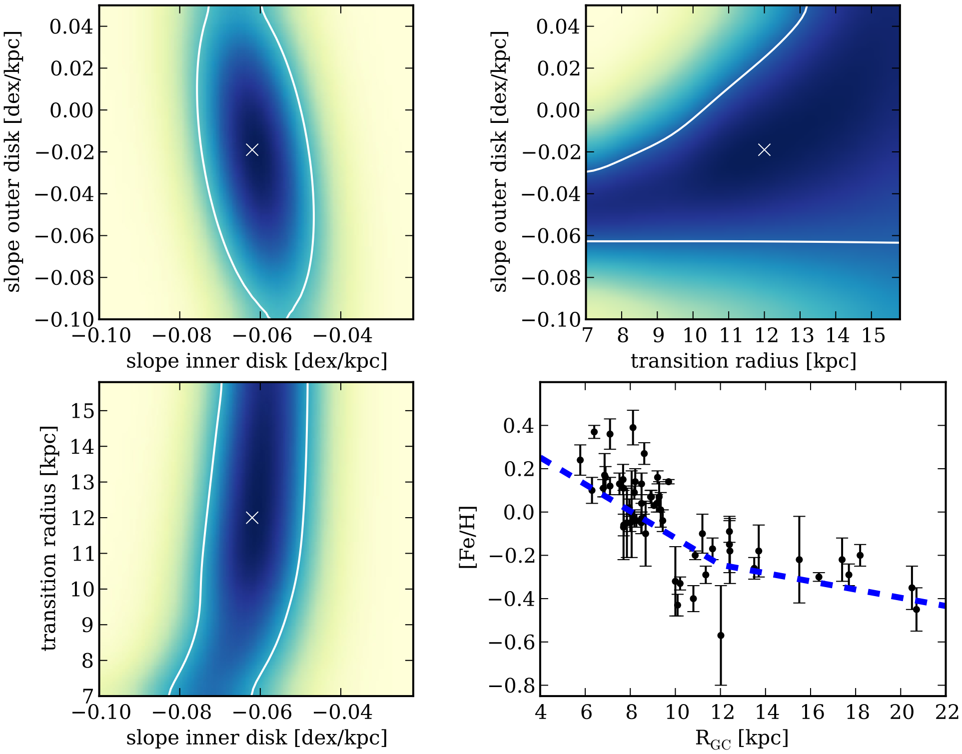

Figure 7.8: Same as Fig.7.6, with a larger dataset: the clusters considered include the sample of Magrini et al. (2009a), Magrini et al. (2010), the results derived in this study, and the preliminary GES DR2-DR3 results (i.e. all but the red squared symbols of Fig. 7.5).

Discontinuity in the metallicity distribution?

The difficulty of fitting a broken slope model through the data is mainly due to the large dispersion in metallicities in the galactocentric distance range 8–12 kpc. Upcoming GES data will help addressing the issue of whether is dispersion is due to uncertain metallicity estimates or if clusters of various metallicities truly coexist at those galactocentric radii.

A better fit can be obtained by relaxing the continuity condition and allowing a discontinuity in metallicity at transition radius (Fig. 7.9). The best-fitting parameters in this case yield an inner gradient of $-0.05 \pm 0.015\,\mathrm{dex\,kpc^{-1}}$ and a flat outer gradient. The relatively low number of objects in our sample in the galactocentric range 8–12 kpc makes it difficult to reliably estimate the position of the transition radius, although the best-fitting value places it 10 kpc from the Galactic centre.

The jump in metallicity at transition radius is rather unrealistic, but arguably the sharp change in gradient featured in the continuous broken slope model is just as unrealistic, since those models are made to quantify the slopes in the inner and outer regions of the disk rather than modelling the transition itself. The low number of objects observed in the region of transition makes is difficult to determine if the metallicity is smoothly decreasing, or more similar to a step-like function.

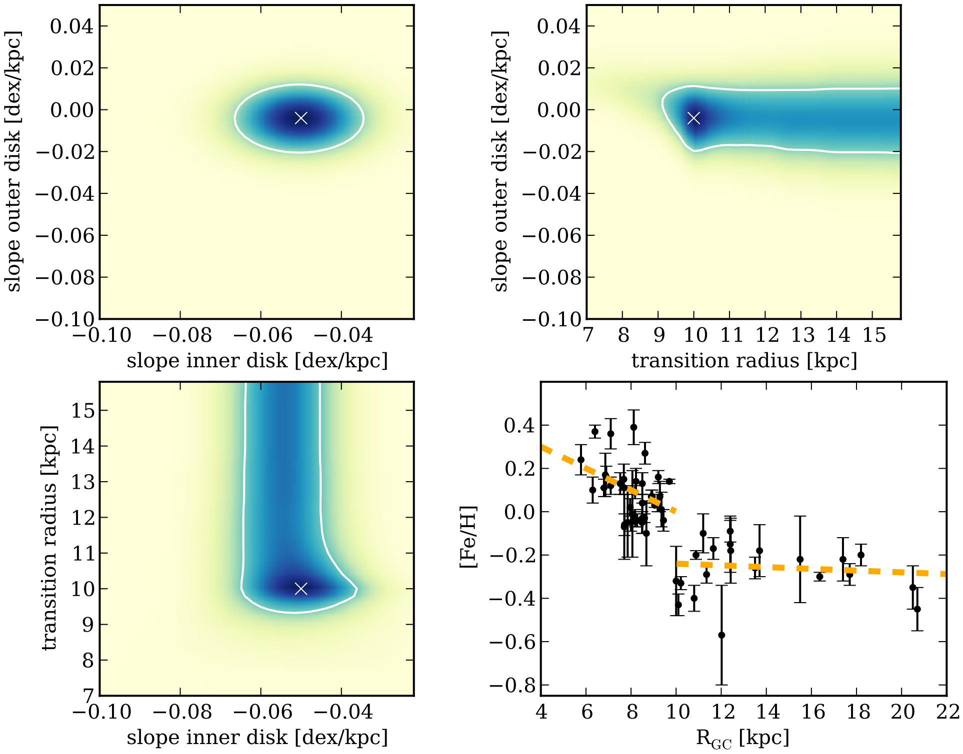

Figure 7.9: Same as Fig.7.8, and using the same dataset, but fitting a discontinuous two-slope model.

7.2.2 Modelling the metallicity gradient

The observed shape of the gradient

The main property of the metallicity distribution in the Galactic disk is that the inner disk is more metal-rich than the outskirts. This simple observational fact can be explained by multiple scenarios. Is the inner disk richer in heavy elements because *i)* it has been existing for a longer time (supporting an "inside-out" formation of the disk), or *ii)* because its star formation rates are higher (and hence it produces heavy elements at a higher rate)?

Hypothesis *i)* (inside-out Galaxy formation) is the scenario supported by Matteucci & Francois (1989) or Chiappini et al. (1997), in which the inner disk accretes more gas in the early phases of Galaxy formation and therefore forms more stars. This scenario can be validated if we could prove that the outer disk is younger. Observationally, an age difference between the inner and outer disk can be difficult to quantify, because in this scenario we expect to find old objects in the outer disk that were not formed there but moved there from the inner disk (and older objects are more likely to be found far away from their birth place due to random motions in the Galaxy). Orbit reconstruction (if proper motions and radial velocities are available) and chemical tagging (Magrini et al., 2014) can help us determine the birth radius of a cluster if it lays on an elliptical orbit (although Blanco-Cuaresma et al., 2014a, point out the difficulty of identifying stars solely by their abundance patterns).

Hypothesis *ii)* is supported by the model of Schönrich & Binney (2009), who considered the consequences of radial gas flows and stellar migration in an analytical model. Migration within galactic disks is an important dynamical process to account for. During its life, a star orbiting the Galaxy may be set on an eccentric orbit by two-body encounters with other stars. This causes "heating" of the disk and a blurring of the observed metallicity gradient, as objects may be observed at a galactocentric radius different from where they were born.

In addition to heating, Sellwood & Binney (2002) have shown that transient spiral patterns generate another phenomenon, "churning": stars may migrate to the inner or outer disk while staying on circular orbits (effectively changing the guiding-centre radius of their orbits). This has important observational consequences, as stars born in situ are kinematically indistinguishable from stars that have been churned from another region of the disk. Roškar et al. (2008) have shown that gas is also affected by churning and must be taken into account when building chemo-dynamical models of the Galaxy.

Stanghellini & Haywood (2010) remark that the current metallicity distribution can alternatively be explained as the superposition of two gradients: a shallow gradient due to old clusters (dominant in the outer disk) and a steeper one due to young clusters (and dominant in the inner disk), thus supporting an outside-in formation model.

The fact that the metallicity diminishes faster with galactocentric radius in the inner regions that in the outer regions of the disk is an important observable that a realistic model must reproduce, using an adequate time and space dependence for the star formation right, gas infall etc. Given the relatively low number of available OCs, most studies settle for the simple approach presented here in Sect. 7.2.1 and, at best, quantify the slope of the gradient in those two regimes. Heiter et al. (2014) point out that since many parameters can affect the metallicity distribution, models relying on very different assumptions can predict similar slopes. For instance, they show that the models of Larson (1972) (extreme inflow model) and Pagel (2009) (simple, instantaneous recycling) lead to a very similar gradient.

Gathering more data around the transition radius can reveal the true shape of the gradient in this region. It will also reveal if the region is populated with objects presenting a larger dispersion in metallicity, and possibly enable us to determine if this rapid change in the gradient is due to dynamical effects linked to the corotation radius of the spiral pattern (see e.g. Amôres et al., 2009), or, for instance, to a change in density between two superposed populations (as suggested by Stanghellini & Haywood, 2010). Such an apparent discontinuity/superposition was observed in the galaxy M83 by Bresolin et al. (2009) (see their Figure 9). The structure present in our own Galaxy and the mechanisms that shape it are currently not well-understood.

Time evolution of the gradient

We can gain insight on the disk formation process by trying to reproduce not only the present-day metallicity gradient, but also its time evolution. On the observational ground, this requires a sample of object with sufficiently precise age determinations. Despite efforts to trace the time evolution of the metallicity distribution from open clusters, some studies suggest older OCs trace a steeper gradient (Friel et al., 2002; Frinchaboy et al., 2013; Jacobson et al., 2011; Magrini et al., 2009a), while some authors quote opposite results (Salaris et al., 2004), and others observe no significant differences (Yong et al., 2012).

The gradient may become steeper if, during Galaxy evolution, the gas accretion rate is higher in the outer parts of the disk. If the accretion is efficient enough to dilute the gas stocks (resulting in a more metal-poor blend) but sufficiently smooth to not increase star-formation, then it is expected that the metallicity increases more slowly in the outer disk (Tosi, 2000) and therefore that older clusters trace a shallower gradient.

Because of radial migration, the gradient traced by old objects does not necessarily reflect the old gradient. The chemo-dynamical models of Minchev et al. (2013) show that even if the gradient was steep in the past, old objects observed today would trace a shallow gradient. Migration does not only wash out gradients, but also introduces a dispersion in metallicity for objects of the same age and same present-day galactocentric radius.

Our current sample does not allow us to tackle the issue of the time evolution of the gradient, simply because of the low number of objects studied to this date. Complemented with age determinations from photometric studies, the *Gaia*-ESO survey will provide a large, homogeneous dataset on which to base future Galactic evolution studies.

7.3 The Galactic anticentre structure

The structure of our Galaxy is usually described in terms of its major components: thin and thick disk, bulge, and spheroidal halo. There is however evidence that not all stars found in deep photometric surveys belong to one of these components, as the outskirts of our Galaxy are not made of a smoothly distributed stellar population. Some regions have been found to present excess stellar densities (see e.g. Belokurov et al., 2006; Yanny et al., 2000) and moving groups with coherent velocities have been been identified in the halo of the Milky Way (Helmi et al., 1999; Majewski et al., 1996). One such example is the tidally stripped Sagittarius dwarf satellite galaxy (Ibata et al., 1994), whose tidal tails circle the Milky Way (see e.g. Belokurov et al., 2014; Johnston et al., 1995; Majewski et al., 2003, and references therein).

The Monoceros structure (also called *Monoceros ring*, or *GASS* for "Galactic anticentre stellar structure") was identified by Newberg et al. (2002) as an overdensity of blue stars in the direction of the Galactic anti-centre at a distance of $11 - 16$ kpc from the Sun, using SDSS data. Ibata et al. (2003) have confirmed the ring-like shape of this structure and show that it essentially lies in the plane of the Milky Way, extending from a galactocentric radius of 15 kpc to 20 kpc while spanning 100° across the sky ($122° < l < 225°$). They also estimate a scale height of 0.75 ± 0.04 kpc. Yanny et al. (2003) estimate a metallicity of [Fe/H]$=-1.6 \pm 0.3$ an propose that the structure is due to a tidally disrupted dwarf satellite of mass 2×10^7 to $2 \times 10^8\,\mathrm{M}_\odot$ forming a ring around the Galaxy. Crane et al. (2003), using a sample of 2MASS M giants, conclude to a higher metallicity of -0.4 ± 0.3, and remark that several GCs have positions and velocities that correlate with the Monoceros structure. They also remark that if the structure is due to a tidally stripped satellite, the core does not appear to be located in Monoceros, and the stream spans several constellations. Rocha-Pinto et al. (2003) argue that rather than a ring circling the Milky Way, this structure presents the morphology of a stream (see also Jurić et al., 2008).

The nature and origin of this structure has been debated. Helmi et al. (2003) explored the possibility that the overdensity is not a dwarf galaxy being disrupted, but a perturbation in the disk due to past minor mergers. Yong et al. (2005) found enhanced α abundances in outer disk OCs, hinting at a recent phase of star formation. They argue that a gas-rich merger could simultaneously explain the peculiar stellar distribution and chemistry observed in the GASS.

Ivezić et al. (2008) report that the Mon structure has kinematics more compatible with disk stars rather than halo stars, although it presents a slightly higher rotational velocity, and a median [Fe/H] of -0.95 with only a ~ 0.15 dex scatter. Momany et al. (2006) have argued that the Monoceros overdensity may be explained in terms of a both warped and flared disk, but (Jurić et al., 2008) show this structure is also well constrained in the radial direction, which is difficult to explain in terms of disk flaring.

Hammersley & López-Corredoira (2011) point out that overdensities are identified by comparing observed stellar counts with expectations from smooth galaxy models, but our current knowledge of the disk structure in the outer regions (in particular the disk cut-off radius) is not complete enough to rule out the possibility of an overdensity of Galactic origin. Lopez-Corredoira et al. (2012) review the latest publications on the matter and conclude that despite the exciting possibility that we are witnessing a dwarf galaxy being cannibalised by the Milky Way, alternative explanations still hold.

GASS clusters

Multiple outer disk clusters have been investigated in order to better understand the peculiar properties of the GASS. They are all old clusters (0.8 to 6 Gyr). Their properties are summarised in Table 7.5.

Following the suggestion of Crane et al. (2003), Frinchaboy et al. (2004) have investigated the positions and velocities of fifteen distant GCs and OCs (including Pal 1, Be 22, Be 29 and Sau 1), and have shown that twelve of them have compatible positions and velocities with the GASS. These clusters also present a tighter age-metallicity relation than the general population of Milky Way clusters, indicating a possible common origin, different from that of the rest of Milky Way clusters. Their results, however, rely on a sample containing both OCs and GCs, do not make use of high-resolution spectroscopy, and is potentially affected by the biases expected when compiling data from inhomogeneous sources.

The results of C04 suggest that Sau 1 and Be 29 feature supersolar α abundances, and are therefore associated with the Monoceros structure. Our results (see Table 7.4 and Fig. 7.3) indicate that these clusters are not significantly α-enhanced. We do however confirm they are more metal-poor than the rest of the outer-disk clusters. Since they are sitting at the extreme edge of the disk, with galactocentric radii larger than 20 kpc, their metallicities are compatible with a shallow negative gradient of -0.02 dex kpc^{-1} in the 10–20 kpc distance range from the galactic centre. However, if it could be proven that the outer

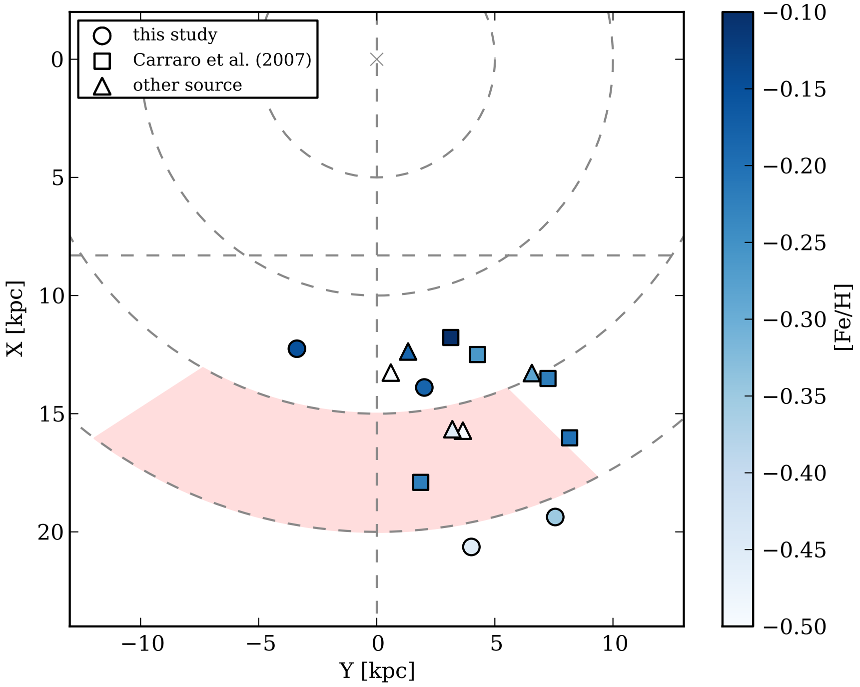

Figure 7.10: Positions of 14 potential GASS clusters, colour-coded by iron abundance. Dots indicate the four OCs for which we derive iron abundances in this Chapter. Squared symbols are the sample of Carraro et al. (2007) (see Table 7.5). The shaded region corresponds to the possible extension of the Monoceros structure.

gradient is shallower than this value (or even flat), the metallicity of these two OCs would appear discrepant. We find no strong hint that any of these clusters is not regular member of the disk population. Other outer disk OCs exhibit low metallicities. Be 20, Be 21 and Be 31, situated between 13 and 16 kpc from the galactic centre, have metallicities of -0.45, -0.53 and -0.57, respectively (see Table 7.5), but so far no open cluster has been observed to be metal-poor enough to meet the Monoceros metallicities quoted in the literature (e.g. Ivezić et al., 2008; Yanny et al., 2003).

Some studies have focussed on the distance of OCs from the galactic plane. Cignoni et al. (2011) estimate that Be 31 lies at Z=700 pc above the plane and suggest it could be a thick disk OC, along with Be 23 (Z=500 pc), and stress that the Galactic position of clusters must be coupled with chemical tagging from high-resolution spectroscopy in order to better characterise them. In that sense, with positions between 1 and 2 kpc above the

Table 7.5: Summary of parameters for a sample of outer disk clusters with high-resolution spectroscopy metallicity determinations.

OC	RA	DEC	RA	DEC	l	b	d$_\odot$	R$_{GC}$	[Fe/H]	age	Ref.
	(J2000)	(J2000)	(hms)	(hms)			[kpc]	[kpc]		[Gyr]	
Sau 1	109.575	1.887	7 18 18	1 53 12	214.317	6.836	13.5	20.5	-0.35	5	C04*
Be 29	103.325	16.917	6 53 18	16 55 00	197.984	8.025	13.1	20.7	-0.45	4.5	C04*
Be 22	89.600	7.833	5 58 24	7 50 00	199.803	-8.052	6.0	13.7	-0.18	3.3	V05*
Be 66	46.075	58.767	3 04 18	58 46 00	139.434	0.218	5.2	12.4	-0.15	4.7	V05*
Be 25	100.317	-16.487	6 41 16	-16 29 12	226.612	-9.629	11.4	18.2	-0.20	5	C07
Be 73	95.500	21.002	6 22 00	21 00 06	190.963	3.267	9.8	17.4	-0.22	1.5	C07
Be 75	102.246	-23.992	6 48 59	-23 59 30	234.299	-11.193	9.1	15.5	-0.22	4	C07
Rup 7	104.467	-13.224	6 57 52	-13 13 25	225.449	-4.589	6.0	12.9	-0.26	0.8	C07
Rup 4	102.225	-10.533	6 48 54	-10 32 00	222.047	-5.339	4.7	11.9	-0.09	0.8	C07
Be 31	104.404	8.355	6 57 37	8 21 18	206.176	5.163	8.3	15.8	-0.57	2.6	Y05†
NGC2141	90.729	10.447	6 02 55	10 26 48	198.044	-5.811	4.3	12.1	-0.18	1.7	Y05†
Be 20	83.250	0.217	5 33 00	0 13 00	203.505	-17.275	8.4	15.7	-0.45	6	Y05†
Tom 2	105.771	-20.817	7 03 05	-20 49 00	232.832	-6.880	8.3	14.5	-0.28	2	F08
Be 21	87.925	21.783	5 51 42	21 47 00	186.840	-2.509	5.0	13.0	-0.53	2.2	Y12†

Notes. References: C04 (Carraro et al., 2004), V05 (Villanova et al., 2005), C07 (Carraro et al., 2007), Y05 (Yong et al., 2005), F08 (Frinchaboy et al., 2008), Y12 (Yong et al., 2012). The locations of these clusters are shown in Fig. 7.10 and Fig. 7.5.

* [Fe/H] values are those derived in this study.

† ages taken from WEBDA.

galactic plane, Sau 1 and Be 29 are clear outliers.

It is also striking that most known outer disk OCs are old systems (see Fig. 1.2 and ages in Table 7.5). If the GASS is a perturbation of the disk density due to minor mergers (Helmi et al., 2003), then the age of the youngest GASS clusters would set an upper limit to the time that separates us from the last merger event.

These tentative results highlight once more the need for a homogeneous study of a large number of objects, in order to rule out if the clusters that are observed to be discrepant truly are representants of a distinct structure. Our current sample does not require components beyond a classical disk to explain the observed chemical distribution.

CHAPTER 8

SUMMARY AND CONCLUSION

Open clusters are ideal tracers of the properties of the Galactic disk, as well as convenient laboratories to study the star formation process in the Galaxy. Studies of OCs available in the literature often concern a limited number of objects, and few large datasets obtained with homogeneous methods exist. In particular, metallicity estimates quoted in the literature are obtained by a variety of methods and no not allow to draw a reliable picture of the metallicity distribution in the disk. The work presented in this thesis aims at building a sample of OCs for which ages, distances and metallicities are obtained in a homogeneous manner.

A significant part of my work took place within the *Gaia*-ESO Survey (Ch. 2). The GES spectroscopic campaing is ongoing, and has already delivered high-quality data for stars in all major components of the Milky Way, as well as 13 intermediate-age and old OCs. Analysing the large amount of data acquired in the GES is a challenge of its own. I have developed the code DOOp (Cantat-Gaudin et al., 2014a) (described in Sect.3.1) which works as an automated wrapper for the code DAOSPEC (Stetson & Pancino, 2008) in order to robustly measure and control equivalent widths in batches of hundreds or thousands of spectra, a task that would be impossible to accomplish by hand. I have been involved in the development of the code FAMA (Magrini et al., 2013) (described in Sect.3.2) which automatically determines stellar parameters and elemental abundances from measured equivalent widths. The GES collaboration involves different groups applying different methods to the same data, and the results are subsequently homogeneised (Smiljanic et al., 2014). This variety of methods offered the possibility to establish a common metallicity scale, a project in which I applied our methods to a set of benchmark stars (Jofré et al., 2014) (see Sect.3.3).

The first GES internal data release contained data for three intermediate-age OCs (NGC 6705, Trumpler 20 and NGC 4815) which happen to be all three inner-disk clusters. The high-resolution UVES spectra collected for those objects allow for membership selection, and the determination of accurate elemental abundances. A current topic of debate is the fundamental difference between GCs and OCs (see Ch. 5.1). Multiple, chemically distinct populations are routinely observed in GCs, but never in OCs. The main driver of this difference may be the inferior mass of OCs, but this idea needs to be verified on a large sample. Despite their high masses (NGC 6705 and Tr 20 are among the most massive known clusters with masses of several thousand $M_{\odot}$), all three clusters are seen to be chemically homogeneous within our uncertainties, and have mean iron abundances $[Fe/H]=0.10 \pm 0.06$ dex, 0.17 ± 0.10 dex, and 0.16 ± 0.05 dex (respectively).

In addition to the dozens of high-resolution spectra obtained with UVES, the GIRAFFE instrument collects medium-resolution data for hundreds of stars all across the CMD of clusters. The radial velocities derived from these spectra allow for a better definition of the membership probability and help improve the comparison of the cluster CMD with theoretical isochrones, in order to estimate the age, distance and interstellar extinction (Ch. 4). The age of NGC 6705 is estimated between 250 and 320 Myr, for a distance of 1995 ± 180 pc. Its mass can be estimated between 3600 and 7000 $M_{\odot}$, but this number is likely to be a lower estimate. NGC 6705 shows strong signs of mass segregation, with low-mass stars distributed as a faint halo in the outskirts of the cluster, and the outer parts are affected by patchy interstellar reddening making it difficult to estimate the total stellar content. Trumpler 20 is older, with an age of 1.25 to 1.66 Gyr depending on the adopted set of theoretical isochrones. This cluster exhibits no sign of mass segregation, and we estimate its mass between 5500 and 8000 $M_{\odot}$. The complete photometric and spectroscopic studies of NGC 6705, Trumpler 20 and NGC 4815 were published in Cantat-Gaudin et al. (2014b), Donati et al. (2014), and Friel et al. (2014), respectively.

The first internal GES data release contains data for the young cluster Gamma Velorum ($\sim$10 Myr), in which Jeffries et al. (2014) have identified two dynamically distinct populations (named A and B). Young clusters can be used to trace the star formation process, because they retain some properties of the giant molecular clouds they originate from (see Ch. 6). Performing dynamical simulations (Mapelli et al., in prep.) and applying satistical tools, we establish that population B is unbound, and less dense than A. It is however not possible to accurately characterise the difference in morphology between the two sub-clusters, as the region covered by GES data only includes the central parts of the system, and B in particular is probably much more extended. Two scenarios can be considered: i) a scenario corresponding to a competitive accretion model, in which A and B formed as dense clusters, and B is being disrupted because of internal dynamical processes, or ii) a case of hierarchical formation, where the stars of A formed as a dense system which will remain bound while the stars of B formed as a less dense system and quickly join the field population. The available data does not allow us to determine which formation mechanism is at work in Gamma Velorum. The *Gaia* mission will deliver parallaxes and proper motions which will help determining cluster membership on a larger scale and establish the physical link between subclusters A and B, shedding light on the star formation process.

To complement the sample of OCs, I have applied the methods developed for the GES to archival high-resolution spectra (from the Keck HIRES spectrograph) of four outer disk clusters: Be 22, Be 29, Be 66 and Sau 1 (Sect. 7.1). Since they lie in the outer parts of the disk (with galactocentric radii larger than 20 kpc for Sau 1 and Be 29) in the third galactic quadrant, those clusters could be associated with the peculiar ring-like overdensity called galactic anticentre structure (GASS). We study abundance ratios for those clusters, and find no significant α-enhancement, which means there is no strong sign that they are associated with the GASS rather than the thin disk (Sect. 7.3).

In total, using GES data from the first internal data release (three clusters), Keck archival data (four clusters) and preliminary results from the second and third GES data releases (ten clusters), I built a sample of 17 OCs with homogeneously derived metallicities (Sect. 7.2). The metallicity gradient traced by this dataset confirms that the gradient in the inner disk is steeper than in the outer disk. The relatively low number of objects does not allow us to precisely estimate the galactocentric radius of the transition between the inner and outer gradient. Complementing the sample with data from other sources helps improve the statistics, at the price of losing homogeneity. Our current sample does not allow to accurately follow the shape of the gradient, in particular around transition radius where few objects are observed. An important study that must be conducted once the sample is larger is to establish the shape and slope of the gradient traced by clusters in different age groups, in order to reconstruct the time evolution of the metallicity distribution across the Galactic disk. The upcoming GES data, and non-GES data analysed with the same methods, will fill the distance-age-metallicity parameter space and help unravel the evolutionary history of the Milky Way.

Large telescopes such as the VLT and multi-object fibre spectrographs such as FLAMES now allow us to collect large amounts of spectra in a reasonable time. The next technological achievement expected to revolutionise our understanding of the Milky Way is the *Gaia* space mission. In addition to providing accurate parallaxes for a billion stars, *Gaia* will measure proper motions which can be used not only for membership determination but also for orbit reconstruction, allowing us to treat clusters not as systems pinned to a fixed galactocentric radius, but as objects migrating through the disk. This approach, along with the progress in chemical tagging, is fundamental for comparisons of the observed Milky Way with chemodynamical models in which dynamical effects play a major role in shaping the metallicity distribution. The combination of the unprecedented astrometric capabilities of *Gaia* with high-quality ground-based spectroscopy is a key to our understanding of the structure and history of the Milky Way.

APPENDIX A

EQUIVALENT WIDTHS AND CURVE OF GROWTH

The absorption features observed in stellar spectra can vary in width, depth and profile shape. A way to associate a single measurement to an absorption feature is to consider its **equivalent width**: the wavelength interval that would be covered by a pefectly opaque absorption feature that removes the same amount of energy from the continuum flux.

In an observed spectrum, the line profile is the convolution of the intrinsic profile of a line with the instrumental profile. At the resolutions that are usually used for EW analyses ($R \sim$15 000 to $R \sim$50 000), the instrumental profile typically dominates and most all lines will exhibit a gaussian profile of the same width. The EW of a spectral line is, however, independent of the instrument, since spectrometers of higher resolving power[1] will produce thinner and deeper lines but the total absorption over the line will be identical, as illustrated in Fig. A.1.

Absorption lines reveal the presence of atoms and ions in a stellar photosphere. Line growth (how the EW of a line relates with the abundance of absorbers) presents three phases. In an optically thin material, doubling the number of absorbers doubles the absorption, and hence double the equivalent width of the corresponding line. This is the regime of **linear** growth: there is a linear relation between the number of absorbers N and

---

[1] The resolving power of an instrument, or resolution of a spectrum, is defined as $R=\frac{\lambda}{\Delta\lambda}$, the smallest difference in wavelength that can be distinguished at a wavelength λ. In most cases it corresponds to the FWHM of the instrumental profile.

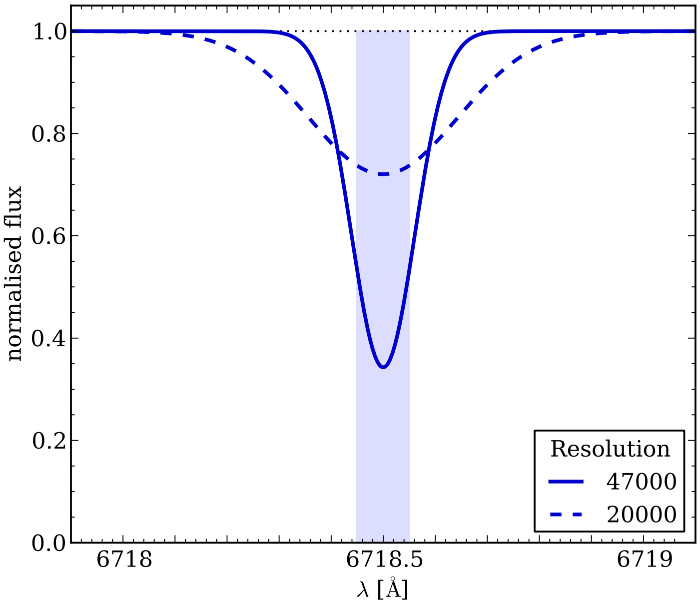

Figure A.1: Observed line profile for a (fictitious) line with EW=100 mÅ, through an instrument of resolution R=47 000 (full line) and R=20 000 (dashed line). The total absorption in both cases is equal to the area of the shaded rectangular section (of width 100 mÅ).

the EW (EW$\propto N$). When a line is strong and its core becomes optically thick, increasing the number of absorber no longer increases the EW linearly because the core is already opaque. This corresponds to the **saturation** regime (EW$\propto \sqrt{\ln N}$). If even more absorbers are added, the wings of the line profile start playing a larger role in the absorption and the EW increases as the square root of the number of absorbers (EW$\propto \sqrt{N}$). Figure A.2 shows the evolution of a line profile through these three different regimes. Note that in a real stellar spectrum the flux at the centre of a line never reaches zero, because the surface of the photosphere is not at a temperature of 0 K.

A representation of the variation of the EW of a line against the abundance of absorbers (for a given model photosphere) is called a **curve of growth**. Figure A.3 shows the curve of growth of a chosen Fe line, obtained by computing elemental abundance with Moog using MARCS model atmospheres. A more complete description of the curve of growth is given in Gray (1992), Ch. 13 and Ch. 14.

In practice, the observed line profile for weak lines (in the linear part of the curve of growth) and mildly saturated lines will be seen as gaussian because of the instrumental

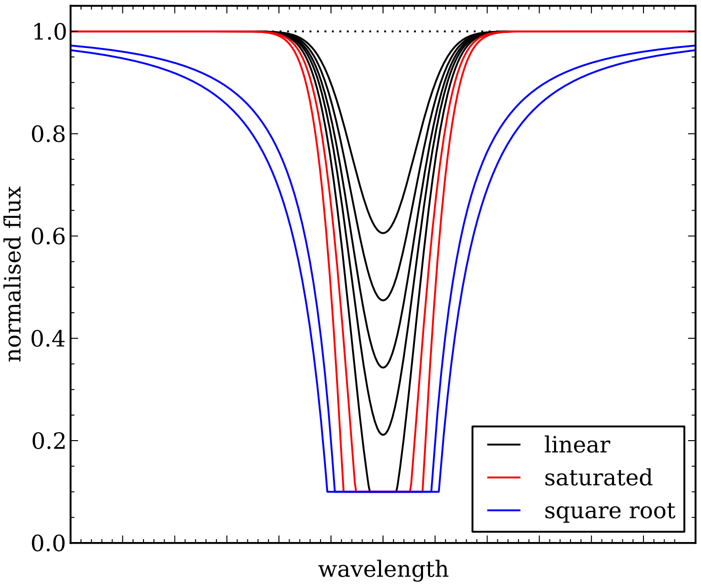

Figure A.2: Sketch of the evolution of the line profile for an increasing abundance of absorbers, showing three different growth regimes.

response of the spectrometer. Measuring reliable EWs for strongly saturated lines is usually more difficult. Those wide lines may also be blended with other lines, making the accurate determination of their intrinsic EW more difficult. Most studies adopt an upper limit and only consider, for instance, lines with EW<140 mÅ.

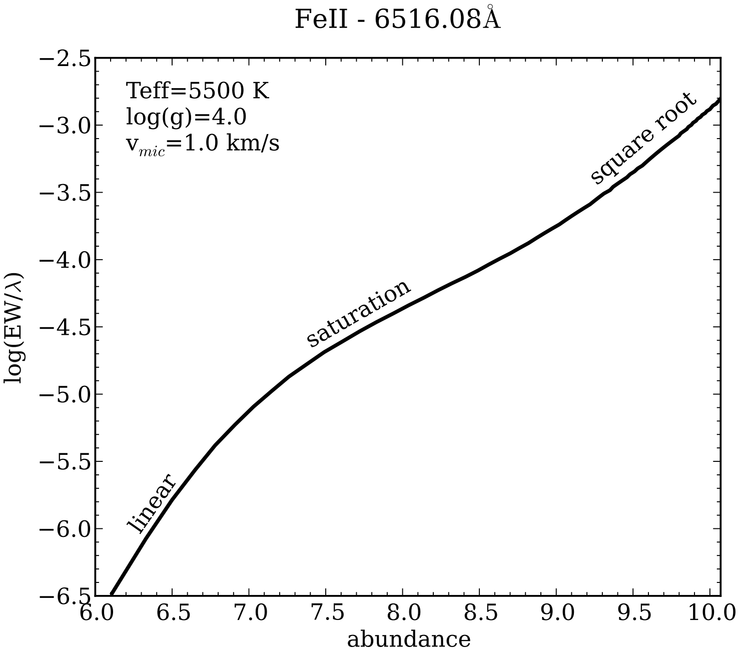

Figure A.3: Curve of growth for a typical Fe line. The three regimes of EW growth against abundance of absorbers are visible.

APPENDIX B

DETERMINING STELLAR PARAMETERS FROM EQUIVALENT WIDTHS

Deriving stellar parameters (effective temperature, surface gravity etc) from an observed stellar spectrum is not a straightforward task. To infer stellar parameters, we rely on **model atmospheres**, which are numerical models describing the physical state of the plasma in the outer layers of a star[1]. Applying the equations of radiative transfer to a model atmosphere[2], it is possible to derive observable quantities, and in particular it is possible to derive the full light spectrum emitted by the photosphere of the modelled star. In addition to the continuum emission, a certain number of **absorption lines** are visible in stellar spectra, revealing the presence of various chemical elements in their photosphere. The presence and depth of each line depends in a complex way on the abundance of the corresponding element, but also on the effective temperature (T_{eff}), on the surface gravity ($\log\ g$), on the microturbulence (v_{mic}) and possibly on other quantities parametrised in the model. If all these parameters are known, a model can predict the equivalent width

---

[1] Popular model atmospheres for F-G-K stars include MARCS (Gustafsson et al., 1975, 2008, 2003; Plez et al., 1992) and ATLAS (Kurucz, 1970, 1993, 2005) (see Bonifacio et al., 2012, for a review of those two sets of models) or MAFAGS-ODF (Grupp, 2004a,b).

[2] Codes applying radiative transfer equations to model atmospheres include Moog (Sneden, 1973; Sneden et al., 2012), SYNTH (Piskunov, 1992), SPECTRUM (Gray & Corbally, 1994), TURBOSPECTRUM (Plez, 2012) or SYNTHE (Kurucz & Avrett, 1981).

of a given absorption line, or produce a synethetic spectrum. A possible approach to stellar parameter determination is to fit a synthetic spectrum to an observed one (see e.g. Bonifacio & Caffau, 2003; Valenti & Piskunov, 1996).

Another way of solving the same equations is to assume a physical state ($\mathrm{T_{eff}}$, log g, v_{mic}) for the photosphere, measure the equivalent width (EW) of a given line, and work out the elemental abundance required to produce the observed EW in that given model. This is the approach we will describe here.

If the assumed model atmosphere is a faithful representation of the observed star, the abundance of an element can in theory be obtained by using any absorption line of this element, and working out the abundance from several lines of the same element should provide the same abundance (within measurement errors). If the lines of a given element do not all lead to agreeing abundance, the assumed model atmosphere is incorrect and a different set of stellar parameters must be used. Trying out thousands of possible sets of parameters in order to find which one provides the best agreement would be a very inefficient approach. Fortunately, it is possible to determine which parameters are incorrect and more importantly **how to adjust them** in order to recover stellar parameters from a list of measured equivalent widths. This Appendix presents the principles of the so-called **excitation/ionisation method**, illustrated with a determination of the stellar parameters of the Sun with a handful of measured iron absorption lines (chosen for the sake of the example).

Adjusting $\mathrm{T_{eff}}$

A code such as Moog solves the equations of radiative transfer for each individual line, and determines the elemental abundance necessary to produce this line and its observed EW (given the model atmosphere assumed by the user). There is no simple analytical expression linking the model parameters, the spectroscopic parameters of a given line, its EW and the elemental abundance. However, under some reasonable approximations, we can describe the behaviour of spectral lines (and hence the inferred abundance for a given EW) when the main stellar parameters vary (see Gray, 1992, in particular Ch. 13 and Ch. 14).

In a hot plasma, not all the atoms are in the same energy state. This means that not all atoms are available to absorb or emit some precise wavelengths. Under the assumption of local thermodynamic equilibrium (LTE), Boltzmann statistics tells us that the population in a given excited state i (with respect to a ground state) depends on the excitation potential EP_i of this state and the effective temperature $\mathrm{T_{eff}}$ through the relation:

$$\log n(\mathrm{FeI})_i \propto e^{-EP_i/k\mathrm{T}_{\mathrm{eff}}} \tag{B.1}$$

where k is the Boltzmann constant. This relation tells us that a wrong choice of $\mathrm{T}_{\mathrm{eff}}$ will bias our abundance determination (too high a $\mathrm{T}_{\mathrm{eff}}$ leads to an underestimate of the abundance), and that lines with lower EP will be more sensitive to $\mathrm{T}_{\mathrm{eff}}$ variations. Using several lines of different excitation potentials, we can exploit this dependence on $\mathrm{T}_{\mathrm{eff}}$ and find the effective temperature which makes all lines yield the same abundance.

We can illustrate this process with three FeI lines measured in a solar spectrum. The true effective temperature of the Sun is 5777 K, and its true iron abundance is [Fe/H]=7.45[3]. The left panel of Fig. B.1 shows the abundance obtained with Moog using MARCS model atmospheres for each of these three lines, at various temperatures. Around the true value of 5777 K, all three yield the same value of 7.45. If the abundance determination is performed with a too high (respectively too low) temperature, the abundances will be underestimated (respectively overestimated). The right panel of Fig. B.1 shows the abundance against excitation potential, obtained for six different choices of $\mathrm{T}_{\mathrm{eff}}$. When a negative trend is seen, the effective temperature of the model needs to be decreased, while a positive trend means $\mathrm{T}_{\mathrm{eff}}$ needs to be increased.

---

[3] In this notation, the abundance of an element is the logarithmic number density with respect to H: [X/H]=$\log n(X) = \log(n_X/n_H) + 12$

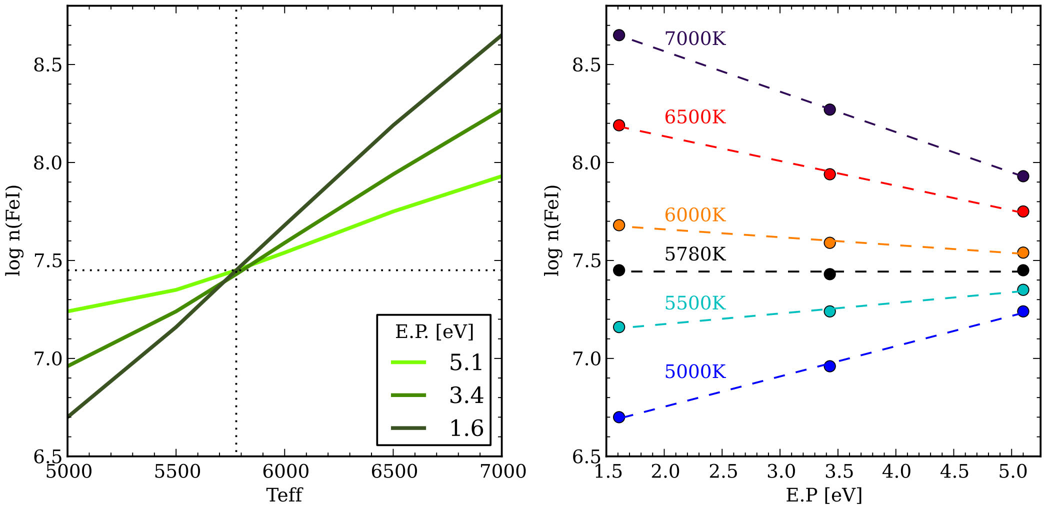

Figure B.1: *Left:* abundance obtained against effective temperature of the adopted model, for three different FeI lines. *Right:* abundance against excitation potential, for six different temperatures. The dashed lines are linear fits through the three data points.

Adjusting log g

Neutral elements are not the only absorbers present in stellar photospheres. A certain number of absorption lines are due to ionised species. Since ions are charged particles they behave differently from neutral atoms and are more sensitive to variations of pressure (or surface gravity). The abundance of FeII ions follows the approximation of Boltzmann-Saha:

$$\log n(\text{FeII}) \propto \log g^{n/3} \tag{B.2}$$

where $n = 1$ in the limit case in which Fe is fully ionised, and $n = 2$ if it is only neutral. FeI abundances are much less sensitive to surface gravity. Therefore, if the determined FeII abundances are inferior to the FeI abundances, the surface gravity of the model is too low with respect to the true value. A correct value of log g is one that produces equal abundances for ions and neutral species. Figure B.2 shows the abundances obtained with models of various log g for three FeI and three FeII lines, measured in the solar specrum. The values all agree when the adopted surface log g corresponds to the true value.

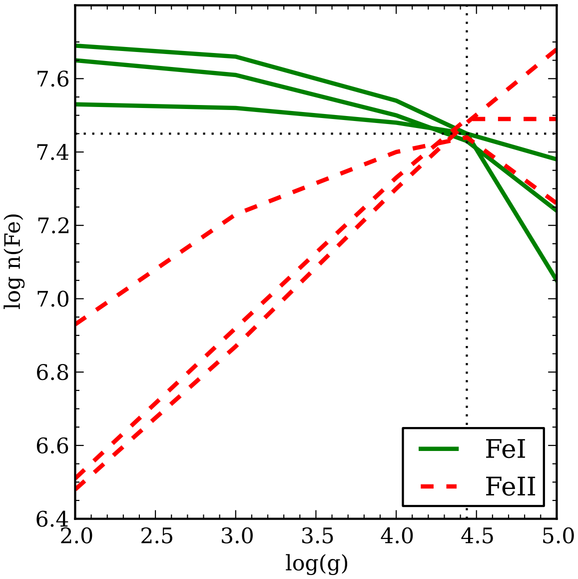

Figure B.2: Abundance derived against assumed surface gravity, for three measured FeI lines and three measured FeII lines.

Adjusting v_{mic}

The **microturbulent velocity** (v_{mic}) parameter of a stellar atmosphere was originally introduced to represent surface convection. An extra broadening of saturated lines is observed, due to small cells of motion in the photosphere. The Doppler shift caused by this turbulence makes it possible for more absorbers to contribute to the line profile, thus broadening the line and increasing the measured EW. In the words of Gray (1992): *"Microturbulence delays saturation by spreading the absorption over a wider spectral band."* This effect is stronger for lines that are closer to saturation (lines of large EW). Weak (non-saturated lines) are much less sensitive to microturbulence. An illustration of the influence of microturbulent velocity on the curve of growth of a given line is shown in Fig. B.4.

To determine whether the assumed v_{mic} is correct, the diagnostic consists in looking for trends between abundances and the **reduced equivalent width** (EWR) $\log(EW/\lambda)$. The left panel of Fig. B.4 shows the abundance obtained against microturbulence for three FeI lines measured in the solar spectrum. Overestimating v_{mic} leads to an underestimate of the true abundance (this effect is stronger for lines of high EWR than low EWR). The right panel of Fig. B.4 shows the abundances of those three lines against reduced equivalent

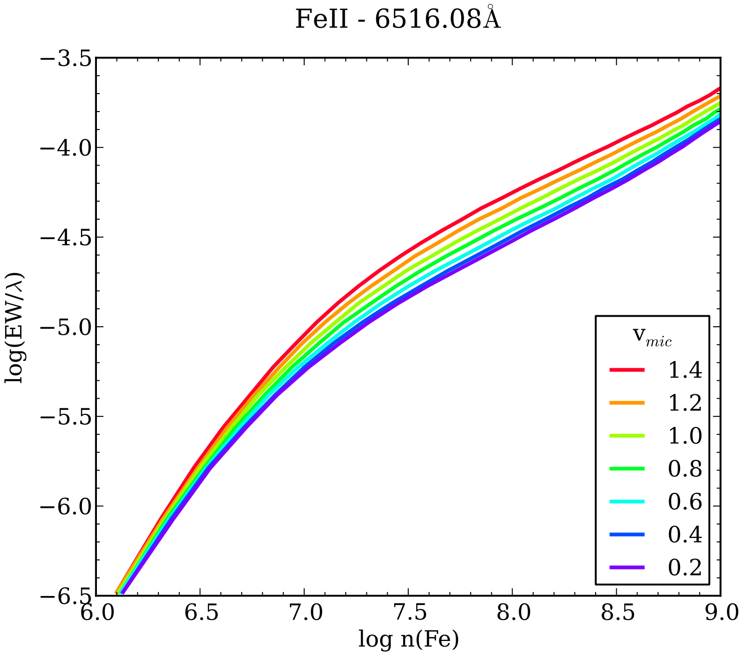

Figure B.3: Curve of growth for a typical Fe line, obtained with models of constant T$_{\rm eff}$ and log g, varying v_{mic}. For any given abundance, the model with higher v_{mic} yields a larger EW (inversely, a given EW corresponds to a lower abundance in atmospheres of higher v_{mic}). This effect is stronger in the saturated part of the curve of growth.

width, for six different choices of v_{mic}. The correct value of v_{mic} is the one that eliminates the trend between abundance and EWR.

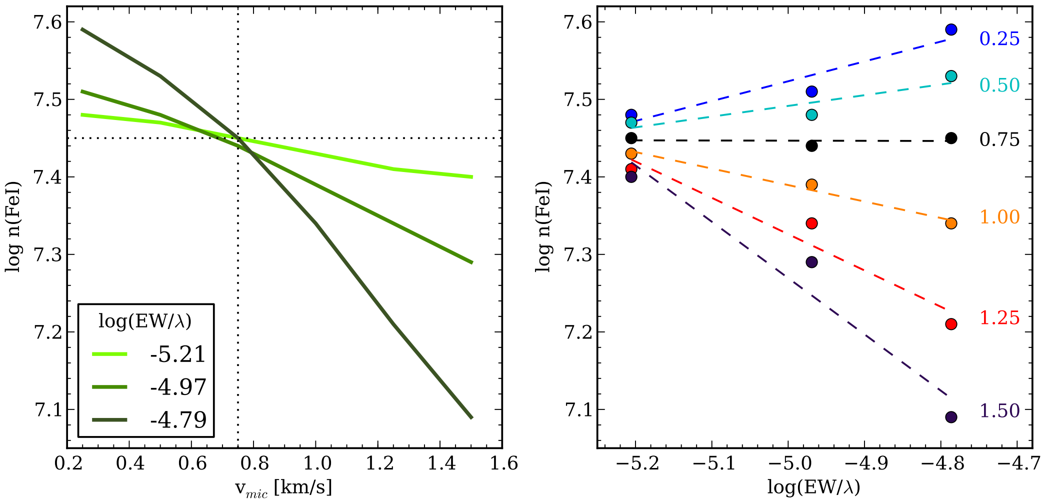

Figure B.4: *Left:* abundance obtained against microturbulence of the adopted model, for three different FeI lines. *Right:* abundance against reduced equivalent width, for six different choices of v_{mic}. The dashed lines are linear fits through the three data points.

Practical considerations

If the excitation equilibrium is satisfied for a given effective temperature, an adjustment of the surface gravity or microturbulence may break the balance. The convergence procedure is an exploratory process which ends when all parameters *simultaneously* fulfill the equilibrium conditions.

In this example the analysis is performed with very few lines. In practice it is important to measure enough lines to constitute a statistically significant sample, because fitting a slope from three data points is most often unreliable. Some lines may be affected by measurement errors, in particular the smaller lines (EW<5 mÅ to EW<20 mÅ depending on the signal-to-noise ratio of the observed spectrum), and others may be blended. A good compromise between a sufficient number of lines and a sample that does not include ill-measured lines is necessary.

A good line list does not only include a large number of uncontaminated lines (for both neutral and ionised species), but must also ensure the lines used for the analysis span a large baseline in both EP and EWR in order to obtain reliable slopes when adjusting $T_{\rm eff}$ and v_{mic}. Virtually all studies rely on Fe lines, because of the large number of both neutral and ionised Fe lines identifiable in the optical range, but conceptually such an analysis could be performed with any element providing enough observable lines.

The presence of a sufficient number of lines ans the possibility to reliably measure their EW is therefore a necessary condition for this method to work. The spectra of hot stars feature few Fe lines in the optical range. Few FeII lines are detectable in the spectra of cool stars. In addition, line crowding and the presence of molecular bands in those cool spectra affect EW measurements by blending lines and making it difficult to estimate the continuum level. Because of those limitations, the "classical EW analysis" method presented in this Appendix is best suited to FGK-type stars.

The first-guess model atmosphere

A reasonable choice of initial model atmosphere can greatly speed up the convergence process and avoid unrealistic results. The effective temperature ($\mathrm{T_{eff}}$) of a star can be estimated from its colour (see e.g. Casagrande et al., 2010), if the extinction along the line of sight (making the star appear redder and therefore colder) is known and the colour excess accounted for. Colour indices computed from infrared photometry (e.g. the 2MASS J, H, K_s passbands) are less sensitive to extinction issues than optical bands.

The surface gravity (log g) of a star can be obtained by comparing its position in a HR diagram with theoretical isochrones, if photometric information is available. If the mass M_* and luminosity L_* of the star are known the surface gravity of a star can be recovered. By definition, the surface gravity g of a star given its mass M and radius R is:

$$g = \frac{GM}{R^2} \implies \frac{g_*}{g_\odot} = \frac{\frac{GM_*}{R_*^2}}{\frac{GM_\odot}{R_\odot^2}} = \left(\frac{M_*}{M_\odot}\right)\left(\frac{R_\odot}{R_*}\right)^2 \tag{B.3}$$

and assuming the star radiates as a black body, its luminosity L is linked to its radius R and effective temperature $\mathrm{T_{eff}}$ through:

$$L = 4\pi R^2 \sigma {\mathrm{T_{eff}}}^4 \implies \frac{L_*}{L_\odot} = \left(\frac{R_*}{R_\odot}\right)^2\left(\frac{\mathrm{T_{eff*}}}{\mathrm{T_{eff\odot}}}\right)^4 \implies \left(\frac{R_\odot}{R_*}\right)^2 = \left(\frac{\mathrm{T_{eff*}}}{\mathrm{T_{eff\odot}}}\right)^4\left(\frac{L_*}{L_\odot}\right)^{-1} \tag{B.4}$$

where σ is the Stefan-Boltzman constant. Finally:

$$\frac{g_*}{g_\odot} = \left(\frac{M_*}{M_\odot}\right)\left(\frac{\mathrm{T_{eff*}}}{\mathrm{T_{eff\odot}}}\right)^4\left(\frac{L_*}{L_\odot}\right)^{-1} \tag{B.5}$$

often referred to as the "canonical equation" and written as:

$$\log\left(\frac{g_*}{g_\odot}\right) = \log\left(\frac{M_*}{M_\odot}\right) + 4\log\left(\frac{\mathrm{T_{eff*}}}{\mathrm{T_{eff\odot}}}\right) - \log\left(\frac{L_*}{L_\odot}\right) \tag{B.6}$$

where g_*, M_*, $\mathrm{T_{eff*}}$, L_*, and R_* refer respectively to the surface gravity, mass, effective temperature, luminosity and radius of the considered star, and $g_\odot$, $M_\odot$, $\mathrm{T_{eff\odot}}$, $L_\odot$, and $R_\odot$ correspond to the solar values.

The value of the microturbulent velocity parameter can be estimated through empirical relations (for instance, Gratton et al., 1996, quote $v_{mic} = 1.19\times10^{-3}\times\mathrm{T_{eff}}-0.90\times\log\ g-2$), although an initial value of $1\,\mathrm{km\,s^{-1}}$ is usually an acceptable default choice.

A reasonable first guess for the initial parameters is especially important when the convergence procedure is carried out by hand. Although codes such as FAMA apply a robust convergence scheme, initial parameters compatible with the spectral type ($\mathrm{T_{eff}}$ within 1500 K) and evolutionary phase (log g within 1 dex) of the star under study is always preferable.

BIBLIOGRAPHY

Allende Prieto, C., Barklem, P. S., Lambert, D. L., et al.: 2004, *A&A* **420**, 183

Allende Prieto, C., Majewski, S. R., Schiavon, R., et al.: 2008, *Astronomische Nachrichten* **329**, 1018

Allison, R. J., Goodwin, S. P., Parker, R. J., et al.: 2009, *MNRAS* **395**, 1449

Amôres, E. B., Lépine, J. R. D., Mishurov, Y. N.: 2009, *MNRAS* **400**, 1768

Anders, E., Grevesse, N.: 1989, *Geochim. Cosmochim. Acta* **53**, 197

Andreuzzi, G., Bragaglia, A., Tosi, M., et al.: 2011, *MNRAS* **412**, 1265

Anthony-Twarog, B. J., Twarog, B. A.: 2006, *PASP* **118**, 358

Arnould, M., Goriely, S., Jorissen, A.: 1999, *A&A* **347**, 572

Asplund, M., Grevesse, N., Sauval, A. J.: 2005, in T. G. Barnes, III and F. N. Bash (eds.), *Cosmic Abundances as Records of Stellar Evolution and Nucleosynthesis*, Vol. 336 of *Astronomical Society of the Pacific Conference Series*, p. 25

Babusiaux, C., Gilmore, G.: 2005, *MNRAS* **358**, 1309

Bagnulo, S., Jehin, E., Ledoux, C., et al.: 2003, *The Messenger* **114**, 10

Bailer-Jones, C. A. L., Andrae, R., Arcay, B., et al.: 2013, *A&A* **559**, A74

Ballester, P., Modigliani, A., Boitquin, O., et al.: 2000, *The Messenger* **101**, 31

Balser, D. S., Rood, R. T., Bania, T. M., et al.: 2011, *ApJ* **738**, 27

Barden, S. C., Jones, D. J., Barnes, S. I., et al.: 2010, in *Society of Photo-Optical Instrumentation Engineers (SPIE) Conference Series*, Vol. 7735 of *Society of Photo-Optical Instrumentation Engineers (SPIE) Conference Series*

Bastian, N.: 2011, in *Stellar Clusters & Associations: A RIA Workshop on Gaia*, pp 85–97

Bastian, N., de Mink, S. E.: 2009, *MNRAS* **398**, L11

Bastian, N., Gieles, M., Ercolano, B., et al.: 2009a, *MNRAS* **392**, 868

Bastian, N., Gieles, M., Ercolano, B., et al.: 2009b, in J. T. Van Loon and J. M. Oliveira (eds.), *IAU Symposium*, Vol. 256 of *IAU Symposium*, pp 45–50

Bastian, N., Goodwin, S. P.: 2006, *MNRAS* **369**, L9

Bastian, N., Lamers, H. J. G. L. M., de Mink, S. E., et al.: 2013, *MNRAS* **436**, 2398

Bastian, N., Silva-Villa, E.: 2013, *MNRAS* **431**, L122

Baumgardt, H., Kroupa, P.: 2007, *MNRAS* **380**, 1589

Bellazzini, M., Bragaglia, A., Carretta, E., et al.: 2012, *A&A* **538**, A18

Belokurov, V.: 2013, *New A Rev.* **57**, 100

Belokurov, V., Koposov, S. E., Evans, N. W., et al.: 2014, *MNRAS* **437**, 116

Belokurov, V., Zucker, D. B., Evans, N. W., et al.: 2006, *ApJ* **642**, L137

Bensby, T., Feltzing, S., Lundström, I.: 2003, *A&A* **410**, 527

Bensby, T., Feltzing, S., Lundström, I., et al.: 2005, *A&A* **433**, 185

Bergemann, M., Ruchti, G. R., Serenelli, A., et al.: 2014, *A&A* **565**, A89

Bianchini, P., Varri, A. L., Bertin, G., et al.: 2013, *ApJ* **772**, 67

Blanco-Cuaresma, S., Soubiran, C., Jofré, P., et al.: 2014a, in S. Feltzing, G. Zhao, N. A. Walton, and P. Whitelock (eds.), *IAU Symposium*, Vol. 298 of *IAU Symposium*, pp 396–396

Blanco-Cuaresma, S., Soubiran, C., Jofré, P., et al.: 2014b, *A&A* **566**, A98

Bland-Hawthorn, J., Karlsson, T., Sharma, S., et al.: 2010, *ApJ* **721**, 582

Boeche, C., Siebert, A., Piffl, T., et al.: 2014, *ArXiv e-prints*

Boeche, C., Siebert, A., Piffl, T., et al.: 2013, *A&A* **559**, A59

Bok, B. J.: 1934, *Harvard College Observatory Circular* **384**, 1

Bonatto, C., Kerber, L. O., Bica, E., et al.: 2006, *A&A* **446**, 121

Bonifacio, P., Caffau, E.: 2003, *A&A* **399**, 1183

Bonifacio, P., Caffau, E., Ludwig, H.-G., et al.: 2012, in M. T. Richards and I. Hubeny (eds.), *IAU Symposium*, Vol. 282 of *IAU Symposium*, pp 213–220

Bonnell, I. A.: 2008, in J. H. Knapen, T. J. Mahoney, and A. Vazdekis (eds.), *Pathways Through an Eclectic Universe*, Vol. 390 of *Astronomical Society of the Pacific Conference Series*, p. 26

Bonnell, I. A., Bate, M. R.: 2006, *MNRAS* **370**, 488

Bonnell, I. A., Bate, M. R., Vine, S. G.: 2003, *MNRAS* **343**, 413

Bonnell, I. A., Smith, R. J., Clark, P. C., et al.: 2011, *MNRAS* **410**, 2339

Borissova, J., Bonatto, C., Kurtev, R., et al.: 2011, *A&A* **532**, A131

Bovy, J., Rix, H.-W., Hogg, D. W.: 2012, *ApJ* **751**, 131

Bragaglia, A., Gratton, R. G., Carretta, E., et al.: 2012, *A&A* **548**, A122

Bragaglia, A., Sestito, P., Villanova, S., et al.: 2008, *A&A* **480**, 79

Bragaglia, A., Sneden, C., Carretta, E., et al.: 2014, *ArXiv e-prints*

Bragaglia, A., Tosi, M.: 2006, *AJ* **131**, 1544

Bragaglia, A., Tosi, M., Andreuzzi, G., et al.: 2006, *MNRAS* **368**, 1971

Brandt, J. C., Stecher, T. P., Crawford, D. L., et al.: 1971, *ApJ* **163**, L99

Bresolin, F., Ryan-Weber, E., Kennicutt, R. C., et al.: 2009, *ApJ* **695**, 580

Bressan, A., Marigo, P., Girardi, L., et al.: 2012, *MNRAS* **427**, 127

Bressert, E., Bastian, N., Gutermuth, R., et al.: 2010, *MNRAS* **409**, L54

Briggs, F. H.: 1990, *ApJ* **352**, 15

Buckner, A. S. M., Froebrich, D.: 2014, *MNRAS* **444**, 290

Burbidge, E. M., Burbidge, G. R., Fowler, W. A., et al.: 1957, *Reviews of Modern Physics* **29**, 547

Burke, B. F.: 1957, *AJ* **62**, 90

Burstein, D.: 1979, *ApJ* **234**, 829

Cabrera-Cano, J., Alfaro, E. J.: 1985, *A&A* **150**, 298

Caimmi, R.: 2008, *New A* **13**, 314

Cameron, L. M.: 1985, *A&A* **147**, 39

Cantat-Gaudin, T., Donati, P., Pancino, E., et al.: 2014a, *A&A* **562**, A10

Cantat-Gaudin, T., Vallenari, A., Zaggia, S., et al.: 2014b, *A&A* **569**, A17

Caputo, F., Marconi, M., Musella, I., et al.: 2001, *A&A* **372**, 544

Carraro, G., Anthony-Twarog, B. J., Costa, E., et al.: 2011, *AJ* **142**, 127

Carraro, G., Baume, G.: 2003, *MNRAS* **346**, 18

Carraro, G., Bresolin, F., Villanova, S., et al.: 2004, *AJ* **128**, 1676

Carraro, G., Costa, E., Ahumada, J. A.: 2010, *AJ* **140**, 954

Carraro, G., Geisler, D., Villanova, S., et al.: 2007, *A&A* **476**, 217

Carraro, G., Ng, Y. K., Portinari, L.: 1998, *MNRAS* **296**, 1045

Carretta, E., Bragaglia, A., Gratton, R., et al.: 2009a, *A&A* **505**, 139

Carretta, E., Bragaglia, A., Gratton, R. G., et al.: 2014, *A&A* **561**, A87

Carretta, E., Bragaglia, A., Gratton, R. G., et al.: 2009b, *A&A* **505**, 117

Carretta, E., Bragaglia, A., Gratton, R. G., et al.: 2010, *A&A* **516**, A55

Cartwright, A., Whitworth, A. P.: 2004, *MNRAS* **348**, 589

Casagrande, L., Ramírez, I., Meléndez, J., et al.: 2010, *A&A* **512**, A54

Cavallo, R. M., Sweigart, A. V., Bell, R. A.: 1996, *ApJ* **464**, L79

Chiappini, C., Matteucci, F., Gratton, R.: 1997, *ApJ* **477**, 765

Chiappini, C., Matteucci, F., Romano, D.: 2001, *ApJ* **554**, 1044

Chiba, M., Beers, T. C.: 2000, *AJ* **119**, 2843

Cignoni, M., Beccari, G., Bragaglia, A., et al.: 2011, *MNRAS* **416**, 1077

Cirasuolo, M., Afonso, J., Bender, R., et al.: 2011, *The Messenger* **145**, 11

Clark, P. C., Klessen, R. S., Bonnell, I. A.: 2007, *MNRAS* **379**, 57

Colavitti, E., Cescutti, G., Matteucci, F., et al.: 2009, *A&A* **496**, 429

Corsaro, E., Stello, D., Huber, D., et al.: 2012, *ApJ* **757**, 190

Cote, P., Welch, D. L., Fischer, P., et al.: 1995, *ApJ* **454**, 788

Cox, A. L., Sparke, L. S., van Moorsel, G., et al.: 1996, *AJ* **111**, 1505

Crane, J. D., Majewski, S. R., Rocha-Pinto, H. J., et al.: 2003, *ApJ* **594**, L119

Daflon, S., Cunha, K.: 2004, *ApJ* **617**, 1115

Dawson, D. W., Ianna, P. A.: 1998, *AJ* **115**, 1076

de Jong, R.: 2011, *The Messenger* **145**, 14

De Marco, O., Schmutz, W.: 1999, *A&A* **345**, 163

Decressin, T., Meynet, G., Charbonnel, C., et al.: 2007, *A&A* **464**, 1029

Dekker, H., D'Odorico, S., Kaufer, A., et al.: 2000, in M. Iye and A. F. Moorwood (eds.), *Optical and IR Telescope Instrumentation and Detectors*, Vol. 4008 of *Society of Photo-Optical Instrumentation Engineers (SPIE) Conference Series*, pp 534–545

Delgado, A. J., Djupvik, A. A., Costado, M. T., et al.: 2013, *MNRAS* **435**, 429

D'Ercole, A., Vesperini, E., D'Antona, F., et al.: 2008, *MNRAS* **391**, 825

Dias, W. S., Alessi, B. S., Moitinho, A., et al.: 2002, *A&A* **389**, 871

Dias, W. S., Lépine, J. R. D.: 2005, *ApJ* **629**, 825

Dickey, J. M., Lockman, F. J.: 1990, *ARA&A* **28**, 215

Donati, J.-F., Semel, M., Carter, B. D., et al.: 1997, *MNRAS* **291**, 658

Donati, P., Bragaglia, A., Cignoni, M., et al.: 2012, *MNRAS* **424**, 1132

Donati, P., Cantat Gaudin, T., Bragaglia, A., et al.: 2014, *A&A* **561**, A94

D'Orazi, V., Lucatello, S., Gratton, R., et al.: 2010, *ApJ* **713**, L1

Dotter, A., Chaboyer, B., Jevremović, D., et al.: 2008, *ApJS* **178**, 89

Drew, J. E., Gonzalez-Solares, E., Greimel, R., et al.: 2014, *MNRAS* **440**, 2036

Drimmel, R.: 2000, *A&A* **358**, L13

Dutra, C. M., Bica, E.: 2001, *A&A* **376**, 434

Edvardsson, B., Andersen, J., Gustafsson, B., et al.: 1993, *A&A* **275**, 101

Eggen, O. J., Lynden-Bell, D., Sandage, A. R.: 1962, *ApJ* **136**, 748

Eisenhauer, F., Genzel, R., Alexander, T., et al.: 2005, *ApJ* **628**, 246

Eldridge, J. J.: 2009, *MNRAS* **400**, L20

Elmegreen, B. G.: 2011, in C. Charbonnel and T. Montmerle (eds.), *EAS Publications Series*, Vol. 51 of *EAS Publications Series*, pp 31–44

Ferrière, K. M.: 2001, *Reviews of Modern Physics* **73**, 1031

Fitzpatrick, E. L.: 1999, *PASP* **111**, 63

Fitzpatrick, M. J., Sneden, C.: 1987, in *Bulletin of the American Astronomical Society*, Vol. 19 of *Bulletin of the American Astronomical Society*, p. 1129

Friel, E. D.: 1995, *ARA&A* **33**, 381

Friel, E. D., Donati, P., Bragaglia, A., et al.: 2014, *A&A* **563**, A117

Friel, E. D., Jacobson, H. R., Barrett, E., et al.: 2003, *AJ* **126**, 2372

Friel, E. D., Janes, K. A.: 1993, *A&A* **267**, 75

Friel, E. D., Janes, K. A., Tavarez, M., et al.: 2002, *AJ* **124**, 2693

Frinchaboy, P. M., Majewski, S. R., Crane, J. D., et al.: 2004, *ApJ* **602**, L21

Frinchaboy, P. M., Marino, A. F., Villanova, S., et al.: 2008, *MNRAS* **391**, 39

Frinchaboy, P. M., Thompson, B., Jackson, K. M., et al.: 2013, *ApJ* **777**, L1

Froebrich, D., Scholz, A., Raftery, C. L.: 2007, *MNRAS* **374**, 399

Fu, J., Hou, J. L., Yin, J., et al.: 2009, *ApJ* **696**, 668

Gamow, G.: 1946, *Physical Review* **70**, 572

García-Ruiz, I., Kuijken, K., Dubinski, J.: 2002a, *MNRAS* **337**, 459

García-Ruiz, I., Sancisi, R., Kuijken, K.: 2002b, *A&A* **394**, 769

Geisler, D., Villanova, S., Carraro, G., et al.: 2012, *ApJ* **756**, L40

Genovali, K., Lemasle, B., Bono, G., et al.: 2013, *A&A* **554**, A132

Gieles, M., Bastian, N., Ercolano, B.: 2008, *MNRAS* **391**, L93

Gilmore, G., Randich, S., Asplund, M., et al.: 2012, *The Messenger* **147**, 25

Gilmore, G., Reid, N.: 1983, *MNRAS* **202**, 1025

Girardi, L.: 1999, *MNRAS* **308**, 818

Girardi, L., Bressan, A., Bertelli, G., et al.: 2000a, *A&AS* **141**, 371

Girardi, L., Eggenberger, P., Miglio, A.: 2011, *MNRAS* **412**, L103

Girardi, L., Mermilliod, J.-C., Carraro, G.: 2000b, *A&A* **354**, 892

Girardi, L., Rubele, S., Kerber, L.: 2009, *MNRAS* **394**, L74

Girichidis, P., Federrath, C., Banerjee, R., et al.: 2011, *MNRAS* **413**, 2741

Glatt, K., Grebel, E. K., Sabbi, E., et al.: 2008, *AJ* **136**, 1703

Goetz, M., Koeppen, J.: 1992, *A&A* **262**, 455

Gomez, M., Hartmann, L., Kenyon, S. J., et al.: 1993, *AJ* **105**, 1927

Gonzalez, G., Wallerstein, G.: 2000, *PASP* **112**, 1081

Goodwin, S. P., Bastian, N.: 2006, *MNRAS* **373**, 752

Gouliermis, D., Keller, S. C., Kontizas, M., et al.: 2004, *A&A* **416**, 137

Gouliermis, D. A., Beerman, L. C., Bianchi, L., et al.: 2014a, *ArXiv e-prints*

Gouliermis, D. A., Hony, S., Klessen, R. S.: 2014b, *MNRAS* **439**, 3775

Gratton, R., Sneden, C., Carretta, E.: 2004, *ARA&A* **42**, 385

Gratton, R. G., Bonifacio, P., Bragaglia, A., et al.: 2001, *A&A* **369**, 87

Gratton, R. G., Carretta, E., Bragaglia, A.: 2012, *A&A Rev.* **20**, 50

Gratton, R. G., Carretta, E., Castelli, F.: 1996, *A&A* **314**, 191

Gratton, R. G., Carretta, E., Matteucci, F., et al.: 2000, *A&A* **358**, 671

Gray, D. F.: 1992, *The observation and analysis of stellar photospheres.*

Gray, R. O., Corbally, C. J.: 1994, *AJ* **107**, 742

Grevesse, N., Asplund, M., Sauval, A. J.: 2007, *SSRv* **130**, 105

Groenewegen, M. A. T.: 2013, *A&A* **550**, A70

Grupp, F.: 2004a, *A&A* **420**, 289

Grupp, F.: 2004b, *A&A* **426**, 309

Guesten, R., Mezger, P. G.: 1982, *Vistas in Astronomy* **26**, 159

Gummersbach, C. A., Kaufer, A., Schaefer, D. R., et al.: 1998, *A&A* **338**, 881

Gustafsson, B., Bell, R. A., Eriksson, K., et al.: 1975, *A&A* **42**, 407

Gustafsson, B., Edvardsson, B., Eriksson, K., et al.: 2008, *A&A* **486**, 951

Gustafsson, B., Edvardsson, B., Eriksson, K., et al.: 2003, in I. Hubeny, D. Mihalas, and K. Werner (eds.), *Stellar Atmosphere Modeling*, Vol. 288 of *Astronomical Society of the Pacific Conference Series*, p. 331

Gutermuth, R. A., Myers, P. C., Megeath, S. T., et al.: 2008, *ApJ* **674**, 336

Hammersley, P. L., López-Corredoira, M.: 2011, *A&A* **527**, A6

Harris, H. C.: 1981, *AJ* **86**, 707

Heiter, U., Soubiran, C., Netopil, M., et al.: 2014, *A&A* **561**, A93

Helmi, A., Navarro, J. F., Meza, A., et al.: 2003, *ApJ* **592**, L25

Helmi, A., White, S. D. M., de Zeeuw, P. T., et al.: 1999, *Nature* **402**, 53

Henry, R. B. C., Kwitter, K. B., Jaskot, A. E., et al.: 2010, *ApJ* **724**, 748

Hills, J. G.: 1980, *ApJ* **235**, 986

Hinkle, K., Wallace, L., Valenti, J., et al.: 2000, *Visible and Near Infrared Atlas of the Arcturus Spectrum 3727-9300 A*

Hou, J. L., Prantzos, N., Boissier, S.: 2000, *A&A* **362**, 921

Hubble, E. P.: 1926, *ApJ* **64**, 321

Ibata, R. A., Gilmore, G., Irwin, M. J.: 1994, *Nature* **370**, 194

Ibata, R. A., Irwin, M. J., Lewis, G. F., et al.: 2003, *MNRAS* **340**, L21

Ivezić, Ž., Sesar, B., Jurić, M., et al.: 2008, *ApJ* **684**, 287

Jacobson, H. R., Pilachowski, C. A., Friel, E. D.: 2011, *AJ* **142**, 59

Janes, K. A.: 1979, *ApJS* **39**, 135

Janes, K. A., Tilley, C., Lynga, G.: 1988, *AJ* **95**, 771

Jeffries, R. D., Jackson, R. J., Cottaar, M., et al.: 2014, *A&A* **563**, A94

Jeffries, R. D., Naylor, T., Walter, F. M., et al.: 2009, *MNRAS* **393**, 538

Jofré, P., Heiter, U., Soubiran, C., et al.: 2014, *A&A* **564**, A133

Johnson, C. I., Pilachowski, C. A.: 2010, *ApJ* **722**, 1373

Johnston, K. V., Spergel, D. N., Hernquist, L.: 1995, *ApJ* **451**, 598

Jurić, M., Ivezić, Ž., Brooks, A., et al.: 2008, *ApJ* **673**, 864

Just, A.: 2002, in E. Athanassoula, A. Bosma, and R. Mujica (eds.), *Disks of Galaxies: Kinematics, Dynamics and Peturbations*, Vol. 275 of *Astronomical Society of the Pacific Conference Series*, pp 117–120

Kaluzny, J.: 1994, *A&AS* **108**, 151

Kennicutt, Jr., R. C.: 1981, *AJ* **86**, 1847

Kerr, F. J.: 1957, *AJ* **62**, 93

Kerr, F. J.: 1969, *ARA&A* **7**, 39

Kharchenko, N. V., Piskunov, A. E., Schilbach, E., et al.: 2013, *A&A* **558**, A53

King, I.: 1962, *AJ* **67**, 471

Klessen, R. S.: 2011, in C. Charbonnel and T. Montmerle (eds.), *EAS Publications Series*, Vol. 51 of *EAS Publications Series*, pp 133–167

Koo, J.-R., Kim, S.-L., Rey, S.-C., et al.: 2007, *PASP* **119**, 1233

Kraft, R. P.: 1979, *ARA&A* **17**, 309

Kraft, R. P.: 1994, *PASP* **106**, 553

Kroupa, P.: 2001, *MNRAS* **322**, 231

Kruijssen, J. M. D.: 2012, *MNRAS* **426**, 3008

Krumholz, M. R., Klein, R. I., McKee, C. F.: 2012, *ApJ* **754**, 71

Kupka, F., Piskunov, N., Ryabchikova, T. A., et al.: 1999, *A&AS* **138**, 119

Kurucz, R. L.: 1970, *SAO Special Report* 309

Kurucz, R. L.: 1993, *SYNTHE spectrum synthesis programs and line data*

Kurucz, R. L.: 2005, *Memorie della Societa Astronomica Italiana Supplementi* **8**, 14

Kurucz, R. L., Avrett, E. H.: 1981, *SAO Special Report* 391

Lada, C. J., Lada, E. A.: 2003, *ARA&A* **41**, 57

Larson, R. B.: 1972, *Nature Physical Science* **236**, 7

Lauberts, A.: 1982, *ESO/Uppsala survey of the ESO(B) atlas*

Launhardt, R., Zylka, R., Mezger, P. G.: 2002, *A&A* **384**, 112

Leavitt, H. S., Pickering, E. C.: 1912, *Harvard College Observatory Circular* **173**, 1

Lee, Y.-W., Joo, J.-M., Sohn, Y.-J., et al.: 1999, *Nature* **402**, 55

Lemasle, B., François, P., Genovali, K., et al.: 2013, *A&A* **558**, A31

Lépine, J. R. D., Andrievky, S., Barros, D. A., et al.: 2014, in S. Feltzing, G. Zhao, N. A. Walton, and P. Whitelock (eds.), *IAU Symposium*, Vol. 298 of *IAU Symposium*, pp 86–91

Lépine, J. R. D., Cruz, P., Scarano, Jr., S., et al.: 2011, *MNRAS* **417**, 698

Levine, E. S., Blitz, L., Heiles, C.: 2006, *Science* **312**, 1773

Li, Z., Mao, C., Chen, L., et al.: 2012, *ApJ* **761**, L22

Lind, K., Asplund, M., Barklem, P. S., et al.: 2011, *A&A* **528**, A103

Lind, K., Primas, F., Charbonnel, C., et al.: 2009, *A&A* **503**, 545

Lindegren, L., Babusiaux, C., Bailer-Jones, C., et al.: 2008, in W. J. Jin, I. Platais, and M. A. C. Perryman (eds.), *IAU Symposium*, Vol. 248 of *IAU Symposium*, pp 217–223

Loktin, A. V.: 1998, *Astronomical and Astrophysical Transactions* **15**, 59

Lopez-Corredoira, M., Moitinho, A., Zaggia, S., et al.: 2012, *ArXiv e-prints*

Lovis, C., Mayor, M.: 2007, *A&A* **472**, 657

Lynga, G.: 1987, *Computer Based Catalogue of Open Cluster Data, 5th ed.*

Maciel, W. J., Costa, R. D. D., Idiart, T. E. P.: 2009, *Rev. Mexicana Astron. Astrofis.* **45**, 127

Magnani, L., Hartmann, D., Speck, B. G.: 1996, *ApJS* **106**, 447

Magrini, L., Randich, S., Friel, E., et al.: 2013, *A&A* **558**, A38

Magrini, L., Randich, S., Romano, D., et al.: 2014, *A&A* **563**, A44

Magrini, L., Randich, S., Zoccali, M., et al.: 2010, *ArXiv e-prints*

Magrini, L., Sestito, P., Randich, S., et al.: 2009a, *A&A* **494**, 95

Magrini, L., Stanghellini, L., Villaver, E.: 2009b, *ApJ* **696**, 729

Majewski, S. R., Munn, J. A., Hawley, S. L.: 1996, *ApJ* **459**, L73

Majewski, S. R., Skrutskie, M. F., Weinberg, M. D., et al.: 2003, *ApJ* **599**, 1082

Mapelli, M., Bressan, A.: 2013, *MNRAS* **430**, 3120

Mapelli, M., Zampieri, L., Ripamonti, E., et al.: 2013, *MNRAS* **429**, 2298

Marino, A. F., Sneden, C., Kraft, R. P., et al.: 2011, *A&A* **532**, A8

Marino, A. F., Villanova, S., Piotto, G., et al.: 2008, *A&A* **490**, 625

Martell, S. L., Smolinski, J. P., Beers, T. C., et al.: 2011, *A&A* **534**, A136

Martínez-García, E. E., Puerari, I.: 2014, *ApJ* **790**, 118

Maschberger, T., Clarke, C. J.: 2011, *MNRAS* **416**, 541

Matteucci, F., Francois, P.: 1989, *MNRAS* **239**, 885

Mayor, M., Pepe, F., Queloz, D., et al.: 2003, *The Messenger* **114**, 20

McNamara, B. J., Sanders, W. L.: 1977, *A&A* **54**, 569

McSwain, M. V., Gies, D. R.: 2005, *ApJS* **161**, 118

Mermilliod, J.-C.: 1995, in D. Egret and M. A. Albrecht (eds.), *Information and On-Line Data in Astronomy*, Vol. 203 of *Astrophysics and Space Science Library*, pp 127–138

Mermilliod, J.-C., Claria, J. J., Andersen, J., et al.: 1997, *A&A* **324**, 91

Mermilliod, J.-C., Mayor, M.: 1989, *A&A* **219**, 125

Mermilliod, J.-C., Mayor, M.: 1990, *A&A* **237**, 61

Messina, S., Parihar, P., Koo, J.-R., et al.: 2010, *A&A* **513**, A29

Miglio, A., Brogaard, K., Stello, D., et al.: 2012, *MNRAS* **419**, 2077

Millour, F., Petrov, R. G., Chesneau, O., et al.: 2007, *A&A* **464**, 107

Milone, A. P., Bedin, L. R., Piotto, G., et al.: 2009, *A&A* **497**, 755

Milone, A. P., Piotto, G., Bedin, L. R., et al.: 2012, *A&A* **540**, A16

Minchev, I., Chiappini, C., Martig, M.: 2013, *A&A* **558**, A9

Miocchi, P.: 2006, *MNRAS* **366**, 227

Molla, M., Ferrini, F., Diaz, A. I.: 1996, *ApJ* **466**, 668

Mollá, M., Ferrini, F., Díaz, A. I.: 1997, *ApJ* **475**, 519

Momany, Y., Zaggia, S., Gilmore, G., et al.: 2006, *A&A* **451**, 515

Morgan, W. W., Sharpless, S., Osterbrock, D.: 1952, *AJ* **57**, 3

Mucciarelli, A., Pancino, E., Lovisi, L., et al.: 2013, *ApJ* **766**, 78

Newberg, H. J., Yanny, B., Rockosi, C., et al.: 2002, *ApJ* **569**, 245

North, J. R., Tuthill, P. G., Tango, W. J., et al.: 2007, *MNRAS* **377**, 415

Offner, S. S. R., Krumholz, M. R.: 2009, *ApJ* **693**, 914

Pagel, B. E. J.: 2009, *Nucleosynthesis and Chemical Evolution of Galaxies*

Panagia, N., Tosi, M.: 1981, *A&A* **96**, 306

Pancino, E., Carrera, R., Rossetti, E., et al.: 2010, *A&A* **511**, A56

Parker, R. J., Bouvier, J., Goodwin, S. P., et al.: 2011, *MNRAS* **412**, 2489

Parker, R. J., Meyer, M. R.: 2012, *MNRAS* **427**, 637

Pasquali, A., Perinotto, M.: 1993, *A&A* **280**, 581

Pasquini, L., Avila, G., Blecha, A., et al.: 2002, *The Messenger* **110**, 1

Peimbert, M., Serrano, A.: 1982, *MNRAS* **198**, 563

Perryman, M. A. C., de Boer, K. S., Gilmore, G., et al.: 2001, *A&A* **369**, 339

Phelps, R. L., Janes, K. A.: 1996, *AJ* **111**, 1604

Pietrinferni, A., Cassisi, S., Salaris, M., et al.: 2004, *ApJ* **612**, 168

Piotto, G.: 2009, in E. E. Mamajek, D. R. Soderblom, and R. F. G. Wyse (eds.), *IAU Symposium*, Vol. 258 of *IAU Symposium*, pp 233–244

Piskunov, A. E., Kharchenko, N. V., Röser, S., et al.: 2006, *A&A* **445**, 545

Piskunov, N. E.: 1992, in Y. V. Glagolevskij and I. I. Romanyuk (eds.), *Physics and Evolution of Stars: Stellar Magnetism*, p. 92

Platais, I., Melo, C., Fulbright, J. P., et al.: 2008, *MNRAS* **391**, 1482

Platais, I., Melo, C., Quinn, S. N., et al.: 2012, *ApJ* **751**, L8

Plez, B.: 2012, *Turbospectrum: Code for spectral synthesis*, Astrophysics Source Code Library

Plez, B., Brett, J. M., Nordlund, A.: 1992, *A&A* **256**, 551

Plummer, H. C.: 1911, *MNRAS* **71**, 460

Portegies-Zwart, S. F., McMillan, S. L. W., Hut, P., et al.: 2001, *MNRAS* **321**, 199

Portinari, L., Chiosi, C.: 1999, *A&A* **350**, 827

Pozzo, M., Jeffries, R. D., Naylor, T., et al.: 2000, *MNRAS* **313**, L23

Prisinzano, L., Carraro, G., Piotto, G., et al.: 2001, *A&A* **369**, 851

Prodanović, T., Fields, B. D.: 2008, *J. Cosmology Astropart. Phys.* **9**, 3

Ramírez, S. V., Cohen, J. G.: 2002, *AJ* **123**, 3277

Ramírez, S. V., Cohen, J. G., Buss, J., et al.: 2001, *AJ* **122**, 1429

Randich, S., Gilmore, G., Gaia-ESO Consortium: 2013, *The Messenger* **154**, 47

Recio-Blanco, A., Bijaoui, A., de Laverny, P.: 2006, *MNRAS* **370**, 141

Recio-Blanco, A., de Laverny, P., Kordopatis, G., et al.: 2014, *A&A* **567**, A5

Reid, M. J.: 1993, *ARA&A* **31**, 345

Roberts, W. W.: 1969, *ApJ* **158**, 123

Robin, A. C., Reylé, C., Derrière, S., et al.: 2003, *A&A* **409**, 523

Rocha-Pinto, H. J., Majewski, S. R., Skrutskie, M. F., et al.: 2003, *ApJ* **594**, L115

Rolleston, W. R. J., Smartt, S. J., Dufton, P. L., et al.: 2000, *A&A* **363**, 537

Romano, D., Karakas, A. I., Tosi, M., et al.: 2010, *A&A* **522**, A32

Rood, R. T., Quireza, C., Bania, T. M., et al.: 2007, in A. Vallenari, R. Tantalo, L. Portinari, and A. Moretti (eds.), *From Stars to Galaxies: Building the Pieces to Build Up the Universe*, Vol. 374 of *Astronomical Society of the Pacific Conference Series*, p. 169

Roškar, R., Debattista, V. P., Quinn, T. R., et al.: 2008, *ApJ* **684**, L79

Rudolph, A. L., Fich, M., Bell, G. R., et al.: 2006, *ApJS* **162**, 346

Rupke, D. S. N., Kewley, L. J., Chien, L.-H.: 2010, *ApJ* **723**, 1255

Sabbi, E., Sirianni, M., Nota, A., et al.: 2007, *AJ* **133**, 44

Sacco, G. G., Jeffries, R. D., Randich, S., et al.: 2015, *ArXiv e-prints*

Sacco, G. G., Morbidelli, L., Franciosini, E., et al.: 2014, *A&A* **565**, A113

Salaris, M., Weiss, A., Percival, S. M.: 2004, *A&A* **414**, 163

Sánchez, N., Alfaro, E. J.: 2009, *ApJ* **696**, 2086

Sánchez Almeida, J., Elmegreen, B. G., Muñoz-Tuñón, C., et al.: 2014, *A&A Rev.* **22**, 71

Santos, Jr., J. F. C., Bonatto, C., Bica, E.: 2005, *A&A* **442**, 201

Saurin, T. A., Bica, E., Bonatto, C.: 2010, *MNRAS* **407**, 133

Scheepmaker, R. A., Lamers, H. J. G. L. M., Anders, P., et al.: 2009, *A&A* **494**, 81

Schlegel, D. J., Finkbeiner, D. P., Davis, M.: 1998, *ApJ* **500**, 525

Schmeja, S., Kharchenko, N. V., Piskunov, A. E., et al.: 2014, *A&A* **568**, A51

Schmeja, S., Kumar, M. S. N., Ferreira, B.: 2008a, *MNRAS* **389**, 1209

Schmeja, S., Kumar, M. S. N., Froebrich, D., et al.: 2008b, in E. Vesperini, M. Giersz, and A. Sills (eds.), *IAU Symposium*, Vol. 246 of *IAU Symposium*, pp 50–54

Schönrich, R., Binney, J.: 2009, *MNRAS* **396**, 203

Searle, L., Zinn, R.: 1978, *ApJ* **225**, 357

Seleznev, A. F., Carraro, G., Costa, E., et al.: 2010, *New A* **15**, 61

Sellwood, J. A., Binney, J. J.: 2002, *MNRAS* **336**, 785

Sestito, P., Bragaglia, A., Randich, S., et al.: 2008, *A&A* **488**, 943

Shapley, H.: 1918, *PASP* **30**, 42

Sharma, S., Pandey, A. K., Ogura, K., et al.: 2008, *AJ* **135**, 1934

Shaver, P. A., McGee, R. X., Newton, L. M., et al.: 1983, *MNRAS* **204**, 53

Simpson, J. P., Colgan, S. W. J., Rubin, R. H., et al.: 1995, *ApJ* **444**, 721

Smartt, S. J., Rolleston, W. R. J.: 1997, *ApJ* **481**, L47

Smiljanic, R., Korn, A. J., Bergemann, M., et al.: 2014, *A&A* **570**, A122

Sneden, C.: 1973, *ApJ* **184**, 839

Sneden, C., Bean, J., Ivans, I., et al.: 2012, *MOOG: LTE line analysis and spectrum synthesis*, Astrophysics Source Code Library

Soubiran, C., Girard, P.: 2005, *A&A* **438**, 139

Soubiran, C., Le Campion, J.-F., Cayrel de Strobel, G., et al.: 2010, *A&A* **515**, A111

Sousa, S. G., Santos, N. C., Israelian, G., et al.: 2007, *A&A* **469**, 783

Sousa, S. G., Santos, N. C., Mayor, M., et al.: 2008, *A&A* **487**, 373

Spitzer, Jr., L.: 1958, *ApJ* **127**, 17

Spitzer, Jr., L.: 1969, *ApJ* **158**, L139

Spitzer, Jr., L., Savedoff, M. P.: 1950, *ApJ* **111**, 593

Stanghellini, L., Haywood, M.: 2010, *ApJ* **714**, 1096

Stanghellini, L., Magrini, L., Casasola, V., et al.: 2014, *A&A* **567**, A88

Stetson, P. B.: 1987, *PASP* **99**, 191

Stetson, P. B., Pancino, E.: 2008, *PASP* **120**, 1332

Sung, H., Bessell, M. S., Lee, H.-W., et al.: 1999, *MNRAS* **310**, 982

Thogersen, E. N., Friel, E. D., Fallon, B. V.: 1993, *PASP* **105**, 1253

Tosi, M.: 1988, *A&A* **197**, 33

Tosi, M.: 2000, in F. Matteucci and F. Giovannelli (eds.), *The Evolution of the Milky Way: Stars versus Clusters*, p. 505

Trumpler, R. J.: 1925, *PASP* **37**, 307

Tsikoudi, V.: 1979, *ApJ* **234**, 842

Tutukov, A. V.: 1978, *A&A* **70**, 57

Twarog, B. A., Anthony-Twarog, B. J.: 1994, *AJ* **107**, 1371

Twarog, B. A., Ashman, K. M., Anthony-Twarog, B. J.: 1997, *AJ* **114**, 2556

Valenti, J. A., Piskunov, N.: 1996, *A&AS* **118**, 595

Vallée, J. P.: 2002, *ApJ* **566**, 261

Vallée, J. P.: 2005, *AJ* **130**, 569

Vallenari, A., Pasetto, S., Bertelli, G., et al.: 2006, *A&A* **451**, 125

Vandame, B.: 2002, in J.-L. Starck and F. D. Murtagh (eds.), *Astronomical Data Analysis II*, Vol. 4847 of *Society of Photo-Optical Instrumentation Engineers (SPIE) Conference Series*, pp 123–134

VandenBerg, D. A., Bergbusch, P. A., Dowler, P. D.: 2006, *ApJS* **162**, 375

Ventura, P., D'Antona, F., Mazzitelli, I., et al.: 2001, *ApJ* **550**, L65

Vila-Costas, M. B., Edmunds, M. G.: 1992, *MNRAS* **259**, 121

Villada, M., Rossi, L.: 1987, *Ap&SS* **136**, 351

Villanova, S., Carraro, G., Bresolin, F., et al.: 2005, *AJ* **130**, 652

Villanova, S., Geisler, D., Carraro, G., et al.: 2013, *ApJ* **778**, 186

Vlajić, M., Bland-Hawthorn, J., Freeman, K. C.: 2011, *ApJ* **732**, 7

Vogt, S. S., Allen, S. L., Bigelow, B. C., et al.: 1994, in D. L. Crawford and E. R. Craine (eds.), *Instrumentation in Astronomy VIII*, Vol. 2198 of *Society of Photo-Optical Instrumentation Engineers (SPIE) Conference Series*, p. 362

Walker, M. G., Mateo, M., Olszewski, E. W., et al.: 2006, *AJ* **131**, 2114

Wallerstein, G., Iben, Jr., I., Parker, P., et al.: 1997, *Reviews of Modern Physics* **69**, 995

Weidner, C., Kroupa, P., Maschberger, T.: 2009, *MNRAS* **393**, 663

Weinberg, M. D., Blitz, L.: 2006, *ApJ* **641**, L33

Westerhout, G.: 1957, *Bull. Astron. Inst. Netherlands* **13**, 201

Wiese, W. L., Fuhr, J. R., Deters, T. M.: 1996, *Atomic transition probabilities of carbon, nitrogen, and oxygen : a critical data compilation*

Worthey, G., España, A., MacArthur, L. A., et al.: 2005, *ApJ* **631**, 820

Yanny, B., Newberg, H. J., Grebel, E. K., et al.: 2003, *ApJ* **588**, 824

Yanny, B., Newberg, H. J., Kent, S., et al.: 2000, *ApJ* **540**, 825

Yoachim, P., Dalcanton, J. J.: 2006, *AJ* **131**, 226

Yong, D., Carney, B. W., Friel, E. D.: 2012, *AJ* **144**, 95

Yong, D., Carney, B. W., Teixera de Almeida, M. L.: 2005, *AJ* **130**, 597

Yuan, H. B., Liu, X. W., Xiang, M. S.: 2013, *MNRAS* **430**, 2188

Zacharias, N., Finch, C. T., Girard, T. M., et al.: 2012, *VizieR Online Data Catalog* 1322

Zaritsky, D.: 1999, in B. K. Gibson, R. S. Axelrod, and M. E. Putman (eds.), *The Third Stromlo Symposium: The Galactic Halo*, Vol. 165 of *Astronomical Society of the Pacific Conference Series*, p. 34

Zaritsky, D., Kennicutt, Jr., R. C., Huchra, J. P.: 1994, *ApJ* **420**, 87

Zhang, Q., Fall, S. M., Whitmore, B. C.: 2001, *ApJ* **561**, 727

Zwitter, T., Siebert, A., Munari, U., et al.: 2008, *AJ* **136**, 421

ACKNOWLEDGEMENTS

The work I have conducted during these three years owes a lot to the constant support and trust from my supervisor Antonella Vallenari. I also wish to thank Rosanna Sordo for her help with everything, from lending me her books, to taming Fortran.

Many thanks to Andreas Korn, Carme Jordi and Ulrike Heiter for their constructive feeback and comments which helped improve this manuscript.

I am grateful for the generous support provided by the Marie Curie “Gaia Research for European Astronomy Training” Initial Training Network, which allowed me to get acquainted with so many new people and new ideas. Without the GREAT-ITN, I may have never met John, Iulia, Lovro, Matthew, Max, and Tanya.

I was lucky to be involved in the *Gaia*-ESO Survey collaboration as a student, and in particular I would like to thank Paolo Donati, Angela Bragaglia, Elena Pancino, Eileen Friel, Heather Jacobson, Simone Zaggia, Emilio Alfaro, Sergi Blanco-Cuaresma and Caroline Soubiran, with whom I have learnt a lot.

Above all I need to thank my family for having been encouraging and supportive of my interest in astronomy, since always. I remember my father taking me to see the 1996 solar eclipse, watching the 1997 Hale-Bopp comet with my grandfather, my mother driving us across France to see the Moon hide the Sun in 1999, and learning about constellations at summer camps. Max, on a suivi des routes différentes mais pour moi l’astronomie, avant d’être la nucléosynthèse et la spectroscopie à haute résolution, c’est toujours passer la nuit à regarder la Voie Lactée.